ION IMPLANTED GaAs SATURABLE ABSORBERS FOR LASER MODE-LOCKING - FUNDAMENTALS AND APPLICATIONS

BY

MAXIMILIAN JOSEF LEDERER

A Thesis Submitted for the
Degree of

Doctor of Philosophy

(Physics)

of

The Australian National University,
Canberra, ACT 0200
Australia

February 1999

CERTIFICATE OF ORIGINALITY

I hereby declare that this submission is my own work and that, to the best of my knowledge and belief, it contains no material previously published or written by another person nor material which, to a substantial extent, was accepted for the award of any other degree or diploma of a university or other institution of higher learning, except where due acknowledgment is made in the text.

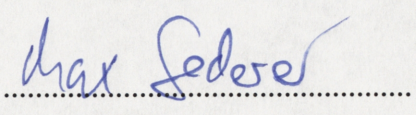

Dedication

To Frances, Josefine and ? (due next week)

ACKNOWLEDGMENT

I am indebted to my supervisors Prof. Barry Luther-Davies, Dr. Yangie Wang and advisors Dr. Yue Gao, Dr. Neil Manson, Dr. Chennupati Jagadish for guidance and many discussions.

I would like to express gratitude to my collaborators at the ANU [Drs. Chennupati Jagadish, Hark Hoe Tan (Electronic Materials Engineering) who performed the MOCVD growth, ion-implantation, RBS-C and TEM; and Dr. Nail Akhmediev (Optical Science Centre)] and the Institute of Quantum Electronics, ETH Zürich [Markus Haiml, Dr. Uwe Siegner and Prof. Ursula Keller who supported my stay at the ETH] for their cooperation.

Thanks to all students, technical and academic staff at the Laser Physics Centre as well as the Department of Electronic Materials Engineering for their support.

I acknowledge the Australian Postgraduate Award - Industry provided by the Australian Government and the support of Electro Optic Systems (EOS) Pty. Ltd. who was my industry partner during this project.

I would also like to thank Prof. Reinhard Höpfl, Dr. Ben Greene and Dr. Yue Gao for the encouragement and mentorship which I have received in the lead-up to the start of my PhD.

PUBLICATIONS

[1] M. J. Lederer, B. Luther-Davies, H. H. Tan, and C. Jagadish, "GaAs Based Anti-resonant Fabry Perot Saturable Absorber Fabricated by Metal Organic Vapour Phase Epitaxy and Ion-implantation," *Appl. Phys. Letters* **70**, pp. 3428-3430, 1997.

[2] N. N. Akhmediev, A. Ankiewicz, M. J. Lederer, and B. Luther-Davies, "Ultrashort pulses generated by mode-locked lasers with either a slow or a fast saturable-absorber response," *Opt Lett.* **23**, pp. 280-282, 1998

[3] N. N. Akhmediev, M. J. Lederer, and B. Luther-Davies, "Exact localized solution for nonconservative systems with delayed nonlinear response," *Physical Review E*, **57**, no. 2, pp. 1-4, 1998

[4] M. J. Lederer, B. Luther-Davies, H. H. Tan, and C. Jagadish, "An Anti-resonant Fabry-Perot Saturable Absorber for Passive Mode-locking Fabricated by Metal Organic Vapour Phase Epitaxy and Ion-implantation - Design, Characterisation and Mode-locking," *IEEE J. Quantum Electron.*, **QE-34**, pp. 2150-2162, 1998

[5] M. J. Lederer, B. Luther-Davies, H. H. Tan, C. Jagadish, M. Haiml, U. Siegner, and U. Keller, "Nonlinear optical absorption and temporal response of As- and O- implanted GaAs", *Appl. Phys. Lett.*, accepted for publication on 5th April 1999.

[6] M. J. Lederer, B. Luther-Davies, H. H. Tan, C. Jagadish, N. N. Akhmediev, and J. M. Soto-Crespo, "Multi-pulse Operation of a Ti:Sapphire Laser Mode-locked by an Ion-implanted Saturable Absorber Mirror," *J. Opt. Soc. Am. B*, accepted for publication

[7] J. M. Soto-Crespo, N. N. Akhmediev, M. J. Lederer, and B. Luther-Davies, "Multisoliton solutions in passively mode-locked lasers," *OSA Annual Meeting*, 1998, October 4-9, Baltimore, Maryland.

[8] N. N. Akhmediev, J. M. Soto-Crespo, M. J. Lederer, and B. Luther-Davies, "Multisoliton regime of lasers passively mode-locked with a semiconductor grating reflector," *ACOFT-98*, Aug. 1998, Melbourne, Australia.

[9] M. J. Lederer, B. Luther-Davies, H. H. Tan, C. Jagadish, and N. N. Akhmediev, "Single and Multi-pulse Soliton States observed in a Ti:Sapphire Laser Mode-locked by an Ion-implanted Anti-Resonant Fabry-Perot Saturable Absorber," *CLEO/Europe*, September 15-17, 1998, Glasgow, Scottland, Talk CWM 6.

[10] M. J. Lederer, B. Luther-Davies, H. H. Tan, and C. Jagadish, "Characteristics of Anti-Resonant Fabry-Perot Saturable Absorbers for Laser Mode-locking Produced by Metal Organic Chemical Vapour Deposition and Ion-

implantation," *CLEO/Europe*, September 15-17, 1998, Glasgow, Scottland, Talk CThK 4.

[11] C. Jagadish, H.H. Tan, J. Jasinski, K.P. Korona, M. Kaminska, R. Viselga, S. Marcinkevicius, A. Krotkus, M.J. Lederer and B. Luther-Davies, "Ion-implanted GaAs for ultrafast optoelectronic applications," *193rd Meeting of the Electrochemical Society*, May 3-8, 1998, San Diego, California (Invited Talk).

[12] M. J. Lederer, B. Luther-Davies, H. H. Tan, and C. Jagadish, "An ion-implanted Anti-resonant Fabry-Perot Saturable Absorber for Passive Mode-locking of Solid State Lasers," *10th Conference on Semiconducting and Insulating Materials (SIMC-X)*, June 1-5, 1998, Berkeley, California.

[13] M. J. Lederer, B. Luther-Davies, C. Jagadish, and H. H. Tan, "The Properties and Performance of Anti-Resonant Fabry-Perot Saturable Absorbers for Passive Mode-Locking Fabricated by Metal Organic Vapor Phase Epitaxy and Ion-Implantation," *11th Annual Meeting of the IEEE Lasers and Electro-Optics Society (LEOS)*, Dec. 1-4 1998, Orlando, Florida (Invited Talk).

[14] M. J. Lederer, B. Luther-Davies, H. H. Tan, and C. Jagadish, "Semiconductor Saturable Absorber Mirrors (SESAMs) for Laser Mode-locking and Q-switching," *Defence Science and Technology Organisation (DSTO) Workshop on Lasers and Optoelectronics*, 6th-7th August 1998, Adelaide, Australia.

[15] M. J. Lederer, B. Luther-Davies, H. H. Tan, C. Jagadish, and N. N. Akhmediev, "Solitonic Mode-locking in a SESAM Modulated Titanium Sapphire Laser," *Defence Science and Technology Organisation (DSTO) Workshop on Lasers and Optoelectronics*, 6th-7th August 1998, Adelaide, Australia.

[16] M. J. Lederer, B. Luther-Davies, H. H. Tan, C. Jagadish, M. Haiml, U. Siegner, and U. Keller, "Nonlinear Optical Properties of Ion-implanted GaAs," *Conference on Optoelectronic and Microelectronic Materials and Devices (COMMAD)*, Dec. 14-16 1998, Perth, Australia, Talk TO7

PATENTS

M. J. Lederer, B. Luther-Davies, "Efficient Thermal Management of Low Conductivity Laser Materials," Australian Provisional Patent Application of The Australian National University, Feb. 1999

ABSTRACT

This thesis is concerned with ion-implanted Gallium-Arsenide (GaAs), grown by Metal Organic Chemical Vapour Deposition (MOCVD), and its application in Semiconductor Saturable Absorber Mirrors (SESAMs) for mode-locking of solid-state lasers. The design and properties of an Arsenic (As) implanted GaAs-based SESAM device are presented and the physics of the operation as mode-locking element is outlined. Using reflectance spectroscopy and ultrafast differential reflectivity measurements, the influence of As implantation and thermal annealing on the SESAM reflectivity, temporal response and saturation behaviour are shown. It is demonstrated that the implantation process shortens the small signal recovery time of the SESAMs by more than two orders of magnitude, whilst for large signals even the unimplanted device possesses ps-response. Similar to Low Temperature (LT) Molecular Beam Epitaxy (MBE) grown GaAs, the implantation process decreases the achievable modulation depth.

Mode-locking experiments incorporating the fabricated SESAMs in a Titanium Sapphire laser are then described. Self-starting soliton mode-locking of pulses as short as 105fs could be achieved around 840nm with output powers of up to 900mW and a tunability range of 50nm. Interestingly, the differences in the laser's operation using different SESAMs were subtle, despite the large range of ion doses used in implantation. Apart from single soliton emission, the laser also produced multiple soliton states with far as well as close separation. The experimental observations are explained within the framework of the Ginzburg-Landau master equation model, relevant for such a laser. Stability conditions for single and multiple solitons in the laser cavity are derived and regions for their existence are found.

On a more fundamental note, results of nonlinear optical absorption bleaching measurements on ion-implanted GaAs are shown. These are relevant for ultrafast nonlinear optical modulator applications of GaAs in general. Arsenic (As) and Oxygen (O) implanted MOCVD-grown GaAs samples were measured in this context for a range of ion doses and annealing temperatures. It is shown that similar combinations of response time τ_A and modulation M_{max} can be achieved using either ion species and different combinations of dose and annealing temperatures, and that the data are all located on a fairly well-defined curve in the (τ_A, M_{max}) plane. This indicates that there exists a limit to the modulation if a specific response time is required and that the defects created by different ion species are of similar nature, i. e. point defects, provided amorphisation, which occurs at high implant doses, is avoided.

Extending the applications of MOCVD-grown, ion-implanted SESAMs towards longer wavelengths, a (diode pumped) Nd:YVO_4 laser, mode-locked in self-starting fashion by InGaAs-based SESAMs, is shown. Continuously variable output pulsewidths in the 10ps regime could be achieved using variable output coupling.

Finally a diode pumped Nd:YVO_4 amplifier design is presented. It is shown through computer simulations and experiments that the design is optimised in order to minimise the thermal gradients and the absolute temperature rise, compensating for the relatively poor thermal conductivity of Nd:YVO_4, whilst making use of its favourable pump absorption and gain cross section. Both oscillator and amplifier are of immediate relevance to EOS' applications in satellite laser ranging with mm accuracy.

CONTENTS

AMENDMENTS

The following amendments to the thesis were made in accordance with the examiners recommendations.

1. *page 2, lines 10-11:* "...InGaAs-based SESAMs for which the growth technology was not available at the time." must read "...InGaAs-based SESAMs for which the growth technology was not available at the ANU at that time."

2. *page 28, line 34:* "Sellmeir" must read "Sellmeier".

3. *page 31, line 12:* "...indirectly proportional to the modulation depth..." must read "...inversely proportional to the modulation depth..."

4. *page 91, line 7:* "...such as dyes [91],..." must read "...such as dyes [91] and semiconductors [91a, 91b],..."
   The references introduced in this context are
   [91a] M. Zirngibl et al., "1.2ps pulses from passively mode-locked laser diode pumped Er-doped fibre ring laser," Electron. Lett., **27**, pp. 1734-1735, 1995
   [91b] H. Lin et al., "Colliding pulse mode-locked lasers using Er-doped fiber and a saturable absorber," Technical Digest, Conference on Lasers and Electro-optics, **15**, paper JTuE1, May 1995

5. *page 94, line 19:* "Two samples were then implanted with 350keV As ions of doses..." must read "Two samples were then implanted with As ions of energy 350keV (for optimal damage distribution inside the absorber) and doses of..."

CHAPTER 1

INTRODUCTION

Recently there has been considerable interest in the creation of very short pulses (<10fs) in the near infra-red using Kerr lens mode-locking (KLM) of broadband solid state laser materials such as Ti:Sapphire [1, 2]. A disadvantage of KLM is the very small parameter space in which self-starting can be obtained [3] due to its very high effective saturation intensity. It was predicted [4] and demonstrated [5-9] that this can be overcome by using resonant passive mode-locking (RPM) where an anti-resonantly coupled external cavity containing a semiconductor resonant nonlinear element provides the starting for mode-locking action. It was later shown that the external cavity could be replaced by a monolithic device known as an anti-resonant Fabry-Perot saturable absorber (A-FPSA) which consists of a multiple quantum well (MQW) or bulk semiconductor absorber sandwiched between a semiconductor Bragg (bottom) mirror and a dielectric (top) mirror [10]. The A-FPSA is therefore essentially a saturable nonlinear laser mirror. Several different designs of A-FPSAs have now been published with varying absorber layer thickness and top mirror reflectivity [11]; different design wavelengths [12-16]; and including limited dispersion compensation [17]. Later the devices were collectively called Semiconductor Saturable Absorber Mirrors (SESAMs) [18]. Self-starting stable mode-locking has been achieved routinely in all cases with the SESAM either providing the saturable nonlinearity for starting the KLM process or as the sole nonlinear modulator allowing the generation of ps pulses or fs pulses when solitonic pulse shaping also occurred [14]. In addition, single quantum well saturable absorber mirrors have been used to mode-lock Ti:Sapphire and other lasers. Such SESAMs are also called low-finesse A-FPSAs or Saturable Bragg Reflectors (SBR) [19-21].

So far, the critical absorber layers in the SESAMs have been grown using Low-Temperature Molecular Beam Epitaxy (LT-MBE) which is known to introduce EL2-like deep-level traps in GaAs, resulting in carrier lifetimes in the ps and sub-ps regime [23]. Short carrier lifetimes, leading to rapid recovery of absorption bleaching, suppress self-Q-switching in laser materials with long upper state lifetimes by increasing the quasi-steady state saturation intensity of the modulator [24]. However, it has been known for more than a decade [25, 26] that ion-irradiated semiconductors also display ps carrier lifetimes. More recent investigations into the optical, electrical and structural properties of ion-implanted GaAs have found [27-29] that the latter is in fact very similar to LT-GaAs. Although the nonlinear absorption modulation of ion-implanted GaAs, which is an important parameter in laser mode-locking applications, was not yet examined the similarity of the two materials was encouraging and prompted the present research. Further, a potential advantage of the route via ion-implantation is its versatility. Structures can be grown at normal temperatures using the more readily available Metal Organic Chemical Vapour Deposition (MOCVD) process, and due to

the lateral selectivity of ion-implantation, different device properties can be created from a single wafer, effectively increasing the yield.

At the starting point of this PhD project was the objective to develop a compact diode-pumped laser system capable of producing kHz-repetition rate picosecond pulses with up to 1 mJ of energy at the wavelength of 1.06μm. This could be used in satellite laser ranging systems of Electro Optic Systems (EOS) Pty. Ltd., the industry partner of this project. In view of the potential of ion-implanted semiconductors for fast saturable absorber applications, it was decided that a passively mode-locked oscillator-amplifier combination should be used, facilitating this technology. However, mode-locking at λ = 1.06μm requires InGaAs-based SESAMs for which the growth technology was not available at the time. Therefore the approach was to thoroughly investigate the nonlinear absorption properties of MOCVD grown ion-implanted GaAs, and explore the use of this material as a saturable absorber in mode-locking of a near-infrared laser. The extension towards longer wavelengths should then be straightforward, given the experience collected with ion-implanted GaAs, and once the relevant materials were available. In parallel to the work on implantation, characterisation and mode-locking applications of ion-implanted GaAs, the design of a laser amplifier was begun, focusing on the improvement of thermal management of poorly conducting laser materials.

The following thesis presents the outcome of the project outlined above. Chapter 2 is concerned with the design and properties of an ion-implanted GaAs-based SESAM. The fabricated SESAMs were incorporated in a Ti:Sapphire laser. Chapter 3 contains both the experiments and theoretical analysis of the single and multi-pulse soliton mode-locking operation of this laser. In chapter 4 the results of nonlinear optical absorption measurements on ion-implanted GaAs are presented. These are of relevance to all nonlinear optical modulator applications of this material. Finally, chapters 5 and 6 cover topics aimed directly at EOS's satellite laser ranging applications. Mode-locking results using an InGaAs-based SESAM in a Nd:YVO_4 laser with continuously variable output pulsewidth are presented in chapter 5, and a compact, thermally optimised Nd:YVO_4 amplifier design is demonstrated in chapter 6. Using computer simulations and experiments, the design is shown to minimise gradients and temperature rise in laser materials with strong pump absorption and poor thermal conductivity.

CHAPTER 2

A GAAS BASED ION-IMPLANTED SESAM FOR MODE-LOCKING OF A NEAR INFRA-RED SOLID-STATE LASER

Section *2.1* is concerned with the design, the fabrication and the description of some basic properties of the ion-implanted SESAM. The relevant physical mechanisms involved in the operation as saturable absorbers are outlined, and the influence of ion-implantation as well as thermal annealing on the reflectivity are shown. Section *2.2* contains the results of time-resolved differential reflectivity measurements, where the emphasis is again on the influence of ion-implantation on the SESAM response when compared to the unimplanted case. Both small and large signal responses are considered.

2.1. Design, Fabrication and Basic Properties

A diagram of the epitaxial design of the SESAM is shown in *Fig. 2.1. - 1a.* The structures consist of 25 high/low index, $Al_{0.15}Ga_{0.85}As$/AlAs, layer pairs grown on a wafer of semi-insulating GaAs and designed to form a Bragg mirror with a centre wavelength of λ_B = 830nm. Upon the mirror a non-absorbing AlAs spacer layer was grown, and on top of this, the 45nm GaAs absorber layer. The lack of a dielectric top mirror causes this SESAM to be classified as a low-finesse μ-cavity, with $R_{top} \approx 0.3$ due to the GaAs-air interface.

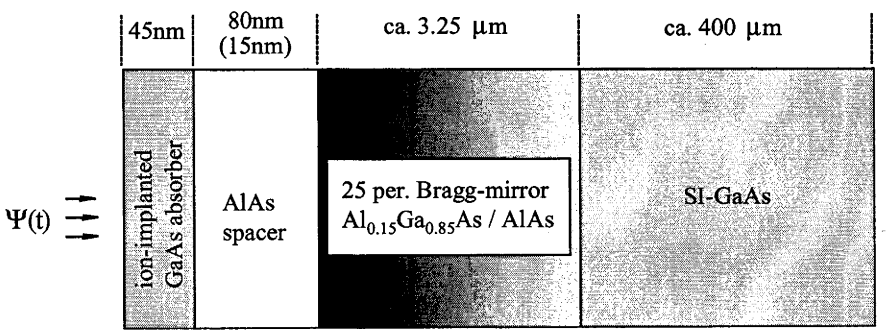

Fig. 2.1. - 1a: Epitaxial design of the ion-implanted low-finesse SESAM

The Aluminium content of 15% in the high index layer of the mirror is a compromise. It ensures the highest possible bandwidth, hence high-low index difference Δn, whilst the optical absorption within the wavelength range of interest remains negligible. The resulting bandgap wavelength is $\lambda_{Al_{0.15}GaAs} \approx 750nm$ and the refractive index is $n_{Al_{0.15}GaAs} \approx 3.5$ [36]. Using the quarter-wave condition, $t = \lambda_B \cdot (4 \cdot n)^{-1}$, for dielectric stacks and the AlAs refractive index of 2.97 one calculates the nominal thicknesses of t_h = 59.3nm and t_l = 69.6nm for the high index and low index layers respectively. A

separately grown Bragg mirror was measured to have a reflectivity of greater than 99.7% at the Bragg wavelength, confirming the quality of the mirrors. Two devices were grown, one with a spacer thickness of 80nm making the SESAM anti-resonant, the other with 15nm making it resonant at the design wavelength (see below). The wafers were diced into 6x6mm pieces and implanted with As ions. The use of Arsenic as the implanter ion is partly a historical hangover. After it was established that the fast carrier capturing in LT-GaAs is due to excess As, present in the GaAs lattice in the form of As-antisite defects (As_{Ga}), attempts were made to achieve similar levels of excess As through implantation. Although this is possible and many optical and electrical properties of LT-GaAs were matched, it was also shown that implantation of other ion species (O, Ga, Si, Ar) showed similar results [33-35], questioning the role played by the As ions. However, As implantation is still commonly used to make ultrafast photoconductive switches [30] and, due to past experience, was a natural choice for the SESAMs. Two implant runs were made using different ion energies, one 40keV, the other 80keV. The use of these values of ion energies was motivated through Monte Carlo simulations of the implantation process using the TRIM95 software [31]. Using Rutherford Backscattering Spectroscopy-Channelling (RBS-C) measurements, this simulation technique was shown to predict the damage profiles in As implanted GaAs rather well [32]. *Fig. 2.1. - 1b* shows the density of vacancies caused by primary as well as secondary 'knock-ons' obtained from such a simulation. For the 40keV ions the damage is entirely restricted to the absorber layer, although with a slightly off-centre maximum. For 80keV the distribution is centred, but a small damage tail extends into the spacer layer. The different ion energies were mainly used in order to determine the influence of the damage distribution in the absorber on the SESAM response.

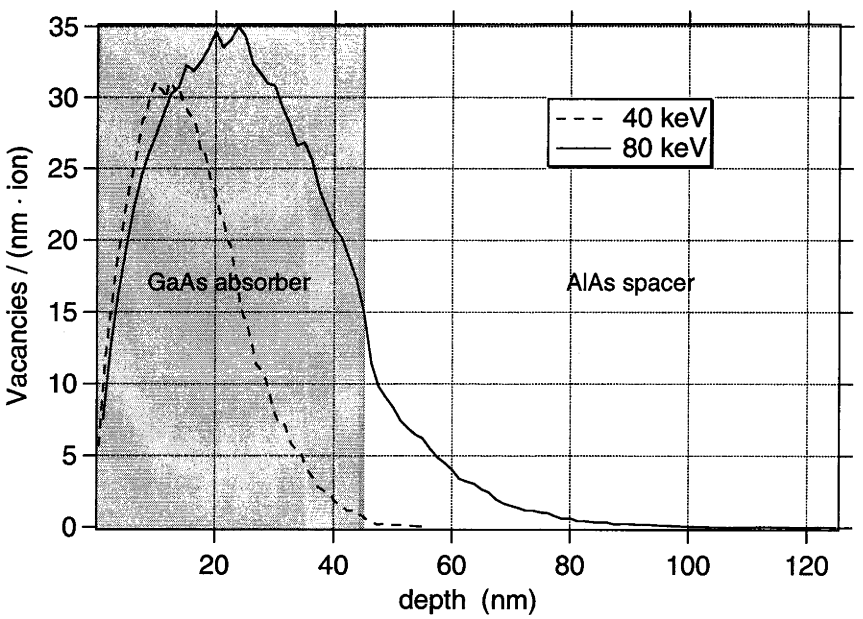

Fig. 2.1. - 1b: Total vacancy distribution due to primary as well as secondary 'knock-ons' obtained from a TRIM95 simulation.

It was undetermined which ion dose would be needed to create a particular SESAM response and therefore a large range of doses had to be covered. For the 40keV implants doses between $8 \cdot 10^{10}$ cm^{-2} and 10^{15} cm^{-2} were used whereas the 80keV implants ranged from $8 \cdot 10^{10}$ cm^{-2} to $5 \cdot 10^{11} cm^{-2}$. The samples then underwent thermal annealing at 600 °C for 20 min in an arsine atmosphere to prevent excessive loss of arsenic from the surface. These conditions were found to remove much of the implantation damage caused by high ion doses whilst retaining short luminescence life times [33]. Several samples implanted with low doses ($8 \cdot 10^{10}$ cm^{-2} → $5 \cdot 10^{11}$ cm^{-2}) also remained unannealed.

Fig. 2.1. - 2a-d illustrate some important properties of the SESAMs. *Figs. - 2a* and *- 2b* show the measured and calculated low intensity reflectivity for the anti-resonant (80nm spacer) and the resonant (15nm spacer) SESAMs respectively before implantation. The reflectivity of the anti-resonant device is almost constant and high over a broad range (ca. 60nm) which is important for ultra-short pulse generation. The degree of anti-resonance in a SESAM of this type can be increased, for example, by widening the spacer layer and decreasing the absorber thickness slightly, permitting theoretical reflectivities of greater than 99% which are necessary for mode-locking of low-gain laser materials like Cr:LISAF.

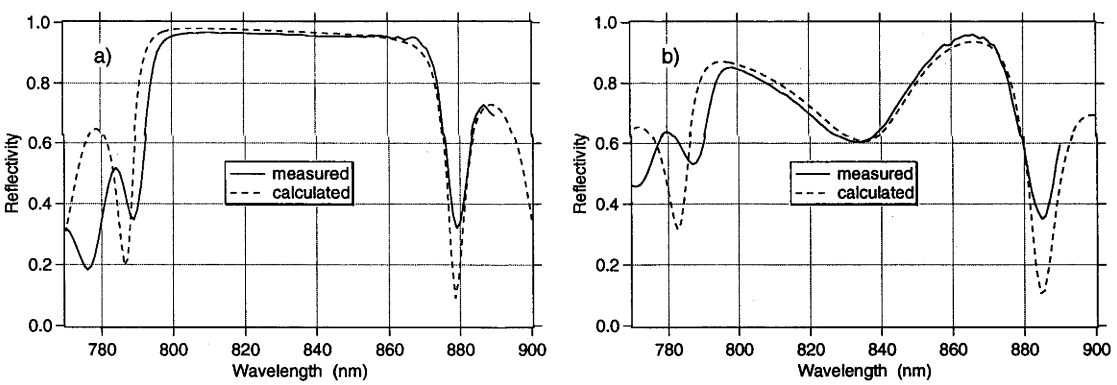

Fig. 2.1. - 2a,b: Measured and calculated reflectivities of (a) anti-resonant SESAM and (b) resonant SESAM.

Fig. - 2c shows the calculated standing wave distribution in front of and inside the resonant and anti-resonant devices. As is evident from *Fig. - 2c*, in the anti-resonant case the node of the standing wave is shifted into the absorber region, whereas in the resonant case it is the anti-node, leading to suppression or enhancement of the double pass extinction due to the GaAs layer. The relatively broad appearance of the resonance dip in *Fig. - 2b* is due to the low finesse of the cavity formed by the Bragg reflector (R≈100%) and the GaAs-air interface (R≈30%).

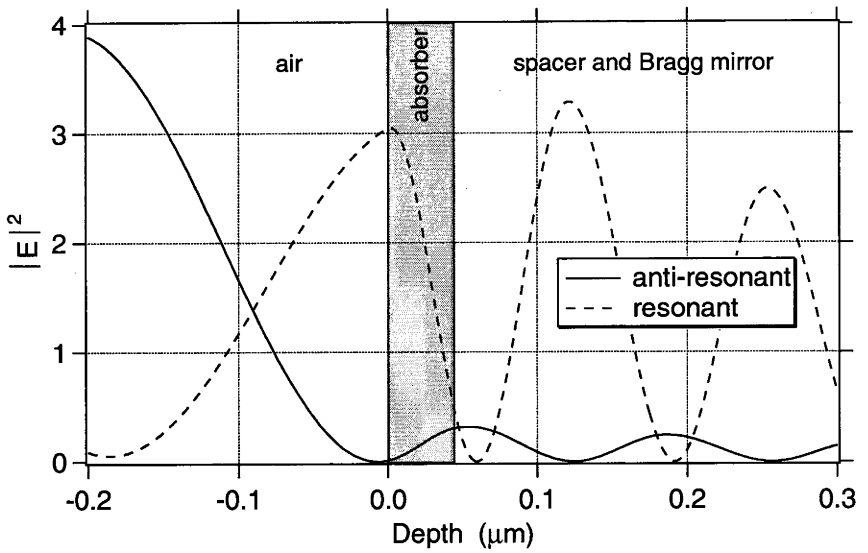

Fig. 2.1. - 2c: Normalised standing wave power distribution in front of and inside the SESAM.

Finally, *Fig. - 2d* shows the calculated Group Delay Dispersion (GDD) and Third Order Dispersion (TOD) of the SESAMs

$$GDD = \frac{d^2\phi}{d\omega^2} \qquad \text{and} \qquad TOD = \frac{d^3\phi}{d\omega^3} \qquad (2.1 - 1)$$

where ϕ is the phase of the complex reflection coefficient r. Within the range of high reflectivity, GDD and TOD lie between +100fs² ... -100fs² and +500fs³ ... 3000fs³. This is low enough for the generation of pulses shorter than 100fs in standard ultrafast laser cavities. On the other hand, the resonant SESAM could not be used as a modulator in a fs-laser cavity, as it introduces too much loss and dispersion.

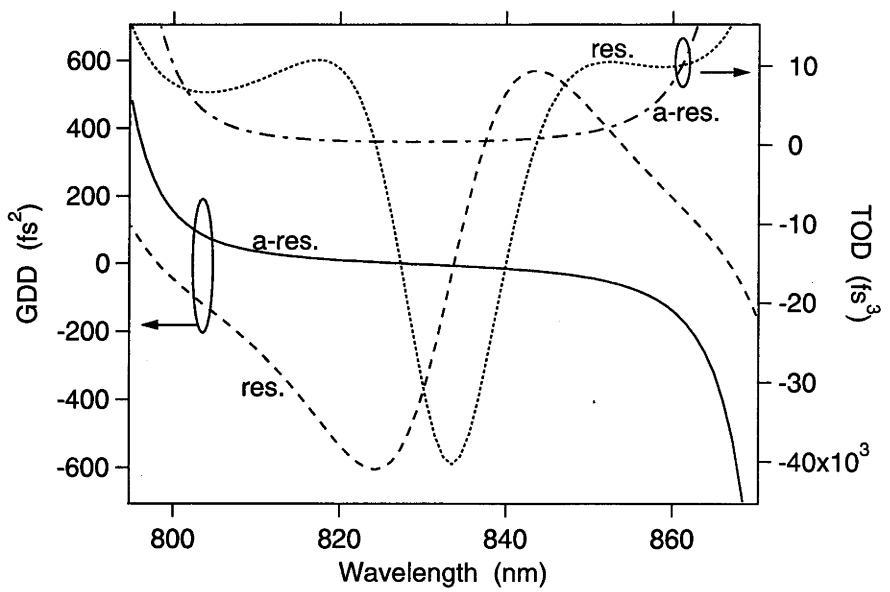

Fig. 2.1. - 2d: Calculated GDD and TOD of resonant and anti-resonant SESAMs.

In the calculations the absorption of GaAs was modelled using Banyai-Koch plasma theory [38] whilst the reflectivity and the standing wave structure inside the device as well as GDD and TOD were calculated using matrix methods [37, 39, 40].

Fig. 2.1 - 3 shows the reflectivity of an implanted resonant as well as anti-resonant device before and after annealing. Here the implantation dose was 10^{15} cm^{-2}, the highest of all implanted doses. It was found that for ion doses $\geq 10^{12}$ cm^{-2}, the implantation induced damage leads to a strong change in the complex refractive index of the absorber layer which severely degrades the reflectivity. As can be shown through modelling, both the imaginary and the real part of the complex index increase, leading, in the case of the resonant structure, to a stronger resonance dip shifted towards longer wavelengths compared with the unimplanted sample. Most importantly, however, the original reflectivity can be fully restored by annealing as is evident from a comparison between *Figs. 2.1 - 2a* , *Fig. 2.1 - 2b* and *Fig. 2.1 - 3*.

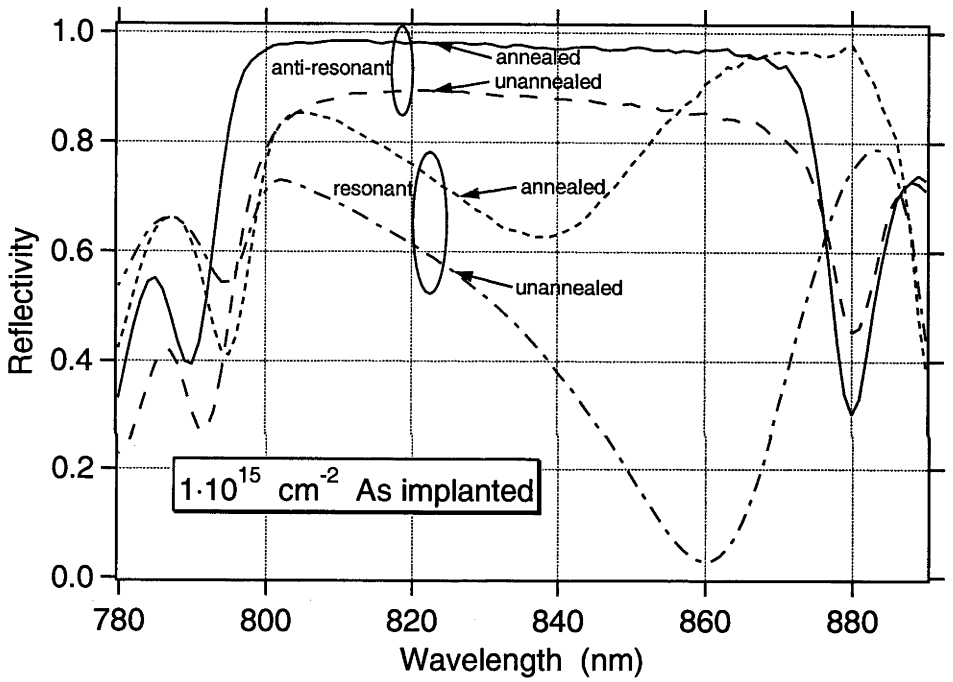

Fig. 2.1. - 3: Effect of $1 \cdot 10^{15}$ cm^{-2} As implantation followed by thermal annealing at 600°C for 20 min under arsine ambient on the SESAM reflectivity.

In the case of an incident optical pulse or cw-radiation with a centre wavelength between 810nm and 870nm, carriers are excited into the conduction and valence bands of the GaAs absorber which has its room temperature bandgap at λ=870nm. The AlAs spacer and the Bragg mirror are non-absorbing over this wavelength range. Generally, the excited carrier density will change both the imaginary (absorptive) and real (refractive) part of the complex refractive index of the absorber. Depending on the duration of the incident pulse and the time scale of interest, the device reflectivity changes in different ways. In unimplanted GaAs grown at normal temperature (600...700°C), using MOCVD or MBE, the reflectivity (or transmission) evolves on both fast (100fs ... ps) and slow (10 ... 100ps) time scales. The

slow time scale is mainly due to impurity induced or surface induced recombination and radiative electron-hole recombination. The associated time constant is usually called the 'carrier lifetime' and the change in reflectivity is referred to as originating from a bandfilling or quasi-steady state nonlinearity. In this regime, both electrons and holes assume quasi-equilibrium Fermi-Dirac distributions within their respective bands [44]. The fast time scale signals originate from spectral hole-burning (i. e. non-thermal carrier distributions) which is followed by thermalisation and cooling of the distribution to the lattice temperature. The latter two effects are mainly accomplished through carrier-carrier and carrier-(LO-)phonon interactions. During the spectral hole-burning phase one speaks of a state-filling nonlinearity. Another fast scattering process which is observed in GaAs is Γ-X inter-valley scattering. However, it gains importance only at excitation wavelengths shorter than 700nm [44], or under strong excitation when free carrier absorption (FCA) and two photon absorption (TPA) gain relevance. A diagram illustrating these mechanisms is shown in *Fig. 2.1 - 4*. The slow and fast time scales both play a role in passive mode-locking. Whereas the slow nonlinearity mainly determines the mode-locking build-up and Q-switching dynamics, it is the fast response that can stabilise the ultra-short pulses by creating a short enough net-gain window to prevent growth of dispersive radiation in the continuum.

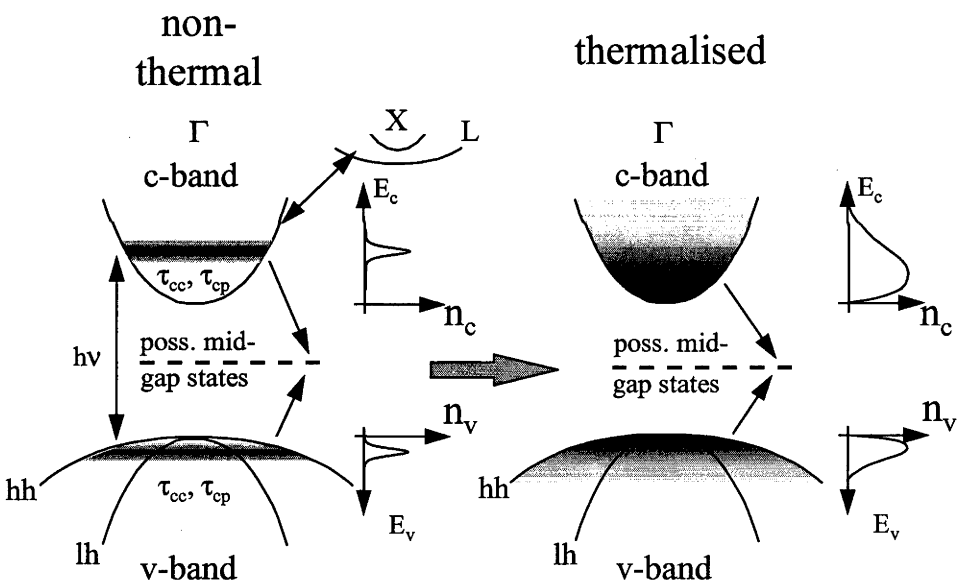

Fig. 2.1 - 4: Schematic band diagram illustrating non-thermal and thermal carrier distributions in GaAs. τ_{cc} and τ_{cp} are carrier-carrier and carrier-phonon interaction time constants. Also shown are mid-gap states introduced through low-temperature growth or ion implantation.

In the case of the SESAMs it is interesting to compare the absorptive and refractive contributions to the nonlinear reflectivity change. Although calculations of the most general case, where the hole-burning phase and carrier-carrier as well as carrier-phonon scattering are included in the kinetics [38] are beyond the scope of this thesis, it is nevertheless useful to consider the situation in quasi-equilibrium. This can

be done using the Banyai-Koch model [38] which gives very realistic results for bulk GaAs in this context. The Banyai-Koch theory calculates the carrier density dependent absorption $\alpha(\omega,N)$ in the effective electron-hole pair approximation, neglecting the reduction of the electron-hole Coulomb attraction due to the filling of energy-momentum states. It takes into account continuum and exciton states, plasma screening and bandgap renormalisation. Once the change of absorption $\Delta\alpha(\omega) = \alpha(\omega,N_2) - \alpha(\omega,N_1)$ has been obtained, the refractive index change due to the injection of the carrier density ΔN is given through the Kramers-Krönig relation [41]

$$\Delta n(\omega, N_2 - N_1) = \frac{c}{\pi \cdot \omega} \cdot P \int_{-\infty}^{\infty} \frac{\Delta\alpha[\Omega]}{\Omega - \omega} d\Omega \qquad (2.1 - 2)$$

where P indicates the principal value of the integral. The result of such a calculation is shown in *Fig. 2.1 - 5a* for a carrier density of $N = 2 \cdot 10^{18}$ cm^{-3}. Note that, although the Kramers-Krönig relation *(2.1 - 2)* is strictly not valid in the nonlinear regime, it can be applied here due to the slow variation of the quasi-steady state (10 ... 100ps).

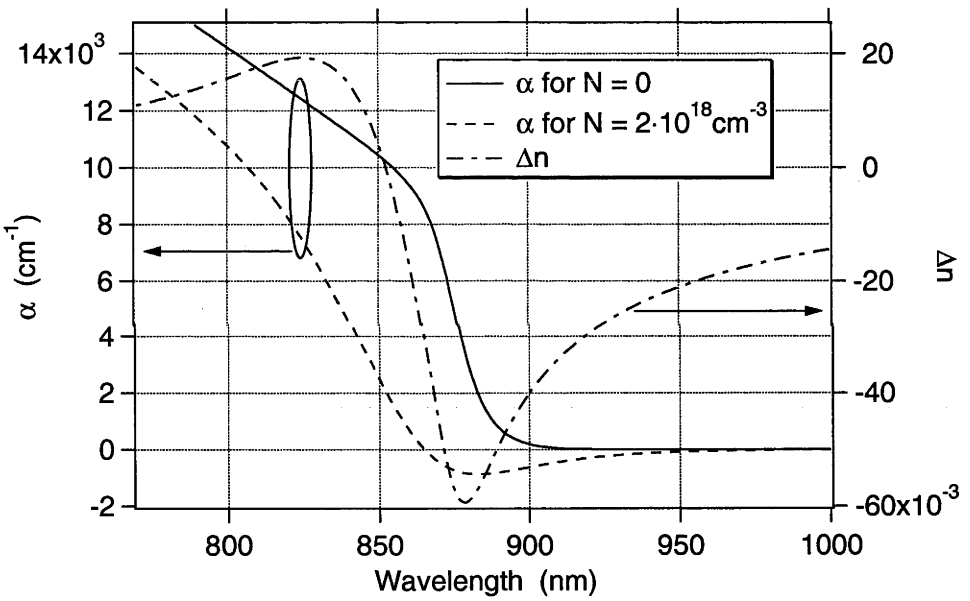

Fig. 2.1 - 5a: Absorption constant α and change of refractive index Δn due to a thermalised carrier density of $N = 2 \cdot 10^{18}$ cm^{-3} as calculated by the Banyai-Koch model.

Figs. 2.1 - 5b and *c* depict the anti-resonant and resonant SESAM reflectivities calculated for $N = 0$ and $N = 2 \cdot 10^{18}$ cm^{-3}, and the insets show the reflectivity change for the cases when the dispersion of the band edge is included or ignored in the reflectivity calculations. Most importantly, as can be seen from the insets, the reflectivity change is dominated by absorption bleaching in both the anti-resonant and resonant SESAMS. Note that, although for $N = 2 \cdot 10^{18}$ cm^{-3} the absorber is effectively inverted for $\lambda > 865$nm and absorption turns into gain, the reflectivity remains below 1 due to the roll-off of the mirror.

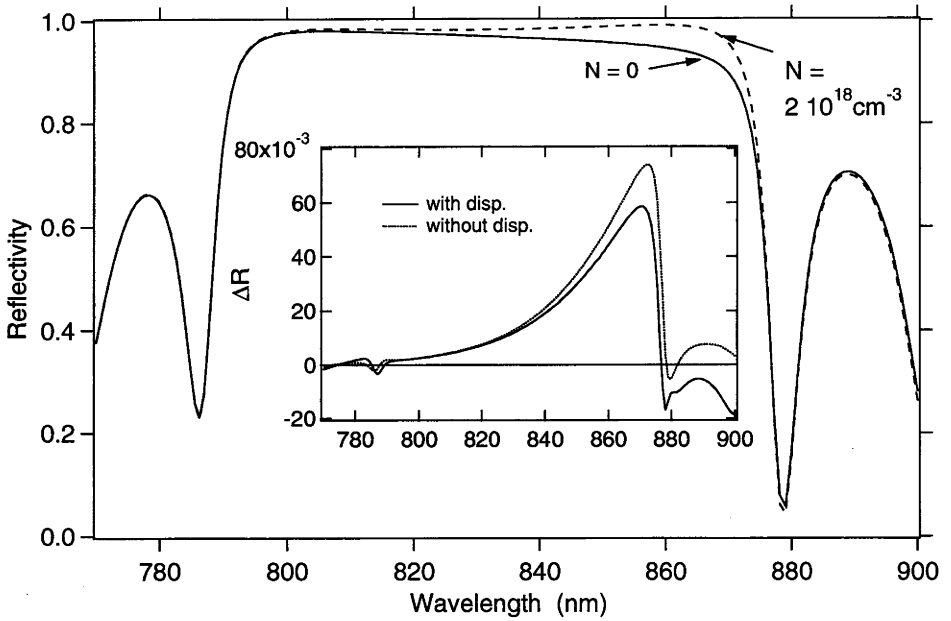

***Fig. 2.1 - 5b*:** Reflectivity of the anti-resonant SESAM for carrier densities of N = 0 and N = $2 \cdot 10^{18}$ cm^{-3}. The inset shows the reflectivity change ΔR. The complex refractive index was calculated using the Banyai-Koch model.

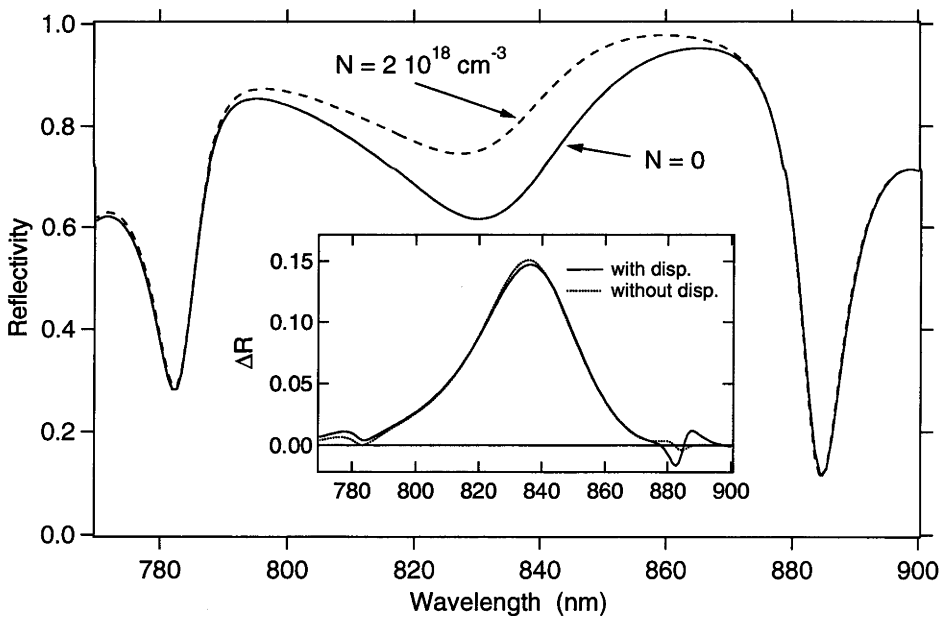

***Fig. 2.1 - 5c*:** Reflectivity of the resonant SESAM for carrier densities of N = 0 and N = $2 \cdot 10^{18}$ cm^{-3}. The inset shows the reflectivity change ΔR. The complex refractive index was calculated using the Banyai-Koch model.

The spectral dependence of the change in reflectivity of the SESAM is, therefore, a complex function of wavelength as well as time. As an example consider the reflectivity of the anti-resonant SESAM for different carrier densities shown in *Fig. 2.1 - 5b*. The carrier induced change in reflectivity in this case is smallest at the shorter wavelengths, because the device is closer to anti-resonance there, and also because the

Fermi-Dirac carrier distribution results in stronger absorption modulation at longer wavelengths. For pulses of several 100fs pulsewidth or shorter, the initial spectral response would contain signatures of partial thermalisation (contributing to a response similar to *Fig. 2.1 - 5b*) and a non-thermal spectral "hole" closely imaging the pulse spectrum. The non-thermal distribution finally thermalises and cools to lattice temperature through carrier-carrier and carrier-phonon scattering with typical time constants of $\tau_{cc} \approx 60$fs and $\tau_{cp} \approx 300$fs respectively [44]. Finally, in materials with a large number of mid-gap traps introduced by ion-implantation or LT-MBE growth (*see Fig. 2.1 - 4*), the response is altered through carrier capturing and recombination via the traps. This is treated in the next section as well as in chapter 4.

2.2. Dynamic Properties

2.2.1. Measurement Setup

The dynamic response was measured using the 75MHz train of 120fs pulses from a Kerr-lens mode-locked Ti:Sapphire laser (Coherent MIRA 900D) and a standard time-resolved, non-collinear, wavelength degenerated pump-probe technique, depicted in *Fig. 2.2.1 - 1*. The angle between the orthogonally polarised pump and probe beams was 7° and the probe intensity was about 30 times smaller than the pump. In order to minimise thermal effects, the pump spot diameter was as small as practicable (30μm), whilst a probe spot diameter about half that of the pump was used to sample the most uniform part of the pump beam. The pump was chopped mechanically and the reflected probe signal monitored using a photodiode and lock-in amplifier. The pump-probe wavelength was tunable around λ=840nm.

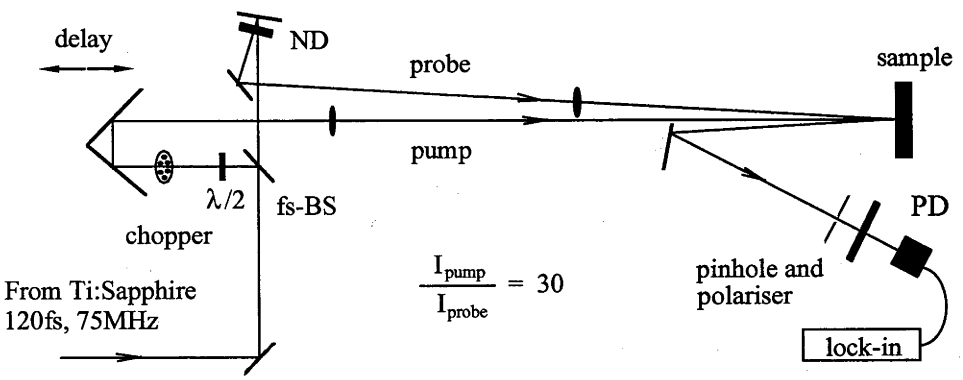

Fig. 2.2.1 - 1: Pump-probe setup used in measurement of the differential reflectivity of the SESAMs. ND (neutral density filter), fs-BS (femtosecond beam splitter), λ/2 (half wave plate).

In order to unambiguously separate the ion-implantation related trapping dynamics from signals associated with spectral hole burning, thermalisation and carrier-phonon interactions, the signals from unimplanted and implanted samples were compared under identical conditions. Because of the better signal to noise ratio

achievable with the resonant SESAMs, the latter were used in the measurements of the carrier dynamics, unless stated otherwise. Signals from the anti-resonant SESAMs are qualitatively the same, as will be shown below. However, due to the anti-resonance, absolute differential reflectivities are typically a factor 10 smaller at 10 times higher pump fluences compared with the case of the resonant SESAMs. From the arguments in the last section, signals from both the resonant and anti-resonant SESAMs are dominated by absorption bleaching.

2.2.2. Small Signal Response

To measure the small signal response, a pump fluence of $F = 1\mu J/cm^2$ was chosen. At this fluence, the average power on the sample was just 0.5mW and no thermal nonlinearity could be detected. Unless stated otherwise, the measurement wavelength was 840nm. The maximum differential reflectivities observed under these conditions ranged from <1% to 3% depending on implantation dose and annealing condition, but also on the wavelength of the design resonance with respect to the pump-probe wavelength. The unimplanted sample gave the largest response, corresponding to an approximate carrier density of $5 \cdot 10^{17}$ cm^{-3} as calculated with the Banyai-Koch model. *Figs. 2.2.2 - 1a* and *1b* show the differential reflectivity signals dR, normalised to the maximum, obtained from unannealed 80keV implanted samples for some doses compared to the unimplanted case. Note that the true peak values of some of the traces were not resolved, but determined through a separate measurement. In the unimplanted case a more or less step function like response is observed (*Fig. 1a*) due to a thermalised carrier distribution (bandfilling nonlinearity). The slight transient in the signal during the first picosecond after pump-probe correlation was positive going for the relatively low fluence of $1\mu J \cdot cm^{-2}$ and became negative going and more pronounced for higher fluences. Generally, this kind of transient is a mixed signal due to thermalisation and carrier-phonon interactions. However, since thermalisation at room temperature in GaAs was measured to have typical time constants of < 60fs [54], the dominant effect here is cooling. The signal decay for long pump-probe delays (*Fig. 1b*) is a combination of radiative, impurity and surface related recombination of the excited electron-hole plasma. Interestingly, for a wavelength of 850nm this decay acquires faster components under otherwise equal conditions. Although speculative, it seems possible that this peculiar behaviour has to do with a slightly different evolution of the generated holes in the heavy-hole and light-hole bands under the influence of LO-phonon scattering (E_{LO} = 36meV above bandgap in GaAs, i. e. $\lambda \approx 846$nm). However, it is of no direct concern here and was not further investigated.

The traces of the unannealed 80keV implanted samples show two distinctly different time scales: fast capturing of free carriers and relatively slow trap emptying. The traces depicted in *Figs. 2.2.2 - 1a* were fitted from the dR = 0.8 crossing following the peak, using the double exponential model

$$dR = K_0 + K_1 \cdot \exp\left(-\frac{t}{\tau_1}\right) + K_2 \cdot \exp\left(-\frac{t}{\tau_2}\right) \qquad (2.2.2 - 1).$$

The fit parameters are listed in *Table 2.2.2 - 1*. Note that, in spite of the phenomenological nature of the fit, it allows the dominant time scales to be extracted. Furthermore, an effective single exponential recovery time τ_{eff} is given in order to be able to better compare the recovery speed of samples. Here, τ_{eff} is defined as

$$\tau_{eff} = \frac{K_1 \cdot \tau_1 + K_2 \cdot \tau_2}{K_1 + K_2} \qquad (2.2.2 - 2),$$

although a different definition, for instance the 1/e level crossing after the peak, would also serve the purpose. As an example, even for the $8 \cdot 10^{10}$ cm^{-2} implanted sample (lowest dose), the response contains an ultrafast capturing transition with a time constant of τ_1 = 238fs, followed by a decay with τ_2 = 31.3ps, mainly associated with trap emptying, which leads to a τ_{eff} = 16.7ps. However, from the fit over delays ranging from several ps to 300ps (*Figs. 2.2.2 - 1b*) one deduces that the decay becomes progressively slower since at least one further time constant, τ = 188.7ps, can be extracted for this sample.

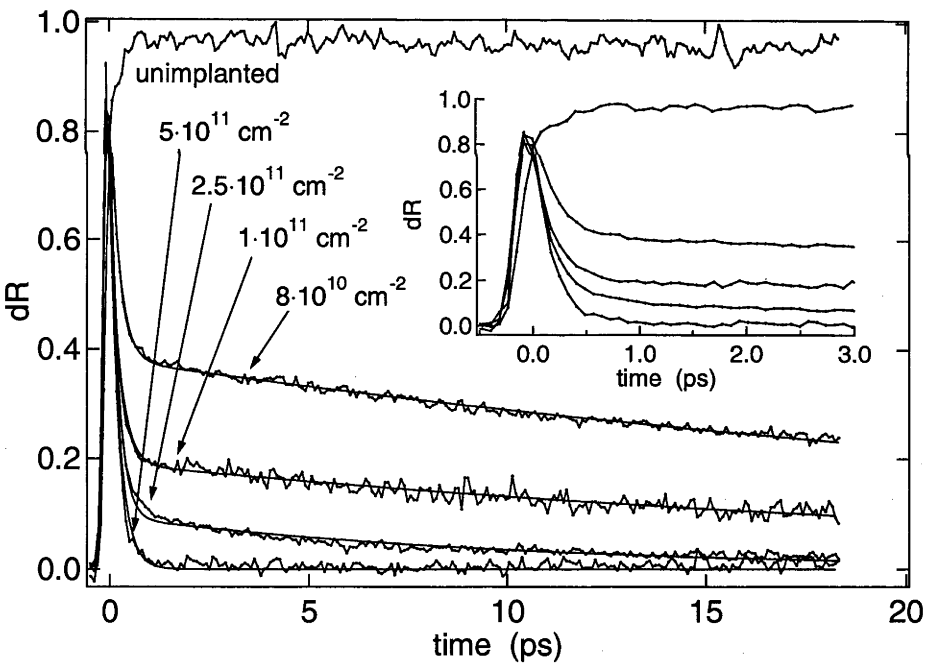

Fig. 2.2.2 - 1a: Short delay dR signals and numerical fit of various doses of 80keV-implanted, unannealed resonant SESAMs compared to the unimplanted case. λ_{pump} = 840nm, F_{pump} = 1μJ/cm^2, P_{av} = 0.5 mW.

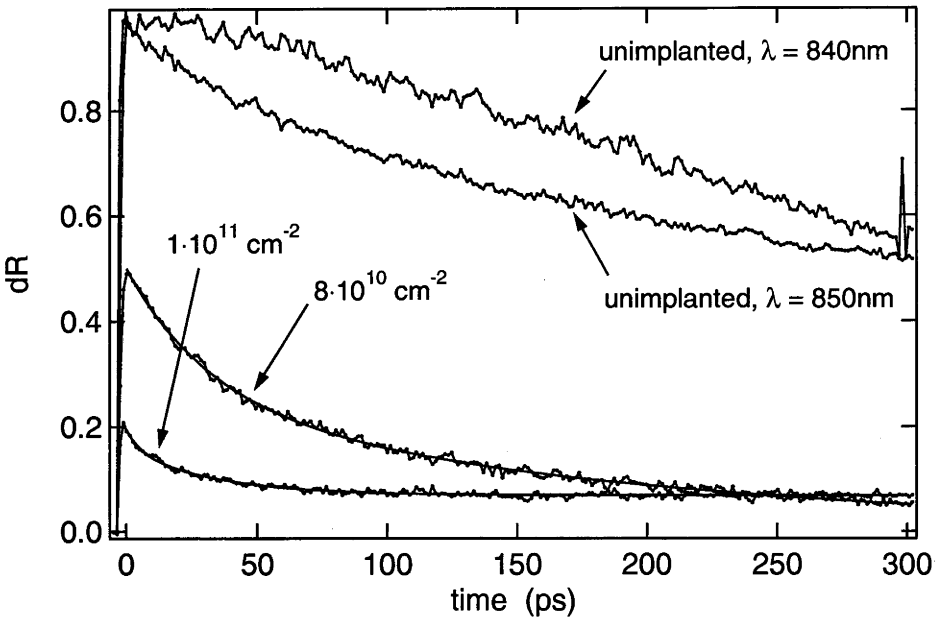

Fig. 2.2.2 - 1b: Long delay dR signals and numerical fit of various doses of 80keV-implanted, unannealed resonant SESAMs compared to the unimplanted case. λ_{pump} = 840nm unless stated otherwise, F_{pump} = 1μJ/cm^2, P_{av} = 0.5 mW.

Fit parameters for 0...18ps, Fig 2.2.2 - 1a

ion dose [cm^{-2}]	K_0	K_1	K_2	τ_1 [ps]	τ_2 [ps]	τ_{eff} [ps]
8·10^{10}	0	0.381	0.461	36.5	0.238	16.7
1·10^{11}	0	0.191	0.494	27.0	0.244	7.70
2.5·10^{11}	0	0.095	0.710	10.0	0.200	1.36
5·10^{11}	0	0.231	0.449	0.24	0.239	0.24

Fit parameters for 3...300ps, Fig 2.2.2 - 1b

ion dose [cm^{-2}]	K_0	K_1	K_2	τ_1 [ps]	τ_2 [ps]
8·10^{10}	0	0.252	0.250	188.7	31.3
1·10^{11}	0.069	0.088	0.038	33.90	5.56

Table 2.2.2 - 1: Fit parameters for some 80keV As implanted, unannealed samples (see *Figs. 2.2.2 - 1a,b*), F_{pump} = 1μJ/cm^2. The fitting model was a double exponential, eqn. (*2.2.2 - 1*).

For direct comparison, *Figs. 2.2.2 - 2a* and *2b* show the differential reflectivity of a selection of the annealed 40keV implanted samples. The traces were again fitted, similar to the unannealed case, using eqns. (*2.2.2 - 1, 2*), and the fitting parameters given in *Table 2.2.2 - 2*. There are a number of differences between the signals from unannealed and annealed samples. Firstly, capturing and emptying times, and therefore τ_{eff}, have increased in the annealed case. However, capturing times of ≤ 0.8ps

are still observed, even for the smallest dose. Note, that whilst the low power reflectivity could be restored completely through thermal annealing, ultrafast response times are nevertheless preserved, indicating the importance of the annealing step especially for high implantation doses. Generally higher ion doses yield the same residual bleaching after capturing as in the unannealed case, indicating damage recovery through thermal annealing whereby the number of capturing and recombination centres is reduced. Clearly, annealing temperature and time are critical parameters which merit further investigation. Secondly, the annealed samples display photo induced absorption (PIA), after pump excitation which evolves extremely slowly. Induced absorption following fast capturing has been previously reported for low temperature grown GaAs [42, 43] and was attributed to optical excitation out of the damage induced mid-gap trap levels. The pump-probe delay at which induced absorption appears depends on the ion dose which in turn determines the trap density: the higher the dose (trap density) the earlier residual bleaching is converted to induced absorption. This results in competition between excitation (absorption) out of mid-gap traps and residual bleaching due to uncaptured electrons and holes. The balance is affected by the trap emptying time and the number of traps relative to the carrier density. In unannealed samples, where trap emptying is relatively fast, induced absorption signals were only observed for very high pump fluences. Capturing must be dominated by electron traps for both annealed and unannealed samples, otherwise bleaching could not be converted to induced absorption. As an example, using a carrier density of $5 \cdot 10^{17}$ cm^{-3} one can therefore estimate a density of electron traps of $\approx$ 3...4$\cdot 10^{17}$ cm^{-3} in the case of the unannealed $8 \cdot 10^{10}$ cm^{-2} implanted sample. Recently, it has been shown that, similar to LT-GaAs, ionised As-antisites (As^{+}_{Ga}) are present in implanted and annealed GaAs [27]. These deep level traps may also play a role in the present samples. However, further research into the nature and density of deep level traps in As- (and other ions) implanted (In)GaAs is clearly needed.

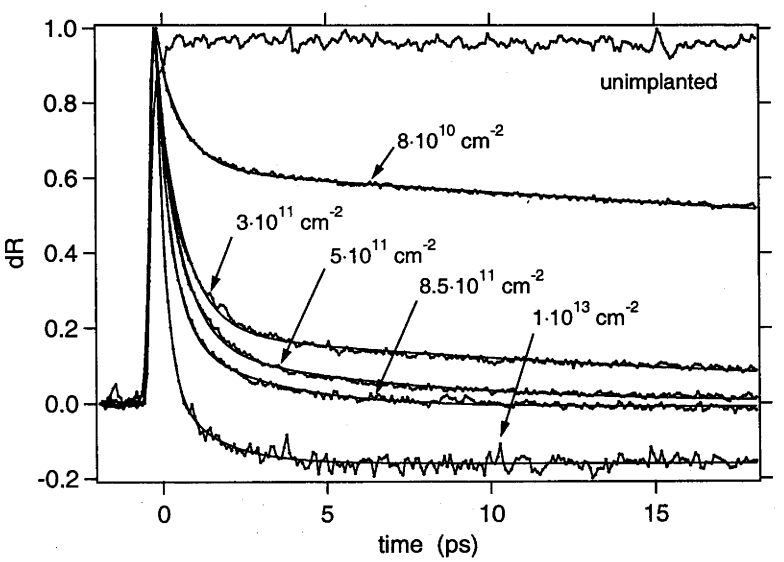

Fig. 2.2.2 - 2a: Short delay dR signals and numerical fit of various doses of 40keV-implanted, annealed resonant SESAMs. λ_{pump} = 840nm, F_{pump} = 1μJ/cm^2, P_{av} = 0.5 mW.

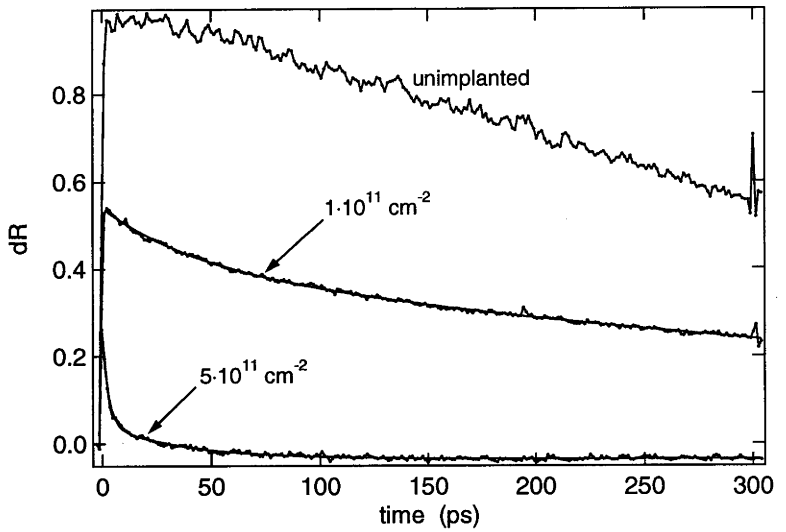

Fig. 2.2.2 - 2b: Long delay dR signals and numerical fit of various doses of 40keV-implanted, annealed resonant SESAMs. λ_{pump} = 840nm, F_{pump} = 1μJ/cm^2, P_{av} = 0.5 mW.

Fit parameters for 0...18ps, Fig 2.2.2 - 2a

ion dose [cm^{-2}]	K_0	K_1	K_2	τ_1 [ps]	τ_2 [ps]	τ_{av} [ps]
8·10^{10}	0	0.623	0.273	97.7	0.798	67.8
3·10^{11}	0	0.191	0.624	22.0	0.805	5.77
5·10^{11}	0	0.161	0.650	6.41	0.725	1.85
8.5·10^{11}	-0.009	0.208	0.607	2.82	0.454	1.06
1·10^{13}	-0.159	0.231	0.791	1.4	0.262	0.52

Fit parameters for 3...300ps, Fig 2.2.2 - 2b

ion dose [cm^{-2}]	K_0	K_1	K_2	τ_1 [ps]	τ_2 [ps]
8·10^{10}	0	0.409	0.125	557	41.8
5·10^{11}	-0.036	0.080	0.203	37.5	2.72

Table 2.2.2 - 2: Fit parameters for some 40keV As implanted, annealed samples (see *Figs. 2.2.2 - 2a,b*), F_{pump} = 1μJ/cm^2. The fitting model was a double exponential, eqn. (*2.2.2 - 1*).

Finally, note that the difference in ion energy (and hence the damage distribution inside the absorber) between unannealed and annealed samples did not play a significant role in the trapping dynamics which was instead dominated by the implantation dose. This was checked by later annealing the 5·10^{11} cm^{-2}, 80keV sample and comparing its response with that of the annealed 40keV sample of the same ion

dose. Similarly, the signals from resonant and anti-resonant SESAMs are more or less identical. These points are illustrated in *Fig. 2.2.2 - 3* where the signals for both the 40keV and 80keV, $5 \cdot 10^{11}$ cm^{-2} implanted, resonant as well as anti-resonant SESAMs are shown.

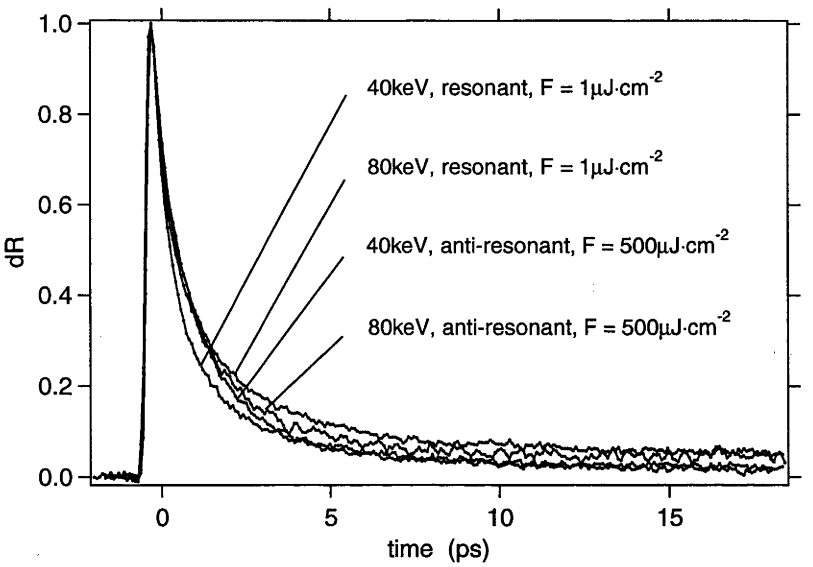

Fig. 2.2.2 - 3: Comparison of differential reflectivity signals obtained from the 40keV and 80keV, $5 \cdot 10^{11}$ cm^{-2} implanted annealed resonant as well as anti-resonant SESAMs. λ_{pump} = 840nm, F_{pump} = 1μJ/cm^2 (resonant), F_{pump} = 500μJ/cm^2 (anti-resonant).

2.2.3. Large Signal Response

Under mode-locking conditions an A-FPSA can be driven 10 times or more above saturation [14] to achieve reliable self-starting and stability against self Q-switching. It is therefore of interest to investigate the device response under high fluence excitation. *Fig. 2.2.3 - 1a* shows the case of unannealed resonant SESAMs at a pump fluence of 56 μJ/cm^2 (slightly below the damage threshold) for various ion doses compared with the unimplanted sample. Annealed samples and anti-resonant SESAMs respond in much the same way although for the latter the pump fluence needs to be a factor 10 to 20 higher due to the anti-resonance. Under these conditions, the lock-in signals before pump-probe correlation are not zero but can be as high as 10% of the peak signal. This indicates the presence of thermal nonlinearity and therefore heating of the pumped spot. Most notably, the difference between unimplanted and implanted samples is now relatively small. Even the unimplanted sample recovers to nearly the background level in only 5ps. *Table 2.2.3 - 1* contains the fitting parameters, using eqns. (*2.2.2 - 1, 2*), of all traces depicted in *Fig. 2.2.3 - 1a*. The effective recovery times τ_{eff} range from 900fs for the unimplanted sample down to 240fs for the $5 \cdot 10^{11}$ cm^{-2} implanted, unannealed sample. Also visible is induced absorption, after a 1ps delay, for the $5 \cdot 10^{11}$ cm^{-2} implanted sample.

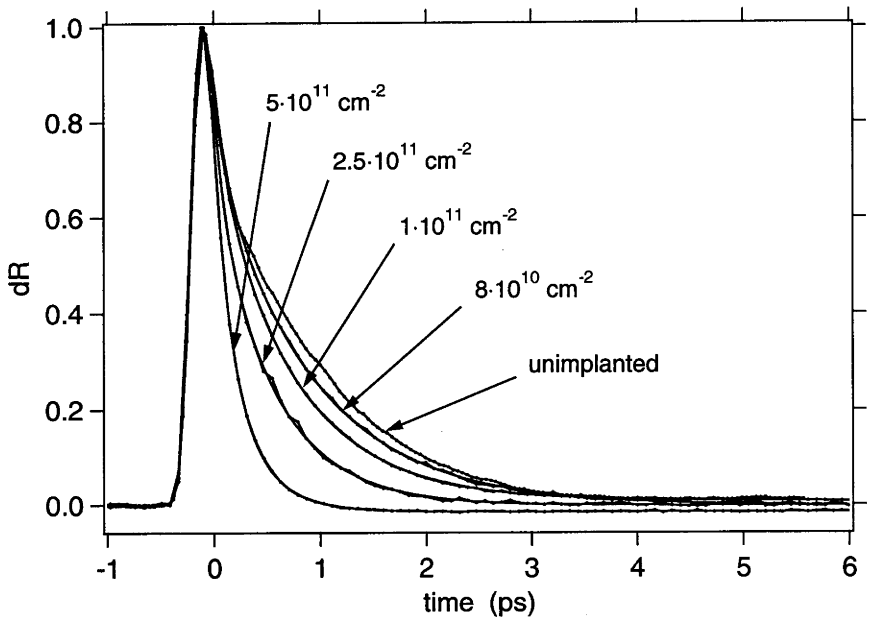

Fig. 2.2.3 - 1a: Response under high fluence excitation of selected 80keV, $5 \cdot 10^{11}$ cm^{-2} implanted, unannealed resonant SESAMs compared to the unimplanted case. λ_{pump} = 840nm, F_{pump} = 56μJ/cm^2.

Fit parameters for 0...6ps, Fig 2.2.3 - 1a

ion dose [cm^{-2}]	K_0	K_1	K_2	τ_1 [ps]	τ_2 [ps]	τ_{eff} [ps]
unimplanted	0.010	0.760	0.095	1.00	0.063	0.90
$8 \cdot 10^{10}$	-0.002	0.731	0.152	0.93	0.112	0.79
$1 \cdot 10^{11}$	0.008	0.716	0.154	0.75	0.129	0.64
$2.5 \cdot 10^{11}$	-0.002	0.661	0.170	0.56	0.098	0.47
$5 \cdot 10^{11}$	-0.015	0.345	0.431	0.34	0.161	0.24

Table 2.2.3 - 1: Fit parameters for some 80keV As implanted, unannealed resonant SESAMs (see *Fig. 2.2.3 - 1a*), F_{pump} = 56μJ/cm^2. The fitting model was a double exponential, eqn. (*2.2.2 - 1*).

Differential transmission signals similar to those observed here for the unimplanted sample have been previously reported for AlGaAs with pump-probe excitation close to the bandgap [45] and were interpreted as a mixture of thermalisation and carrier-phonon interaction signals. *Fig. 2.2.3 - 1b* shows dR signals obtained from an unimplanted anti-resonant SESAM for a number of different fluences. The absolute value of differential reflectivity at a pump-probe delay of 7ps (quasi-steady state) is annotated at the end of each curve. One can see that the values are essentially constant and correspond to carrier densities of $<1 \cdot 10^{18}$ cm^{-3} if a lattice temperature of 300K is assumed. This would mean that the quasi-steady state carrier density is essentially independent of the pump fluence. On the other hand, for the highest pump fluence, the maximum differential reflectivity at pump-probe correlation

is 2.25%, leaving about 0.75% of the SESAM reflectivity unbleached. This indicates that there is sufficient absorption available to suggest that the excited carrier density, and therefore the value of dR at quasi-steady state, should increase with pump fluence. At present there is no definitive explanation for this behaviour. For the highest pump fluence given in *Fig. 2.2.3 - 1b*, the excited carrier density N is estimated to lie in the low 10^{19} cm^{-3}. At this density the expected inverse Auger recombination rate $(N^2 \cdot A)^{-1}$ is still > 100ps, where $A = 7 \cdot 10^{-30}$ $cm^6 \cdot s^{-1}$ was used [46]. Therefore, the Auger process is unlikely to be the cause for the observed behaviour. However, it is possible that strong local heating of the pumped spot occurs for high pump fluences. This causes a shrinkage of the bandgap energy, which means that the sample is now pumped higher above the bandgap, where the density of states is higher. Additionally, the carrier distribution is now thermalised to the hot lattice, resulting in a much shallower Fermi-Dirac distribution and therefore little absorption bleaching due to bandfilling. Most importantly, however, this shows clearly that a response time of 1ps and nearly complete recovery to background are achieved under saturated conditions - even without a low temperature grown or ion-implanted absorber layer. However, this statement applies only to the design of GaAs-based SESAM considered here (low finesse with thin absorber layer) and pulsewidths of around 100fs. For considerably shorter or longer pulses the response may be different. Similarly for a high finesse SESAM with thicker absorber layer (for instance 0.5μm) and dielectric top mirror.

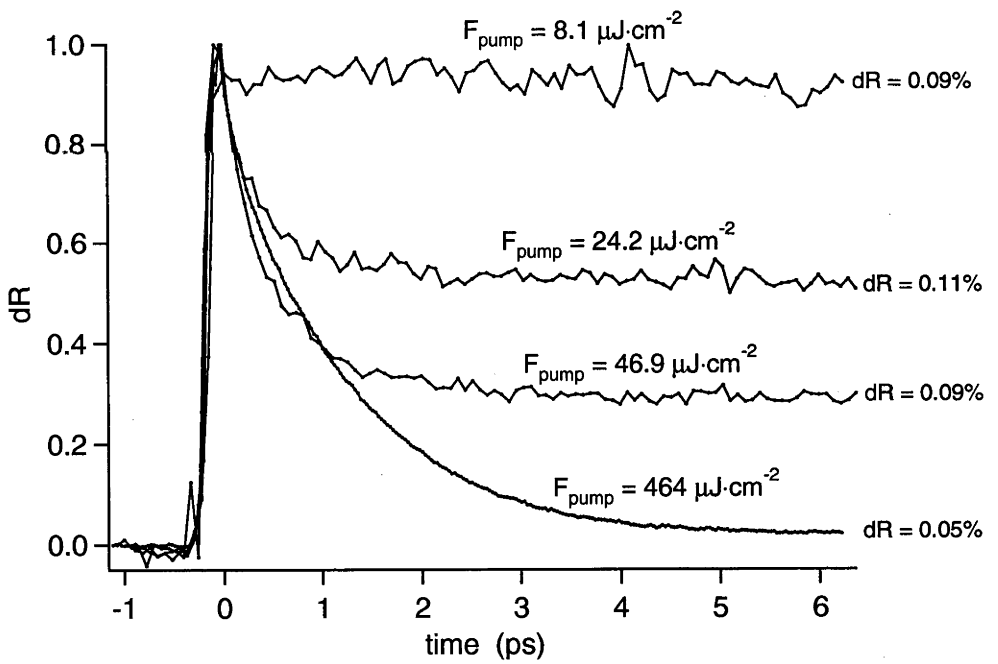

Fig. 2.2.3 - 1b: Response of the unimplanted anti-resonant SESAM for different fluences. λ_{pump} = 840nm. The absolute differential reflectivities at a delay of 6ps are printed at the right hand side of each trace.

Fig. 2.2.3 - 2 shows, representative for all samples, the saturation behaviour of three resonant SESAMs. The points of each curve represent the absolute differential reflectivity

$$dR = \frac{R_{max} - R_0}{R_0} \qquad (2.2.3 - 1)$$

at a particular pump fluence during pump-probe correlation with crossed polarisations. The laser wavelength was chosen to coincide with the resonance dip of each sample. Defining a saturation fluence is slightly ambiguous because of the fluence-dependent bi-temporal response. It is well known that for very long response times compared to the excitation pulsewidth, a two-level rate-equation absorber model saturates with energy, i. e. $q = q_0/e$ for $F = F_{sat}$, where q is the absorption. However, the condition for saturation with energy is not strictly fulfilled for any of the SESAMs due to the presence of fast processes such as thermalisation, cooling and capturing. In the extreme case of a very fast absorber recovery, saturation follows peak power, i. e. $q = q_0/2$ for $F = F_{sat}$. There are also models which were devised in an attempt to take geometrical factors of the SESAM design into account [22]. In the case of the two-level rate-equation model, from *Fig. 2.2.3 - 2*, an approximate saturation fluence $F_{sat} \approx 10...15\mu J \cdot cm^{-2}$ can be deduced for all samples. This is somewhat surprising at first but reflects the similarity of the temporal response of all samples under high fluence excitation. For the anti-resonant SESAMs F_{sat} is higher by a factor of 8...12, as estimated from the ratio of overlap integrals of standing wave power and absorber thickness in the resonant and anti-resonant cases. This leads to an $F_{sat} \approx 100\mu J \cdot cm^{-2}$ for the anti-resonant SESAMs.

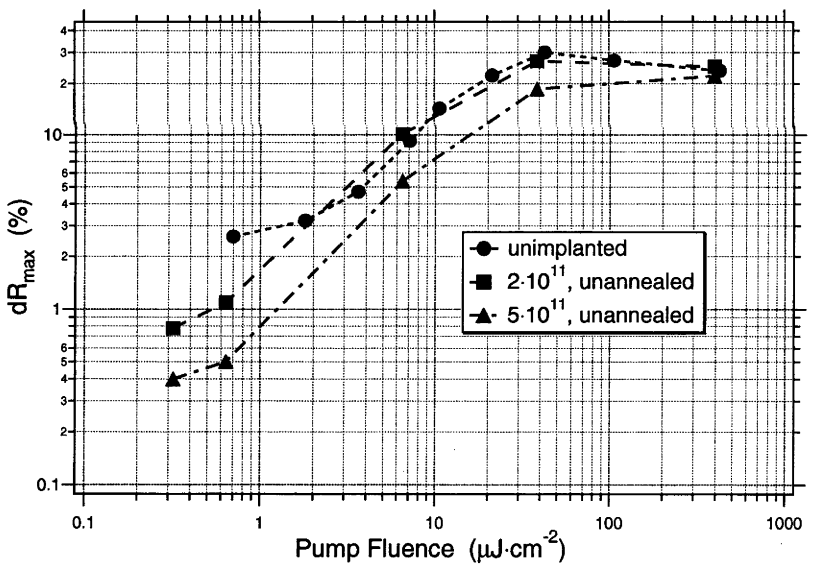

Fig. 2.2.3 - 2: Saturation behaviour of some resonant SESAMs representative for all. A saturation fluence of $F_{sat} \approx 10...15\mu J \cdot cm^{-2}$ can be deduced in all cases. The points correspond to the maximum differential reflectivity during pump-probe correlation.

Laser induced damage of the resonant samples was found to occur at fluences beyond which the differential reflectivity clearly decreased (beyond $\approx 50..60\mu J \cdot cm^{-2}$ for the unimplanted sample in *Fig. 2.2.3 - 2*). However the onset of damage was sample dependent with a trend towards a higher damage threshold for unannealed samples at high ion dose. The damage thresholds for anti-resonant samples were not specifically

measured due to lack of high enough extra-cavity pulse energy fluences. However, in lasing experiments it was found that typical damage thresholds for the anti-resonant SESAMs lay around 4mJ·cm^{-2}.

Fig. 2.2.3 - 3 compares the differential reflectivities at pump-probe correlation of implanted anti-resonant SESAMs with the unimplanted case. The pump fluence was 560μJ·cm^{-2}, the highest achievable with the pump-probe setup. Several trends are visible. The nonbleachable losses clearly increase with dose in both the annealed and unannealed cases although much more rapidly for unannealed samples. In this sense the implantation dose is the parameter analogue to the growth temperature in LT-growth, where the nonbleachable losses are higher for lower growth temperatures [22]. For a dose of 5·10^{11} cm^{-2} it is again possible to compare the annealed 40keV and 80keV implants. It appears that the broader damage profile of the 80keV implant, and possibly the damage tail inside the spacer layer, introduce almost twice the nonbleachable losses of the narrower profile 40keV implant.

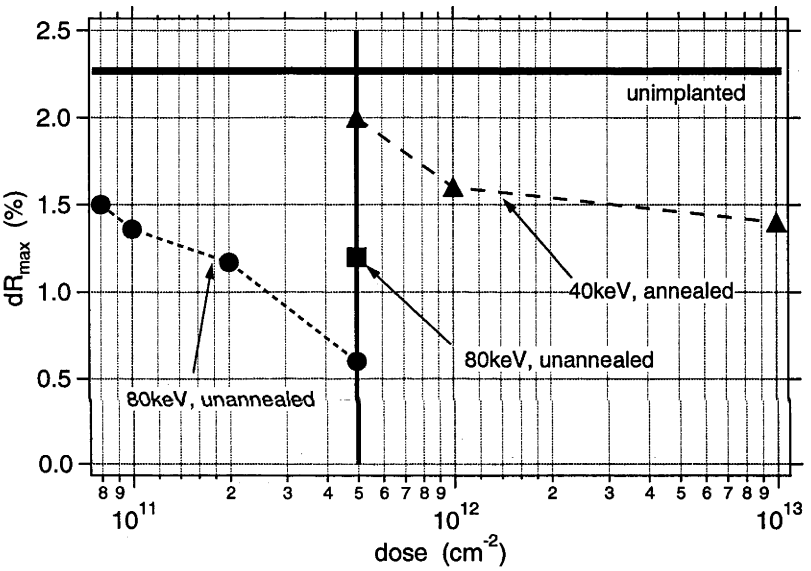

Fig. 2.2.3 - 3: Maximum differential reflectivity of 40keV implanted (annealed), 80keV implanted (unannealed) and 80keV implanted (annealed) anti-resonant SESAMs for different doses compared with the unimplanted case.

Since the error in the measurement of the absolute low power reflectivity of the samples was around 1%, it is difficult to give exact numbers for the nonbleachable losses. However, the unimplanted sample with a nominal low power reflectivity of 97% at a wavelength of 840nm can be used as reference, since it has the maximally achievable differential reflectivity. Note that nonbleachable losses are also present in the unimplanted sample and are most likely due to free carrier absorption and two photon absorption. The origin of the increase in nonbleachable losses due to ion implantation is currently a matter of speculation. However, a plausible explanation could be absorption due to neutral mid-gap traps. Chapter 4 will deal with the issue of nonbleachable absorption in a more systematic manner.

2.3. Summary

Chapter 2 was concerned with the design and properties of a GaAs-based ion-implanted SESAM device. In section *2.1* the SESAM design was introduced and some basic properties such as reflectivity, standing wave power distribution and dispersion were given. Several aspects of the ion-implantation process, such as the choice of ion species, ion energy and dose were explained. It was shown that As-implantation with doses above $1 \cdot 10^{12} cm^{-2}$ had reduced the reflectivity of the devices severely, making them useless for mode-locking applications. However, the reflectivity could be restored completely through thermal annealing at 600°C for 20min in arsine atmosphere. Finally, the nonlinear processes relevant for mode-locking applications of the SESAMs were explained.

In Section *2.2* the dynamic response of the SESAMs was investigated using wavelength degenerate pump-probe measurements. The traces obtained from the implanted samples were compared with those from unimplanted samples to unambiguously separate thermalisation and cooling signals from those due to trapping. Under low fluence excitation ($1 \mu J \cdot cm^{-2}$) the trapping time constants lay below 250fs for all unannealed samples, and below 800fs for the annealed case. Trap emptying and recombination signals could not be characterised by a single time constant, however. In the unannealed case, their evolution started with time constants in the order of several tens of ps for the lowest dose (faster for higher doses), but, became progressively slower for longer times. In the annealed case, these signals were further prolonged. Additionally, photo induced absorption (PIA) appeared following the pump-probe correlation - the higher the implantation doses, the earlier and more pronounced was the appearance of PIA. As for the case of LT-GaAs, the appearance of PIA was attributed to the excitation of captured carriers which are trapped for long times due to a small recombination rate. It was further shown that the small signal response of samples was dominated by the implantation dose rather than the exact shape of the damage profile from 40keV and 80keV implants respectively.

Under strong excitation the response of all samples became similar, and response times between 0.2 and 1ps were measured. Interestingly, even the unimplanted sample recovered to background with a time constant of around 1ps under these conditions. This behaviour, although not completely understood as yet, was tentatively associated with carrier thermalisation and cooling to a hot lattice. From further large signal measurements, approximate saturation fluences of 10 $\mu J \cdot cm^{-2}$ for the resonant SESAM and 100 $\mu J \cdot cm^{-2}$ for the anti-resonant SESAM were deduced, which did not depend strongly on the implantation dose and annealing conditions. Finally, it was shown that the ion-implantation process, similar to low temperature growth, introduced nonbleachable losses which were highest for the unannealed samples and which increased with ion dose. Here it was found that the broader damage distribution of the 80keV implant caused a marked increase in those losses.

CHAPTER 3

MODE-LOCKING OPERATION OF A TI:SAPPHIRE LASER USING THE GAAS-BASED ION-IMPLANTED SESAMS

Chapter *3* will be concerned entirely with the mode-locking performance of the ion-implanted SESAMs. Firstly, the laser used in the experiments is described in section *3.1*, then detailed accounts are given of its single-pulse (section *3.2*) as well as multi-pulse operations (section *3.3*). The experimental observations are explained within the framework of the Generalised Complex Ginzburg-Landau Master Equation.

3.1. The Laser

The laser used in the following mode-locking experiments was a commercial Ti:Sapphire laser (Coherent Mira 900D) pumped by up to 8 W in all lines of an Argon-ion laser. The Mira has three different cavity configurations for operation in cw- ps- and fs-mode. In order to allow operation over the greatest possible wavelength range, it comes with three mirror sets, each covering a section of the fluorescence bandwidth of Ti:Sapphire. The following discussion concentrates on the fs-cavity configuration only. There the Mira is Kerr Lens Mode-locked (KLM), for which a vertical slit is placed near the output coupler forming a horizontal aperture for a high power mode. Since the KLM process is not self-starting in the Mira, a mechanical starting aid in the form of two Brewster plates is present. To start KLM, the Brewster plates perform small oscillations, thereby perturbing the cavity mode and generating intense noise spikes on the circulating radiation. Once KLM has started, it provides less loss than the unlocked cavity, the starting mechanism is switched off, and the Mira operates very stably producing 90-150fs pulses. Also necessary for the fs-operation, are the dispersion compensating prism pair P_1 and P_2 and the Birefringent tuning filter (BRF). The SF10 prism pair provides an overall negative dispersion per round trip and the BRF allows for tunability and operation at a specific wavelength.

In order to incorporate the SESAMs into the Mira fs-cavity, the latter had to be redesigned to some degree, however, with the restriction that no permanent hardware change be made. Given this restriction the only feasible option was to place the SESAM not as cavity end mirror, as is usually the case, but part way along the cavity as shown in *Fig. 3.1 - 1*. The starting aid and slit for KLM operation were removed and the BRF was placed near the output coupler. The SESAM focusing mirror had a radius of curvature of 100mm and was steered at an angle of around 13° off normal for the first reflection and 3° off normal for the second one. This resulted in a lateral beam shift upon exit of 10mm: enough to steer the beam towards the BRF and output coupler. As will be shown below, this arrangement introduces asymmetry and astigmatism which leads to separate, narrow bands of resonator stability. Also, mode-

locked pulses pass the SESAM twice per round trip introducing twice the amount of nonbleachable loss and twice the modulation q_0 of a single reflection per round trip. All components necessary for the SESAM extension were mounted on a separate aluminium base plate inside the Mira housing. This arrangement avoids the spatially angled or spectrally dispersed output beams which are common when the SESAM is used as end mirror. Last but not least, use could be made directly of Mira's convenient alignment analysis features. For all experiments the Mira had the mid-range optics installed allowing operation between 780nm and 880nm. At λ = 840nm the output coupler had a transmission of 14%.

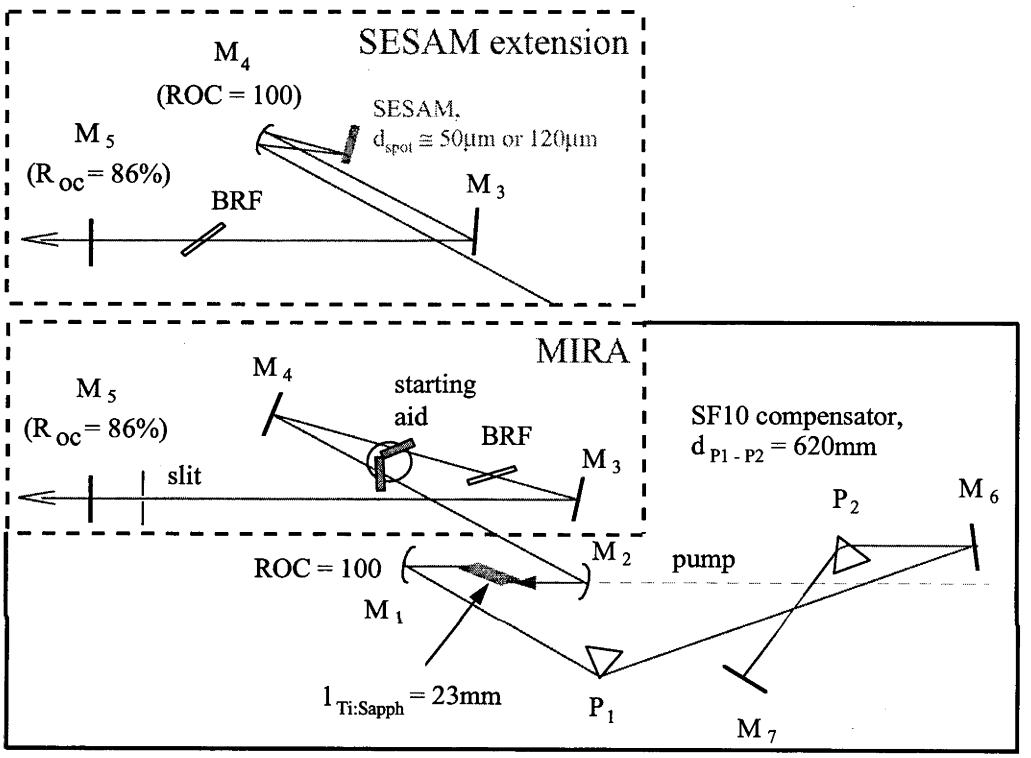

Fig. 3.1 - 1: fs-cavity of Coherent Mira 900D and SESAM extension

3.1.1. Some Cavity Calculations

In order to accomplish the above cavity extension, all of Mira's resonator dimensions were measured and an ABCD-matrix calculation performed. To within the accuracy of the measurements, the Mira's astigmatically compensated resonator [48] is symmetric with respect to the folding mirrors M_1 and M_2. For a slit-operated KLM laser this was found to result in best performance and even self-starting operation for a very small range of M_1-M_2 separations, y, and crystal positions, x [49]. Using the cavity data, and following the theory of Magni et al. [49], calculations of Mira's KLM sensitivity, i. e. the derivative of the mode radius with respect to the power P, evaluated at P = 0,

$$\xi = \left[\frac{1}{2 \cdot \omega} \cdot \frac{d\omega}{dP} \right]_{P=0} \qquad (3.1.1 - 1)$$

were performed. This was mainly done for consistency. *Fig. 3.1.1 - 1a* shows the contours of the KLM sensitivity in the tangential plane for an aperture near the output coupler M_5; regions with the highest negative values, hence highest sensitivity, are darkest. The measured values of x and y are in good agreement with the high sensitivity region at y ≈ 118.5mm and x ≈ 50mm. Since at y ≈ 118.5mm, the calculated output spot radii (*Fig. 3.1.1 - 1b*) match the measured radii, y = 118.5mm was therefore used in all further calculations.

Introducing the SESAM in the above outlined manner leads to the conditions shown in *Fig. 3.1.1 - 2a, b*. The cavity has two narrow stability bands with respect to movement of M_4, with d_{SESAM} being the total path between consecutive bounces off M_4. The output spot (*Fig. - 2a*) in one of the bands is elliptical whereas in the other the spot is round and about 3 times smaller. Finally, the more important beam sizes are those on the SESAM shown in *Fig. 3.1.1 - 2b*. They are inversely related to the output spot dimensions with the smaller one ($\omega_{SESAM} \approx 25\mu m$) corresponding to the larger output spot and the larger one ($\omega_{SESAM} \approx 65\mu m$) corresponding to the smaller output spot. Whilst a measurement of the mode size on the SESAM was not feasible, it was confirmed experimentally that the location and width of the stability bands as well as the associated output beam sizes agreed with the calculations. Using a saturation fluence of $F_{sat} \approx 100\mu J/cm^2$ the calculated SESAM spot radii lead to saturation energies of $E_a \approx 2nJ$ and of $E_a \approx 10nJ$ respectively.

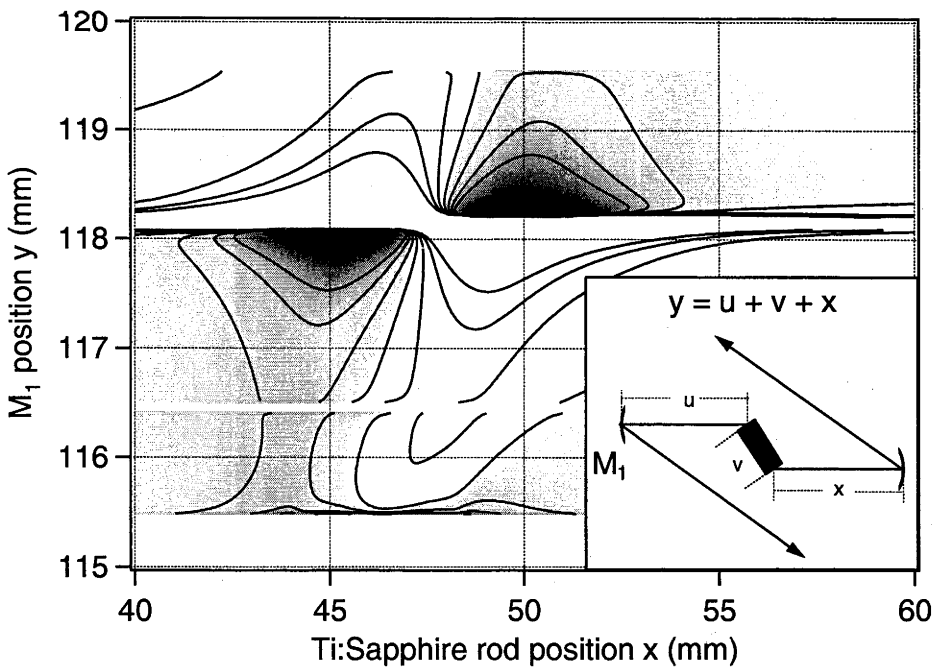

Fig. 3.1.1 - 1a: Contours of Mira's KLM sensitivity ξ in tangential plane; darkest regions show highest sensitivity.

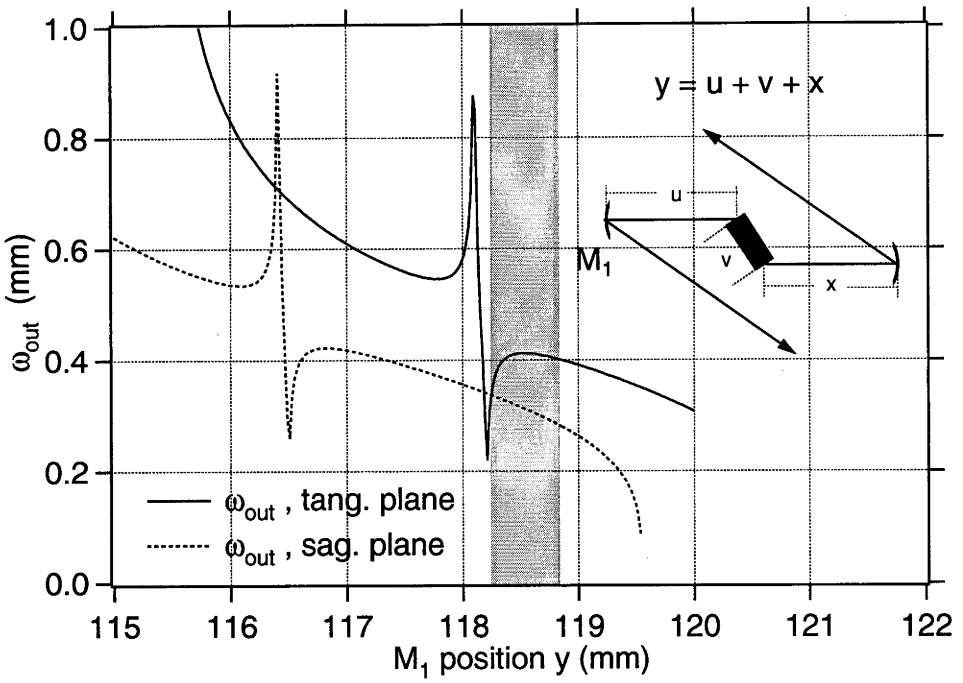

Fig. 3.1.1 - 1b: Mira's output beam radii in tangential and sagittal plane vs. y (separation of M_1 and M_2) . The shaded area indicates the region of operation.

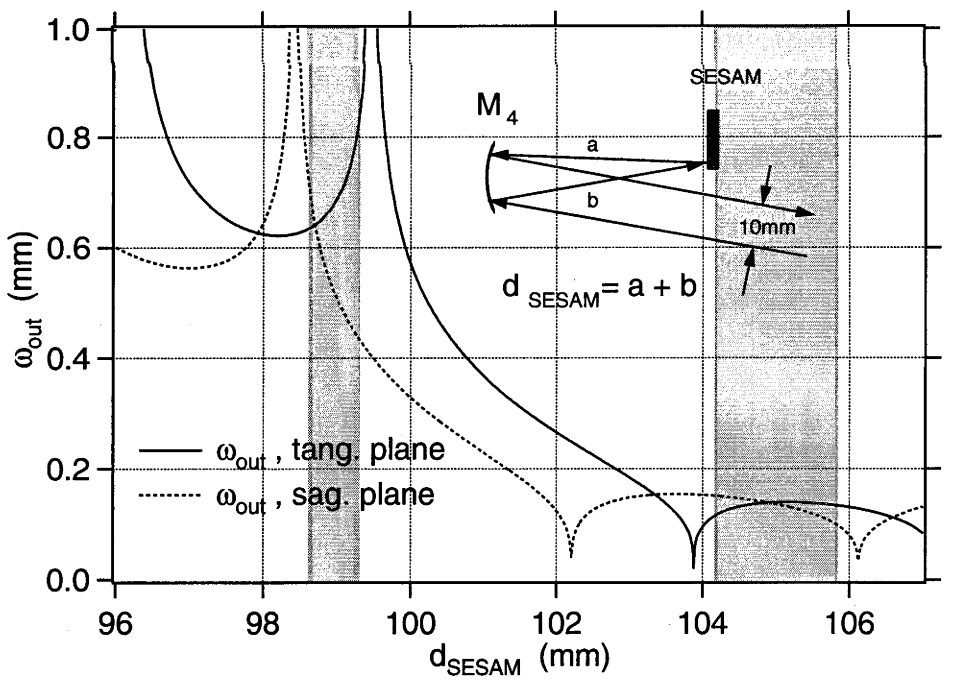

Fig. 3.1.1 - 2a: Output beam radii (with SESAM extension) in tangential and sagittal plane vs. d_{SESAM}. The shaded areas indicate the two stability bands.

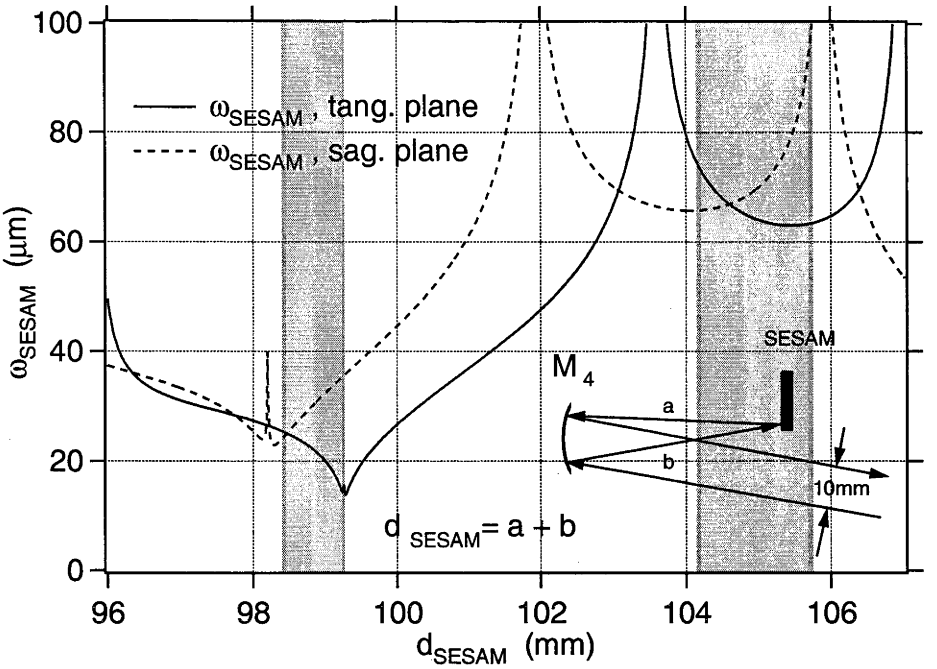

Fig. 3.1.1 - 2b: Beam radii on SESAM in tangential and sagittal plane vs. d_{SESAM}. The shaded areas indicate the two stability bands.

3.1.2. Self-phase Modulation, Dispersion and Filter

In a soliton mode-locked laser, apart from the loss modulation due to the Kerr lens effect or a SESAM, pulse shaping and stabilisation are also determined by the presence of Self-Phase-Modulation (SPM) and Group Delay Dispersion (GDD). Due to the tight focus of the laser mode in the Ti:Sapphire crystal the refractive index change due to the third order nonlinear index n_2 becomes appreciable. In the spatial domain n_2 leads to self-focusing which can lead to the KLM effect. In the time domain n_2 causes self-phase modulation characterised by a phase shift ϕ_{nl} per round trip. Similarly, a linear phase shift is caused by the dispersive nature of propagation through the various elements in the laser. The optical phase per round trip can therefore be represented by the dispersion relation

$$\phi(\omega) = \phi_0 + \frac{d\phi}{d\omega}\cdot(\omega-\omega_0) + \frac{1}{2}\cdot\frac{d^2\phi}{d\omega^2}\cdot(\omega-\omega_0)^2 + \frac{1}{6}\cdot\frac{d^3\phi}{d\omega^3}\cdot(\omega-\omega_0)^3 + \phi_{nl} \qquad (3.1.2\text{ - }1)$$

where the expansion of the linear phase shift around the circular frequency ω_0 was taken to third order. The term in first order is the group delay, $\frac{1}{2}\cdot\frac{d^2\phi}{d\omega^2}$ is usually called Group Delay Dispersion (GDD), and $\frac{1}{6}\cdot\frac{d^3\phi}{d\omega^3}$ is the Third Order Dispersion

(TOD). Also in use is the terminology $\beta_2 = \frac{d^2\phi}{d\omega^2}$ and $\beta_3 = \frac{d^3\phi}{d\omega^3}$. In later chapters both GDD and β_2 will be used, knowing that $\beta_2 = 2 \cdot GDD$.

Since n_2 in Sapphire is due to electronic processes, and hence is instantaneous for the time scales of interest here, the nonlinear phase shift can be written as

$$\phi_{nl}(t) = k_0 \cdot n_2 \frac{P(t)}{A_{eff}} \cdot 2l_L = \kappa \cdot P(t) = \frac{16 \cdot n_2 \cdot l_L}{\lambda_0 \cdot d_{eff}} \cdot P(t) \approx 1 \cdot 10^{-6} \frac{1}{W} \cdot P(t) \qquad (3.1.2 - 2)$$

where P(t) is the instantaneous power, d_{eff} is the effective mode diameter inside the crystal, and l_L is the length of the Ti:Sapphire crystal. The value of $\kappa = 1 \cdot 10^{-6}$ 1/W was calculated from λ_0 = 840nm, l_L = 23mm, $n_2 = 2 \cdot 10^{-20}$ m²/W, and d_{eff} = 94µm. The time dependence of ϕ_{nl} means that a typical optical pulse modulates its own phase leading to a positive frequency chirp (up-chirp) $C = -\frac{d\phi_{nl}}{dt}$.

So called 'bright' solitons are formed when the frequency chirp due to SPM is exactly balanced by the chirp due to negative (anomalous) GDD, very similar to soliton propagation in optical fibres [75]. To take advantage of the solitonic pulse shortening, the cavity therefore requires an overall negative GDD. As was shown in [50, 51] this can be achieved by using a prism pair in the cavity which results in a wavelength dependence of the optical path, such that the GDD of the prism pair becomes negative. Although formulae for β_2 and β_3 of the prism pair and the laser crystal are given in [50, 51] their use is somewhat limited in the present case since β_2 and β_3 of all mirrors remain unknown.

For a soliton mode-locked laser of the kind presented here it is nevertheless possible to obtain a good estimate (±50fs²) of β_2 in the following way. With the laser operating SESAM mode-locked with the smallest possible pump power (hence small signal gain), and the laser mode passing through the apex of prism P_1, prism P_2 is inserted while observing the intensity autocorrelation and time-integrated spectrum. Typically one observes a shortening of the pulse followed by the appearance of two closely spaced double pulses, followed by unsteady autocorrelation traces which are finally followed by the emission of chirped ps-pulses. For further explanation of these observations the reader is referred to section 3.3. The transition from stable double pulse emission to that of ps-pulses marks the crossing from negative to positive GDD and is well defined with respect to the amount of inserted P_2-glass $l_{P2-glass}^{zeroGDD}$ (±0.5mm) since the small signal gain is very low. This leads to a maximally achievable negative dispersion in the cavity of

$$\beta_{2,max} = -\left[\beta_2^{SF10}\left(l_{P2-glass}^{zeroGDD}\right) - \beta_2^{SF10}\left(l_{P2-glass}^{apex}\right)\right] = -2200 \pm 50 fs^2 \qquad (3.1.2 - 3)$$

where the Sellmeir equation and parameters for the calculation of the material dispersion of SF10 were taken from [118], using the formula given in [51]. Given the linearity of β_2 with the insertion of prism glass the total intra-cavity β_2 is therefore

known for arbitrary insertions of P_2. As for β_3 the contributions due to the prism pair and the Ti:Sapphire crystal were calculated to lie between β_3 = -21000...-26000fs^3 for β_2 = 0...-2200fs^2. However, a determination of the total β_3 was not possible.

Finally, for the modelling in later sections it is necessary to have an estimate of the birefringent filter (BRF) bandwidth. Ref. [47] gives the following formula for the power transmission $|m|^2$ of a BRF in a linear cavity

$$|m|^2 \approx 1 - 2\pi^2 \cdot \frac{\left(1+q^2\right)\cdot\left(1+q^2\cdot p^2\right)}{\left(1+q^4\cdot p^2\right)} \cdot N^2 \cdot \left(\frac{f-f_0}{f_0}\right)^2 \qquad (3.1.2\text{ - }4)$$

where $q = 2n / (n^2 + 1)$ is the loss experienced by the S-polarised wave on exiting the birefringent crystal quartz, p is the polarisation dependent loss in the cavity determined by the two Brewster interfaces on the Sapphire crystal, N is the order in which the birefringent plate operates and f_0 is the optical centre frequency. Assuming standard values for refractive indices, operation in first order at a wavelength of 840nm results in a factor in front of the $(f-f_0)^2$ term of $(1 / \Delta f)^2 = (1 / 39\text{Thz})^2$. Note that *(3.1.2 - 4)* is identical to the expansion to second order of a Lorentzian line shape with a half width at half maximum (HWHM) of Δf which can therefore be taken as the bandwidth parameter of the filter. However, due to the wavelength dependence of gain and mirrors, the total filter bandwidth per round trip is certainly less than the calculated value of Δf would indicate. In the modelling in later chapters the value Δf = 25Thz was used which produced good agreement with the experimental observation.

3.2. Single Pulse Operation

3.2.1. Experimental

Using the ion-implanted SESAMs in the above described laser, self-starting mode-locking was achieved in either stability band for ion doses in the ranges $8\cdot10^{10}$ cm^{-2} → $1\cdot10^{14}$ cm^{-2} (annealed) and $8\cdot10^{10}$ cm^{-2} → $4\cdot10^{11}$ cm^{-2} (unannealed). For samples with higher doses, a reluctance to self-start was observed which was attributed to their higher quasi-steady state saturation intensity. Not surprisingly, from the temporal response data presented in section 2.2.3, the unimplanted sample also mode-locked the laser stably. *Table 3.2.1 - 1* summarises the conditions for which mode-locking was observed.

P_{pump}	P_{out}	τ_{ac}	τ_{bu}	tunability
4.9...8W	125...900mW	164...450fs	30µs...3ms	50nm

Table 3.2.1 - 1: Conditions for which mode-locking was achieved. τ_{ac} is the FWHM of the intensity autocorrelation and τ_{bu} is the mode-locking build-up time.

As an example, *Figs. 3.2.1 - 1a* and - *1b* show a normalised autocorrelation trace and spectra respectively for the case of operation with the $2.5 \cdot 10^{11}$ cm^{-2} implanted, unannealed SESAM.

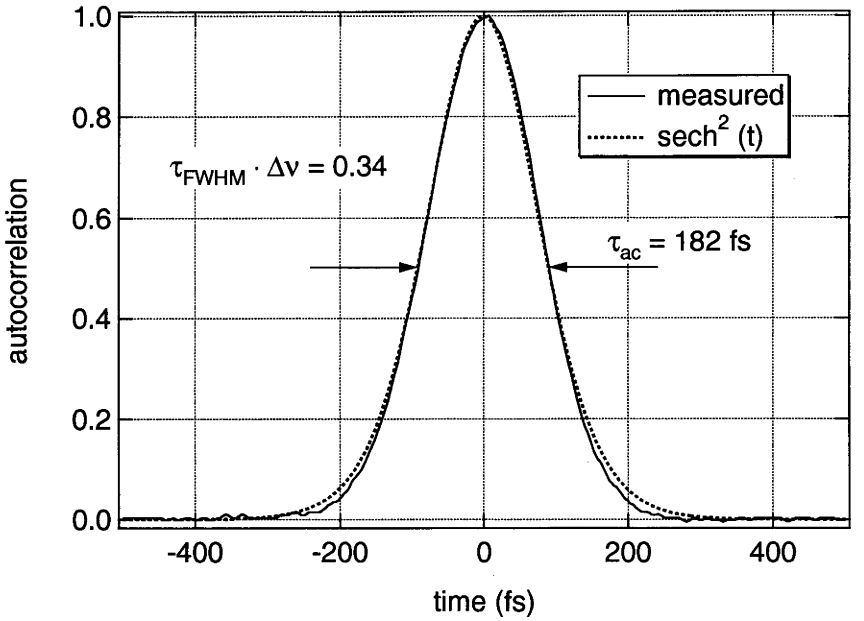

Fig. 3.3.1 - 1a: Intensity autocorrelation of shortest pulses achieved at λ=850nm and P_{out}=125mW with 80kev, $2.5 \cdot 10^{11}$ cm^{-2} implanted unannealed SESAM. Also shown: autocorrelation of ideal sech^2(t) pulse. τ_{FWHM} = 118fs, $\Delta\lambda$ = 7nm and $\Delta\nu \cdot \tau_{FWHM}$ = 0.34.

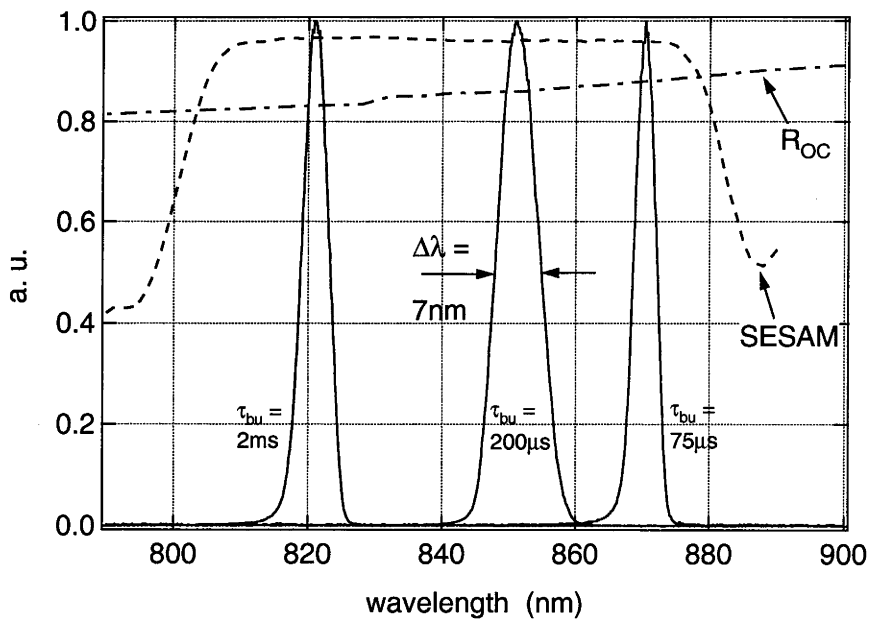

Fig. 3.2.1 - 1b: Spectra of pulses achieved for P_{out}=125mW with 80kev, $2.5 \cdot 10^{11}$ cm^{-2} implanted unannealed SESAM with annotated build-up times. Also shown: SESAM reflectivity and output coupler reflectivity. For $\Delta\lambda$ = 7nm, τ_{FWHM} = 118fs and $\Delta\nu \cdot \tau_{FWHM}$ = 0.34.

Together with the autocorrelation trace a $sech^2(t)$ function is shown which fits the measured curve well. Therefore, assuming a $sech^2(t)$ pulse shape, from τ_{ac}=182fs and the spectral width of $\Delta\lambda$ = 7nm, a pulsewidth of $\tau_{FWHM} = \tau_{ac}/1.54$ = 118fs and a time-bandwidth product of $\tau_{FWHM} \cdot \Delta\nu$ = 0.34 result, compared with the transform limited value of $\tau_{FWHM} \cdot \Delta\nu$ = 0.315. The tuning range over which self-starting was obtained was 50nm. For all SESAMs longer build-up times (annotated to the spectra in *Fig. 3.2.1 - 1b*) were observed at the short wavelength compared to the long wavelength end of the tuning range. This is attributed to a combination of the smaller available modulation depth due to a higher degree of anti-resonance, as well as the larger output coupling at short wavelengths (see *Fig. 3.2.1 - 1b*). Calculations of the build-up rate of saturable absorber mode-locking [52] show indeed that the mode-locking build-up times are essentially indirectly proportional to the modulation depth q_0 for otherwise equal conditions.

Examples of the mode-locking build-up process, recorded with a photo diode and digital oscilloscope at 850nm and 820nm, are shown in *Figs. 3.2.1 - 2a,b* respectively. The cavity switch-on time was approximately 1µs, allowing to resolve the initial relaxation oscillations following the switch at 0 (see *Fig. - 2a*). This is followed by ca. 25µs of cw operation and the final build-up to cw mode-locking at ≈ 45µs. However, there is evidence of further relaxation oscillations following the build-up. These are shown in more detail in *Fig. - 2c*, where an analogue oscilloscope was used with an x-scaling of 10µs/Div. Assuming that the relevant mode-locking mechanism is soliton mode-locking (more supporting evidence is provided below) this behaviour can be explained as follows. Initially a relatively long pulse (1 ... 10ps), originating from the mode-locking driving force of the saturable absorber, is circulating in the cavity, containing already most of the total intra-cavity energy [69]. After several hundred round trips the modulation instability starts compressing the pulse strongly, since the soliton number of such a long pulse can be as large as N = 5-10. During the compression phase the pulse spectrum broadens and filter dispersion becomes a sizeable loss factor whilst the absorber saturates and its loss therefore decreases.

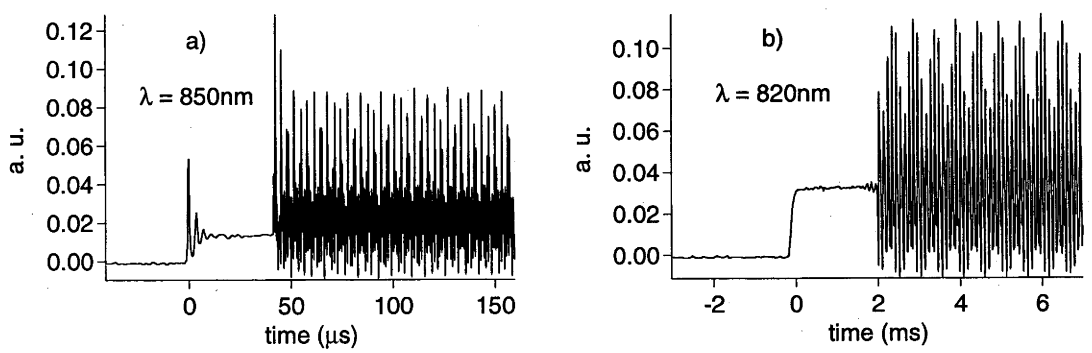

Fig. 3.2.1 - 2a,b: Mode-locking build-up process for (a) λ = 850nm and (b) λ = 820nm, recorded with a photo diode and digital oscilloscope. The modulation on the mode-locking signal is due to under-sampling.

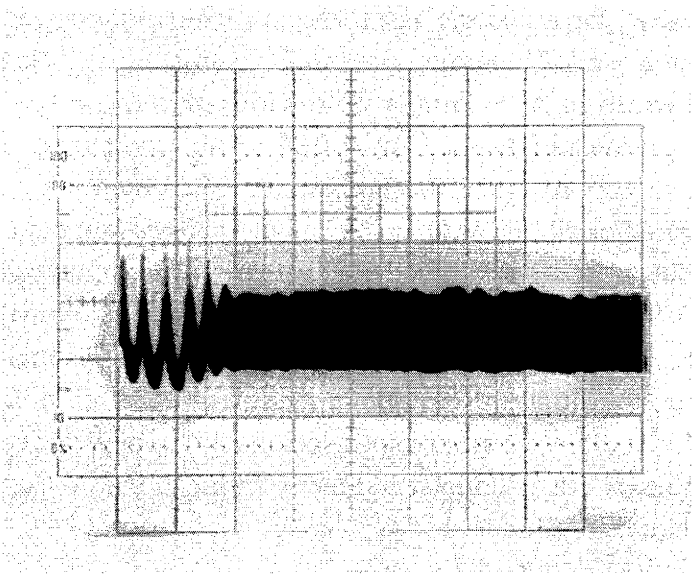

Fig. 3.2.1 - 2c: Relaxation oscillations at the beginning of the cw mode-locked pulse train (recorded with a photo-diode and analog oscilloscope), x-scaling: 10μs/Div. The operating conditions are the same as for *Fig. 3.2.1 - 1a.*

Since the compression phase is usually short (≈10 round trips) compared to the upper state life time of the gain material, the changes in absorber and filter loss provide an impulse-like perturbation to the saturated gain, followed by multiple energy-pulsewidth readjustments through the interaction of the pulsewidth (hence energy) dependent filter loss, the absorber loss and the saturated gain.

To confirm that mode-locking was stabilised solely by the SESAM it was replaced by a dielectric mirror. It is well known that under certain cavity conditions the transverse gain profile in the laser crystal can form an effective aperture for the cavity mode through which KLM can occur [14, 53]. However, the laser did not mode-lock with the dielectric in place and using the well known starting techniques, e. g. tapping of mirrors. It was also checked that self-starting was not sensitive to translation of M_1 or M_4 within the stability margins. Due to the sensitivity of KLM to such changes this is usually taken to indicate the absence of KLM. However, due to the small width of the stability bands, it may be less indicative in the present case.

Comparing the performance of different samples revealed that they provided varying stability against Q-switched mode-locked operation. To demonstrate this the necessary output power was recorded at which the laser operated at the margin of Q-switched mode-locking with the intra-cavity dispersion fixed at its maximum negative value of $\beta_2 = -2200fs^2 +/-50fs^2$ for various samples. The threshold for Q-switching was determined by monitoring the amplitude of the self-Q-switching induced side bands in the RF spectrum of the output pulse train, depicted in *Figs. 3.2.1 - 3a* and *3b*. Under stable conditions (*Fig. - 3a*) the side bands were effectively invisible and the noise floor was suppressed at > 32.5dB (optical). At threshold (*Fig. - 3b*) the side bands rose above the noise floor, although were still suppressed by about 20dB (optical). Under these

conditions any slight misalignment of the laser would cause it to change to Q-switched mode-locking operation.

(a) (b)

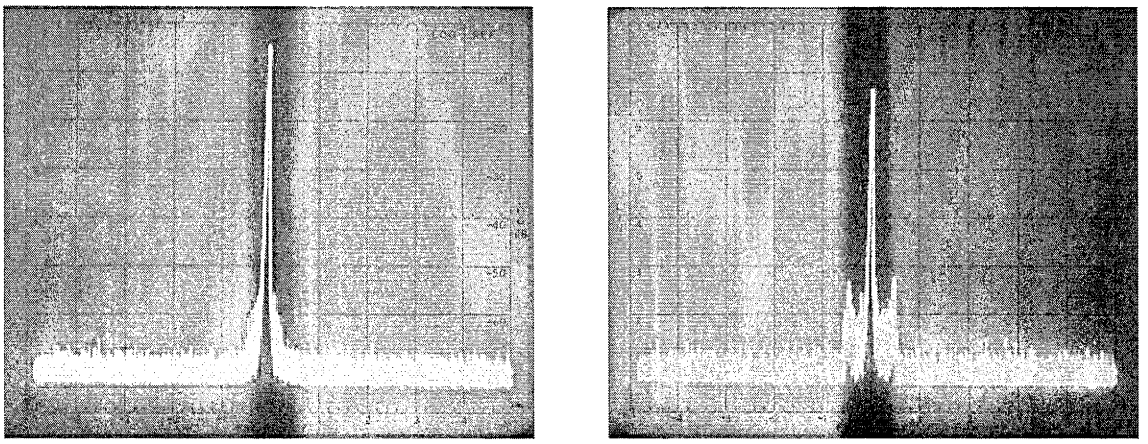

Fig. 3.2.1 - 3a,b: (a) RF-spectrum (log display) of cw mode-locked pulse train for stable operation. The noise floor is suppressed by > 65dB (electrical) (> 32.5dB optical). (b) Operation at threshold of Q-switching instability. The side bands are raised but still suppressed by ca. 40dB (electrical) (20dB (optical).

It was found that for increasing implantation dose, the minimum output power for stable operation decreased for both unannealed and annealed samples as shown in *Fig. 3.2.1 - 4*. This behaviour can be explained by considering the linearised analysis given in [52] which describes the driving force for Q-switched mode-locking as

$$-2 \cdot E_P \frac{dq_p}{dE_P} = 2 \cdot q_0 \cdot \frac{1 - \exp\left(-\frac{E_P}{E_A}\right) \cdot \left[\frac{E_P}{E_A} + 1\right]}{\frac{E_P}{E_A}} < \frac{1}{T_L} \cdot \left(1 + \frac{P}{P_L}\right) \qquad (3.2.1 - 1)$$

Here P is the average intra-cavity power; P_L is the saturation power of the gain material; T_L is its upper state life time normalised to the cavity round trip time; q_0 is the maximum amplitude modulation depth; E_P and E_A are the pulse and absorber saturation energies respectively; and q_p is the energy loss per round trip.

The inequality *(3.2.1 - 1)* must be true for the laser to operate without the Q-switching instability. The data on saturation fluences, although measured with the resonant SESAMs, indicate no substantial variation with implantation dose. This, plus the fact that the modulation depth q_0 clearly depends on implantation and annealing conditions (see *Fig. 2.2.3 - 3*), leads to the conclusion that the variation in the onset of Q-switched mode-locking is most likely due to the different q_0 rather than carrier lifetime controlled saturation fluence. The concept of a 'carrier lifetime' is to be taken *cum grano salis* in this context considering the greatly different time scales and power dependence found in the measurements presented in sections 2.2.2 and 2.2.3.

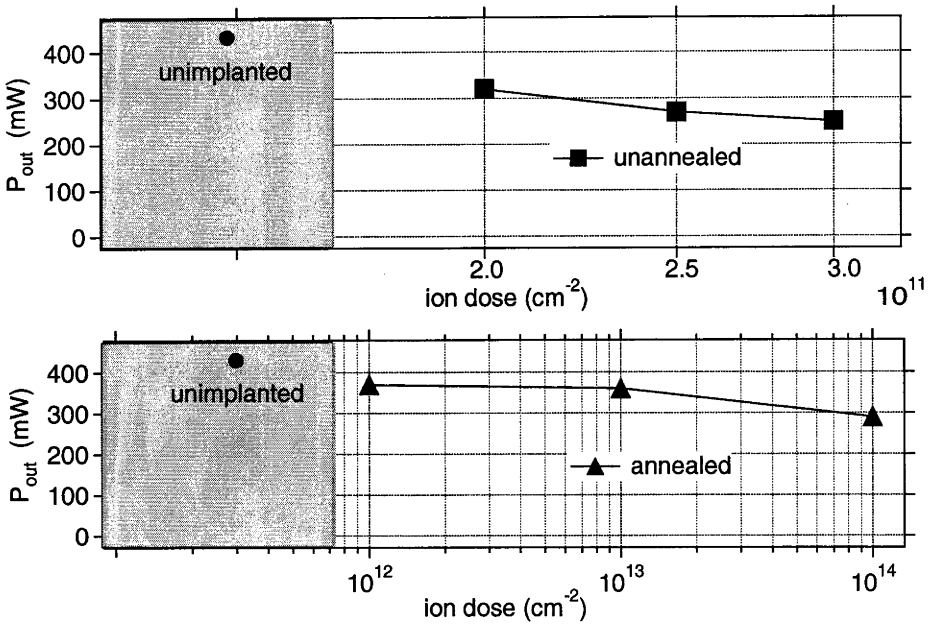

Fig. 3.2.1 - 4: Output power needed for marginally stable cw mode-locking operation for various doses of unannealed and annealed SESAMs compared to the unimplanted case.

Interestingly, for all samples including the unimplanted one, the Q-switching instability could be suppressed by inserting P_2 further, hence decreasing $|\beta_2|$ from its maximum value. This is not predicted by the analysis in [52]. However, it indicates the importance of solitonic pulse shaping within the laser. Note, that eqn. *(3.2.1 - 1)* was derived assuming that the pulses are much shorter than the absorber recovery time and hence saturation is due to the total pulse energy alone. As noted above this is not necessarily the case, at least for pulses longer than the carrier thermalisation time of ≈ 60fs [54]. As a result, stronger absorber saturation, i. e. less energy loss, can occur for a given pulse energy, if the peak power of the pulse is increased by decreasing the negative intra-cavity GDD, and hence pulse duration, in accordance with the soliton model for mode-locking [55, 59]. Finally, stronger saturation leads to a weaker Q-switched mode-locking driving force according to the general definition given on the lhs. of eqn. *(3.2.1 - 1)*. However, it will be shown in Appendix I. through a stability analysis that there is another, more important, reason for the suppression of the Q-switched mode-locking operation in a soliton mode-locked laser. This is due to the fact that, for solitons, changes in the filter and absorber losses due to a change in energy always have opposite signs which raises the threshold for Q-switched mode-locking (see Appendix I).

Further comparison between different samples reveals that the output pulsewidth remained essentially constant when operating under the same conditions, i. e. fixed output power and dispersion. This is to be expected from the soliton model of mode-locking where the pulsewidth of a stable soliton depends only on its energy and on the dispersion (see next section) . On the other hand, it was shown through

soliton perturbation theory [55] that the shortest stable single pulsewidth from a soliton mode-locked laser with saturable absorber is approximately given by

$$\tau_{FWHM}^{min} = \frac{1.763}{\sqrt{6}\cdot 2\pi\Delta f}\left(\frac{T_A \cdot g^{3/2}}{q_0 \cdot \left|\frac{\beta_2}{2}\right|^{1/2}}\right)^{1/3} \qquad (3.2.1 - 2)$$

where Δf is the HWHM filter bandwidth, T_A and q_0 are the absorber response time and modulation respectively, and g is the saturated gain. Therefore, due to the varying T_A and q_0 of the implanted samples, one should expect differences in τ_{FWHM}^{min}. However, no conclusive trend could be observed, which is most likely due to the fact that a faster response time is achieved only with a penalty in the modulation depth, as was shown in section 2.2.3, resulting in a cancellation of the trends.

For a given energy within one round trip, the pulsewidth of the mode-locked pulses was controlled by varying β_2 using P_2. The autocorrelation width depended linearly on β_2 as shown in *Fig. 3.2.1 - 5a*. Note that, in order to achieve constant pulse energy for the data in *Fig. 3.2.1 - 5a*, the pump power had to be readjusted slightly. On the other hand, for a fixed β_2, a hyperbolic type dependence resulted with respect to the intra-cavity energy as depicted in *Fig. 3.2.1 - 5b*. Both figures also show theoretical predictions valid for solitons of the Nonlinear Schrödinger Equation (NLSE) (see next section). Whilst the agreement with the NLSE model in *Fig. - 5a* is very good, the discrepancy seen in *Fig. - 5b* is most likely due to a thermal lensing induced change of the cavity mode, hence SPM and pump overlap, since the departure becomes more severe for higher powers.

Finally, given the little difference between the samples' mode-locking performance, one may wonder if there is any advantage at all in using ion-implanted or low-temperature grown saturable absorbers for passive mode-locking. Furthermore, the differences which were found (stability against Q-switched mode-locking) were related to the implantation induced reduction of the modulation depth which could also be controlled through the SESAM design. To answer this question a few facts must be stated to begin with. Firstly, the response times of around 1ps achieved with operation at and above the saturation level may not be fast enough to suppress growth of dispersive continuum for much shorter pulses than achieved here. This is particularly the case for lasers with large perturbations within one round trip (large output coupling etc.) which enhance the shedding of continuum. Secondly, it will be shown in chapter 4 that the strong dependence of the response time of unimplanted GaAs on the excitation fluence is not present in thicker absorber layers where the recovery times remain in the order of tens of ps. Thirdly, in order to guarantee stability even when the SESAM is operating at or below saturation, it remains advantageous to have a swift recovery to background or, even better, below background (PIA). Under these conditions the unimplanted SESAM does not recover to background completely. In the light of these arguments it seems that for the type of SESAM design presented

here an implant of 40keV As-ions with a dose of around $5 \cdot 10^{11}$ cm^{-2} followed by thermal annealing at 600°C for 20 min presents a compromise showing fast recovery at any fluence whilst preserving about 90% of the modulation depth of the unimplanted SESAM.

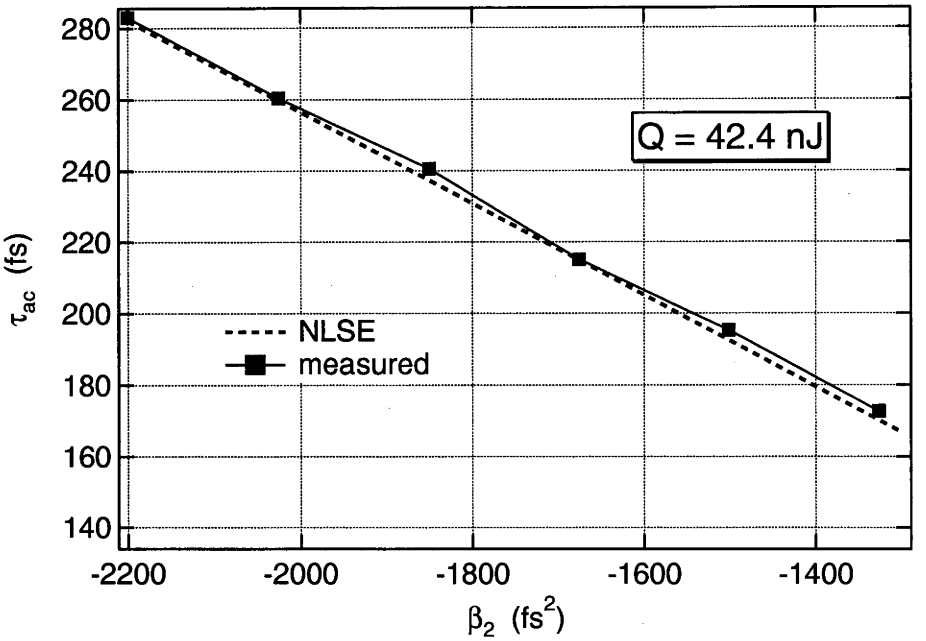

Fig. 3.2.1 - 5a: Autocorrelation width vs. β_2 with intra-cavity energy Q =42.4 nJ. Also shown: NLSE prediction for the same parameters.

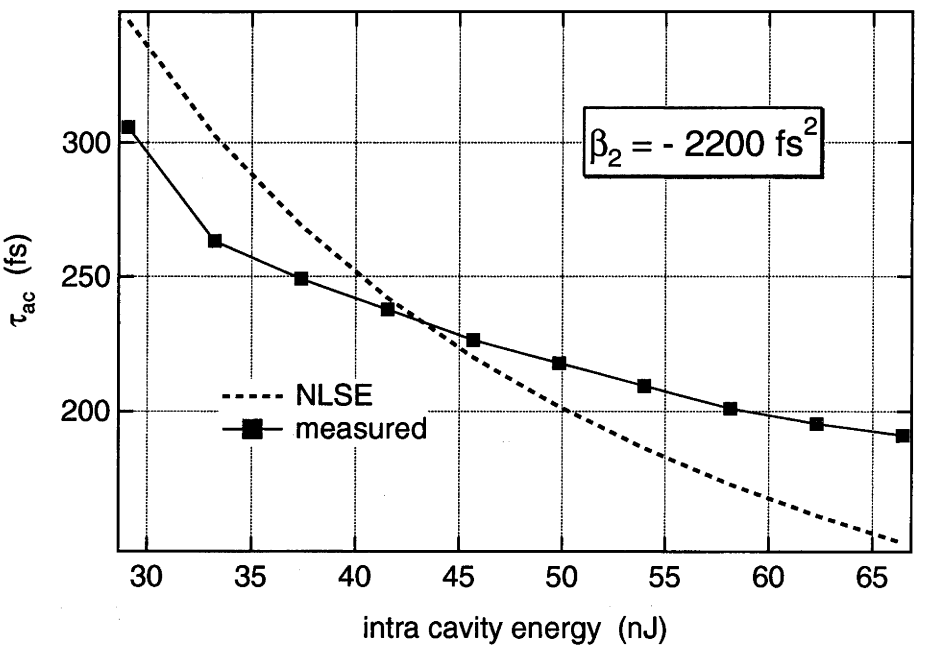

Fig. 3.2.1 - 5b: Autocorrelation width vs. intra-cavity energy Q with β_2 = -2200 fs^2. Also shown: NLSE prediction for the same parameters.

3.2.2. Theoretical

The findings in the last section, in particular the dependence of pulsewidth on dispersion and pulse energy (*Figs. 3.2.1 - 4a, b*), suggest that the mode-locked pulses were solitons. A well known model describing envelope solitons, for instance in optical fibres, is the Nonlinear Schrödinger Equation (NLSE) [56]. For negative dispersion β_2 the solutions of the NLSE are bright solitons:

$$\psi = \sqrt{\frac{\kappa \cdot Q^2}{4 \cdot |\beta_2|}} \cdot \operatorname{sech}\left(\frac{\kappa \cdot Q}{2 \cdot |\beta_2|} \cdot t\right) \cdot \exp\left(i \cdot \frac{Q^2 \cdot \kappa^2}{8 \cdot |\beta_2| \cdot T_R} \cdot T\right) \qquad (3.2.2 - 1a)$$

whose pulsewidth is given by:

$$\tau_{FWHM} = 1.763 \cdot \frac{2 \cdot |\beta_2|}{Q \cdot \kappa} = 1.763 \cdot t_0 \qquad (3.2.2 - 1b)$$

Here, Q is the soliton energy and κ is the self phase modulation (SPM) parameter calculated from the nonlinear refractive index, n_2, and other parameters as outlined in section *3.1.2*. Solitons are formed by a balance between the effects of negative intra-cavity GDD and SPM, very similar to soliton propagation in optical fibres. However, in a laser, soliton formation is influenced by gain, linear losses and absorption modulation as well as higher order and gain/filter dispersion. One critical difference between pulse propagation in fibre and a laser lies in the fact that GDD, SPM and other effects are applied discretely during every round trip. For solitons of the NLSE, the soliton period is the distance over which higher order solitons evolve periodically for a given β_2 and self-phase modulation. One can therefore take the ratio of round trip time to soliton period as a measure for the strength of solitonic pulse formation [69].

$$r = \frac{Q^2 \cdot \kappa^2}{2 \cdot \pi \cdot |\beta_2|} = \frac{Q \cdot \kappa}{\pi \cdot t_0} \qquad (3.2.2 - 2)$$

Therefore if r << 1 one can expect that the discreteness does not play a major role and a soliton model (i. e. NLSE plus perturbations) can provide useful insight into the laser dynamics [55]. For the conditions given in *Table 3.2.1 - 1* the r-parameter was of the order of 0.1 or smaller, therefore motivating the use of a mean-field model. The master equation which is used to describe the laser is a Generalised Complex Ginzburg-Landau Equation (GCGLE) [70-72], the lhs. of which is in fact the NLSE.

$$i \cdot T_R \cdot \psi_T - \frac{\beta_2}{2} \cdot \psi_{tt} + \kappa \cdot |\psi|^2 \psi = i[g - q - l_0]\psi + \frac{\beta_3}{6} \cdot \psi_{ttt} + i\beta \cdot \psi_{tt} \qquad (3.2.2 - 3)$$

Here T_R is the round trip time; β_2 is the second order dispersion; κ is the self phase modulation coefficient; g is the saturated gain per round trip; q is the absorption modulation; l_0 is the total linear loss per round trip (incl. output coupling); β_3 is the third order dispersion; and $\beta = 1/(2\pi\Delta f)^2$ is the filter dispersion constant. T is the slow time progressing in cavity round trips whereas t is the soliton or fast time which

resolves the mode-locked pulses described by the intra-cavity field ψ. As usual, subscripts of t and T indicate the partial derivatives with respect to these variables. The absorption modulation due to the SESAM is modelled by a single time constant rate-equation with respect to the fast time

$$q_t = -\frac{q - q_0}{T_a} - \frac{|\psi|^2 \cdot q}{E_a} \qquad (3.2.2 - 4)$$

with the absorber recovery time T_a, saturation energy E_a and the maximum modulation depth q_0. *Fig. 3.2.2 - 1* shows the measured normalised response of the $2.5 \cdot 10^{11}$ cm^{-2} implanted unannealed SESAM and a fit produced by solving eqn. *(3.2.2 - 4)* numerically. The fluence was 500μJ/cm², approximately the same as the intra-cavity fluence of the pulses in *Fig. 3.2.1 - 1a, b*, E_a=3nJ and T_a=0.4ps, leading to a saturation level of approximately 4 times when the cavity was operating with a SESAM spot diameter of 50μm. Finally, the laser gain per round trip is described by a rate-equation with respect to the slow time

$$g_T = -\frac{g - g_0}{T_g} - \frac{Q \cdot g}{P_g \cdot T_g \cdot T_R} \qquad (3.2.2 - 5)$$

where T_g is the upper state life time; P_g is the gain saturation power; g_0 is the small signal gain depending on the pump level; and Q is the total energy within one round trip.

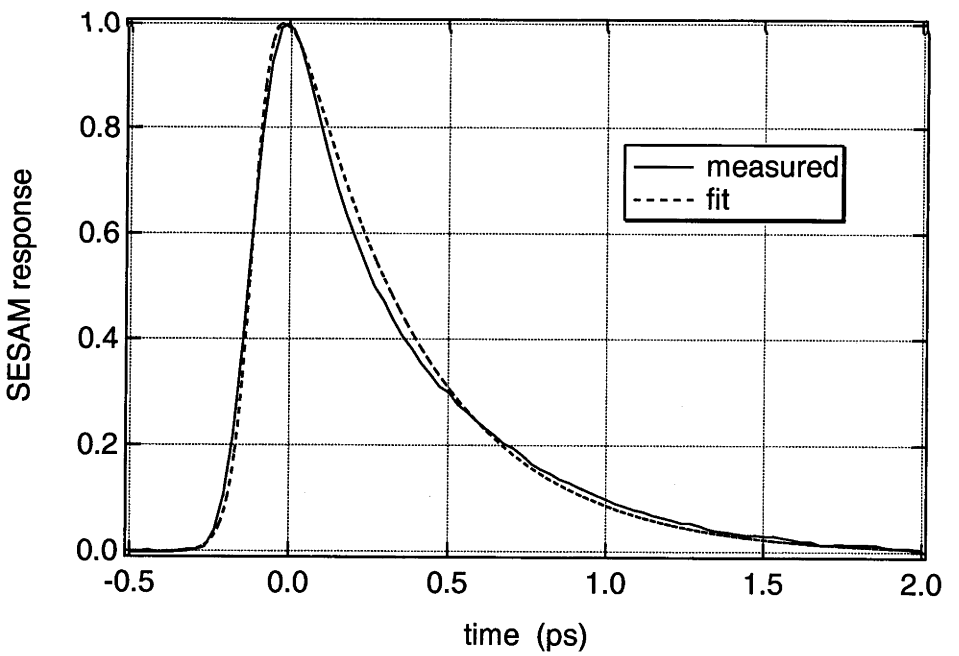

Fig. 3.2.2 - 1: Measured response of 80keV, $2.5 \cdot 10^{11}$ cm^{-2} implanted SESAM for λ=850nm (F=500μJ/cm²) together with a fit produced by solving eqn. (3.2.2 - 4) numerically. T_A=0.4ps, E_A=3nJ.

Eqns. *(3.2.2 - 3,4,5)* were solved numerically. For information on the numerics see Appendix II. As initial condition for the calculation, it was assumed that a pulse of several ps width containing all the intra-cavity energy [69] and originating from the mode-coupling driving force of the saturable absorber existed in the cavity. In order to further confirm that soliton mode-locking in the laser was stabilised by the SESAM without additional ultra-fast loss modulation due to KLM, the experimental conditions were matched as closely as possible in the simulation. All relevant parameters are listed in *Table 3.2.2 - 1*.

Figs. 3.2.2 - 2a-d show the evolution of the intra-cavity energies over 25000 round trips (*Fig. - 2a*), linear and logarithmic plots of the intra-cavity power (*Fig. - 2b, c*) of the final pulses for $\beta_2 = -300fs^2$ and $\beta_2 = -260fs^2$, as well as the spectra for the same values of β_2 (*Fig. - 2d*). The final pulsewidths are $\tau_{FWHM} = 120fs$ and $\tau_{FWHM} = 113fs$ respectively. Most importantly, for $\beta_2 = -300fs^2$ the pulse evolution is stable and growth of continuum is effectively suppressed as can be seen from the logarithmic plot. For $\beta_2 = -260fs^2$ appreciable continuum is present in the energy spectral density (*Fig. - 2d*) which becomes stabilised after 50000 round trips (not shown) when the pulsewidth becomes 114fs. The simulation indicates that the shortest stable single pulses for the parameters given in *Table 3.2.2 - 1* are 115...120fs. This is in good agreement with the experiments, suggesting that KLM is not necessary to create the observed pulsewidths. Additionally, the modulation depth used in the simulation ($q_0 = 0.006$) is a conservative value since the SESAM is passed twice per round trip. For smaller GDD, multiple pulse formation was observed both in the experiments and the simulations which will be treated in the next section. *Figs. 3.2.2 - 2b,c* also show the result of a simulation where a typical value of third order dispersion was present ($\beta_3 = -21000fs^3$, see section *3.1.2*). As can be seen, this increased the pulsewidth slightly and thereby suppressed the continuum present for $\beta_3 = 0$. Over the first several thousand round trips the energy of the pulses (see *Fig. 3.2.2 - 2a*) is not constant and varies in an oscillatory fashion. This behaviour was also observed in the experiment (*Fig. 3.2.1 - 2c*) and is explained as energy-pulsewidth readjustments through the interaction of the pulsewidth dependent filter loss, the absorber loss and the saturated gain.

Finally, one may compare the regime of stable single pulse generation observed in the simulations with the predictions made by soliton perturbation theory [55]. Using the parameters as given in *Table 3.2.2 - 1* in eqn. *(3.2.1 - 2)* a shortest possible stable pulsewidth of $\tau_{FWHM} \approx 25fs$ results compared to ca. 115fs found here. The discrepancy is not surprising, however, since the perturbation theory of [55] assumes a somewhat idealised (V-shaped) absorber response and saturation purely with energy, which is violated in the present case.

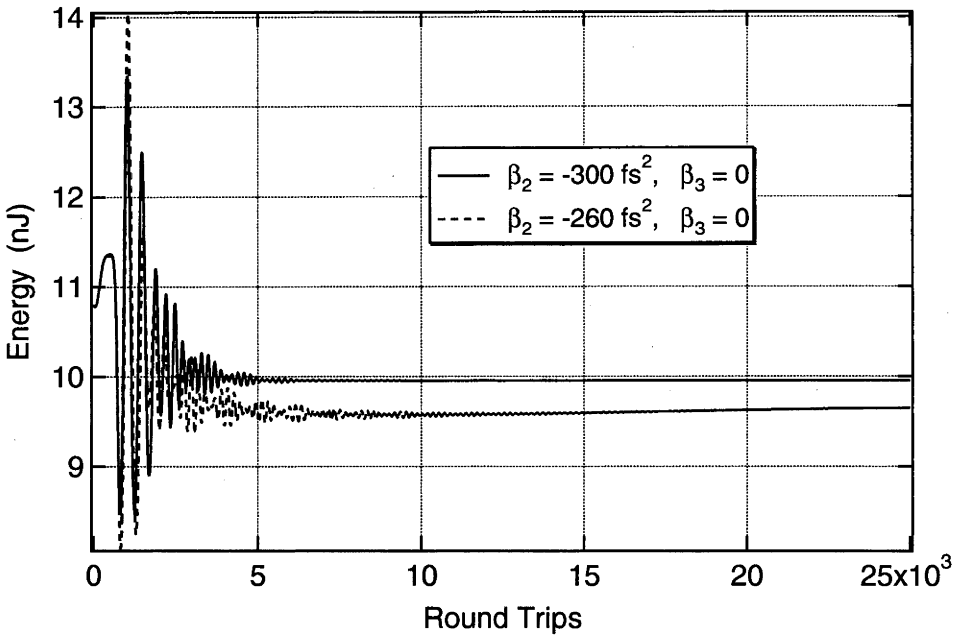

***Fig. 3.2.2 - 2a*:** Intra-cavity pulse energy evolutions over 25000 round trips for β_2 = -300fs^2 and β_2 = -260fs^2, β_3 = 0.

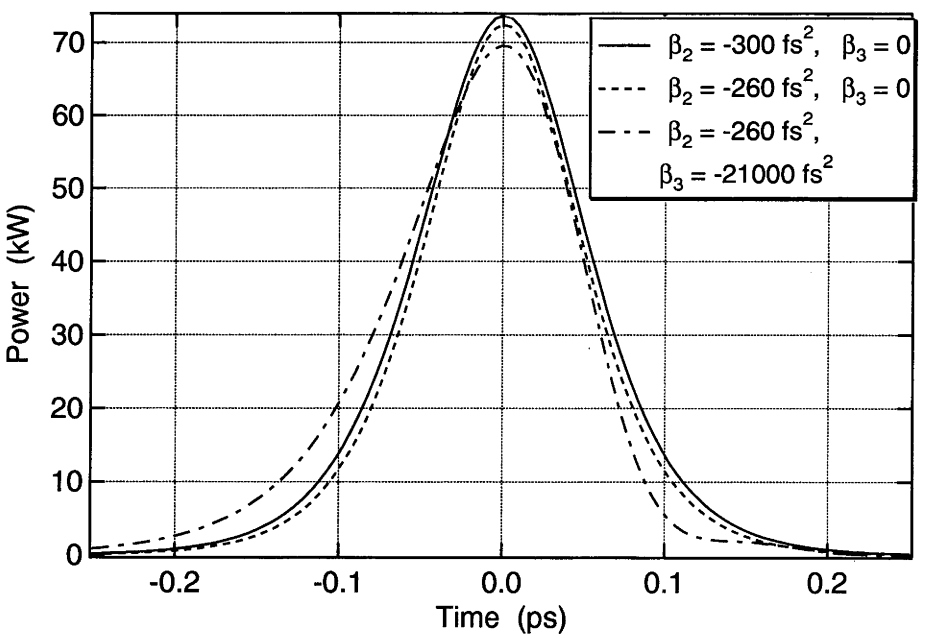

***Fig. 3.2.2 - 2b*:** Linear plots of intra-cavity pulse power after 25000 round trips for β_2 = -300fs^2, β_3 = 0; β_2 = -260fs^2, β_3 = 0; as well as β_2 = -260fs^2, β_3 = -21000fs^2.

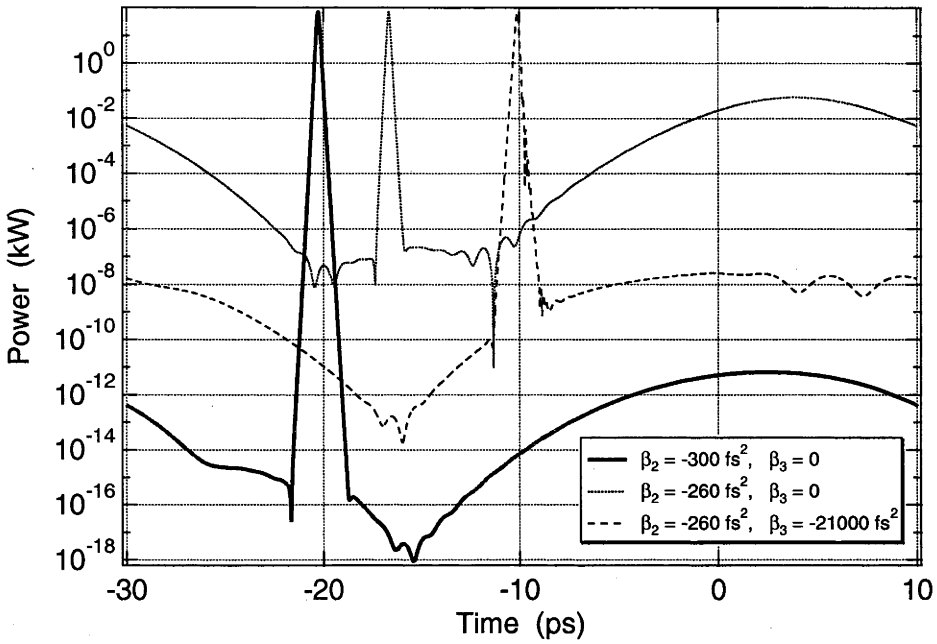

Fig. 3.2.2 - 2c: Logarithmic plots of intra-cavity pulse power after 25000 round trips for $\beta_2 = -300fs^2$, $\beta_3 = 0$; $\beta_2 = -260fs^2$, $\beta_3 = 0$; as well as $\beta_2 = -260fs^2$, $\beta_3 = -21000fs^2$.

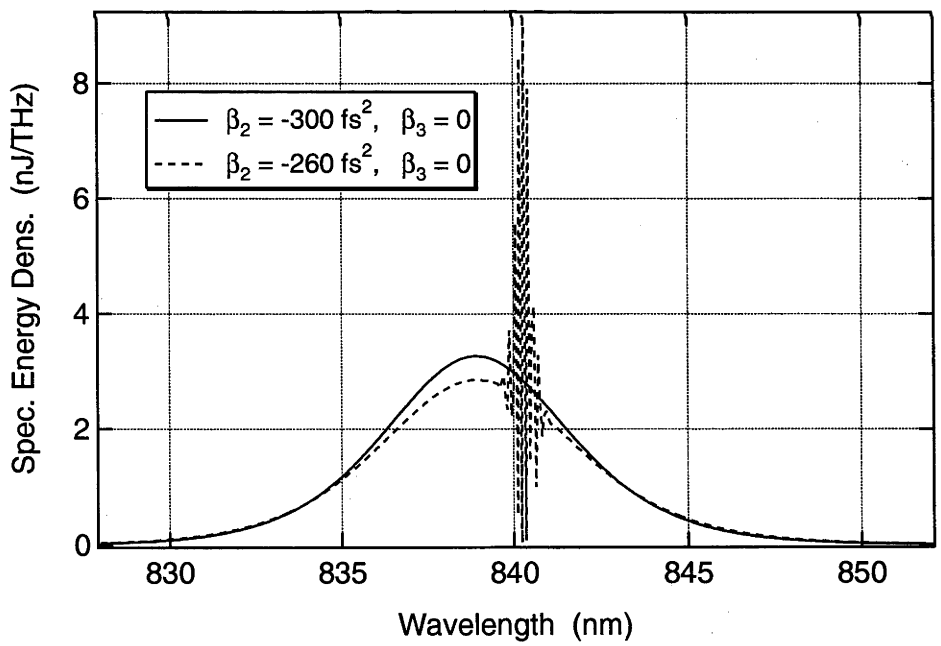

Fig. 3.2.2 - 2d: Intra-cavity energy spectral densities after 25000 round trips for $\beta_2 = -300fs^2$, $\beta_3 = 0$ and $\beta_2 = -260fs^2$, $\beta_3 = 0$.

Parameter	Value	Description
R_{out}	0.86	output coupler reflectivity
q_{nb}	0.005	nonbleachable loss per reflection on SESAM
l_0	(1-Rout) / 2 + 2 · q_{nb} = 0.08	total linear loss per round trip
T_R	12ns	round trip time
β	$1/(2\pi\cdot\Delta f)^2 = 1/(2\pi\cdot 25\text{THz})^2$	filter dispersion
β_2	variable	second order dispersion
β_3	variable	third order dispersion
l_L	23mm	length of laser crystal
n_2	$2\cdot10^{-20}$ m²/W	nonlinear refr. index of Sapphire
d_{eff}	94µm	eff. mode diam. in Ti:Sapphire
λ	850nm	wavelength
κ	$16\, n_2\, l_L / (\lambda\, d_{eff}^2) = 1\cdot10^{-6}$ 1/W	SPM coeff.
q_0	$\Delta R_{max} / 2 = 0.006$	ampl. modulation of SESAM
E_a	3nJ	sat. energy of SESAM
T_a	0.4ps	absorber recovery time
σ_g	$3.8\cdot10^{-19}$ cm²	Ti:Sapphire gain cross section
T_g	2.5µs	exc. state life time of Ti:Sapphire
P_g	$\pi\cdot h\cdot c\cdot d_{mode}^2 / (4\cdot\lambda\cdot\sigma\cdot\tau) \approx 4$W	sat. power of Ti:Sapphire
P_{av}	900mW	average intra-cavity power
Q_{init}	$P_{av} \cdot T_R$ = 10.8nJ	energy of initial cond. (sech²)
τ_{FWHM}	2ps	pulsewidth of initial cond. (sech²)
g_0	0.1033	small signal round trip gain (calc. for balance of sat. gain and all losses seen by initial cond.)

Table 3.2.2 - 1: Laser parameters for single pulse simulations.

3.3. Multiple Pulse Operation

Multiple pulse operation of soliton lasers has been reported from time to time over the last decade. An early report of the observation of higher order solitons is that of double humped pulses from a Colliding Pulse Mode-locked (CPM) dye laser [57]. The autocorrelation and spectral features resembled closely those of asymmetric N=2 solitons of the Nonlinear Schrödinger Equation (NLSE). On the other hand, a large number of randomly spaced solitons within the cavity were observed in a figure of eight fibre laser [58]. In this context, it was found that the intra-cavity energy was quantised, increasing in steps with the number of solitons present. More recently, the break-up of single pulses into multiple pulses was seen in a Kerr Lens Mode-locked (KLM) Ti:Sapphire laser [59] as well as other solid state lasers mode-locked by Semiconductor Saturable Absorber Mirrors (SESAMs) [60]. In these cases, the spacing between pulses was generally much larger than a single pulsewidth, was irregular and subject to spontaneous changes.

The appearance of multiple pulses within a laser cavity is of significance to the production of high repetition rate soliton pulse sources for optical fibre communication systems. In this context considerable effort is being directed towards refining harmonic mode-locking in both Erbium doped fibre lasers [61-65] as well as a Cr^{4+}:Yag bulk laser [66]. In these systems, either nonlinear polarisation rotation or a Semiconductor Bragg Reflector (SBR) were used as the passive mode-locking mechanisms. The observation of self-organisation of the intra-cavity pulse spacing was attributed to a number of mechanisms, such as coupling of the solitons via dispersive continuum and acoustic waves [61, 63, 67], and gain dynamics [65, 68]. However, explanations of the conditions leading to the formation of multiple solitons have generally been of a rather qualitative nature [64, 66, 73].

Section *3.3* and its subsections are concerned with the multiple pulse operation of the laser described in sections *3.1* and *3.2*. In addition to far separated double, triple and quadruple pulses with irregular spacings, it was found that closely coupled states can exist which are the result of interplay between the saturable absorber and filter losses, saturated gain and the coherent interaction of solitons. Emphasis lies on the explanation of these observations as well as the mechanisms involved in the multiple pulse transitions within the framework of the Ginzburg-Landau master equation used to model the laser.

3.3.1. Experimental

Once mode-locking had been established, tuning the intra-cavity dispersion through insertion of P_2 resulted in consistent evolution of the pulse properties (see *Fig. 3.1.1 - 1*). This behaviour is summarised as follows.

Starting from single pulse operation at large negative dispersion ($\beta_2 = -2000fs^2$), decreasing $|\beta_2|$ led to a linear reduction in the single pulse autocorrelation width τ_{ac} from 250fs down to 155fs at $\beta_2 = -1250fs^2$, as would be expected for solitonic mode-

locking (see also *Fig. 3.2.1 - 4a*). The reduction in dispersion was accompanied by a slight decrease in average output power suggesting that the intra-cavity dynamic losses increased as the dispersion was lowered. In the case of the data shown in *Fig. 3.1.1 - 1*, this was however counteracted through slight readjustment of the pump power to keep P_{out} constant at 510mW. A further decrease in dispersion below β_2 = -1250fs^2 led to an abrupt transition from a single pulse to double pulses circulating within the resonator. This transition was accompanied by an increase in P_{out} to 560mW, whilst the autocorrelation widths of the individual pulses in the double pulse pair also increased compared with the single pulse autocorrelation width on the high dispersion side of the transition. Similar transitions were reported previously in other SESAM and SBR mode-locked soliton lasers [60, 66]. However, from the pulse energies, and assuming first order solitons for both the single and double pulse cases, one should expect a larger jump in pulsewidth than that indicated in *Fig. 3.1.1 - 1*. Therefore, the soliton numbers $N = \sqrt{\frac{\kappa \cdot Q \cdot t_0}{2 \cdot |\beta_2|}}$ [75] were annotated to the measured values of τ_{ac} assuming sech^2-pulses. Here, Q is the pulse energy, κ is the self-phase modulation parameter, and $t_0 = \frac{\tau_{FWHM}}{1.763}$. Whilst the pulses in the single pulse regime are virtually ideal first order solitons, N becomes around 0.8 in the double pulse case. Such a change of N could indicate that the double pulses underwent non-negligible nonlinear formation within one round trip. Alternatively the switch from single to double pulses could have caused a slight readjustment of the mode size in the laser crystal whereby the self-phase modulation parameter κ was changed. However, the exact cause of the decrease in N was not investigated since analyses assuming N = 1 in later sections will remain qualitatively valid.

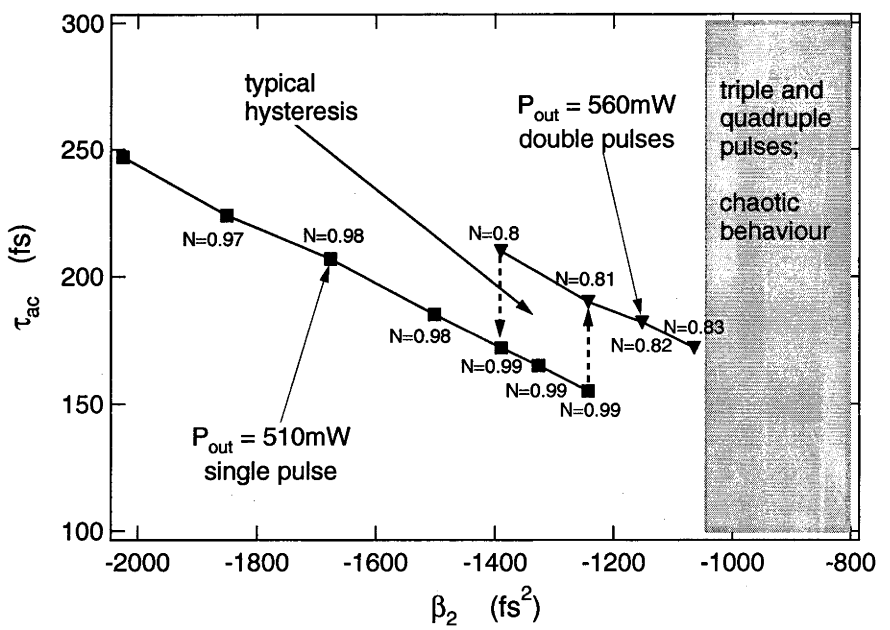

Fig. 3.3.1 - 1: Measured autocorrelation width versus total intra cavity dispersion β_2 in the range of the single-to-double soliton transition.

Note that the following arguments concentrate on dispersion as the variable to induce transitions between the various pulse states. However, these could also be changed by adjusting the pump power, hence small signal gain g_0. As a result, for fixed dispersion on the single pulse side of the transition, an increase in pump power also caused the appearance of double pulses.

Once in double pulse mode, the laser could be forced back to single pulse operation by increasing $|\beta_2|$. The transitions from 'single-to-double' and 'double-to-single' generally occurred with hysteresis in $|\beta_2|$ indicating a form of bistability. Note, however, that the exact nature of the pulses (their separation and relative phase) in the double pulse state near the transition could vary as the laser was cycled through the transition zone or when it was started with a $|\beta_2|$ value in the double pulse region. In fact, the observed pulse-to-pulse spacings ranged between several 100fs and several ps as seen from sample autocorrelation traces in *Figs. 3.3.1 - 2a-d.* In general there was a tendency towards larger pulse spacings when operating at high pump power. The time-integrated spectra corresponding to the data of *Figs. 3.3.1 - 2a-d* provide information, albeit limited, about the relative phases between the pulses in the double pulse states. The spectra suggest that a number of possible phase states could exist including fully rotating relative phase (*Fig. - 2b*); fixed at or alternating around $\phi \approx \pi$ (*Fig. - 3c*); and $\phi \approx 0$ (*Fig. - 3d*). Spectra corresponding to either fixed or fully rotating phase states were observed for far separated doublets indicating that rather weakly selective processes were responsible for determining the relative phase in this case.

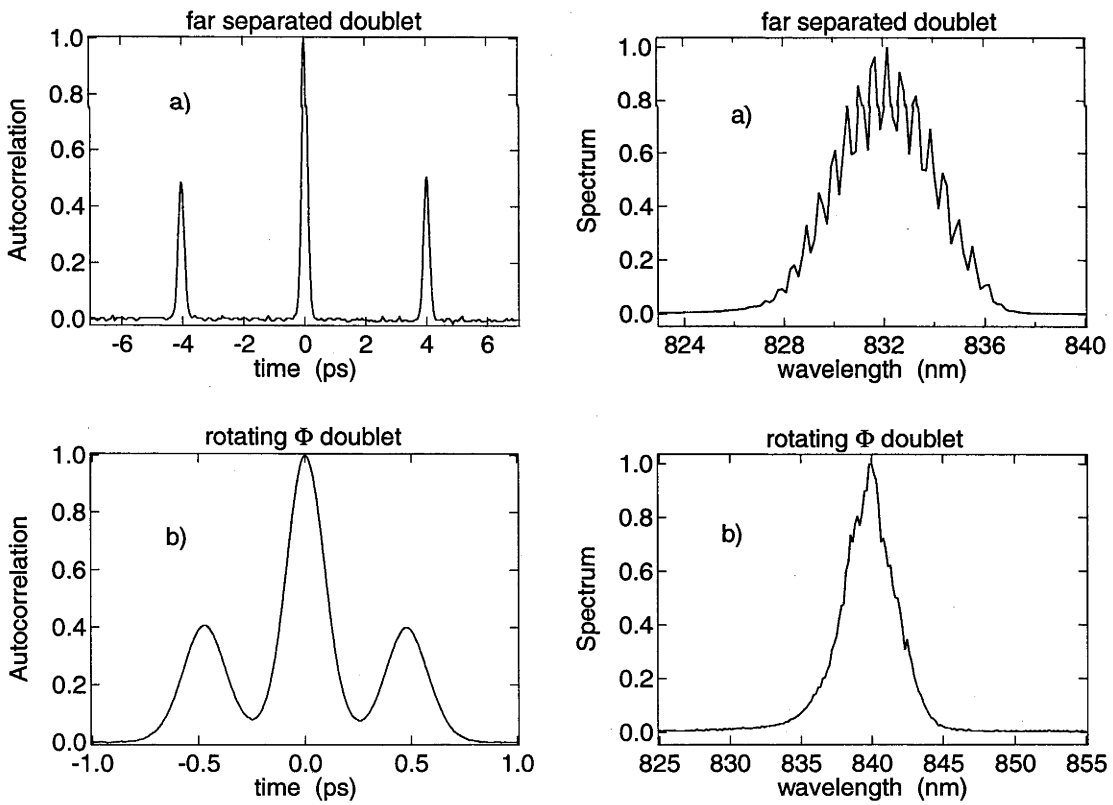

Fig. 3.3.1 - 2a-b: Autocorrelation traces and spectra of (a) far separated doublet and (b) rotating ϕ doublet.

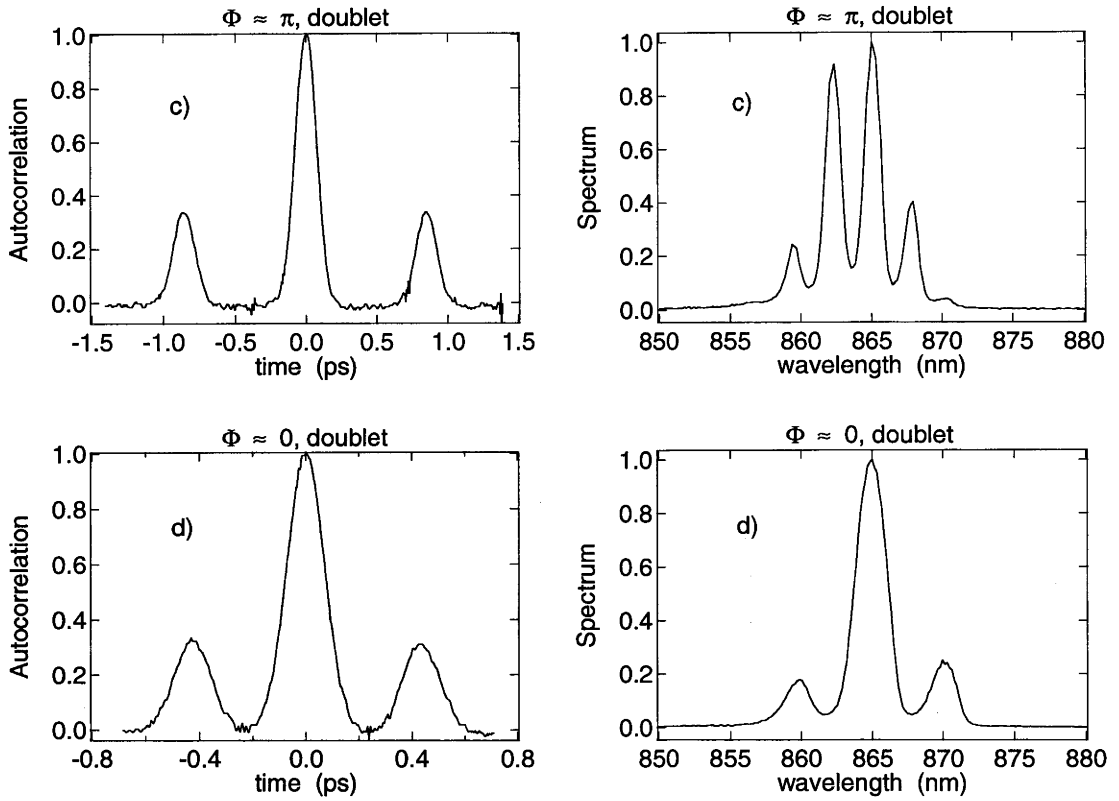

Fig. 3.3.1 - 2c,d: Autocorrelation traces and spectra of (c) $\phi \approx \pi$ doublet, and (d) $\phi \approx 0$ doublet.

Starting with double pulses, a further reduction of $|\beta_2|$ led again to a linear decrease of τ_{ac} and finally to the appearance of triple pulses at $\beta_2 = -1100fs^2$. The double to triple pulse transition was again accompanied by a jump in average laser power; an increase in the autocorrelation widths of the pulses on the low $|\beta_2|$ relative to the high $|\beta_2|$ side; and variability in the exact pulse spacing and relative phase of the pulses after the transition. The transition from triple pulses to double pulses could be induced with hysteresis by increasing $|\beta_2|$. For triple pulses the separation could differ widely (from several 100fs to several ns). Autocorrelation traces and spectra of some triple pulse states are shown in *Fig. 3.3.1 - 3a-c.* The spectral modulation due to the far separated pulse in *Fig. - 3a* is not resolved. The relative phases between triple pulses can be defined using the phase of the central pulse as the reference. For reasons of symmetry, in the case of the triplet in (*Fig. - 3b*), the central pulse must be π out of phase with its companions. It is therefore referred to as a $\phi \approx \pi$ triplet, whilst (*Fig. - 3c*) shows a $\phi \approx 0$ triplet. There was a clear tendency for both double and triple pulses to be closely spaced with apparently fixed phase, only when the laser was tuned at the long wavelength end of the SESAM's range of operation, (i. e. where it exhibited the largest modulation depth), and only when operating with the smaller SESAM spot size, (i. e. under strong saturation). With a further reduction in $|\beta_2|$, quadruple pulse states also appeared but were always separated at large distances (>1ns). However, the dispersion ranges for triple and quadruple pulses were small and somewhat ill defined.

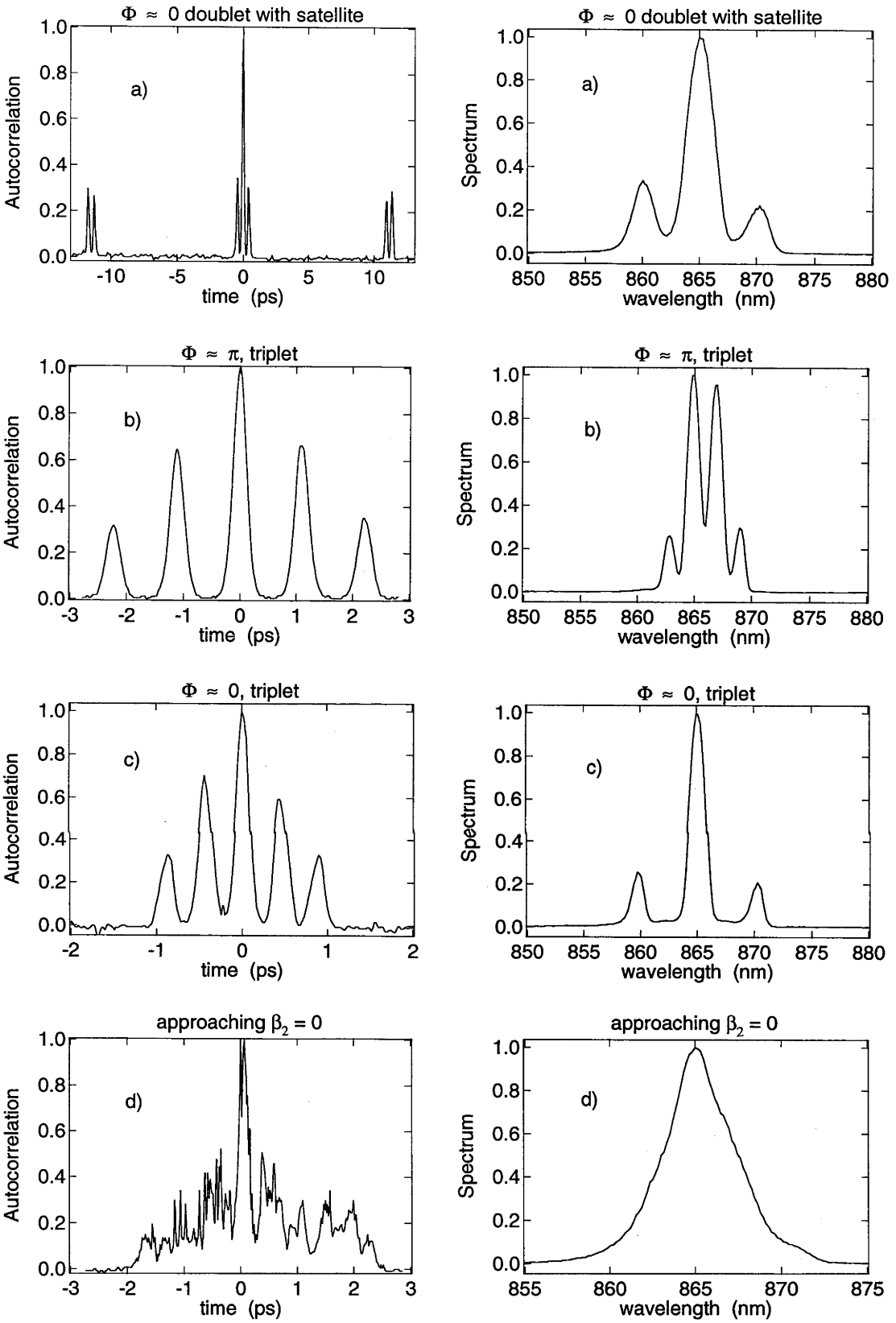

Fig. 3.3.1 - 3a-d: Autocorrelation traces and spectra of (a) doublet with far separated companion, (b) $\Phi \approx \pi$ triplet, (c) $\Phi \approx 0$ triplet, (d) irregular behaviour for small $|\beta_2|$.

Any further decrease of $|\beta_2|$ resulted in irregular, chaos-like behaviour, indicated by unsteady autocorrelation traces (*Fig. - 3d*). The transition to irregular output occurred earlier when the laser was operating at a low small signal gain g_0, where only closely spaced double pulses were seen within a narrow range of $|\beta_2|$. Finally, crossing to positive dispersion caused the laser to emit strongly chirped ps-pulses (*Fig. - 3e*).

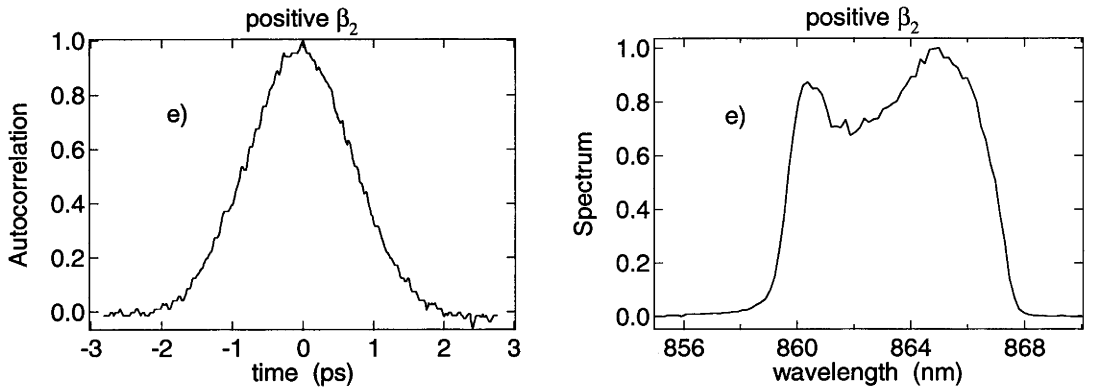

Fig. 3.3.1 - 3e: Autocorrelation traces and spectra of chirped ps-pulse for positive β_2.

Finally, self-starting the laser with a $|\beta_2|$-value in the multiple pulse regime could lead to a different final state compared with when it was forced from single to multi-pulse operation via a gradual change of dispersion towards the same final $|\beta_2|$-value. Although the observed multiple-pulse states could be stable over extended periods, the global stability of the laser was poor when compared to that of single pulse operation, and slight perturbations could provoke a change in pulse separation.

These observations provide the essential clues to identifying the important parameters affecting the appearance of multiple pulses in the laser. Clearly the transitions between pulse states display similarities indicating that they result from the same underlying physical processes. Furthermore the equivalent effect of changing dispersion or small signal gain to cause a transition suggests these two parameters must be intimately linked in any model of the process. The observation that a transition is accompanied by a distinct change in average output power indicates that a change in saturated gain occurs, which can only be caused by a change in the dynamic losses in the cavity. The dynamic losses also increase as $|\beta_2|$ is reduced in the regions of stable single, or stable multiple pulses since the average laser power decreases. Within the multiple pulse regions, only very weak processes determine the pulse separation and relative phase, since there is no strongly favoured state.

Qualitatively most of these factors can be linked by recognising that the laser produces solitons, i. e. the pulse duration and spectral bandwidth are directly related to intra-cavity dispersion and pulse energy. Secondly, it must be recognised that the intra-cavity dynamic losses are determined by the spectral bandwidth of the pulse through its interaction with a band-pass filter within the laser (explicitly included in our system as a birefringent tuning filter), and also by the circulating pulse power through interaction with the saturable absorber modulator in the cavity. In explaining the observations, therefore, the focus will be on the relation between filter and

saturable absorber losses to the solitons within the resonator. Also, the regions where the laser becomes destabilised leading to a transition to a lower loss state will be defined.

3.3.2. Theoretical

In order to investigate the above observations, the master equation approach was again used. The relevant equations have been introduced in section *3.2.2* (eqns. *(3)-(5)*) and the discussion given there is also valid here. As initial condition for the simulations performed in the following sections, either a ps pulse containing all the intra-cavity energy was used, or fields suitably close to the final solution were assumed. The parameters for the simulations are given in *Table 3.3.2 - 1* and in the text when the need arises.

3.3.2.1. Single ↔ Double Transition, Relevant Mechanisms and Far Separated Pulses

It was pointed out in [71, 73] that the stability of a soliton in the laser, when subject to perturbations from a filter and an absorber, can only be maintained as long as the growth of dispersive continuum radiation is effectively suppressed. This is the case when $l_s < l_c$ where

$$l_s = \delta + \alpha = \frac{\beta}{3 \cdot t_0^2} + \frac{1}{2 \cdot t_0} \cdot \int_{-\infty}^{\infty} \mathrm{sech}^2\left(\frac{t}{t_0}\right) \cdot q(t) dt \qquad (3.3.2 - 1a)$$

with

$$t_0 = \frac{2 \cdot |\beta_2|}{\kappa \cdot Q} = \frac{\tau_{FWHM}}{1.763} \qquad (3.3.2 - 1b)$$

Here, l_s is the total energy loss per round trip of the soliton consisting of filter loss δ and absorber loss α, t_0 is the soliton pulsewidth for the given energy, dispersion and self-phase-modulation and l_c is the loss experienced by the continuum. For a particular $|\beta_2|$ the latter depends, in a roughly inverse manner, mainly on the absorber recovery time T_a and the maximum modulation depth q_0, as was shown through soliton perturbation theory [71]. However, for an arbitrary absorber the continuum loss cannot be calculated analytically. In the following discussion, the exact knowledge of l_c is not needed and its role will be clarified whenever necessary. In the real laser, apart from filter and absorber perturbations, the discreteness of all effects (SPM, dispersion, gain...) as well as the higher order dispersion also cause shedding of continuum by the soliton. Whilst higher order dispersion can be included in the master equation, it was found not to be necessary for a satisfactory explanation of the experimental observations. To take into account the discreteness of the laser would require a model which allows for pulse shaping dynamics within one round trip. This is not covered by

the current model but will become important for cases when $r \approx 1$ or larger. Generally, for the laser in equilibrium the condition of energy balance

$$g - l_0 - \delta - \alpha = 0 \qquad (3.3.2 - 2)$$

must be fulfilled, where δ and α are the energy losses per round trip due to the filter and the absorber for both solitons and continuum, if present. The graphical representation of this condition is shown in the inset of *Fig. 3.3.2 - 1a*. Depending on δ and α, the laser will adjust its saturated gain g such that eqn. *(3.3.2 - 2)* will remain fulfilled. The frame defined by the two lines separated by q_0 therefore moves with respect to the zero gain line. Clearly, if the line $g - l_0 - q_0$ crosses the zero line due to an increase in δ for instance, continuum growth is possible, even for solitonic mode-locking schemes using ultrafast saturable absorbers such as the Kerr lens or nonlinear polarisation rotation. For a slow absorber the net gain window remains open longer and growth can occur slightly earlier, indicated by $\varepsilon \neq 0$, but the physical process is the same. The onset of continuum growth is the critical condition which destabilises the soliton pulse in the laser cavity. The condition for continuum growth in the presence of a single soliton with energy Q_1, and hence the threshold for the transition from single to multiple pulses, is simply

$$[\alpha_1 + \delta_1 + \varepsilon]_{Q1} \geq q_0 \qquad (3.3.2 - 3a)$$

where ε was introduced to account for the effect of a slow absorber. $\varepsilon = 0$ for the ideally fast absorber.

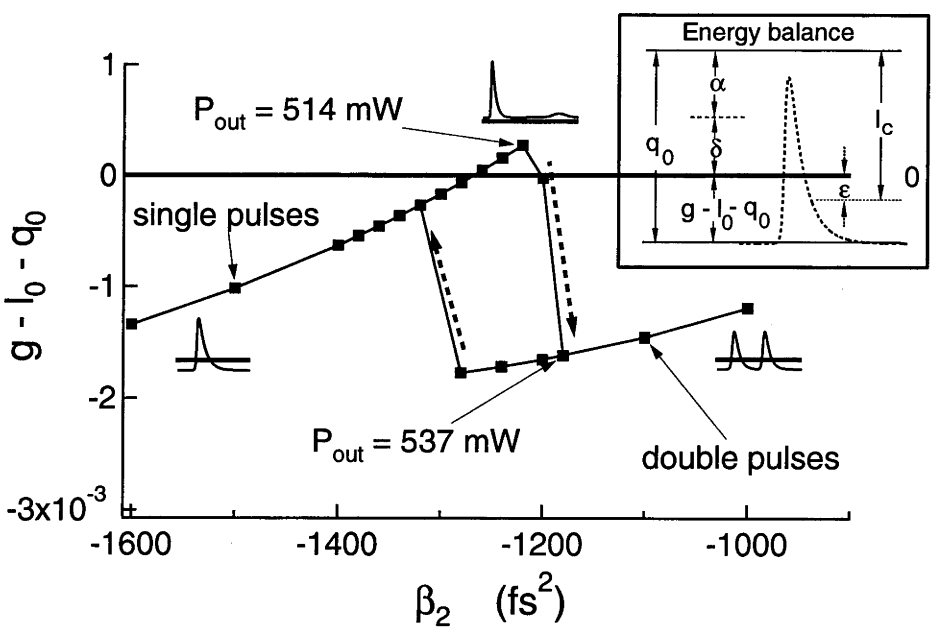

Fig. 3.3.2 - 1a: $g - l_0 - q_0$ as a function of β_2 around the single-to-double transition. The inset shows a diagram clarifying the energy balance in equilibrium. $g_0 = 0.1687$, $q_0 = 0.006$, $T_a = 0.3$ps, $E_a = 10$nJ, $P_g = 4$W, see also *Table 3.3.2 - 1.*

If a second stable soliton is formed at a distance >>T_a the two pulses have approximately half the total intra cavity energy each and twice the width of the single pulse before break-up. Generally, this decreases δ but increases α which leads to the condition

$$[\alpha_1 + \delta_1]_{Q1} > [\alpha_2 + \delta_2]_{Q2} \qquad (3.3.2 - 3b)$$

for the formation of two stable solitons. Here, Q_2 is the total intra-cavity energy of two pulses, which is slightly larger (a few %, see also *Fig. 3.3.1 - 1*) than Q_1. The indices 1 and 2 refer to the losses experienced by one and two pulses with the total energies Q_1 and Q_2 respectively. From *(3.3.2 - 3b)* one infers that, upon switching from a single to a double soliton, as long as the decrease in filter loss is greater than the increase in absorber loss, the total losses are decreased, the growth of continuum is suppressed, and two stable solitons are formed. Note, however, that *(3.3.2 - 3a)* is the break-up condition and as such a prerequisite for *(3.3.2 - 3b)*. Eqn. (21) in [73] is the same as *(3.3.2 - 3b)*, although it was assigned a different significance there, namely that of another break-up condition besides that of continuum growth. However, the numerical results show that even if *(3.3.2 - 3b)* is satisfied, stable single pulses exist in the resonator (e. g. *Fig. 3.3.2 - 1a*, at $\beta_2 \approx$ -1400fs²), unless *(3.3.2 - 3a)* is also satisfied. Finally, whether the initial growth of the continuum will lead to a second soliton or will become stabilised depends on how far g - l_0 - q_0 has been driven above zero and therefore also on the degree of saturation and response time T_g of the gain medium.

The stability of the pair of solitons is, however, bounded by two limits. The first, towards smaller $|\beta_2|$, is that of renewed shedding and growth of continuum if $[\alpha_2 + \delta_2 + \varepsilon]_{Q2} > q_0$, similar to the single soliton case *(3.3.2 - 3a)*. This eventually drives the transition from double to triple pulses. The second limit, towards larger $|\beta_2|$, is not immediately obvious because from the above argument, the pulse pair always appears to experience lower loss than a single pulse with the same total energy, because of the dominant influence of the filter loss. However, the situation becomes clearer by deriving a stability criterion from the evolution of the pulse energies Q_a and Q_b as well as the gain g in the framework of soliton perturbation theory. This leads to

$$T_R \cdot \frac{dQ_a}{dT} = 2 \cdot \left[g(Q_a + Q_b) - l_0 - \delta_a - \alpha_a \right] \cdot Q_a \qquad (3.3.2 - 4)$$

$$T_R \cdot \frac{dQ_b}{dT} = 2 \cdot \left[g(Q_a + Q_b) - l_0 - \delta_b - \alpha_b \right] \cdot Q_b \qquad (3.3.2 - 5)$$

$$\frac{dg}{dT} = -\frac{g - g_0}{T_g} - \frac{(Q_a + Q_b) \cdot g}{P_g \cdot T_g \cdot T_R} \qquad (3.3.2 - 6)$$

where the filter and absorber losses are given by the expressions in *(3.3.2 - 1a,b)*. The underlying assumption to this treatment is, apart from far separation between pulses, that despite the perturbations due to filter and absorber, the pulses remain solitons in

the adiabatic sense, i. e. eqns. (3.2.2 - 1*a, b*) are still valid. Eqns. *(3.3.2 - 4,5,6)* can be analysed for their stability around a working point $\left(\tilde{Q}_{a,b}, \tilde{\delta}_{a,b}, \tilde{\alpha}_{a,b}, \tilde{g}\right)$ through linearisation. Inserting

$$\begin{pmatrix} Q_{a,b} & \rightarrow & \tilde{Q}_{a,b} + \Delta Q_{a,b} \\ \delta_{a,b} & \rightarrow & \tilde{\delta}_{a,b} + \Delta\delta_{a,b} \\ \alpha_{a,b} & \rightarrow & \tilde{\alpha}_{a,b} + \Delta\alpha_{a,b} \\ g & \rightarrow & \tilde{g} + \Delta g \end{pmatrix} \qquad (3.3.2 - 7)$$

in *(3.3.2 - 4,5,6)* leads to equations for the changes in the soliton energies and the gain

$$T_R \cdot \frac{d\Delta Q_{a,b}}{dT} = 2 \cdot \left[\tilde{Q}_{a,b} + \Delta Q_{a,b}\right] \cdot \left[\Delta g - \Delta\alpha_{a,b} - \Delta\delta_{a,b}\right] , \qquad (3.3.2 - 8)$$

$$\frac{d\Delta g}{dT} = -\Delta g \cdot \left(\frac{1}{T_g} + \frac{\left(\tilde{Q}_a + \tilde{Q}_b\right)}{P_g \cdot T_g \cdot T_R} \right) - \frac{\left(\Delta Q_a + \Delta Q_b\right) \cdot \left[\tilde{g} + \Delta g\right]}{P_g \cdot T_g \cdot T_R} \qquad (3.3.2 - 9)$$

Neglecting the terms in 2nd order $(\Delta Q \cdot \Delta g)$, and using the facts that $\tilde{Q}_a = \tilde{Q}_b = \frac{Q_{tot}}{2} = const.$ and $\Delta Q_a = -\Delta Q_b$, eqn. *(3.3.2 - 9)* becomes obsolete. Then, *(3.3.2 - 8)* renders the condition for the stability of either of the two solitons

$$\Delta\delta > -\Delta\alpha \qquad (3.3.2 - 10)$$

This means that any small perturbation of one of the solitons leading to a change of energy, and hence pulsewidth, can be counteracted by a change in filter loss as long as the latter is larger than the negative change in absorber loss at the current working point. If the stability condition *(3.3.2 - 10)* is violated the laser will switch to single pulse operation. One can expect *(3.3.2 - 10)* to be violated when $|\beta_2|$ is increased since that results in an increase in pulse duration which reduces the absolute filter losses as well as the incremental variation in filter losses caused by the appearance of an energy imbalance. Given that the total intra cavity energy always changes slightly when switching between states ($Q_1 \neq Q_2$, due to changes of loss and gain saturation) it is apparent that the observed hysteresis is a consequence of $Q_1 \neq Q_2$ in conjunction with *(3.3.2 - 3)* and *(3.3.2 - 10)*.

Fig. 3.3.2 - 1a shows the evolution of g - l_0 - q_0 as function of $|\beta_2|$ for the transition from one to two solitons. The parameters were chosen to match the experimental conditions of *Fig. 3.3.1 - 1* as closely as possible. Starting the calculation well within the regime of single pulse operation, $|\beta_2|$ was gradually changed towards smaller values so as to mimic a dispersion change in the real laser. Each gradual dispersion change was accomplished over 2000 round trips which was then followed by 25000 round trips of unperturbed evolution. *Fig. 3.3.1 - 1a* clearly illustrates the main mechanisms involved: *(a)* shedding and growth of continuum as

$[\alpha_1 + \delta_1 + \varepsilon]_{Q1} \geq q_0$, *(b)* formation of a second soliton to reduce the total dynamic loss moving g - l_0 - q_0 well below the level needed for continuum growth (note that due to the relatively fast absorber $\varepsilon \approx 0$), *(c)* hysteresis in switching back to a single soliton as $\Delta\delta < -\Delta\alpha$. Due to the lack of analytical solutions, the stability condition *(3.3.2 - 10)* was checked numerically for perturbations in the energy, i. e.

$$\Delta\delta = \frac{\partial\delta}{\partial Q} \cdot \Delta Q \quad > \quad -\Delta\alpha = -\frac{\partial\alpha}{\partial Q} \cdot \Delta Q \qquad (3.3.2 - 10a)$$

For the given parameters and pulse energies this leads to single pulse operation for $|\beta_2| > 1315$ fs², in agreement with the simulation. Note that the single-to-double soliton transition in the simulation occurs at the same dispersion β_2 as in the real laser (see *Fig. 3.3.1 - 1*), indicating the validity of the master equation model in this case. *Fig. 3.3.2 - 1b* shows the evolution of the single pulse into two pulses with equal energies at dispersion $\beta_2 \approx$ -1200 fs². Since continuum is suppressed by 20 orders of magnitude (not shown) and the observed separation (ca. 5ps) is too large for the two pulses to interact coherently or through the absorber recovery tail, they remain at a constant mean separation due to their equal energies. It must be noted that this explanation of the pulse spacing is only valid in the framework of the present model. It does not take into account the possibility of gain dynamics within one round trip as considered in [68], or acoustic effects [67]. However, due to the relatively large perturbations per round trip (14% output coupling, SPM, dispersion and filter) in this laser, one would expect gain dynamics and acoustic effects not to be dominant in the self-organisation of far separated pulses. As was mentioned in the experimental section, reliably reproducible pulse patterns for far separated multiple pulses were not observed and the mechanisms of self-organisation are therefore not investigated here.

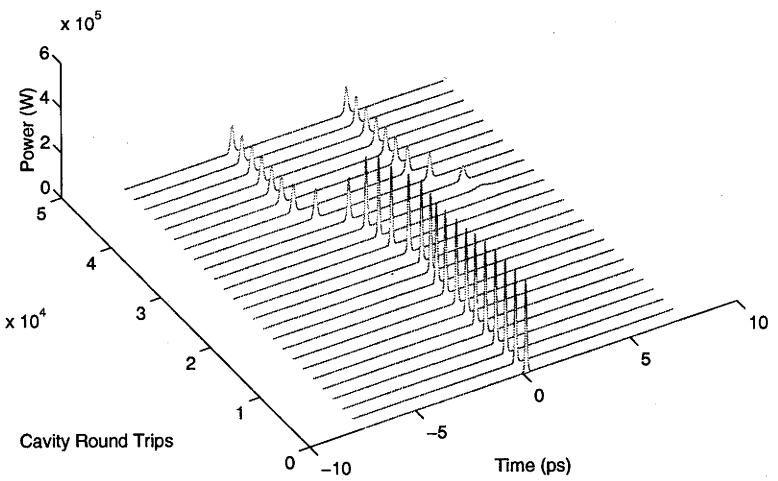

Fig. 3.3.2 - 1b: Evolution of the single soliton into two solitons with approx. 5ps separation at $\beta_2 \approx$ -1200 fs². $g_0 = 0.1687$, $q_0 = 0.006$, $T_a = 0.3$ps, $E_a = 10$nJ, $P_g = 4$W, see also *Table 3.3.2 - 1*.

3.3.2.2. Closely Spaced Pulses

It is well known that solitons of the Nonlinear Schrödinger Equation (NLSE) interact [75] depending on their relative phase and amplitude. A phase of $\phi = 0$ leads to attraction and periodic collapse, whereas even small differences in amplitude and phase prevent this collapse; for $\phi = \pi$ the evolution becomes aperiodic. Due to the similarity of the laser master equation with the NLSE, it can be expected that soliton-soliton interaction also plays a role in the formation of closely spaced multiple pulses of this laser. Further, if two pulses are separated by less than $\approx 5 \cdot T_a$ the second one will reach the absorber when it is still partly bleached, therefore incurring less absorber loss than the first pulse, and possibly have larger amplitude. In fact, the total absorber loss α_{tot} seen by the two pulses per round trip depends on both the separation and the relative phase between the pulses. Similarly for the filter loss, since the spectral energy of a $\phi = \pi$ pulse pair is relocated somewhat into the wings of the spectrum where the filter loss is higher. Clearly, there are limits to both separation and phase difference of double pulses. For instance, since the laser operates in the multiple pulse regime, two pulses which attract each other due to a zero phase difference between them cannot merge completely to form a stable single soliton since the merged state is inherently unstable! Simulations show however, that two pulses can merge and separate periodically where the period is usually much longer than the soliton period of the given energy, dispersion and self phase modulation. Here the gain dynamics plays a decisive role, reacting to the strong increase of filter loss during the merging of the pulses, when one of them compresses whilst the other nearly disperses.

It would seem more likely that stable pulse pairs exist with small separation if the relative phase were rotating such that attractive and repulsive forces would compensate in the mean. Additionally, the dependence of the filter and absorber losses on the separation and phase of the pulses will also play a role. As a simple example, *Fig. 3.3.2 - 2* shows the total loss for two solitons of equal energies, E_p, as a function of their separation and for different phases, ϕ, and absorber saturation energies, E_a. *Fig. 3.3.2 - 2* has been calculated neglecting the nonlinear pulse superposition that occurs for closely spaced pulses, and hence is only strictly valid at separations for which the phase influence becomes negligible (at a separation of $\approx$ 1ps for the given parameters). However, it is apparent that the total loss for the two pulses increases with separation before it flattens off to the value seen by well-separated pulses. This weak potential gradient tends to favour relatively closely spaced pulses, although the gradient is sufficiently weak and similar for different pulse phases that there is little selection between the various possible pulse conditions. One could deduce that a range of final states could exist for identical initial conditions as observed experimentally. Obviously if the absorber is strongly saturated, the total loss becomes dominated by the filter and little absorber dynamics is to be expected.

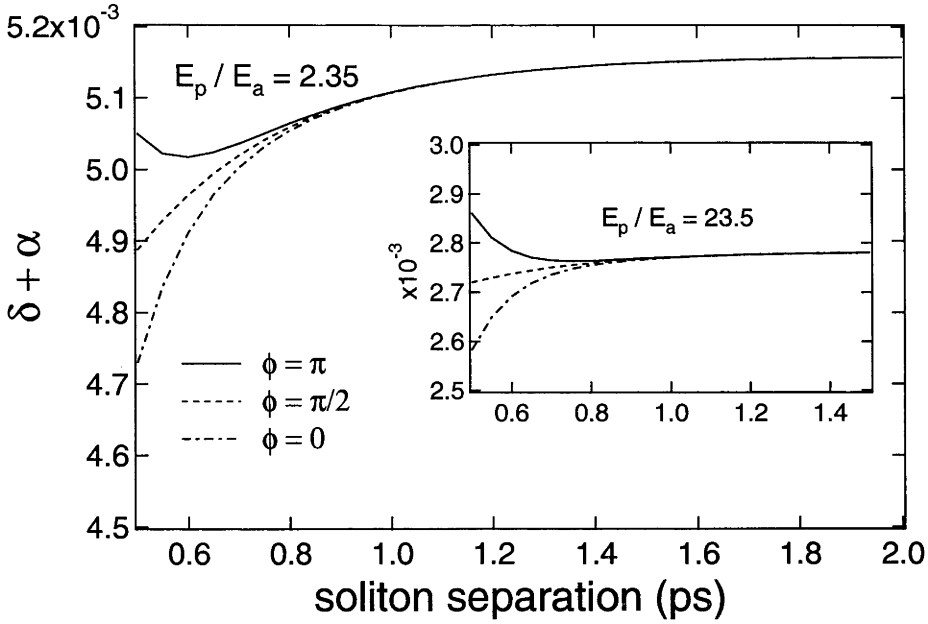

Fig. 3.3.2 - 2: Total soliton loss vs. separation of two solitons of equal energy for $\frac{E_p}{E_a} = 2.35$ and $\frac{E_p}{E_a} = 23.5$ (inset). β_2 = -900 fs^2, T_a = 0.3ps, E_a = 10nJ, q_0 = 0.006, t_0 = 77 fs, see also *Table 3.3.2 - 1.*

Using parameters realistically close to the ones pertaining to the laser, the possibility of closely spaced double pulses in the GCGLE master equation was investigated through simulations. Firstly, *Figs. 3.3.2 - 3a-d* show the intensity autocorrelation *(Fig. - 3a)*, time-integrated spectrum *(Fig. - 3b)* and evolutions in the time domain *(Fig. - 3c)* as well as in the interaction plane *(Fig. - 3d)* for a pair of pulses with rotating relative phase. The interaction plane is essentially a polar plot of the pulse-to-pulse separation ρ and the relative phase Φ [72]. The evolution is stable and the pulse-to-pulse separation ρ assumes a constant value while the phase is increasing linearly in multiples of 2π. Both autocorrelation and spectrum are in very good agreement with the ones obtained experimentally (see *Fig. 3.3.1 - 2b),*) with the laser operating in either stability band. Note that the power of the first pulse is smaller than that of the second one, as expected from the above argument.

Similarly, *Figs. 3.3.2 - 4a-d* and *Figs. 3.3.2 - 5a-d* show simulations of double pulses where the time-integrated spectra resemble those of $\Phi \approx \pi$ and $\Phi \approx 0$ phase difference. Most notably, these were achieved with a strongly saturated absorber which correlates with the fact that features in the experimental spectra of closely spaced pulses were only observed when operating with the smaller SESAM spot size, hence under strong saturation. Further, as can be seen from the interaction plane, Φ and ρ are not constant but can evolve periodically in complex loops with mean values of Φ either closer to π or to 0. Although the case of closely spaced triple pulses is not treated in the current simulations, it is a straight forward extension requiring larger small signal gain g_0 and/or smaller dispersion $|\beta_2|$ as well as strong absorber saturation.

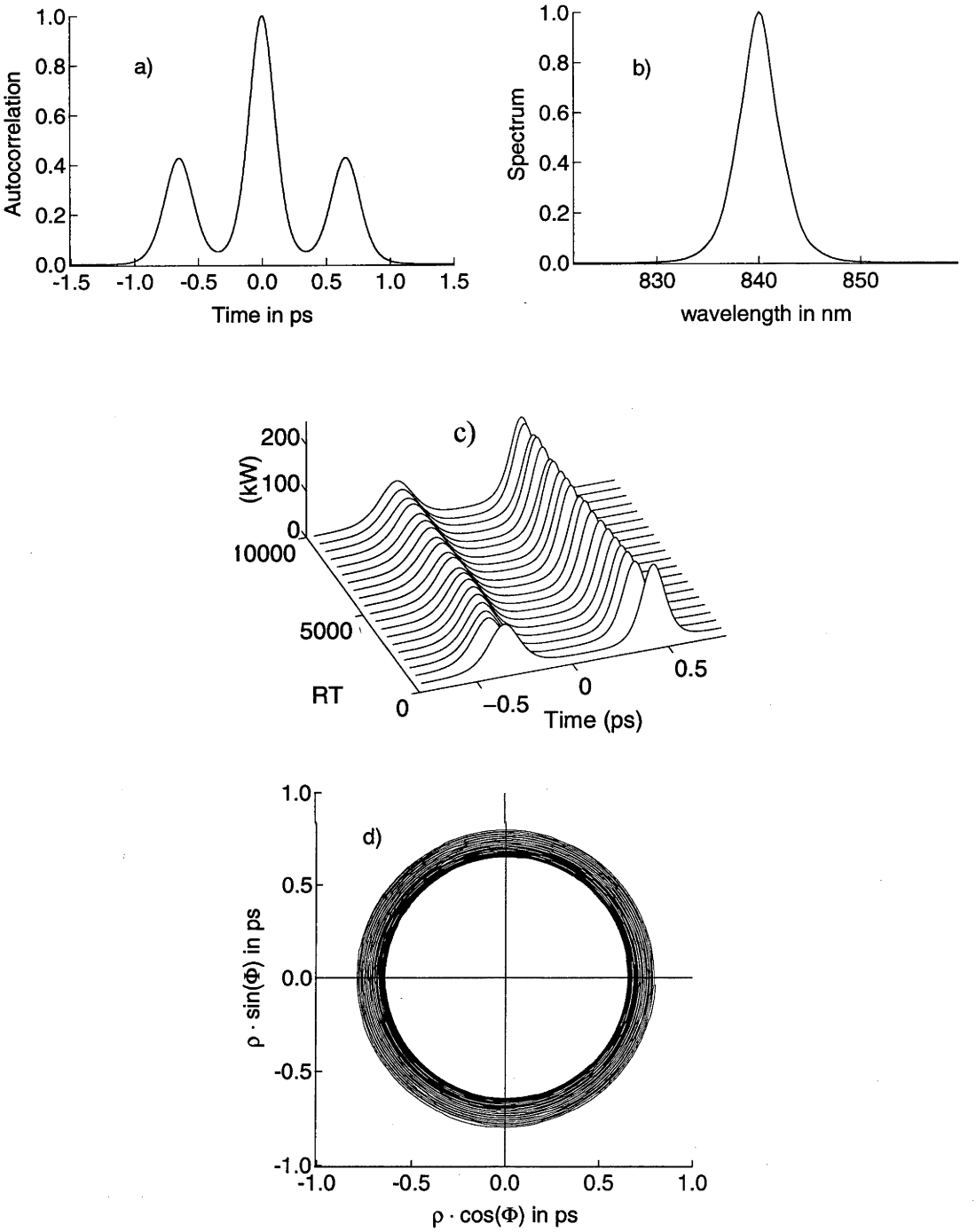

Figs. 3.3.2 - 3a-d: Simulation results after 10000 round trips: (a) intensity autocorrelation, (b) time-integrated spectrum, (c) evolution in time domain, and (d) interaction plane of two closely spaced pulses with rotating phase difference. β_2 = -1100 fs^2, T_a = 0.3ps, E_a = 10nJ, q_0 = 0.006, g_0 = 0.2441, P_g = 2W, see also *Table 3.3.2 - 1.*

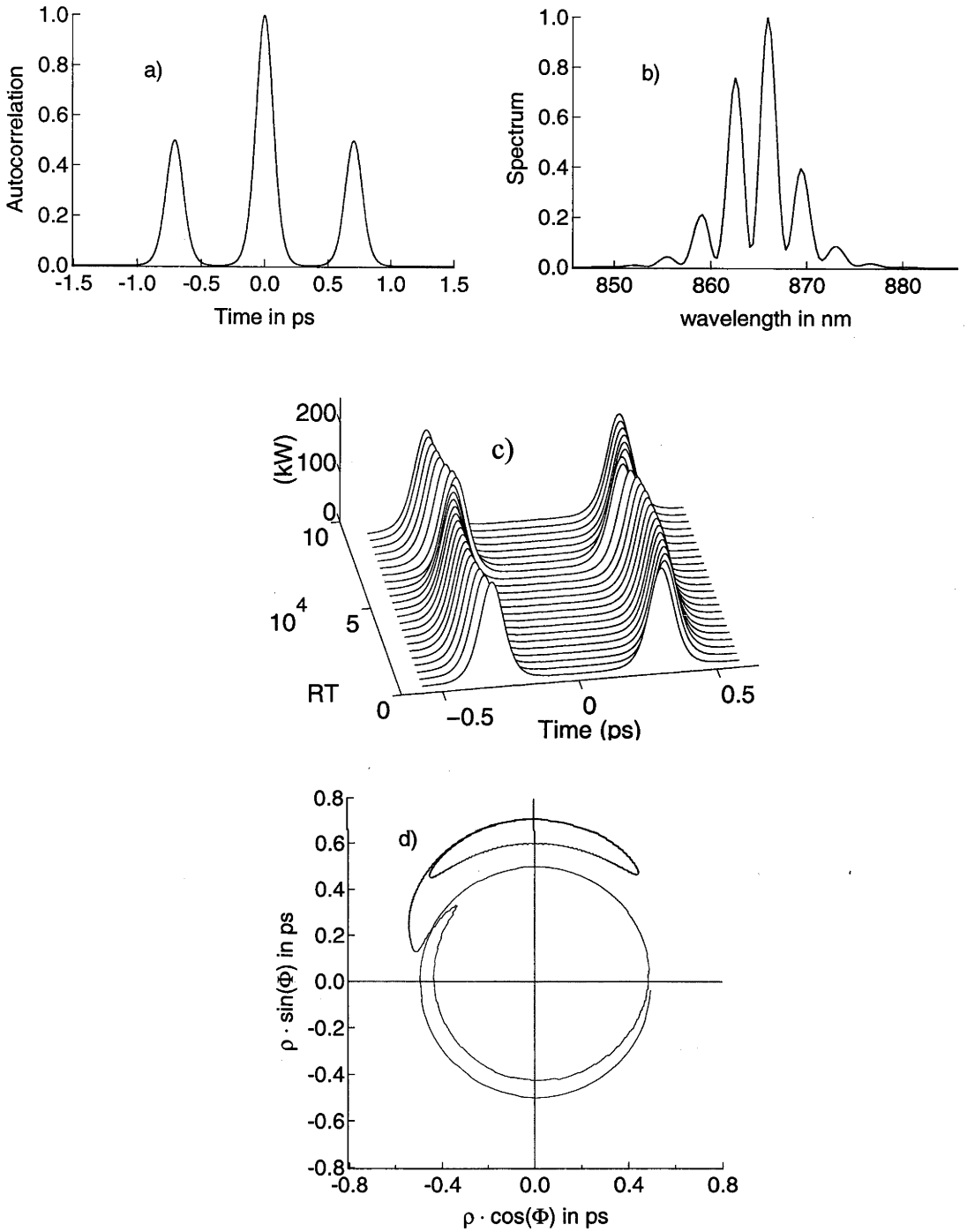

Fig. 3.3.2 - 4a-d: Simulation results after 94000 round trips: (a) intensity autocorrelation, (b) time-integrated spectrum, (c) evolution in time domain, and (d) interaction plane of two closely spaced pulses with mean phase difference between $\pi/2$ and π. $\beta_2 = -688\ fs^2$, $T_a = 0.1ps$, $E_a = 3nJ$, $q_0 = 0.01$, $g_0 = 0.25$, $P_g = 2W$, see also *Table 3.3.2 - 1.*

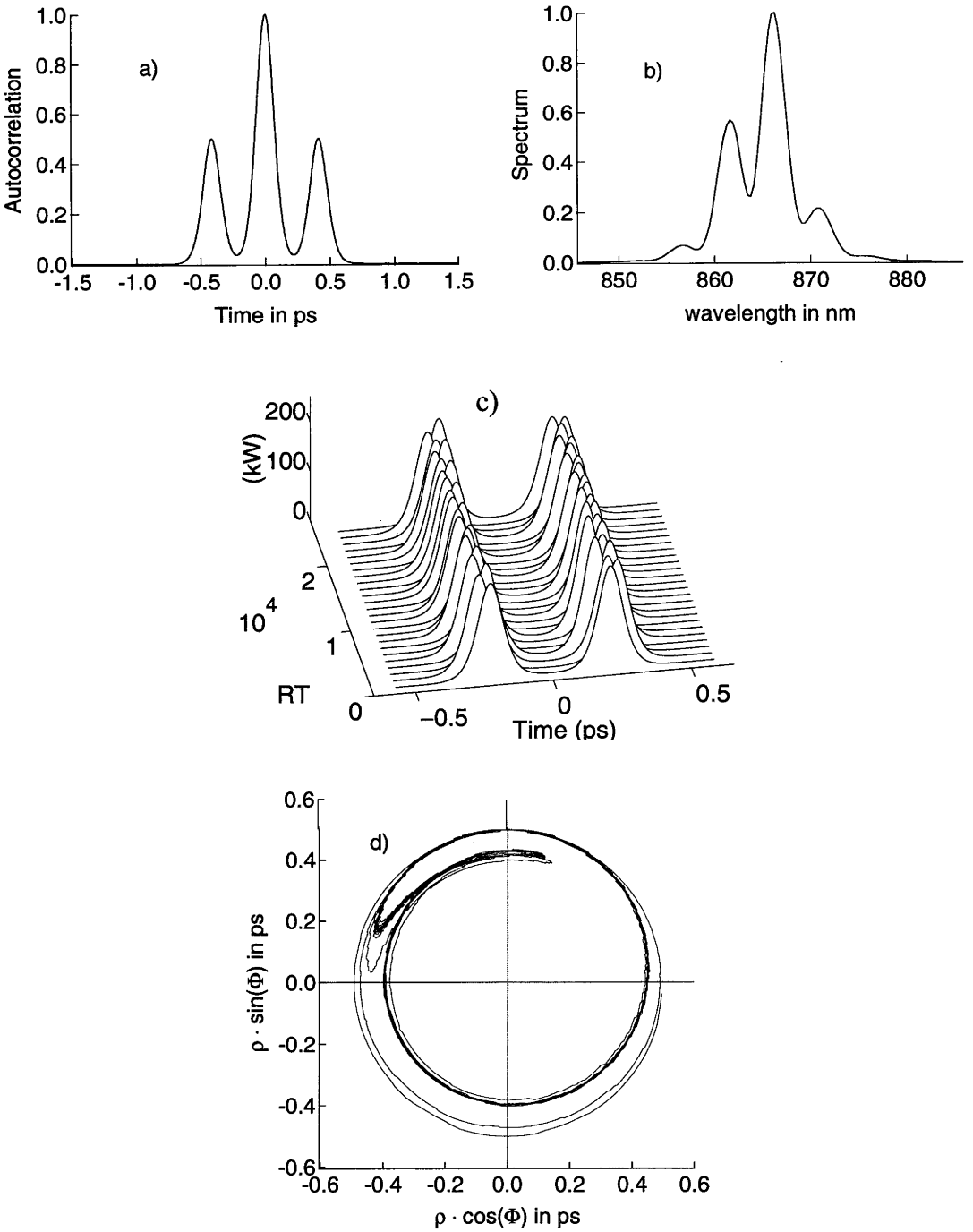

Fig. 3.3.2 - 5a-d: Simulation results after 25000 round trips: (a) intensity autocorrelation, (b) time-integrated spectrum, (c) evolution in time domain, and (d) interaction plane of two closely spaced pulses with mean phase difference between 0 and $\pi/2$. β_2 = -688 fs^2, T_a = 0.2ps, E_a = 3nJ, q_0 = 0.01, g_0 = 0.249, P_g = 2W, see also *Table 3.3.2 - 1.*

Finally, despite the good agreement of the simulations in *Figs. 3.3.2 - 4a-d* and *Figs. 3.3.2 - 5a-d* with the experiment, there are possible shortfalls as well. For instance, the SESAM differential reflectivity is only approximately described by the simple two-

level rate-equation. Generally the response is at least bi-temporal with a fast (≈60fs) transient due to carrier thermalisation and a slower one associated with carrier cooling, capturing and recombination. Both may also depend on the excitation level due to many-body and trap filling effects. Strictly, one should also consider the nonlinear dispersive effects in the saturable absorber. Most importantly, for r-parameters little smaller than one and strong absorber saturation, the discreteness of the laser may influence closely spaced pulses differently compared to far separated ones. For these cases a more refined model should be developed, taking into account the intra-cavity dynamics within one round trip.

3.3.2.3. Regions of Existence of Single and Multiple Pulses

In order to investigate the regions of existence of single, double and triple pulses for different values of the small signal gain g_0 and the dispersion β_2, further simulations were performed. The laser parameters (see caption of *Fig. 3.3.2 - 6* and *Table 3.3.2 - 1*) were those pertaining to operation with the larger SESAM spot size, i. e. E_{sat} = 10nJ. In a first simulation only far separated solitons were allowed, neglecting the possibility of closely spaced pulses. This simplifies the numerics considerably, since instead of the complete GCGLE, one can use eqns. *(3.3.2 - 4, 5, 6)* with the number of soliton energies adjusted appropriately. Setting arbitrary initial conditions the system was allowed to relax to the final state where the number of solitons, the saturated gain g and the losses α and δ were noted. *Fig. 3.3.2 - 6* shows the (g_0, β_2)-plane where the single and multiple pulse regions are indicated in different shades of grey. Within the white bands between neighbouring regions, the final state could fall either to the left or to the right depending on the initial condition, indicating bistability. In order to underline further the sequence leading to the appearance of multiple pulses, the values of $g - l_0 - q_0$, α and δ are depicted (see insets) for constant small signal gain $g_0 = 0.16$ and variable dispersion (indicated by the horizontal line), as well as for constant dispersion $\beta_2 = -600\ fs^2$ and variable small signal gain (indicated by the vertical line). Here, the simulations were further simplified by solving the energy balance in steady state (eqn. *(3.3.2 - 2)*), applying $\alpha + \delta \geq q_0$ as switching condition. Although this treatment neglects the finite recovery time of the absorber, it emphasises the principle that with varying dispersion or small signal gain, the laser will try to balance out the changes in the filter and absorber losses by adjusting the saturated gain such that the energy balance eqn. *(3.3.2 - 2)* is fulfilled for a first order soliton. However, once the dynamic losses become equal to the maximum possible modulation q_0 (i. e. $g - l_0 - q_0 \approx 0$), energy is transferred to another first order soliton. The increased number of solitons renders the laser stable, since the total dynamic losses have dropped, until, upon a decrease in $|\beta_2|$ or increase in g_0, they become equal to $q_0 - \varepsilon$ again (and so forth). For fixed g_0 and variable $|\beta_2|$, the width of the bands is variable. This is mainly due to the dependence of the absorber loss on the energy of the single solitons, which is inversely proportional to the number of solitons. Clearly, the bands would become arbitrarily narrow for $|\beta_2| \rightarrow 0$. On the other hand, for fixed $|\beta_2|$ and variable g_0, the width of the bands is constant, since the necessary energy for an

increase in the number of solitons is supplied through an increase in g_0. The energy of the single solitons, and therefore the losses, remain approximately constant. However, the increasingly saturated gain for a large number of solitons provides a decreased stability margin. The inserts nicely illustrate the periodic nature of the transitions between pulse states, underlining the fact, deduced from our experimental observations, that the same physical process is responsible for each transition.

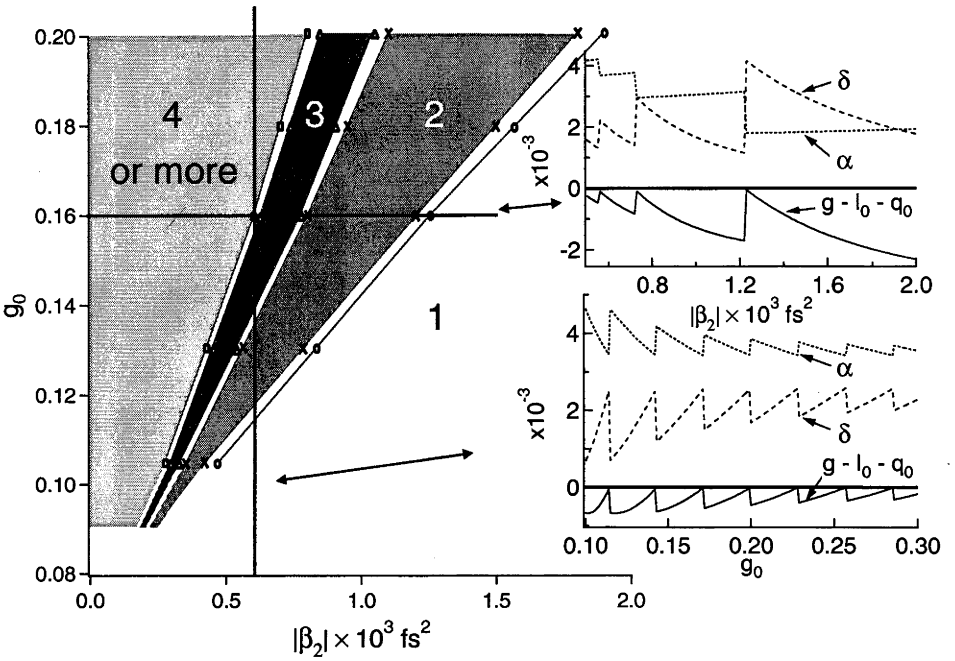

Fig. 3.3.2 - 6: $(g_0, |\beta_2|)$-plane showing regions of existence for single and multiple pulses according to simulations in the framework of soliton perturbation theory (eqns. *(3.3.2 - 4, 5, 6)*). The insets show $g - l_0 - q_0$, δ and α for constant $g_0 = 0.16$ and $|\beta_2| = 600\text{fs}^2$ respectively, as calculated from the steady state energy balance (eqn. *(3.3.2 - 2)*) using $\alpha + \delta > q_0$ as switching condition. $T_a = 0.3$ps, $E_a = 10$nJ, $q_0 = 0.006$, $P_g = 4$W, see also *Table 3.3.2 - 1.*

A simulation of the (g_0, β_2)-plane using the full GCGLE model, also allowing closely spaced pulses [74], produces virtually identical regions to the ones found here, justifying the simple approach via soliton perturbation theory (eqns. *(3.3.2 - 4, 5, 6)*). The only major difference between the two approaches is that the GCGLE model allows for interaction between pulses via the phase and distance dependent absorber and filter losses and the soliton-soliton interaction. As was shown in the last section these effects can lead to the appearance of quasi-stable closely spaced double and triple pulses. If the multiple pulse regions are narrow, or for $|\beta_2|$ values corresponding to a transition region, $g - l_0 - q_0$ is close to $-\varepsilon$. Then the interaction between closely spaced pulses doesn't allow even quasi-stable states and the laser is in permanent non-equilibrium. An example of the resulting complex behaviour is shown in *Fig. 3.3.2 - 7a*, where the energy balance condition $g - l_0 - \alpha - \delta = 0$ is seen to be permanently violated, leading to unsteady and nonperiodic pulse evolution, as seen from the insets showing $|\psi|^2$ after various numbers of round trips.

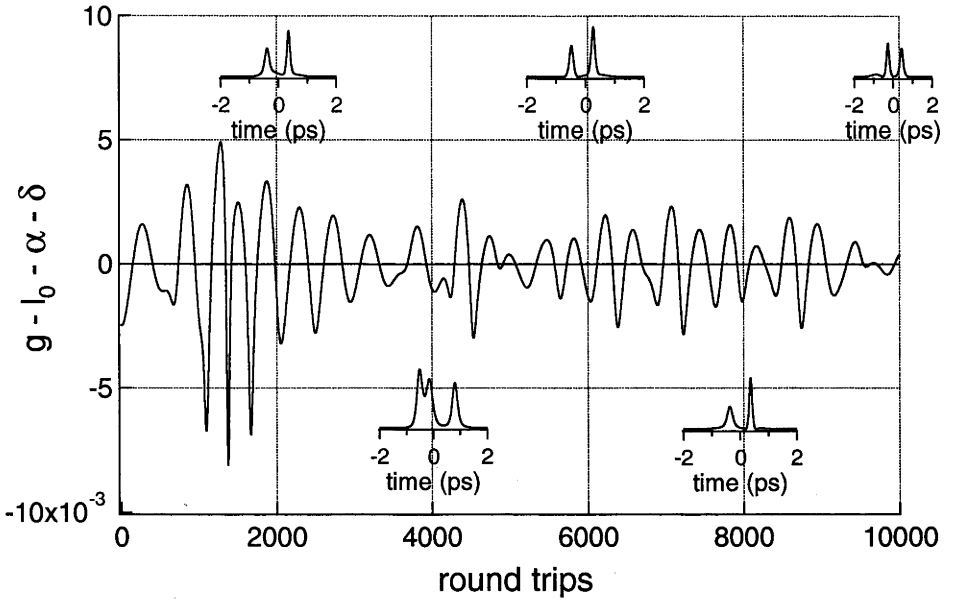

Fig. 3.3.2 - 7a: Simulation of the laser in non-equilibrium. The energy balance condition $g - l_0 - \alpha - \delta = 0$ is permanently violated. Also shown are the intra-cavity $|\psi|^2$ after various numbers of round trips. $\beta_2 = -200fs^2$, $g_0 = 0.1022$, $T_a = 0.3ps$, $E_a = 10nJ$, $q_0 = 0.006$, $P_g = 4W$, see also *Table 3.3.2 - 1.*

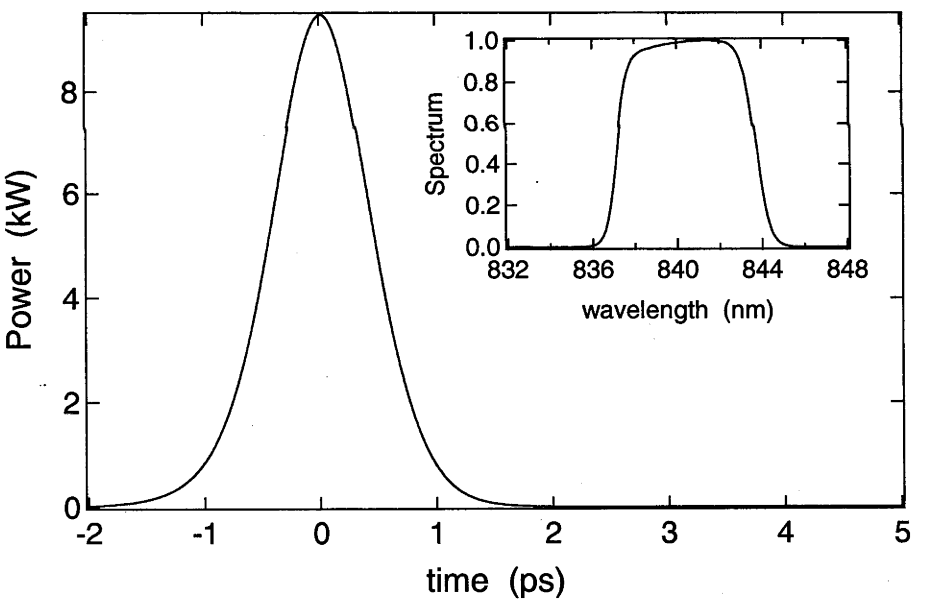

Fig. 3.3.2 - 7b: Simulation of the laser for positive dispersion. Shown are the intra-cavity $|\psi|^2$ and the spectrum after 10000 round trips. $\beta_2 = +200fs^2$, $g_0 = 0.1022$, $T_a = 0.3ps$, $E_a = 10nJ$, $q_0 = 0.006$, $P_g = 4W$, see also *Table 3.3.2 - 1.*

Experimentally this was observed in the form of unsteady autocorrelation traces (see *Fig. 3.3.1 - 3d*). It is suppressed in the case of the rotating phase doublet, and, to some degree, by operating the absorber in strong saturation since then the dynamic losses are mainly determined by the filter alone, allowing closely spaced

double and triple pulses to appear. Crossing over to positive dispersion makes the laser stable again. However, it now produces ps pulses as is evident from *Fig. 3.3.2 - 7b* as well as *Fig. 3.3.1 - 3e* (experiment). Since the laser is not operating in the soliton regime the chirp due to SPM remains uncompensated and the pulses are therefore strongly chirped.

Parameter	Value	Description
l_0	0.08	total linear loss per round trip
T_R	12.5ns	round trip time
Ω	$2\pi \cdot 25$THz	filter HWHM
β_2	variable	net intra-cavity dispersion
κ	$1 \cdot 10^{-6}$ 1/W	SPM coeff.
q_0	ΔR_{max} / 2, variable	max. ampl. modulation of SESAM
E_a	variable	sat. energy of SESAM
T_a	variable	SESAM recovery time const.
T_g	2.5μs	upper state life time of Ti:Sapphire
P_g	variable	sat. power of Ti:Sapphire
g_0	variable	small signal round trip gain

Table 3.3.2 - 1: Relevant modelling parameters.

3.4. Summary

Sections *3.1* - *3.3* have covered the mode-locking performance of the ion-implanted GaAs-SESAMs. A commercial Ti:Sapphire laser (Coherent Mira 900D) was redesigned for incorporation of the SESAMs and the crucial cavity parameters were introduced in section *3.1*.

Section *3.2* dealt with the single pulse operation of the laser. It was found that all SESAMs, except for those with the highest implantation doses, mode-locked the laser, including the unimplanted sample. In the latter case, mode-locking was stabilised by the fast response times under strong saturation (≈1ps). It was concluded that for the type of SESAM design presented here an implant of 40keV As-ions with a dose of around $5 \cdot 10^{11}$ cm^{-2} followed by thermal annealing at 600°C for 20 min presents a compromise showing swift recovery at any fluence whilst preserving about 90% of the modulation of the unimplanted SESAM. Single pulses as short as 105fs were produced in self-starting fashion with a tuning range of ≈50nm and mode-locking

build-up times ranging from 30μs to 3ms. A major difference between the samples' performance was found in their ability to suppress the Q-switching instability, which was attributed to the different modulation depths caused by the ion-implantation rather than to a carrier life time controlled saturation fluence. The observed increase of the laser's stability against Q-switched mode-locking was shown to be a result of the soliton mode-locking operation and the associated dependence of the filter loss δ on energy. The variation of the pulsewidth for varying GDD and energy were found to be in agreement with the soliton model of mode-locking, and computer simulations of the GCGLE showed good agreement with the experimental observations.

In section *3.3* the multi-pulse operation of the laser was investigated in detail. It was observed that transitions between single and multiple pulse states could be induced by steadily reducing the value of the intra-cavity dispersion (or by increasing the small signal gain). The multiple pulses could be either well separated (ps ... ns) without reliably reproducible spacings, or closely spaced (< ps) and have their relative phase rotating, or near 0 or π. The experimental observations were explained in the framework of the Generalised Complex Ginzburg-Landau Equation (GCGLE).

Being representative of all transitions between pulse states, the single to double pulse transition was analysed in detail. It was found that for a single soliton to break up into two solitons, the condition for shedding and growth of dispersive continuum must be fulfilled $[\alpha_1 + \delta_1 + \varepsilon]_{Q1} \geq q_0$, i. e. when the absorber and filter losses experienced by the soliton exceed the maximum possible modulation q_0 corrected by a margin ε mainly determined by the recovery time of the absorber (ε=0 for an instantaneous recovery). On the other hand, two well separated solitons in the laser become unstable and coalesce to form a single soliton when a change in filter loss, introduced by a slight energy imbalance, is outweighed by the simultaneous change in absorber loss $\Delta\delta < -\Delta\alpha$. The latter stability criterion in conjunction with the difference in total energy before and after the switching between states, $Q_1 \neq Q_2$, was interpreted as the origin of the observed switching hysteresis. Using computer simulations, quasi-stable closely spaced pulse solutions of the GCGLE were shown which originate from a balance involving soliton-soliton interactions, the pulse separation, phase and saturation dependent absorber loss, and the filter loss. The simulations were in good agreement with the experimental observations indicating the existence of rotating phase, $\phi \approx \pi$ and as $\phi \approx 0$ doublets. Finally, the regions of existence of single and multiple pulses in the (g_0, β_2)-plane were mapped through simulations. For fixed small signal gain g_0 the regions were shown to become narrower for decreasing dispersion $|\beta_2|$ resulting in permanent non-equilibrium as observed in the experiment.

CHAPTER 4

FUNDAMENTAL STUDIES OF NONLINEAR ABSORPTION PROPERTIES OF ION-IMPLANTED GAAS

Motivated by the results on SESAMs reported in chapter 2, a more extensive study of the nonlinear optical absorption properties of ion-implanted GaAs was clearly warranted. Unlike the SESAMs, the test structures of the study presented here were free of Fabry-Perot resonances and contained a much thicker absorber layer in order to allow more generally valid conclusions. Further background is given in section *4.1* followed by the introduction of the set of samples and the measurement methods in section *4.2*, and the experimental results in section *4.3*.

4.1. Aim of this Investigation

Apart from passive mode-locking, semiconductor saturable absorbers have also found applications in all-optical switching for ultrahigh bit-rate optical communication systems [77]. In both cases it is beneficial to have devices with fast response times ($\tau_A \leq 1\text{ps}$) while retaining as much modulation as possible. Additionally, in the case of all-optical switching, the nonlinearity should be high, i. e. the pulse energy fluence needed for switching should be low. As was outlined before, there are two main approaches to the generation of a short τ_A in III-V semiconductor materials. One involves the growth at low temperature (LT) using Molecular Beam Epitaxy (MBE) [78]; the other is via ion-implantation [28, 79] of high temperature grown material.

It is well known that LT-grown materials may contain excess Arsenic to very high concentrations (up to 2%), forming deep-level defects known as As-antisites (As_{Ga}), As-interstitials (As_i), Ga-vacancies (V_{Ga}), and complexes of these defects [80]. Electron parametric resonance (EPR) measurements showed that, in the as-grown state of LT-GaAs, up to $5 \cdot 10^{18}$ cm^{-3} ionised As-antisites ($As_{Ga}+$) are present which are compensated by the same density of Ga vacancies (V_{Ga}) acting as acceptors [81]. The ultrafast response times observed in LT-GaAs have been attributed to the donors $As_{Ga}+$ which act as deep level electron traps. However, it was also argued that the acceptors V_{Ga} are responsible for hole capturing [43]. The ratio of ionised to non-ionised antisites, $As_{Ga}+$ / As_{Ga}, in LT-GaAs is usually small (around 0.1), and the comparatively high concentration of As_{Ga} is thought to be the cause of the high nonbleachable absorption losses in LT-GaAs, detrimental to nonlinear modulator applications. As a promising remedy for these problems, thermal annealing as well as Beryllium doping of LT-GaAs were considered recently [82]. The Beryllium, being a shallow acceptor, is thought to raise the $As_{Ga}+$ / As_{Ga} ratio, thereby enhancing electron capturing whilst reducing the nonbleachable absorption losses. Beryllium doping was also used in a low-temperature grown InGaAs/InAlAs multiple quantum well (MQW)

based all-optical switch at the communication wavelength of 1.55μm to shorten the response time of the device [77].

On the other hand, ion bombarded materials for saturable absorber applications have not received as much attention as the LT-grown. Studies of the ultrafast properties of implanted GaAs have so far been restricted to the measurement of the response times using various techniques, such as time-resolved ultrafast photoluminescence [28], differential surface reflectivity [119] and photo-current autocorrelation [83]. However, in saturable absorber applications, both the response time as well as the modulation depth and nonlinearity can play equally important roles.

Therefore, for this study it was the goal to measure the response times as well as the modulation of ion-implanted GaAs. Furthermore, a large enough database should be established in order to be useful in a later comparison with as-grown, annealed and Be-doped LT-GaAs. The data should be as versatile as possible, allowing the identification of generally valid trends such as dependencies on dose and annealing conditions, and, if possible, it should be free of design and geometry factors. Finally, the data should be useful also in conjunction with the results of magnetic circular dichroism of absorption (MCDA) and near infrared absorption (NIRA) measurements [81]. MCDA, NIRA and positron annihilation measurements, which are being performed at the time of writing, are aimed at determining the concentration of As-antisites in the neutral (As_{Ga}^{0}) and singly ionised charge-state (As_{Ga}^{+}) as well as Ga-vacancies (V_{Ga}) respectively. Although it has been shown that As_{Ga}^{+} are present in ion-implanted GaAs [27], it will be important to correlate their concentration, if detectable, with the ultrafast response in order to gain further insight into the mechanisms of trapping and recombination in ion-implanted GaAs. Since the extent of this project is considerable it cannot be contained fully in this thesis and will be ongoing, involving groups at the ANU, ETH Zürich and UC Berkeley.

4.2. Sample Set and Experimental Techniques

The test structures were grown using low pressure Metal Organic Chemical Vapour Deposition (MOCVD) and consisted of a Bragg-reflector (25 periods of $Al_{0.15}Ga_{0.85}As$/AlAs on semi-insulating GaAs) followed by 500nm of GaAs. The Bragg mirror was centred at λ=830nm and had a typical reflectivity of greater than 99% over a range of 70nm. After growth the samples were implanted with 700keV As-ions or 250keV O-ions, in doses ranging from $8 \cdot 10^{10}$ to $1 \cdot 10^{16}$ cm^{-2} and annealed at 500, 600 or 700°C for 20 min under arsine ambient, or remained unannealed (see also *Table 4.2 - 1*). The ion energies for the implants were chosen, using TRIM95 [31], so that the damage distribution lay solely inside the 500nm GaAs layer with no damage extending into the Bragg mirror. *Fig. 4.2 - 1* shows the calculated total vacancy distribution, due to primary and secondary 'knock-ons', inside the GaAs absorber layer for both ions. The vacancy density of the O-implant is approximately 8-fold smaller and somewhat more symmetric than that of the As-implant. Therefore, one would expect that an O-implant,

in order to cause the same volumetric damage density, should be done at around eight times the dose of an As-implant. Note also, that the difference in size and weight between O (16 amu) and As (75 amu) results in the lower ion-energy needed for O (250keV) compared with As (700keV).

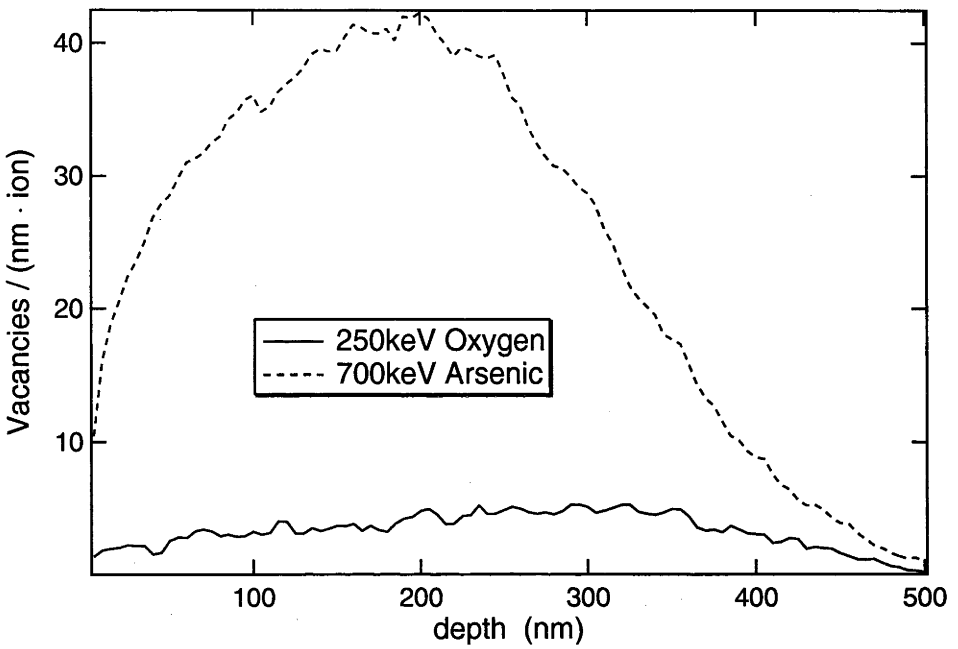

Fig. 4.2 - 1: Total vacancy distribution inside the GaAs absorber layer due to primary as well as secondary 'knock-ons' obtained from a TRIM95 simulation.

ion	dose [cm^{-2}]	annealing condition
As	$8{\cdot}10^{10} \rightarrow 5{\cdot}10^{11}$	unannealed
	$1{\cdot}10^{11} \rightarrow 1{\cdot}10^{13}$	500°C/20min
	$8{\cdot}10^{10} \rightarrow 1{\cdot}10^{16}$	600°C/20min
	$8{\cdot}10^{10} \rightarrow 1{\cdot}10^{16}$	700°C/20min
O	$8{\cdot}10^{11}$, $8{\cdot}10^{12}$	unannealed
	$8{\cdot}10^{11} \rightarrow 8{\cdot}10^{13}$	500°C/20min
	$8{\cdot}10^{11} \rightarrow 8{\cdot}10^{15}$	600°C/20min
	$8{\cdot}10^{11} \rightarrow 8{\cdot}10^{15}$	700°C/20min

Table 4.2 - 1: Implantation doses and annealing conditions for the complete set of samples. The annealing was done under arsine ambient in the MOCVD reactor.

After the implantation and annealing procedures, an 830nm anti-reflection (AR-) coating was applied to the samples in order to minimise Fabry-Perot effects since all optical measurements were done in reflection. The reflectivity spectra of the AR-coated unimplanted sample, S11, as well as the Arsenic implanted samples S27 ($1 \cdot 10^{12}$ cm^{-2}, unannealed) and S37 ($1 \cdot 10^{14}$ cm^{-2}, 700°C/20min annealed), are shown in *Fig. 4.2 - 2*. For an ideal AR-coating, the reflectivity of the samples is an image of the transmission over twice the absorber thickness, because of the presence of the Bragg mirror. However, as can be shown through modelling similar to that in section *2.1*, a slightly non-ideal AR-coating ($R_{res} \approx 0.005$) can cause the appearance of a residual Fabry-Perot resonance. The latter is apparent in the traces of samples S11 and S27, whereas S37 displays a more or less ideal behaviour. For the complete set of samples, the uncertainty due to the non-ideal AR-coating in the linear (low power) reflectivity R_{lin} at λ = 830nm was approximately ±0.05. Additionally, for the $1 \cdot 10^{12}$ cm^{-2} Arsenic implanted, unannealed sample (S27), one clearly observes an increased absorption, similarly observed in the unannealed SESAMs (section *2.1*) for doses $\geq 1 \cdot 10^{12}$ cm^{-2}.

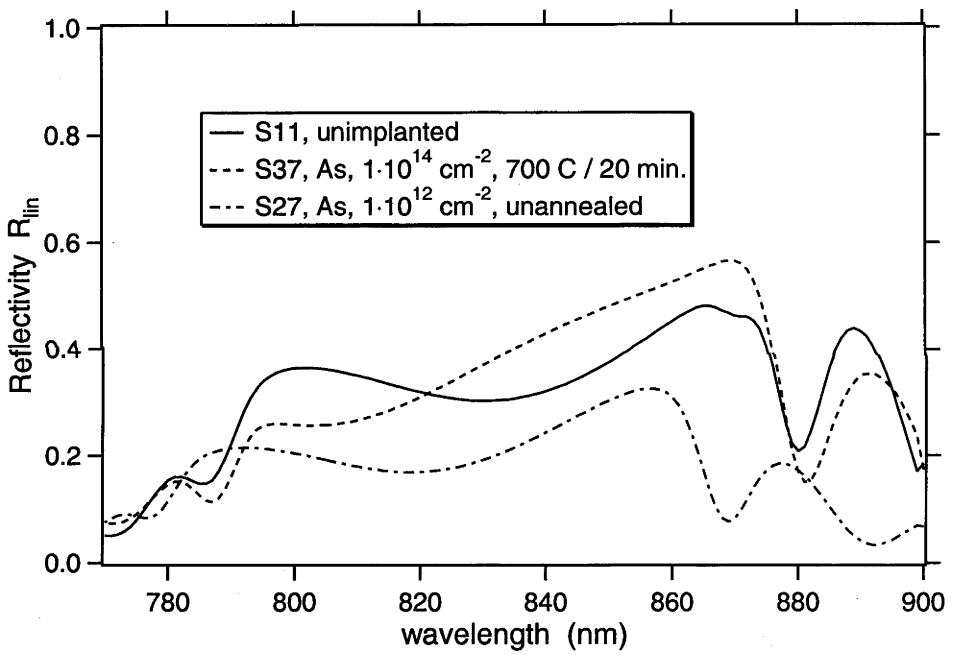

Fig. 4.2 - 2: Low power reflectivity spectrum (R_{lin}) of samples S11, S27, S37. Note the increased absorption of the unannealed, $1 \cdot 10^{12}$ cm^{-2} Arsenic implanted sample (S27) and the residual Fabry-Perot resonance present in S11 and S27 due to slightly non-ideal AR-coatings.

The samples were subject to two types of ultrafast optical measurements using 830nm, 80MHz, 100fs pulse trains from a commercial Kerr Lens Mode-locked (KLM) laser: (a) the fluence dependent reflectivity $R(F_p) = P_{out} / P_{in}$ using single beam excitation; and (b) the time resolved differential reflectivity dR for different pump fluences and delay times as long as 300ps, using a pump-probe setup. These measurements are fairly standard [22], but are nevertheless described here for completeness. In order to reduce the thermal nonlinearity to a negligible level, the

output of the laser was modulated at a frequency of 125kHz and a duty cycle of 1:20 using an acousto-optic modulator (AOM). This resulted in bursts of 400ns length, containing ca. 30 pulses, every 8μs. This minimises both the effects of thermal nonlinearity which has a typical response time of 2μs [84], and the edge effects which appear for too short burst widths due to the limited switching times of the AOM. Lock-in detection was used in both measurements, for which the beam (pump beam in the pump-probe measurement (b)) was further chopped mechanically at a frequency of 3.5kHz. For measurement (a) the single beam was focussed down to a spot diameter of d_{spot} = 15μm whilst P_{in} and P_{out} were measured in collinear fashion. In measurement (b) the pump and probe beams had an angle of 30° between them, the pump and probe spot diameters were 25μm and 8μm respectively, and the probe fluence was between 40 and 400 times weaker than the pump fluence. The (pump) fluence could be varied over three orders of magnitude using continuously variable and fixed neutral density (ND) filters. In order to increase the signal to noise ratio (SNR) in all measurements, an averaging method was employed whereby a particular measurement was repeated at high scanning speed as many times as feasible, after which the average of all traces was taken as the signal. This method allows for considerable suppression of the 1/f noise (laser drift etc.), which is not achievable through an increase in lock-in time constant. Generally, the SNR improves with the number N of scans as $SNR \propto \sqrt{N}$.

Finally, one should notice, that due to the anti-reflection coating, changes in $R(F_p)$ as well as the differential reflectivity signals dR of the structures were dominated by absorption bleaching in the GaAs layer, causing the reflectivity to increase. This can be shown through modelling similar to that in section *2.1*, assuming typical changes of the real part of the complex refractive index of <0.1 [38]. Since the underlying Bragg mirror is nonabsorbing for wavelengths above 750nm it does not contribute to the nonlinear response but merely acts as a 100% reflector. This was confirmed through measurement of a separately grown Bragg mirror.

4.3. Experimental Results

Section *4.3* covers the nonlinear reflectivity data $R(F_p)$ (*4.3.1*), the pump-probe data (*4.3.2*) and the modulation vs. response time performance (*4.3.3*) of the test structures.

4.3.1. Nonlinear Reflectivity $R(F_p)$

Typical traces of reflectivity versus pulse energy fluence (averaged over the beam area) are shown in *Fig. 4.3.1 - 1* for the unimplanted (S10), $1 \cdot 10^{13} cm^{-2}$ As-implanted, 600°C/20min annealed (S33) and the $8 \cdot 10^{13} cm^{-2}$ O-implanted, 500°C/20min annealed (S55) samples. The traces for each sample in *Fig. 4.3.1 - 1* are composed of two scans, each spanning two orders of magnitude in fluence (1 → 100μJ·cm^{-2} and 10 → 1000μJ·cm^{-2}), as is evident from a slightly imperfect overlap.

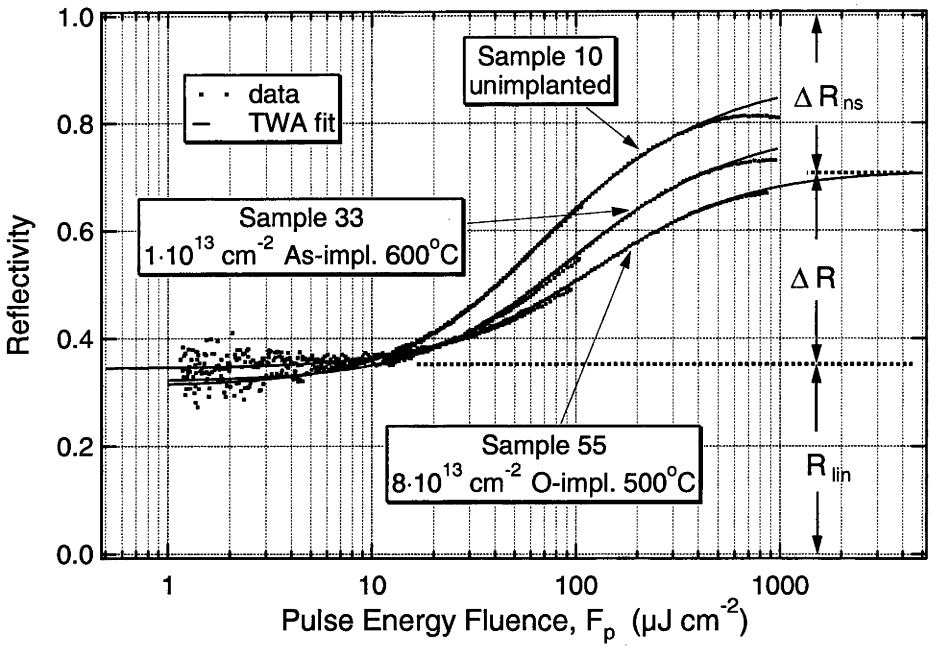

Fig. 4.3.1 - 1: Nonlinear reflectivity versus pulse fluence for samples S10 (unimplanted), S33 ($1{\cdot}10^{13}$ cm^{-2}, As, 600°C/20min) and S55 ($8{\cdot}10^{13}$ cm^{-2}, O, 500°C/20min). Also shown are numerical fits using the TWA model (see below and Appendix III). The fits were performed for fluences between 10 and 400 μJ·cm^{-2}. R_{lin}, ΔR and ΔR_{ns} are defined as indicated.

It is possible to extract values for the low fluence reflectivity R_{lin}, modulation ΔR and nonbleachable reflectivity ΔR_{ns} directly from the data, whilst an effective saturation fluence F_{sat}, hence a nonlinearity parameter, could be defined as $F(\Delta R/2)$. However, this approach does not attempt to relate the measured data to the physics of the saturable absorber sample. Furthermore, in cases where the available pulse fluence is not high enough to reach the maximum modulation this approach fails. It has become customary, therefore, to attempt a fit of the reflectivity data using a model for a travelling wave, two level saturable absorber (TWA) [22]. Since the TWA fitting model will also be used in the context of this work, it will be explained in some detail in Appendix III. The fits, some of which are also displayed in *Fig. 4.3.1 - 1*, are very good for the most interesting fluence range whereas the disagreement found for fluences higher than 500μJ·cm^{-2} is mainly attributed to effects such as free carrier absorption (FCA) and two photon absorption (TPA), which were not included in the model. The latter effects could also be responsible for the incomplete bleaching achieved in unimplanted GaAs. From the TWA fits, the values of R_{lin}, ΔR, ΔR_{ns} and F_{sat} are deduced, neglecting TPA and FCA. The fit allows one to deduce values for ΔR and ΔR_{ns} consistently between samples, although the actual values deduced from the data directly are different.

Fig. 4.3.1 - 1 clearly shows that the modulation of the ion-implanted sample is smaller than in the unimplanted case, and that ΔR_{ns} has increased. Generally, ΔR_{ns} increases and ΔR decreases for higher doses or lower annealing temperatures. For instance, the O-implanted sample (S55) has $\Delta R = 0.39$ and $\Delta R_{ns} = 0.26$ which compares

with the values for the unimplanted sample, where $\Delta R_{GaAs} = 0.59$ and $\Delta R_{ns,\,GaAs} = 0.1$. Like in LT-GaAs [43], these changes are attributable to deep levels, created by the implantation, which give rise to additional transitions to states high in the bands. One should expect that these transitions are difficult to bleach due to the large density of states high in the bands. The deep level transitions also contribute to the linear absorption resulting in a smaller linear reflectivity R_{lin}. However, the data show that any change in R_{lin} was smaller than the uncertainty of ±0.05, arising from slight differences in the anti-reflection coatings of different samples. This explains the slightly higher R_{lin} of the O-implanted sample compared to the unimplanted case. Since $R_{lin} + \Delta R + \Delta R_{ns} = 1$, any increase in ΔR_{ns} primarily corresponds to a reduction of ΔR.

Figs. 4.3.1 - 2a-d show the results of the TWA-fits for all samples. In summary, the following trends can be observed. For both As- and O-implanted samples the modulation ΔR decreases with increasing implantation dose and/or decreasing annealing temperature *(Fig. 4.3.1 - 2a)*. The unannealed samples have rather low modulation, particularly for the As-implant (heavier ion) where the $1 \cdot 10^{12}$ cm^{-2} implanted sample (not displayed) had virtually no modulation. Furthermore, under high fluence excitation, the unannealed samples were unstable and their ΔR increased on a time scale of seconds to minutes, indicating an in-situ annealing process which was more pronounced for higher doses. The low modulation as well as the instability at higher fluence render unannealed samples somewhat less useful for applications. *Fig. 4.3.1 - 2b* shows the saturation fluence F_{sat} for both implants. All F_{sat} values lie between 20 and 90 $\mu J \cdot cm^{-2}$ which constitutes a small variation given the range of implantation doses. However, there is a clear trend to higher values for higher implantation doses and/or lower annealing temperatures. Note, that this trend appears broken for As-implants with doses above $1 \cdot 10^{14}$ cm^{-2}. Finally, *Figs. 4.3.1 - 2c* and *- 2d* depict the nonbleachable losses ΔR_{ns} and the low fluence reflectivity R_{lin} respectively. Most importantly, *Figs. - 2c,d* show that, to within the above mentioned uncertainty due to the AR-coating, R_{lin} remains constant for all doses whilst ΔR_{ns} increases at the expense of ΔR, in accordance with the relationship $R_{lin} + \Delta R + \Delta R_{ns} = 1$. Thermal annealing was therefore very effective in recovering the damage induced changes in R_{lin} of the samples implanted with high doses.

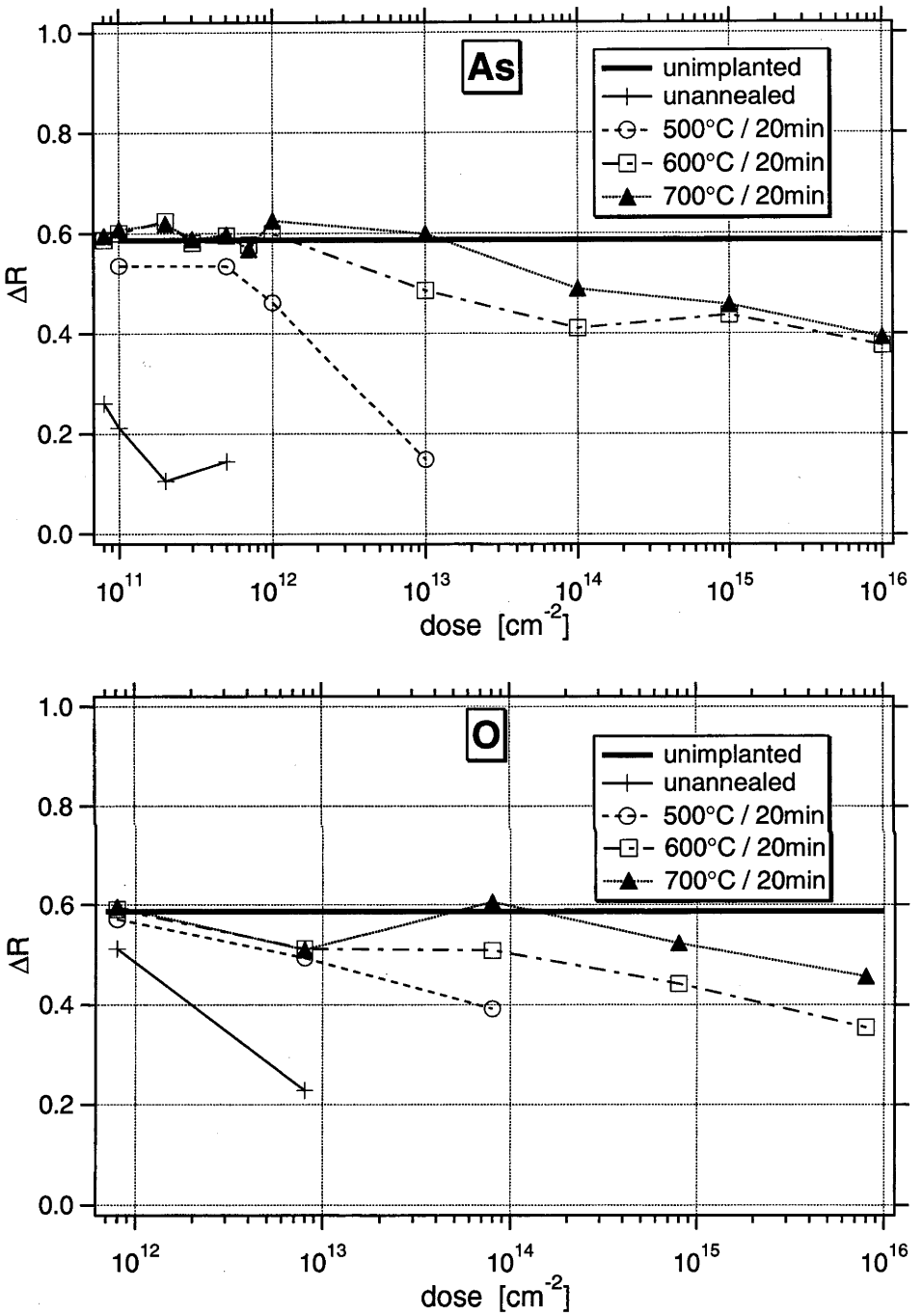

Fig. 4.3.1 - 2a: Modulation ΔR from the TWA-fit versus dose for Arsenic and Oxygen implanted GaAs, annealed at 500 - 700°C / 20min as well as unannealed.

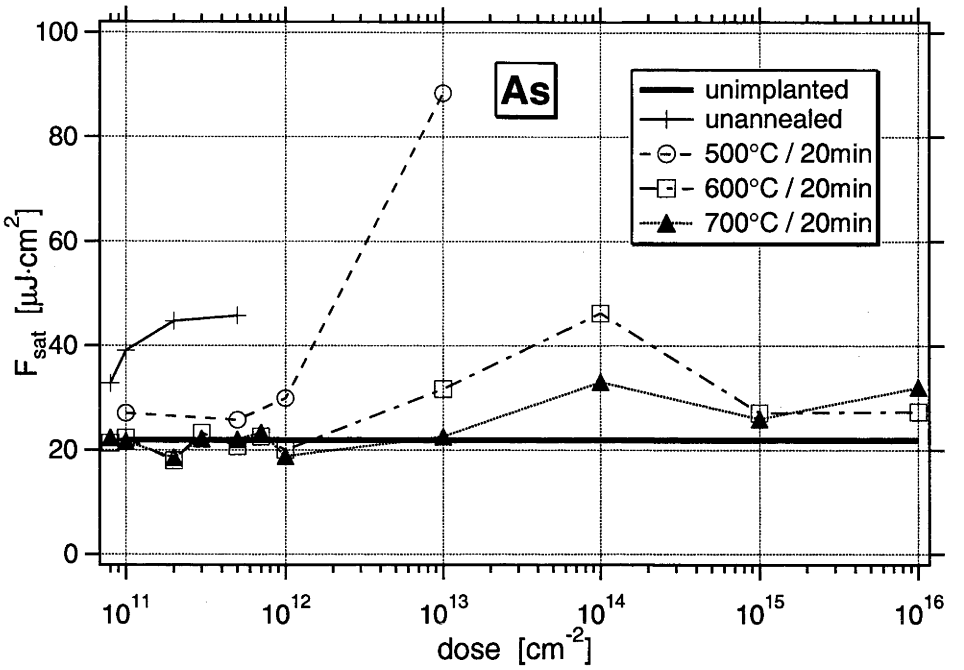

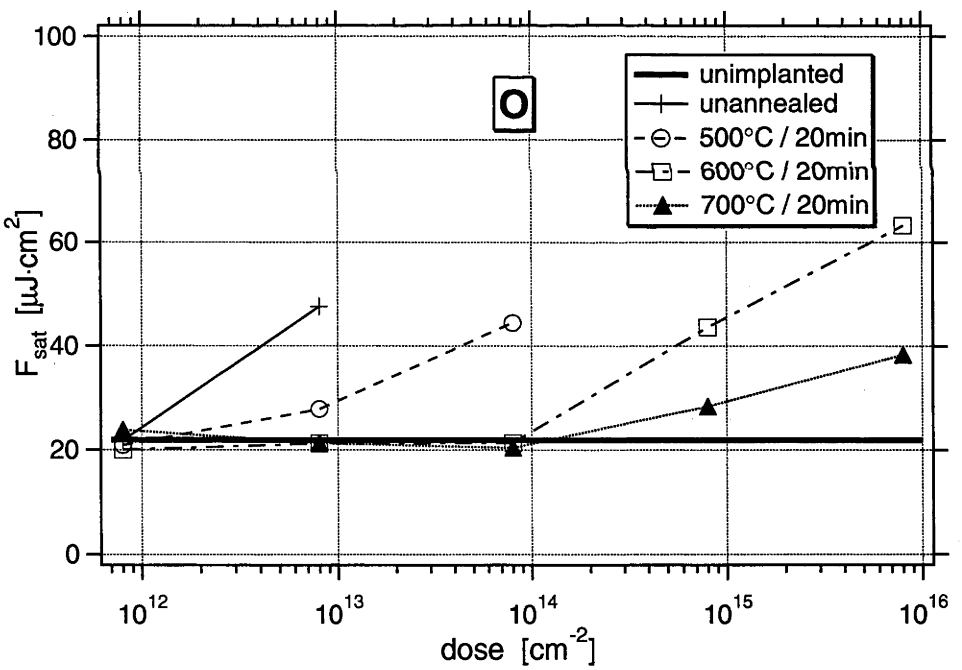

Fig. 4.3.1 - 2b: Saturation fluence F_{sat} from the TWA-fit versus dose for Arsenic and Oxygen implanted GaAs, annealed at 500 - 700°C / 20min as well as unannealed.

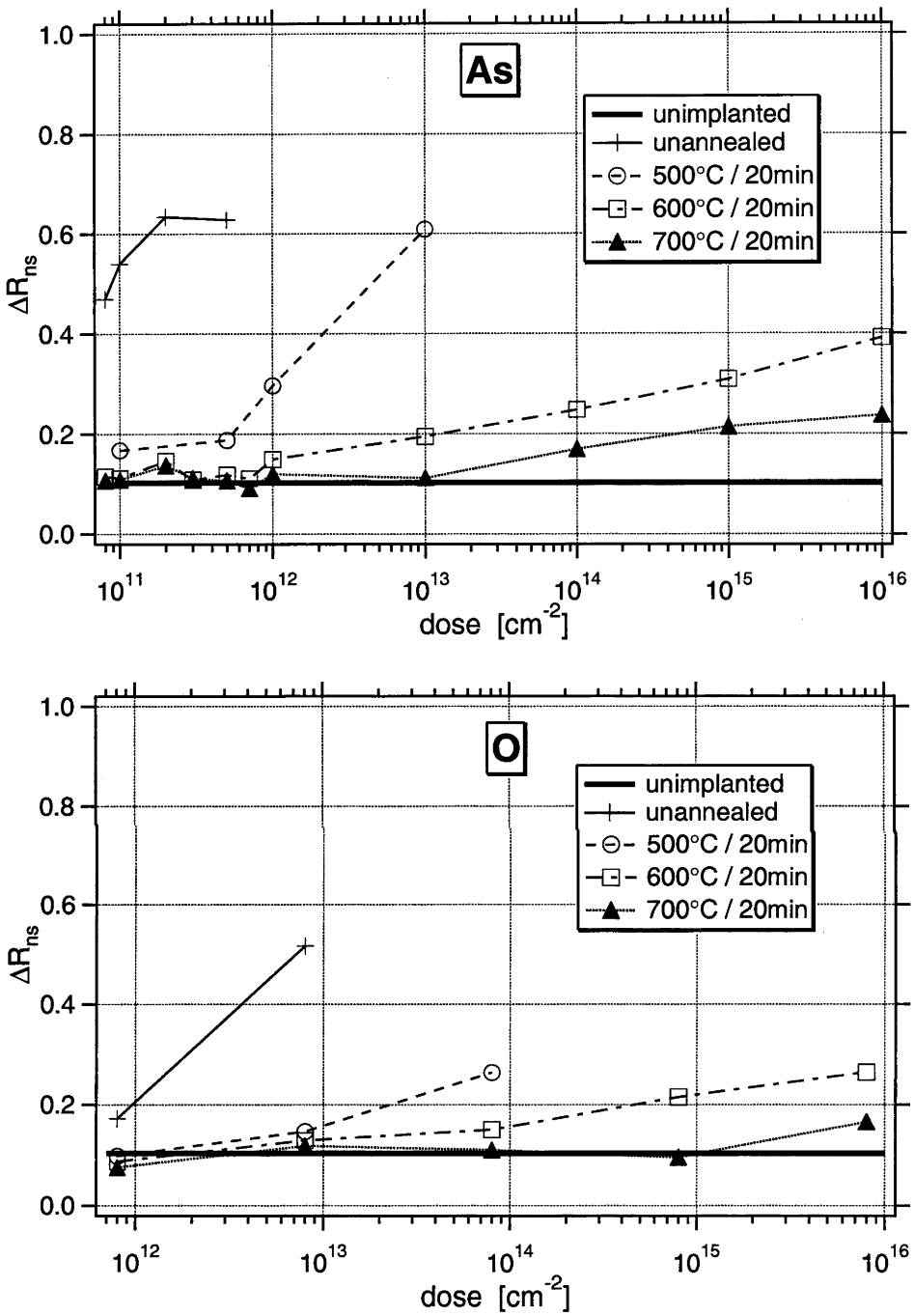

Fig. 4.3.1 - 2c: Nonbleachable reflectivity ΔR_{ns} from the TWA-fit versus dose for Arsenic and Oxygen implanted GaAs, annealed at 500 - 700°C / 20min as well as unannealed.

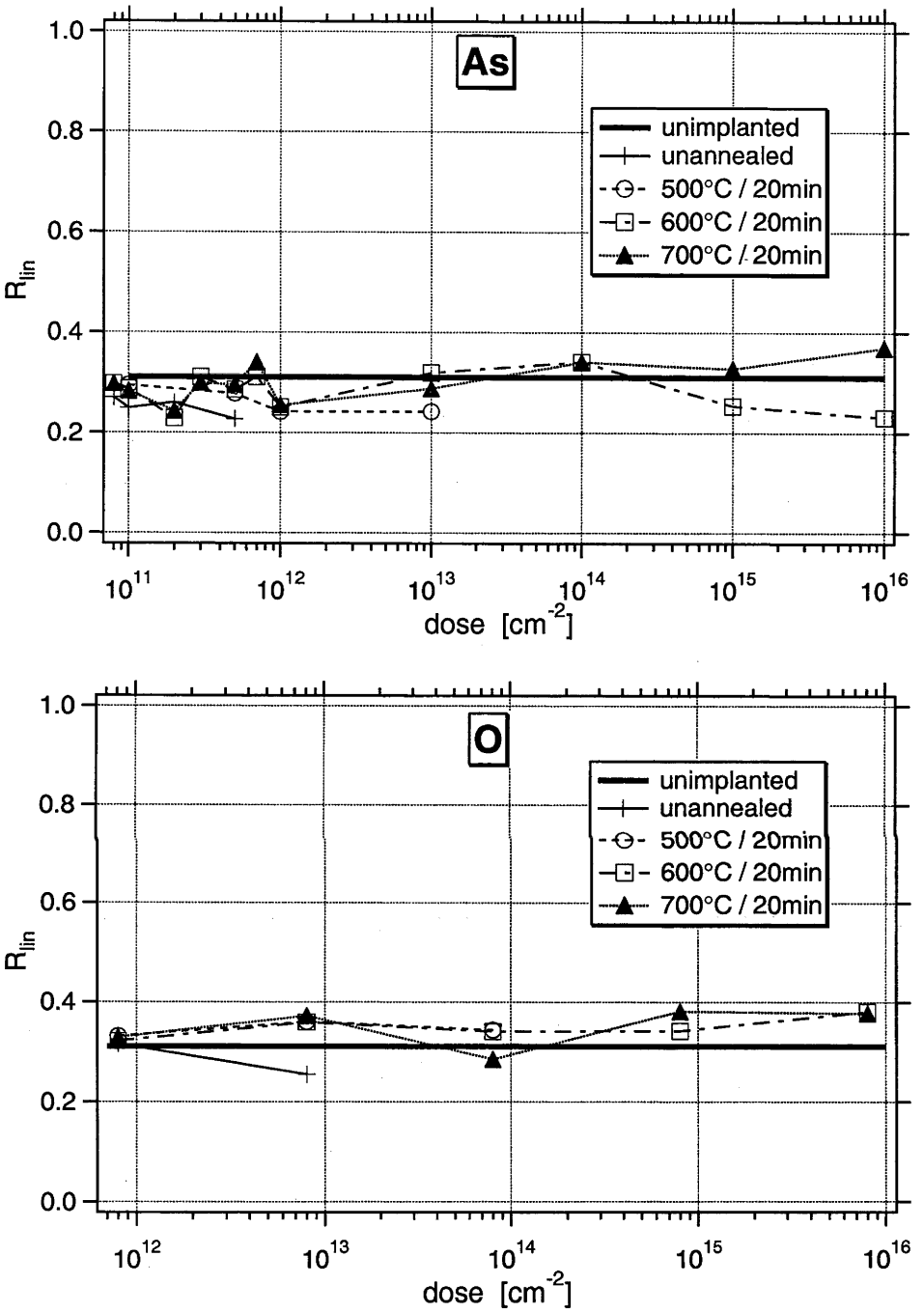

Fig. 4.3.1 - 2d: Low fluence reflectivity R_{lin} from the TWA-fit versus dose for Arsenic and Oxygen implanted GaAs, annealed at 500 - 700°C / 20min as well as unannealed.

Finally, it is interesting to observe the behaviour of the samples under very high fluence excitation. As an example *Fig. 4.3.1 - 3* shows $R(F_p)$ of the unimplanted as well as the $8 \cdot 10^{13}$ cm^{-2} O-implanted, 500°C annealed sample. In both cases the reflectivity actually decreases, following a peak which is located at ca. 700μJ·cm^{-2} in the unimplanted case and at ca. 1100μJ·cm^{-2} in the implanted case. However, in either case the samples incurred damage when subject to fluences beyond those corresponding to R_{peak} for prolonged times (minutes or longer). This damage was initially noticeable through an overall decrease in $R(F_p)$ and became clearly visible under the microscope after longer exposure. The inset in *Fig. 4.3.1 - 3* shows the linear plot of $R(F_p)$ of the unimplanted sample together with an extrapolated TWA-fit (performed for $F <$ 400μJ·cm^{-2}) as well as the difference between them. Interestingly, the difference is rather linear, indicating that a process such as TPA could indeed be responsible for the decrease of $R(F_p)$. The inset also shows a fit which includes TPA using a travelling wave model. It was assumed that the saturable absorption and TPA were independent, allowing the use of $R_{TWA} \times R_{TPA}$ as the fitting model (see Appendix III). From this fit a TPA constant of β = 230 cm/GW is deduced, which is 6-7 times larger than typical values quoted for LT-GaAs when measured close to the bandgap (λ = 900nm) [86]. This indicates that most likely the observed behaviour, hence the β-value, is due to both TPA and FCA, which is effectively a delayed two-photon process. Both effects cause strong carrier heating and, through the carrier-phonon interaction, also lattice heating which could be the cause of the observed damage. From this picture one concludes that, in unimplanted GaAs, the observed nonbleachable losses, and part thereof in the implanted case, are due to TPA and FCA.

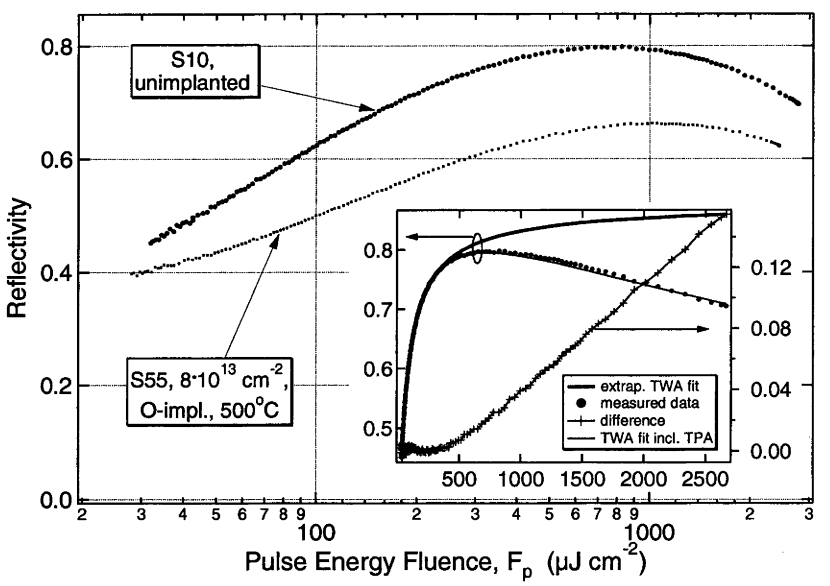

Fig. 4.3.1 - 3: $R(F_p)$ for high fluences of samples S10 (unimplanted) and S55 ($8 \cdot 10^{13}$ cm^{-2}, O, 500°C). The inset shows a linear plot of $R(F_p)$ and an extrapolated TWA-fit (performed for F_p<400μJ·cm^{-2}) as well as the difference between both. The $R(F_p)$ data in the inset was fitted with a travelling wave model including TPA (see Appendix III), resulting in β=230cm/GW.

4.3.2. Temporal Response

In the second, pump-probe, measurement the time resolved differential reflectivity was determined for different pump fluences using pump-probe delays as long as 300ps. As an example, *Figs. 4.3.2 - 1a,b* show the normalised differential reflectivity, dR, for some Arsenic (- *1a*) and Oxygen (- *1b*) implanted samples for different doses and annealing conditions compared with the unimplanted case. As in the first measurement, the dominating mechanism causing the reflectivity change is absorption bleaching in the GaAs layer. Contributions to dR originating from changes in the real part of the complex refractive index of GaAs are negligible here. The pump-excited carrier density in the probed volume lay between 1.5 and $3.5 \cdot 10^{18} cm^{-3}$ at a pump fluence of $F_P = 28 \mu J \cdot cm^{-2}$. To estimate the carrier density it was assumed that the peak of the radial carrier distribution was probed. This is valid since the probe spot was more than 3 times smaller than the pump spot. Then, using the samples' $R(F_P)$ - data, the carrier density calculates as

$$N = \left[1 - R\left(F_p\right)\right] \cdot \frac{2 \cdot F_p \cdot \lambda}{d_{abs} \cdot h \cdot c} \qquad (4.3.2 - 1)$$

where d_{abs} is the absorber thickness and the factor of 2 is due to the peak fluence. Strictly speaking, N is the density of absorbed photons and only corresponds to the carrier density as long as the carrier generation process is dominated by single-photon transitions. This is the case for a pump fluence of $28 \mu J \cdot cm^{-2}$.

All samples displayed a multi-exponential response corresponding to carrier thermalisation and cooling within the first several 100fs, and trapping and recombination via deep-level traps introduced by ion-implantation. As is apparent from the sample data in *Figs. 4.3.2 - 1a,b*, increasing implantation dose or decreasing annealing temperature both result in faster capturing-related signal decay, indicating that the density of deep-level traps is higher under these conditions, as would be expected. Furthermore, the fastest signals (unannealed and $1 \cdot 10^{13}$ cm^{-2} As implanted , 500°C/20min annealed samples) decay with effectively a single exponential with time constants <200fs and are dominated by carrier capturing, masking even the cooling process. Signals dominated by fast capturing evolve to negative differential reflectivity, i. e. photo induced absorption (PIA), levelling off at a dR value, usually a few percent or less, below zero. This is then followed by very slow (several 100ps) evolution to dR=0 (see inset in *Fig. 4.3.2 - 1b*). This has been similarly observed in the ion-implanted SESAMs described in chapter 2 as well as in LT-GaAs [43], and was attributed to slow recombination of captured carriers which provide additional transitions from mid-gap to high levels in the bands, after bleaching from band-filling has ceased due to fast and complete capturing. In contrast to the case of LT-GaAs [43], the ion-implanted samples did not display any slow (> 100ps) residual bleaching attributable to completely filled traps, even at the highest fluence used in the measurements. Furthermore, PIA, if present, is very small. This could indicate the presence of an efficient trap emptying mechanism. As mentioned in section *4.1*, it is

hoped that the micro-structural studies, under way, will shed more light on the nature and density of deep level traps in ion-implanted GaAs.

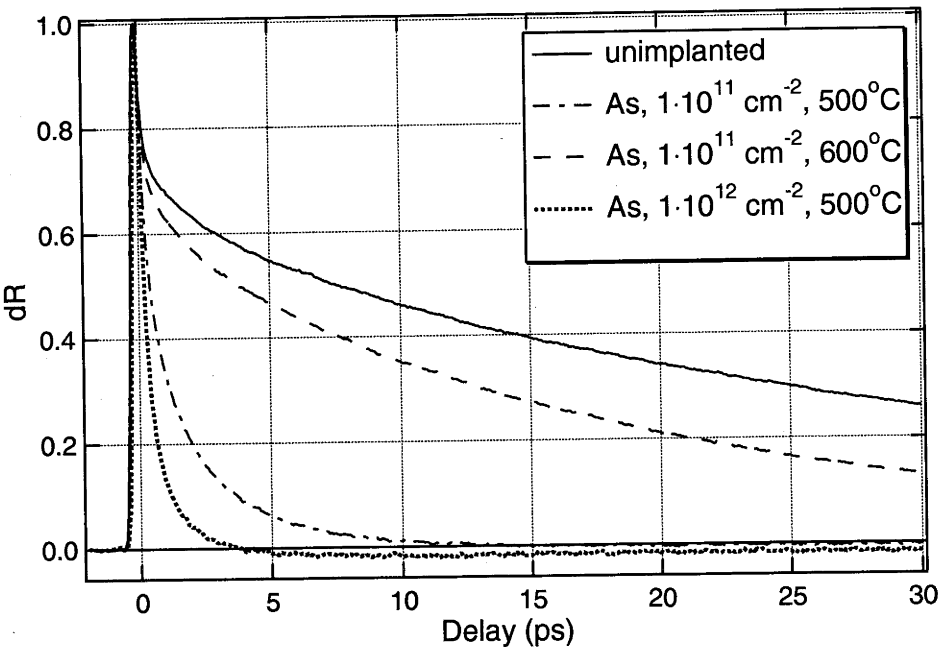

Fig. 4.3.2 - 1a: Differential reflectivity dR for Arsenic implanted GaAs for different doses and annealing conditions. The carrier density was approximately $2.5 \cdot 10^{18} cm^{-3}$ at a pump fluence of $28 \mu J \cdot cm^{-2}$.

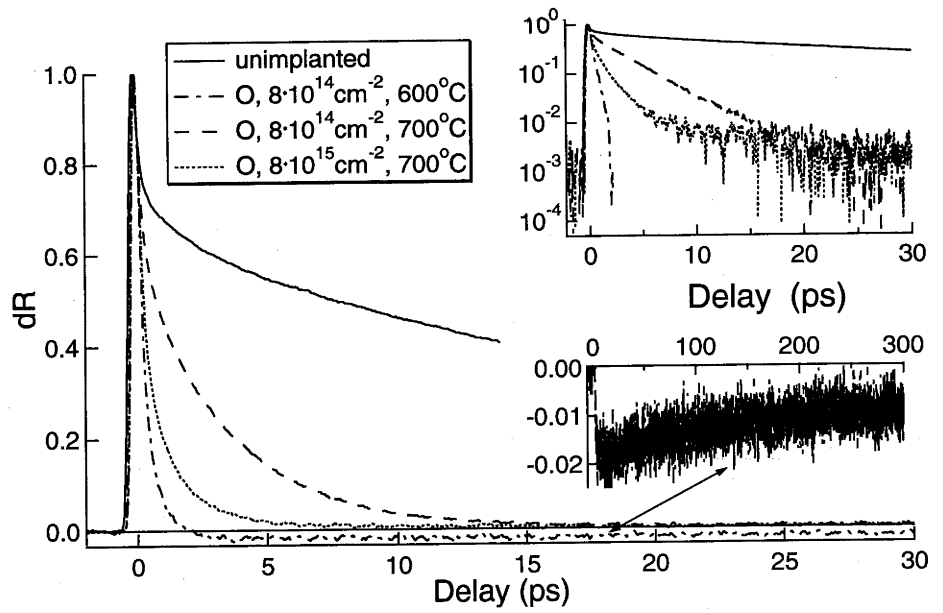

Fig. 4.3.2 - 1b: Differential reflectivity dR for Oxygen implanted GaAs for different doses and annealing conditions. The carrier density was approximately $2.5 \cdot 10^{18} cm^{-3}$ at a pump fluence of $28 \mu J \cdot cm^{-2}$. The insets show the evolution on a logarithmic scale and photo-induced absorption (PIA) respectively.

In order to compare the differential reflectivity data of all samples, an effective recovery time τ_A was defined as the delay, following the maximum, at which the dR signal crossed the 1/e level. This definition of τ_A is not the only possible one. For instance, the data could be fitted with a multi-exponential, the fit normalised suitably, and an effective single exponential time constant calculated through integration. However, the 1/e level crossing method is less complicated and serves well as a means of comparison. *Figs. 4.3.2 - 2a,b* depict τ_A for both implants as a function of dose and for the different annealing conditions. Interestingly, τ_A = 17.5ps for the unimplanted sample, which is much faster than expected from pure radiative recombination in GaAs (τ > 1ns). Similar response times have been observed in GaAs grown at normal temperature with MBE [84], and are attributed to impurity and surface recombination. The general trends are as expected for both implants. Firstly, the higher the annealing temperature the slower τ_A and, secondly, the higher the ion dose the faster τ_A. Note that the fastest response times displayed (≤200fs) are limited by the measurement pulsewidth. However, for the Arsenic implant the trend clearly becomes reversed for doses > $1 \cdot 10^{14}$ cm^{-2} where τ_A increases again. This seems to correlate with the F_{sat} data of section *4.3.1*, where a decrease of F_{sat} was observed under the same conditions. In the case of the Oxygen implant a similar reversal is anticipated only for much higher doses (> $1 \cdot 10^{16}$ cm^{-2}), as is evident from the line for the 600°C anneal. Furthermore, slightly shorter τ_A seem to be possible with the Oxygen implant and the variation of τ_A with the ion dose appears faster for the Arsenic compared to the Oxygen implant.

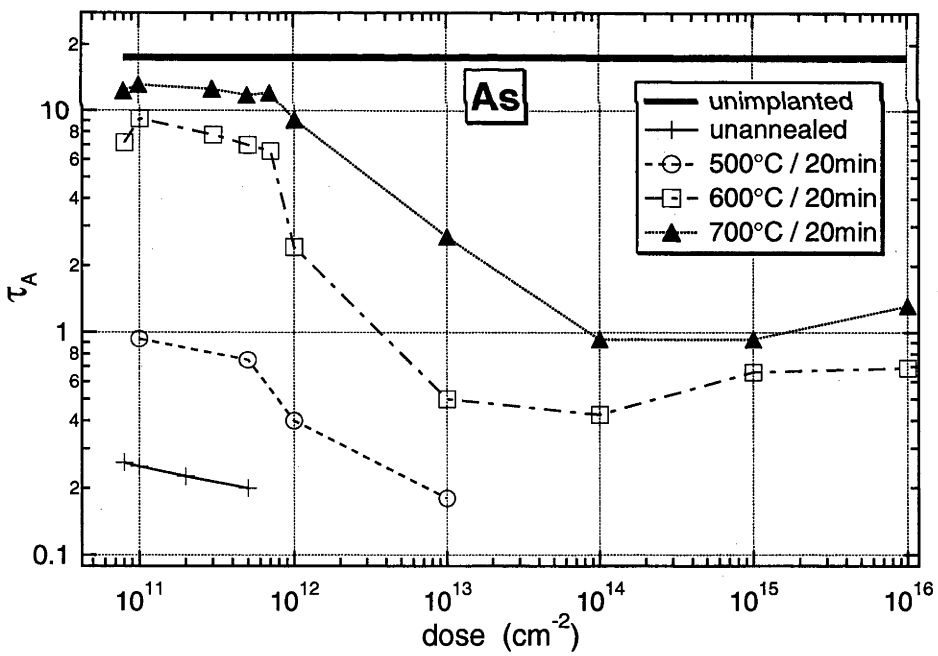

Fig. 4.3.2 - 2a: Effective response time τ_A versus dose for Arsenic implanted GaAs, annealed at 500 - 700°C / 20min as well as unannealed. The fastest τ_A (<200fs) are pulsewidth limited. The probed carrier density was approximately $2.5 \cdot 10^{18}$cm^{-3} at a pump fluence of 28μJ·cm^{-2}.

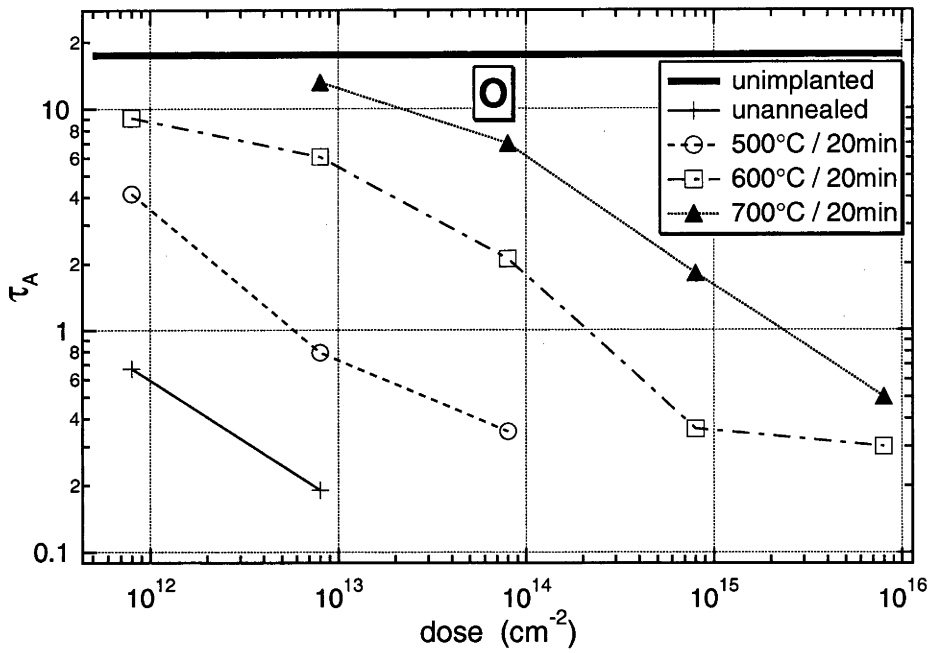

Fig. 4.3.2 - 2b: Effective response time τ_A versus dose for Oxygen implanted GaAs, annealed at 500 - 700°C / 20min as well as unannealed. The fastest τ_A (<200fs) are pulsewidth limited. The probed carrier density was approximately $2.5 \cdot 10^{18} cm^{-3}$ at a pump fluence of $28 \mu J \cdot cm^{-2}$.

In order to characterise the samples further, their temporal response was also measured for varying pump excitation. *Fig. 4.3.2 - 3a* shows a 3D plot of the absolute reflectivity of the unimplanted sample as function of time and pump fluence. Most importantly, this figure shows that the response of the unimplanted sample changes markedly for $F_p > 100 \mu J \cdot cm^{-2}$, where a second reflectivity maximum appears at a delay of around 5ps. The absorption actually turns into gain for $F_p > 400 \mu J \cdot cm^{-2}$, and at $F_p = 769 \mu J \cdot cm^{-2}$ a maximum reflectivity of 1.3, corresponding to a gain constant of $2600 cm^{-1}$, is observed (see *Fig. 4.3.2 - 3b* for a projection of a number of traces on the time axis). This is a remarkably high gain for bulk GaAs at room temperature and λ=830nm. The appearance of this is explained as follows. For low fluences ($<100 \mu J \cdot cm^{-2}$) the generation of free carriers is dominated by single-photon absorption. However, the single-photon transition becomes progressively bleached for increasing pump fluence and two-photon processes such as FCA and TPA start carrier heating. The latter is most likely dominated by FCA, considering the large discrepancy between typical TPA constants for GaAs and the fitting constant found in section *4.3.1*. Therefore, whilst the single-photon transition is nearly bleached, the two-photon processes provide an efficient absorption mechanism, creating hot carriers which cool to the lattice temperature with time constants of several 100 fs. Once cool, the carrier density is high enough to cause gain at the pump-probe wavelength. Signals, virtually equal to those observed here (except for the appearance of gain), were seen in GaAs/AlGaAs semiconductor waveguide saturable absorbers [87, 88] where the above intuitive picture was supported through simulations in the framework of the density matrix approach. Using an intraband thermalisation time constant of τ_{th} = 50fs and electron

and hole cooling time constants of τ_e = 650fs and τ_h = 200fs respectively, these simulations reproduced the secondary maximum at t = 5ps. Further evidence that hot carrier generation through FCA and TPA is responsible for the appearance of the secondary reflectivity maximum is obtained from carrier density calculations. Using the R(F_p)-data of the unimplanted sample, together with *(4.3.2 - 1)*, results in a density of absorbed photons of N ≈ $2.5 \cdot 10^{19} cm^{-3}$ in the probed volume for the case of the highest pump fluence (F_p = 769μJ·cm²). On the other hand, it is possible to use the Banyai-Koch plasma theory [38] to model the absorption (gain) of the unimplanted sample at pump-probe delays greater than the thermalisation and cooling times, for instance at t = 5ps. When incorporated in the device modelling, this results in a necessary carrier density of N ≈ $5...6 \cdot 10^{18} cm^{-3}$, assuming a lattice at room temperature, in order to achieve R=1.3 at 5ps and λ=830nm. The difference between the two densities could be explained through the presence of a three-particle process (Auger). However, using typical values for the Auger constant in GaAs (A = $7 \cdot 10^{-30}$ $cm^6 \cdot s^{-1}$ [46]) and N = $2.5 \cdot 10^{19} cm^{-3}$, the calculated inverse Auger rate, $(N^2 \cdot A)^{-1}$, is still > 200ps and therefore too slow to create the difference in the calculated carrier densities. Therefore, the observed gain at 5ps delay must be due to "chilled" hot carriers, generated through FCA and TPA which are also responsible for the discrepancy in the density of absorbed photons and the carrier density calculated with the Banyai-Koch model at t = 5ps. Finally, *Fig. 4.3.2 - 3b* shows that the peak of the response during pump-probe correlation occurs at a fixed, fluence independent time, for F_p < 100μJ·cm², i. e. the regime dominated by single-photon transitions. For higher fluences this peak shifts to earlier times, indicating the onset of the carrier heating regime. Here FCA and TPA increase the total absorption around the peak of the pump pulse, causing the reflectivity to drop off earlier compared to the single-photon case where the response is close to integrating.

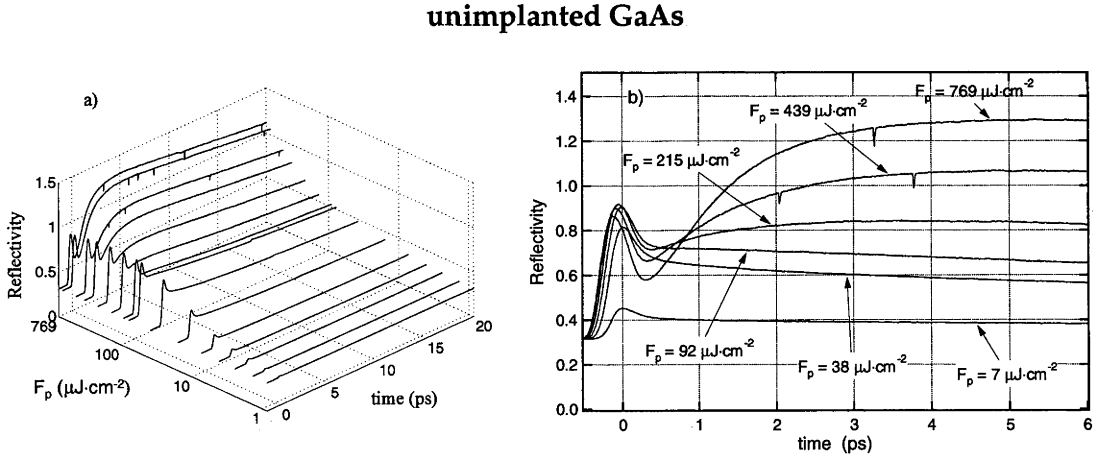

Fig. 4.3.2 - 3: Fluence and time dependent response: (a) unimplanted sample and (b) projection on time axis for some fluences.

In contrast to the unimplanted sample, *Figs. 4.3.2 - 4,5,6,7,8* show the response of the samples Arsenic $1 \cdot 10^{14}$ cm^{-2}, 600°C/20min (- *4*), 700°C/20min (- *5*) and $1 \cdot 10^{13}$ cm^{-2}, 500°C/20min (- *6*) as well as Oxygen $8 \cdot 10^{14}$ cm^{-2}, 600°C/20min (- *7*) and $8 \cdot 10^{15}$ cm^{-2},

600°C/20min (- *8*). For all samples annealed at or above 600°C/20min, remnants of the hot carrier tail are present, and only for the unannealed (not shown) and $1{\cdot}10^{13}$ cm^{-2} Arsenic implanted, 500°C/20min annealed samples does it vanish completely for the fluences used in the measurements. For a given fluence, the prominence of the hot carrier tail depends on the dose and the annealing temperature. This is to be expected since the density of deep-level traps also depends on these parameters. Assuming a model where cool and hot carriers are captured at equal rates, one can give a rough estimate for the trap density in the implanted samples. Using a carrier density of $0.5...1{\cdot}10^{19}$ cm^{-3} at F_p = 700µJ·cm^{-2}, the density of deep level traps must lie below this value even for the highest dose implants annealed at or greater than 600°C/20min, since a slight residual bleaching is observed which indicates that the traps are filled. Preliminary results from the NIRA and MCDA measurements show indeed that the density of As_{Ga}^{+} lay in the low 10^{18} cm^3 for O-implanted samples annealed at 600°C or higher. However, in these first measurements, no clear correlation could be found between the implantation dose and the measured As_{Ga}^{+} densities. So far it is not clear if this is due to the proximity of the detection limit in the measurement, or if the As_{Ga}^{+} play a less dominant role as traps in these ion-implanted samples. On the other hand, the trap density in the sample Arsenic, $1{\cdot}10^{13}$ cm^{-2}, 500°C/20min (*Fig. 4.3.2 - 6*) must be higher than $0.5...1{\cdot}10^{19}$ cm^{-3} since no residual bleaching is observed. For that sample, the response is clearly pulsewidth limited whilst the modulation is strongly reduced. Although signals from residual bleaching are undesirable in an actual application, their relevance must be put into perspective here. Firstly, operation under high fluence excitation, i. e. at the peak of $R(F_p)$ (see *Fig. 4.3.1 - 1*), leads to gradual damage and should be avoided. Secondly, for the fastest samples with still appreciable modulation (e. g. O, $8{\cdot}10^{14}$ cm^{-2}, 600°C/20min), the residual bleaching is small and vanishes within 5ps, recovering to the low fluence reflectivity R_{lin}, with only 1 or 2% of PIA. This is again an indication for the presence of an effective recombination mechanism between captured carriers, which empties the bands even if the traps are overfilled.

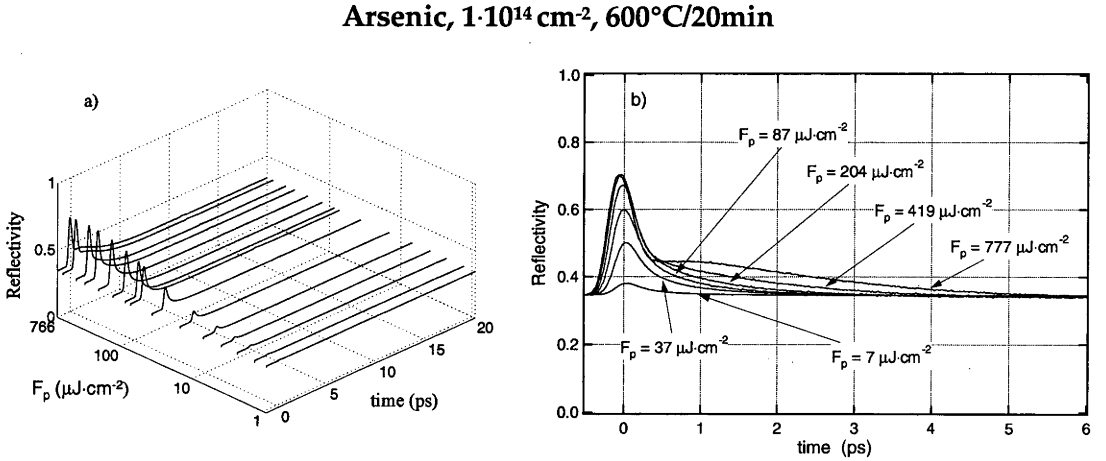

Fig. 4.3.2 - 4: Fluence and time dependent response of the sample: (a) Arsenic, $1{\cdot}10^{14}$ cm^{-2}, 600°C/20min and (b) projection on time axis for some fluences.

Arsenic, $1 \cdot 10^{14}$ cm^{-2}, 700°C/20min

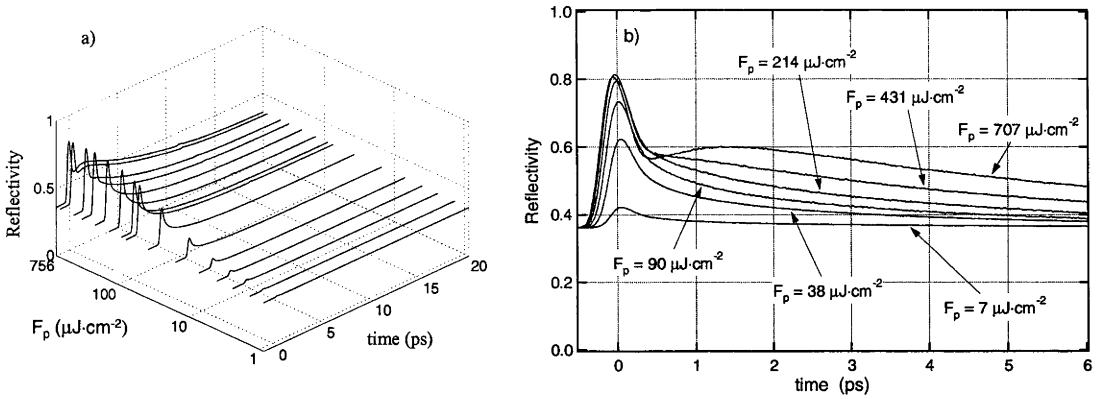

Fig. 4.3.2 - 5: Fluence and time dependent response of the sample: (a) Arsenic, $1 \cdot 10^{14}$ cm^{-2}, 700°C/20min and (b) projection on time axis for some fluences.

Arsenic, $1 \cdot 10^{13}$ cm^{-2}, 500°C/20min

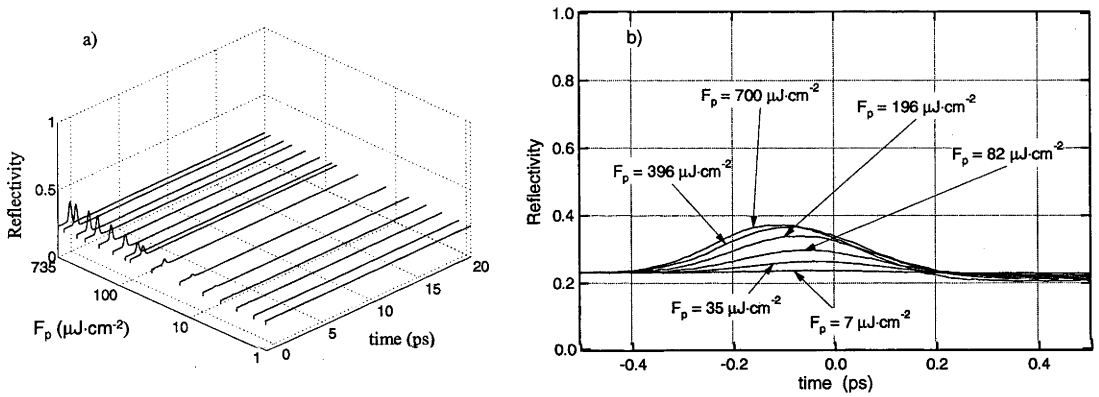

Fig. 4.3.2 - 6: Fluence and time dependent response of the sample: (a) Arsenic, $1 \cdot 10^{13}$ cm^{-2}, 500°C/20min and (b) projection on time axis for some fluences. Note the different time scale in (b).

Oxygen, $8 \cdot 10^{14}$ cm^{-2}, 600°C/20min

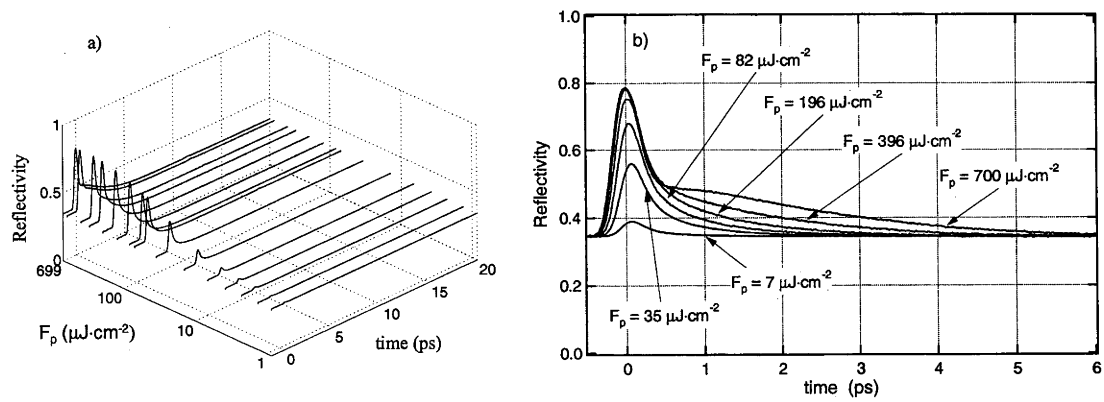

Fig. 4.3.2 - 7: Fluence and time dependent response of the sample: (a) Oxygen, $8 \cdot 10^{14}$ cm^{-2}, 600°C/20min and (a) projection on time axis for some fluences.

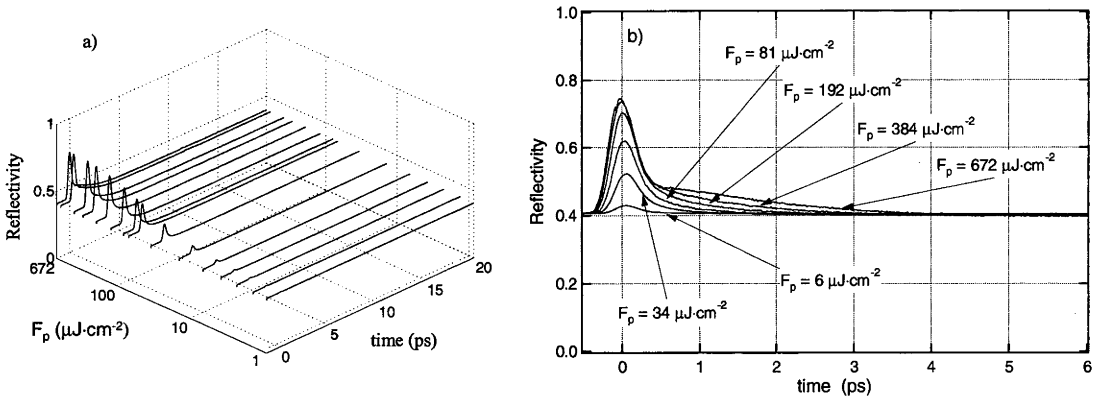

Fig. 4.3.2 - 8: Fluence and time dependent response of the sample: (a) Oxygen, $8 \cdot 10^{15}$ cm^{-2}, 600°C/20min and (b) projection on time axis for some fluences.

Finally, it is in order at this point to compare the large signal SESAM response discussed in section 2.2.3 with the signals observed here. The major difference between the two cases is the following. Whilst the unimplanted SESAM became faster with increasing pump fluence and no evidence of a hot carrier tail was observed, the latter is clearly present here. At the time of writing there is not enough evidence to explain the difference conclusively. One could surmise, however, that the lattice temperature in the SESAM case is much higher than in the case of the test structures since the absorber thickness is a factor 10 smaller, and no acousto-optic modulator was used for the suppression of thermal effects. In this case, almost no cooling signal would be observed and the fast transient could be explained as signals due to hole-burning and thermalisation only.

4.3.3. Modulation vs. Response Time Performance

Using the results of the modulation and pump-probe measurements, the different samples can be characterised by plotting their modulation behaviour normalised to that of unimplanted GaAs, using the parameter $M_{\max} = \frac{\Delta R}{1 - R_{lin}} \cdot \frac{1 - R_{lin,GaAs}}{\Delta R_{GaAs}}$, against the effective recovery time τ_A. Note that for all samples, except for the high dose implanted and unannealed ones, R_{lin} was approximately constant and hence $M_{\max} \approx \frac{\Delta R}{\Delta R_{GaAs}}$. However, M_{max} was introduced for generality since a reduction in R_{lin}, (even if ΔR_{max} remained unaffected after implantation) should be reflected by a poorer assessment of modulator performance, and this would be masked if the potential effect of R_{lin} were omitted. Samples implanted with different ions and doses, and annealed under different conditions are, therefore, represented as points in the (τ_A , M_{max}) plane. This is shown in *Fig. 4.3.3 - 1* for the complete set of annealed samples. The unannealed samples are not shown

because, although extremely fast, their M-value was very low and varied due to in situ annealing under high fluence excitation (see section *4.3.1*).

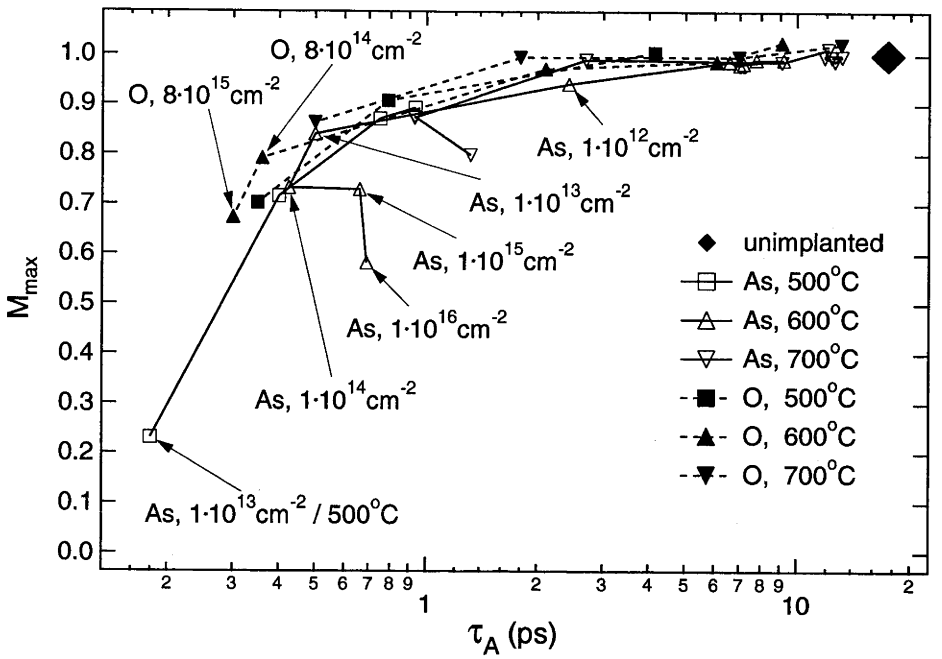

Fig. 4.3.3 - 1: (τ_{eff} , M_{max}) plane with all annealed samples, each represented by a single point.

There is a clear tendency for the data to fall on a well-defined curve relating the achievable modulation to the speed of recovery. Unimplanted GaAs is located on the right hand side of this graph, whilst increasing the implant dose, for a particular annealing condition, progressively moves the data to the left (shorter τ_A and smaller M_{max}). On the other hand, increased annealing temperatures, at a particular implantation dose, move the points back to the right (towards longer τ_A and larger M_{max}). Generally more than an order of magnitude higher dose is required using an O-implant compared with As to achieve the same combination of response time and modulation depth. *Fig. 4.3.3 - 1* underlines the fact that a specific (τ_A , M_{max}) combination can be achieved by using a range of different combinations of ion species, doses and annealing conditions. This suggests that the types of defects in annealed As and O implanted GaAs are quite similar and the projected curve defines a rather general relationship between τ_A and M_{max}.

There are, however, outlying cases. Firstly, for Arsenic doses above $1{\cdot}10^{12}$ cm^{-2}, annealed at 500°C/20min, M_{max} drops rapidly whilst τ_A becomes pulsewidth limited, increasing the uncertainty on the location of the point As, $1{\cdot}10^{13}$ cm^{-2}, 500°C/20min. Secondly, Arsenic doses above $1{\cdot}10^{14}$ cm^{-2} actually reverse the general trend (see sections *4.3.1* and *4.3.2*), such that whilst M_{max} decreases, τ_A increases. This is apparent in the lines for As, 600°C/20min and 700°C/20min, the latter indicating also the irreversibility of the change even at higher annealing temperatures. It will be shown below that the departure indicates a change in the nature or composition of the defects created by the implantation process. Earlier time resolved differential reflectivity

measurements on unannealed H^+-implanted GaAs [79] revealed a so-called 'lifetime saturation' which was attributed to the formation of an amorphised layer in the implanted material. In order to investigate this possibility on the microscopic level, Rutherford Backscattering Spectroscopy-Channelling (RBS-C) measurements [32] were performed on the Arsenic implanted samples for doses ranging from $1{\cdot}10^{13}$ cm^{-2} to $1{\cdot}10^{16}$ cm^{-2} before and after annealing at 600°C/20min. The RBS-C data, shown in *Figs. 4.3.3 - 2a,b*, reveal that for a dose of $1{\cdot}10^{14}$ cm^{-2} a buried amorphous layer was formed in the unannealed sample (- *2a*), which recrystallised upon annealing giving a dechannelling yield only a fraction higher than that of the unimplanted, fully crystalline, sample (- *2b*). For higher doses the amorphous layer extends to the surface and further towards the Bragg mirror, recrystallisation upon annealing is poor, and RBS-C signals typical of those of extended defects are observed (- *2b*). This was further confirmed by cross-sectional Transmission Electron Microscopy (TEM) measurements. *Figs. 4.3.3 - 3a,b* show the micrographs for the $1{\cdot}10^{14}$ cm^{-2} (- *3a*) and $1{\cdot}10^{15}$ cm^{-2} (- *3b*) implanted samples before and after annealing. Visible are the amorphous layers followed by a crystalline region, formed upon implantation, in both cases. Thermal annealing resulted in good recrystallisation with small clusters as well as dislocation loops in the case of the $1{\cdot}10^{14}$ cm^{-2} implanted sample. For the $1{\cdot}10^{15}$ cm^{-2} implant, poor recrystallisation is observed, with a top polycrystalline layer followed by a region of dislocation loops.

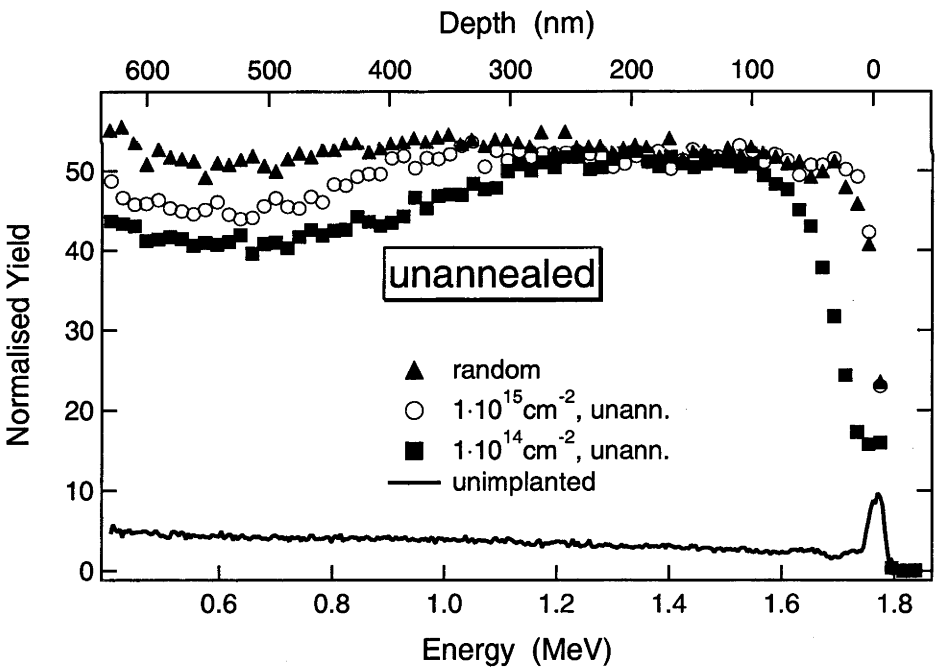

Fig. 4.3.3 - 2a: RBS-C data of $1{\cdot}10^{14}$ cm^{-2} and $1{\cdot}10^{15}$ cm^{-2} Arsenic implanted, unannealed test structures. For comparison the unimplanted and random cases are also shown.

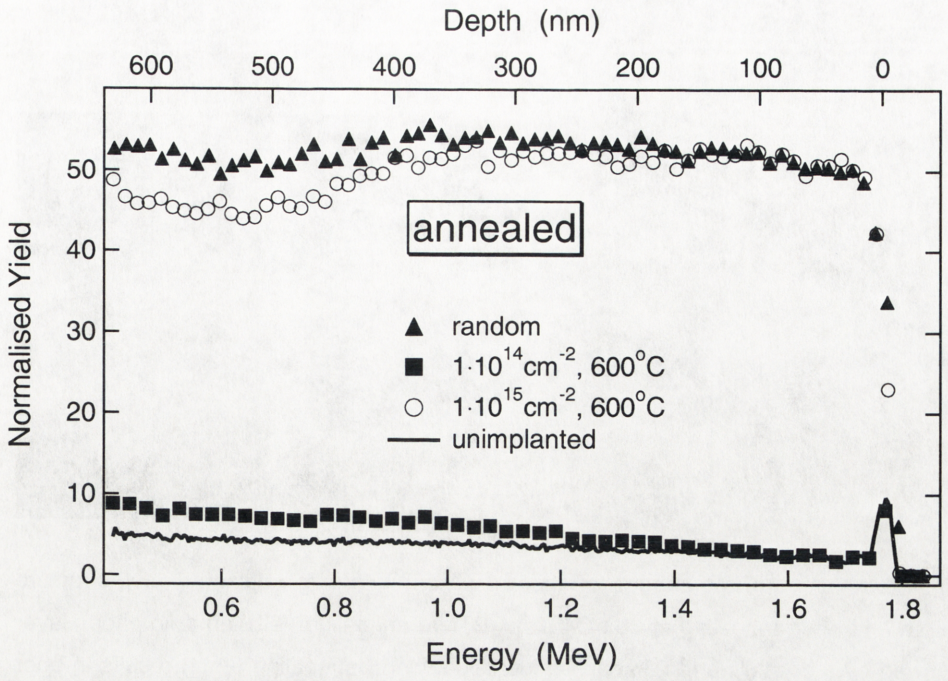

Fig. 4.3.3 - 2b: RBS-C data of $1 \cdot 10^{14}$ cm^{-2} and $1 \cdot 10^{15}$ cm^{-2} Arsenic implanted, 600°C/20min annealed test structures. For comparison the unimplanted and random cases are also shown.

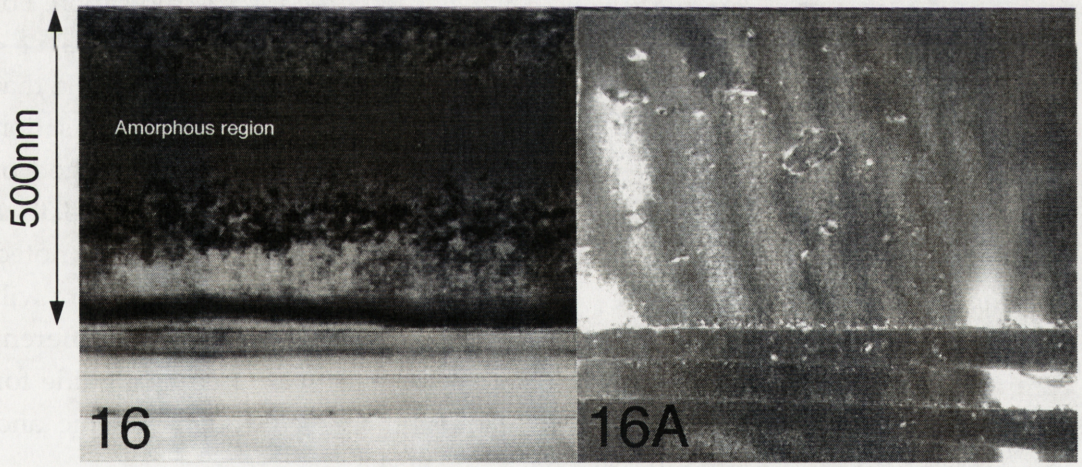

Fig. 4.3.3 - 3a: TEM images of $1 \cdot 10^{14}$ cm^{-2} Arsenic implanted test structure before and after annealing at 600°C/20min. Before annealing (left), an amorphous layer followed by a crystalline region can be identified, whilst annealing (right) results in good recrystallisation with small clusters as well as dislocation loops.

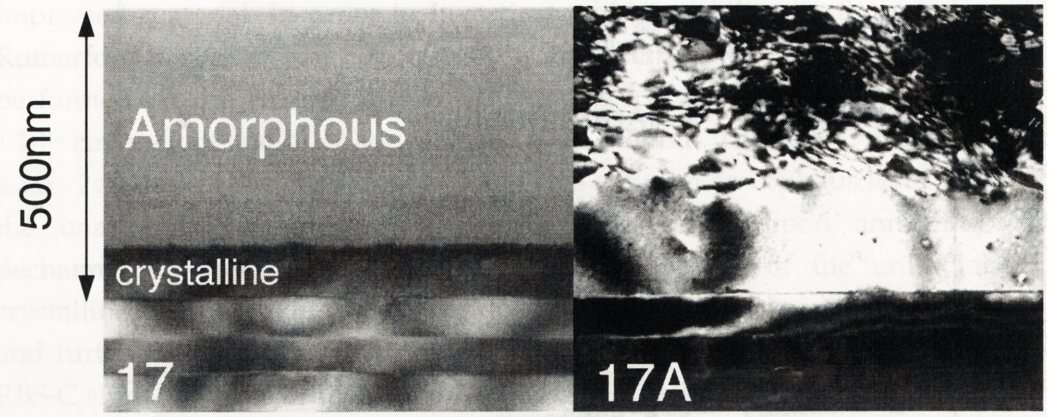

Fig. 4.3.3 - 3b: TEM images of the $1 \cdot 10^{15}$ cm^{-2} Arsenic implanted test structure before and after annealing at 600°C/20min. Before annealing (left), an amorphous layer followed by a crystalline region can be identified, whilst annealing (right) results in poor recrystallisation with a top polycrystalline layer followed by a region of dislocation loops.

For nonlinear optical modulator applications, implantation doses which generate amorphous layers are clearly undesirable, even if recrystallisation is possible, since the onset of a departure from the projected M_{max} vs. τ_A curve can already be observed under these conditions. For O implants higher doses are needed for amorphisation since O is lighter than As. This suggests that, with O implantation, shorter τ_A can be obtained since higher doses can be used without amorphisation. For instance, the $8 \cdot 10^{14}$ cm^{-2} O-implanted, 600°/20min annealed sample, achieves a $\tau_A <$ 400fs, preserving 80% of the modulation M_{max} of unimplanted GaAs. It is possible that lighter ions would allow one to produce even shorter τ_A by avoiding amorphisation and thereby also preserving the highest possible modulation. A different method of avoiding amorphisation would be to implant at elevated temperatures. *Fig. 4.3.3 - 1* clearly motivates further study to explore these concepts. Finally, it should be noted that specific devices with GaAs absorber thicknesses different from that used here will require a change in implant energy and in turn will lead to slightly different amorphisation thresholds. Nevertheless, the present study can be used as a guide for achieving a specific recovery time and modulation in GaAs through Arsenic and Oxygen ion implantation for an arbitrary device geometry.

4.4. Summary

In summary, a study of the nonlinear absorption modulation and recovery time of a large set of As- and O-ion implanted GaAs samples was performed. The samples (0.5µm of AR-coated GaAs on a Bragg-mirror) were measured in reflection with a single beam as well as a pump-probe configuration, using 100fs laser pulses at 830nm. The fluence dependent reflectivity ($R(F_p)$) data were fitted with a travelling wave saturable absorber (TWA) model from which the low fluence reflectivity R_{lin}, the

bleachable and nonbleachable reflectivities ΔR and ΔR_{ns}, as well as a saturation fluence F_{sat} were deduced, and a normalised modulation parameter M_{max} defined. From the pump-probe data (differential reflectivity dR) each sample was further characterised by an effective recovery time τ_A.

It was shown that both the response time τ_A and modulation M_{max} decrease through ion implantation with the decrease in M_{max} being due to increasing non-bleachable losses, ΔR_{ns}, for annealed samples. Using a Rutherford Backscattering technique, it was shown that, for doses below the amorphisation threshold, the data from all annealed samples lay on a well-defined curve in the (τ_A , M_{max}) plane. This suggests that the residual defects after annealing of As- and O-implanted GaAs are of a similar nature (point defects) and that the curve defines the achievable (τ_A , M_{max}) performance of ion implanted GaAs. Oxygen, being the lighter ion, can be implanted at higher doses than As without amorphisation, creating more point defects and leading to shorter τ_A whilst preserving highest possible modulation. For the $8 \cdot 10^{14}$ cm^{-2} O-implanted, 600°/20min annealed sample τ_A < 400 fs and F_{sat} = 44 $\mu J \cdot cm^{-2}$ at 80% of the modulation of unimplanted GaAs were measured. Note, that the saturation fluence is only about twice that of unimplanted GaAs whilst the response time is reduced by a factor of 50.

Under high fluence excitation (F_p > 100$\mu J \cdot cm^{-2}$) the temporal response of the samples acquires a secondary peak following the pump-probe correlation. These signals were attributed to the cooling of hot carriers generated through carrier heating due to free carrier and two-photon absorption during the pump pulse. Most prominently, this leads to the appearance of a very high optical gain of 2600 cm^{-1} at 5ps delay in the unimplanted sample. Depending on implantation dose and annealing condition, the hot carrier peak is strongly suppressed or not present for the implanted samples.

Overall, it was shown that ion-implantation is a useful and extremely versatile process for making ultrafast absorption modulation devices.

CHAPTER 5

A SESAM MODE-LOCKED ND:YVO_4 LASER WITH VARIABLE OUTPUT PULSEWIDTH

A Nd:YVO_4 laser, mode-locked by unimplanted as well as Arsenic implanted InGaAs SESAMs is presented in section *5.1.* Using mode-locking experiments and computer simulations, it is shown in section *5.2* that pulsewidth control by a factor of 2-3 is possible through variable output coupling whilst self-starting is maintained.

5.1. Introduction and Cavity Design

There are several well established techniques for the generation of ps-pulses in solid-state lasers. These include active mode-locking [89, 90], passive mode-locking with saturable absorbers such as dyes [91], Kerr-lens mode-locking (KLM) [94], coupled cavity and SESAM mode-locking [7, 10], and passive Q-switching of micro-cavity lasers [92]. Generally, active mode-locking involves the use of an acousto-optic modulator, rf-driver and cavity length stabilisation, which increase the cost and size of systems considerably. However, for the generation of pulse energies at the mJ level with kHz repetition rate, the 'active-active' (actively mode-locked and Q-switched) configuration is still a commonly used option [93]. The use of dye-jets as saturable absorbers for passive mode-locking suffers from the relatively fast degradation and the inconvenience of handling of the dye. It has been shown that KLM is a feasible option for the generation of ps-pulses in solid state laser materials such as Nd:YAG [94, 95]. When a glass of high nonlinear refractive index, such as SF57, was introduced in a second intra-cavity focus, KLM was self-starting in a Nd:YAG laser [95]. However, the stringent requirements for cavity alignment associated with self-starting KLM are a considerable disadvantage when the long term stability of a laser system is an issue. With the advent of coupled cavity mode-locking, in particular the resonant passive mode-locking (RPM), a relatively low maintenance mode-locking mechanism became available [5]. The coupled cavity typically contained a semiconductor saturable absorber and was tuned to anti-resonance, thereby minimising the intra-cavity losses and providing nonlinear modulation of a few tenths of a percent. These conditions generally allowed for a stable cw mode-locking operation which was self-starting due to the resonant nonlinearity of the semiconductor saturable absorber (bulk GaAs or InGaAs multiple quantum well structures) inside the coupled cavity. Additionally, the response time of the saturable absorber could be chosen by varying the growth temperature of the molecular beam epitaxy (MBE) process. However, it was soon realised that the dimensions of the coupled cavity could be shrunk to those of a micro-cavity, arriving at the monolithic device called anti-resonant Fabry-Perot saturable absorber (A-FPSA) or semiconductor saturable absorber mirror (SESAM) [10]. As was outlined in the introduction (chapter *1*), over the last 5 years, SESAMs were thoroughly

successful in mode-locking large variety of solid-state laser materials. Their advantages are clear: they are compact and allow simple cavity designs; they produce self-starting mode-locking of ps and fs pulses; and their properties can be tuned to cover a large range of lasing wavelengths. Additionally, SESAMs can be used as passive Q-switches in high gain micro-cavity lasers, adding essentially no further length to the cavity, and thereby allowing the generation of Q-switched pulses in the ps regime [92].

In this chapter, a Nd:YVO_4 laser mode-locked by an InGaAs-based SESAM is presented. SESAM mode-locking of this crystal with very attractive lasing properties (a comparison between Nd:YVO_4 and Nd:YAG is given in chapter *6*, *Table 6.1.1*) has been reported earlier [16, 96]. The high gain and absorption cross-section of Nd:YVO_4 make it an ideal choice for diode-pumping, where the overlap of the pump with the laser mode is usually much worse than for Ti:Sapphire pumping. The relatively large absorption bandwidth relaxes the pump-diode specifications, hence reduces cost. The excited state lifetime of Nd:YVO_4 is $\approx 90\mu s$. In the context of cw mode-locking stability, this value compares favourably with those of Nd:YAG or Nd:YLF (> 200μs). Therefore, Nd:YVO_4 is an ideal laser material for the development of a diode-pumped SESAM mode-locked laser, producing ps pulses for Electro Optic Systems' satellite laser ranging applications. Furthermore, for reasons explained in chapter *6*, it was decided that an amplifier head, developed in parallel, should make use of the excellent gain available from Nd:YVO_4. Therefore, to match oscillator and amplifier wavelengths, this material is the natural choice for the construction of an oscillator. At $\lambda = 1.06\mu m$, the typical pulsewidth obtained from a SESAM mode-locked Nd:YVO_4 laser was around 6ps [96]. For mm accuracy ranging, pulsewidths of >10ps are required at this wavelength. Therefore, the oscillator should preferably feature 'on-the-fly' continuously adjustable output pulsewidth, τ_{FWHM}, ranging from the shortest possible to $\tau_{FWHM} \approx 20ps$.

The laser used in the experiments is shown in *Fig. 5.1 - 1*. The cavity has the 1.1% doped Nd:YVO_4 gain medium at one end (GE-cavity). Due to the gain flattening through enhanced spatial hole burning (SHB), the GE configuration was shown to produce pulses up to three times shorter than gain-in-the-middle (GM) lasers [97, 98]. The crystal has a wedge of 5° and suitable anti-reflection (AR) and high-reflection (HR) coatings on its surfaces. The transmission of the end mirror for the pump wavelength of 808.5nm was measured to be 85%. The cavity uses AR-coated lenses instead of the usual curved mirrors to produce foci inside the laser crystal as well as on the SESAM. There is no particular advantage in using lenses, although the mode does not display any astigmatism in this case. The losses introduced by lenses are usually higher than those of mirrors. Variable output coupling was implemented using a thin film polariser (TFP) in conjunction with an AR-coated zero order $\lambda/4$ plate. Nd:YVO_4 is a highly birefringent crystal with its highest gain cross-section along the crystallographic c-axis (vertical). Therefore, with the axis of the $\lambda/4$ plate aligned vertically, output coupling can be minimised whilst a rotation causes output coupling equivalent to that of a mirror with reflectivity

$$R_{out}(\Theta) = \cos^2(2 \cdot \Theta) \qquad (5.1 - 1)$$

where Θ is the rotation angle. Essentially, the output coupler transmission, $T_{out}(\Theta) = 1 - R_{out}(\Theta)$, generated by the combination of the TFP and the $\lambda/4$ plate is equivalent to that of a $\lambda/2$ plate between two crossed polarisers. Therefore, with proper alignment of the laser crystal c-axis and the TFP angle of incidence, *(5.1 - 1)* can be expected to give accurate values for the output coupler reflectivity.

It will be shown below that varying the output coupling, and hence the cavity loss, the output pulsewidth of the laser can be varied by a factor of up to three, still maintaining self-starting mode-locking.

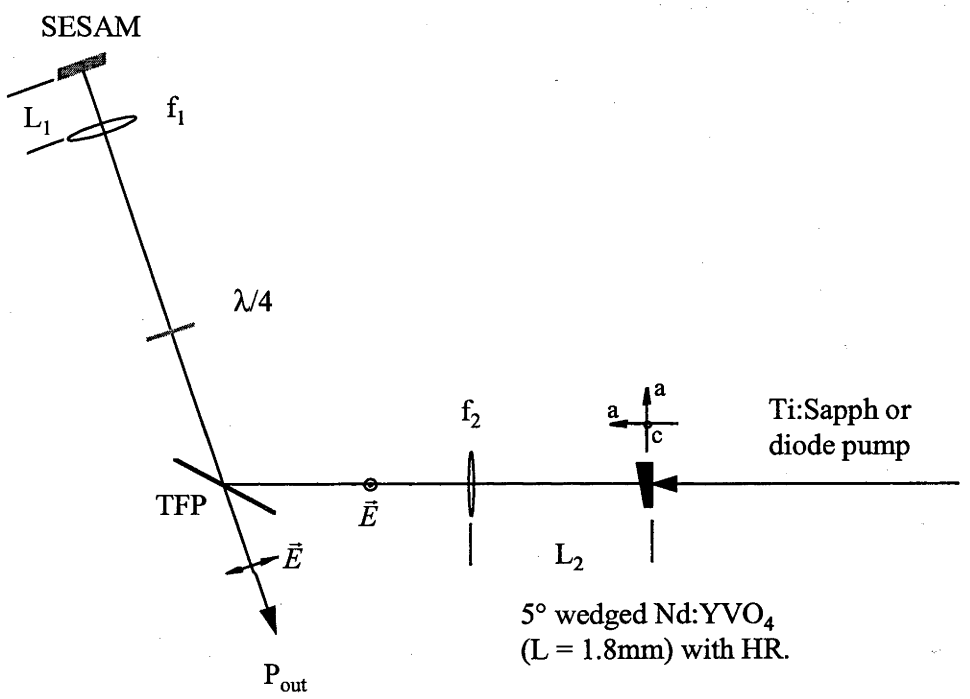

Fig. 5.1 - 1: SESAM mode-locked $Nd:YVO_4$ laser cavity with variable output coupling.

The total length of the cavity was 1.4m, leading to an approximate mode-locking repetition rate of 105MHz. Depending on the pump source, different focal length lenses were used. For Ti:Sapphire pumping f_1 = 38.1mm and f_2 = 100mm were used. Then, for L_1 = 38.8mm and L_2 = 100mm the mode radii are calculated to be 15μm on the SESAM and 56μm inside the gain medium, when operating in the middle of the stability band. The pump mode radius was ≈ 40μm in this case. Due to the large absorption ($\alpha \approx 30cm^{-1}$), no pump light was transmitted through the 1.8mm length of $Nd:YVO_4$ when Ti:Sapphire pumping was used. For diode-pumping, a fibre-coupled 808nm diode provided > 1.2W output from the NA=0.25, d=100μm core. Although the absorption length for diode-pumping is larger ($\alpha_{eff} \approx 12cm^{-1}$) due to the diode's wavelength spread and unpolarised output, it is still possible to achieve good extraction efficiencies by simply butting the fibre output to the end face of the laser crystal, leaving ≈100μm free space. This is largely due to the high gain cross-section in combination with an absorption length of < 1mm. Under the described conditions, a

pump beam radius of < 100μm can be maintained inside the Nd:YVO_4 over a distance of ≈ 500μm. Therefore, the laser mode size must be increased accordingly. It was found that a mode radius of ≈100μm was large enough to prevent instabilities from higher order transverse modes when mode-locking. This results in f_1 = 50mm and f_2 = 125mm with the mode radii of 15μm on the SESAM and 100μm inside the gain medium for L_1 = 51.8mm and L_2 = 110mm and operation in the middle of the stability band.

For mode-locking a number of different high-finesse InGaAs-based SESAMs were available. All samples were grown by MOCVD at high temperatures and included a 25-period GaAs/AlAs Bragg mirror centred at 1064nm, followed by a strained $In_{0.4}Ga_{0.6}As$/GaAs multiple quantum well (MQW) structure with 5nm well thickness and 10nm barrier thickness. These thicknesses are in accordance with Matthews' rules for the prevention of cross-hatching in the strained InGaAs/GaAs system [99]. Although no cross-hatching was observed, an inspection under the microscope revealed a μm-sized roughness which is most likely due to strain. The exciton wavelength in this design was calculated to be around 1100nm, although no room temperature photoluminescence could be detected, and optical absorption measurements of an AR-coated sample showed a pronounced absorption tail without excitonic enhancement. Typical absorption values at λ = 1064nm were ≈ 3000 cm^{-1}. Two samples were then implanted with 350keV As ions of doses $5 \cdot 10^{10}$ and $1 \cdot 10^{13}$ cm^{-2} respectively. The $1 \cdot 10^{13}$ cm^{-2} sample was to be annealed. However, due to technical difficulties, annealing could not be performed and only the unannealed $5 \cdot 10^{10}$ cm^{-2} implanted sample could be used for mode-locking. Three samples remained unimplanted and were coated with 5-, 7- and 9-layer TiO/SiO_2 top mirrors respectively whilst the $5 \cdot 10^{10}$ cm^{-2} implanted sample was coated with a 7-layer top mirror. *Fig. 5.1 - 2a* shows the reflectivity of a typical SESAM sample before and after the top mirror was applied. The low power reflectivity of the sample with a 7-layer top mirror is ≈ 98%.

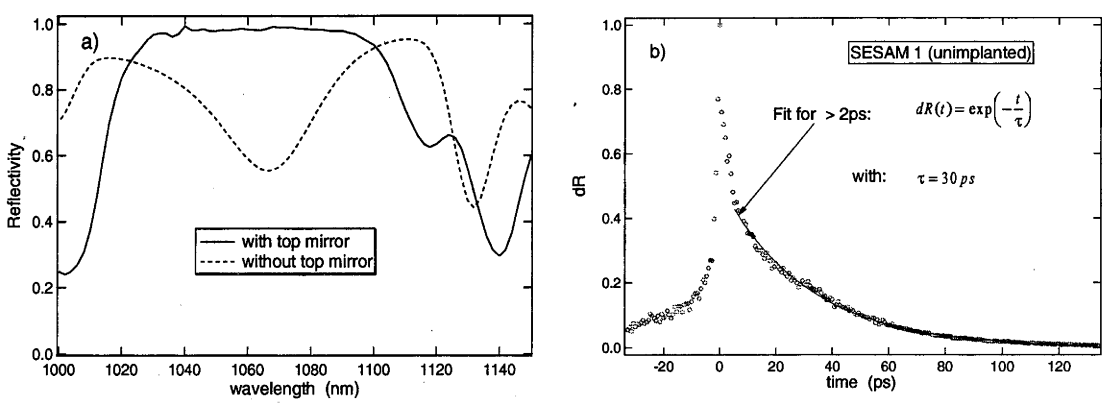

Figs. 5.1 - 2a,b: (a) Low power reflectivities of SESAM without top mirror coating and with 7-layer top mirror. (b) Differential reflectivity of unimplanted SESAM without top mirror, measured with 1.7ps pulses. The single exponential fit, starting at a delay of 2ps, results in a τ_A = 30ps.

In order to determine the SESAMs' carrier lifetime, the 1.7 ps pulses from an actively mode-locked Nd:YLF laser with fibre/grating compressor were used in a pump-probe measurement. The compressed pulses had residual pedestals of 10% with respect to the peak. *Fig. 5.1 - 2b* shows the pump-probe trace of the unimplanted sample without top mirror. Neglecting the effects of the pedestals, a single exponential fit starting at a delay of 2ps gives a recovery time constant of τ_A = 30 ps. From the experience gained with As implanted GaAs of similar thickness (see chapter *4, Fig. 4.3.2 - 2a*), the $5 \cdot 10^{10}$ cm^{-2} implanted unannealed sample (not measured) is expected to display response times of < 1ps, although fluence dependence of the recovery is anticipated.

For the sample without top mirror, a maximum modulation of dR = 10% was measured. This is a relatively low value when compared with that for unimplanted GaAs. In order to estimate the modulation depth of a coated SESAM from that of the uncoated, the low power reflectivity of the coated structure should be known. Usually, measurements of the absolute reflectivity of anti-resonant SESAMs with specular reflectance techniques suffer from errors of around 1%. However, careful modelling of the SESAM structures indicates that the reflectivities at λ = 1064nm are 98%, 99% and 99.6% for the 5-, 7-, and 9-layer top mirror samples. Here, a Bragg mirror reflectivity of 100% was assumed and scattering losses were neglected. Using these low power reflectivities and the modulation data of the uncoated sample, one calculates the maximum modulation depths of 0.31%, 0.15% and 0.06% respectively for the 5-, 7- and 9-layer top mirror SESAMs. However, due to scattering losses (µm-sized roughness, nonideal Bragg mirror), the true low power reflectivities of the SESAMs are likely to be around 1% lower than the calculated values. For the saturation fluence the following argument is employed [22]: The degree to which the top mirror weakens the effect of the field inside the absorber layer is calculated from the ratio of standing wave - absorber overlaps in the two cases. For the 7-layer top mirror SESAM this leads to a factor of

$$\xi = \frac{\int_0^{d_{abs}} |E_{SESAM}|^2 dz}{\int_0^{d_{abs}} |E|^2 dz} = 0.0286 \qquad (5.1 - 2)$$

where E_{SESAM} and E are the electric fields of the standing wave inside the absorber with and without the top mirror respectively. The standing wave power distribution inside the absorber can be calculated, for instance, using matrix methods [37, 39, 40]. Then, the saturation fluence of the sample with top mirror is given by

$$F_{sat}^{SESAM} = \xi^{-1} \cdot F_{sat} \qquad (5.1 - 3)$$

Defining a saturation fluence F_{sat} of the sample without top mirror as the fluence where $dR = 0.5 \cdot dR_{max}$, then $F_{sat}^{7L} = 1.05\, mJ \cdot cm^{-2}$ with $F_{sat} \approx 30\ \mu J \cdot cm^{-2}$. For the 5-layer

and 9-layer samples the ξ-factors become 0.0629 and 0.0130, respectively, with the associated saturation fluences of $F_{sat}^{5L} \approx 480\ \mu J \cdot cm^{-2}$ and $F_{sat}^{9L} \approx 2300\ \mu J \cdot cm^{-2}$.

5.2. Experiment

Most of the data presented in this section were obtained with Ti:Sapphire pumping. This ensured well defined conditions, i. e. constant pump wavelength and absorption when the pump power was varied. It is stressed, however, that diode-pumping resulted in basically equal performance.

In any kind of laser, it is of interest to obtain an estimate of the linear losses, l_0. For a four-level laser like Nd:YAG and Nd:YVO_4, the commonly used technique in this context is the Findlay-Clay analysis [100]. Here, the measured threshold pump powers at different output coupling, normalised by the threshold at zero output coupling, are plotted versus the logarithm of the inverse output coupler reflectivity. The curve is then fitted by

$$\frac{P_{th}}{P_{th0}} = 1 + \frac{1}{l_0} \ln\left(\frac{1}{R_{out}}\right) \qquad (5.2\text{ - }1)$$

which is the theoretically expected behaviour, and which is used to deduce the loss constant per round trip, l_0, from the slope of the graph. Whilst it can be very inconvenient to implement this procedure when different output mirrors have to be used, it is straightforward when for the cavity shown in *Fig. 5.1 - 1* where the R_{out} values are adjustable and calculated using *(5.1 - 1)*. Furthermore, one can calculate the small signal gain constant per round trip, g_0, from the same analysis since at threshold the gain saturation can be neglected. This leads to

$$g_0 = \ln\left(\frac{1}{R_{out} \cdot \exp(-l_0)}\right) \qquad (5.2\text{ - }2)$$

Fig. 5.2 - 1 shows the results of the Findlay-Clay procedure for a dielectric high reflector (HR) in place of the SESAM, as well as for the 7-layer top mirror SESAMs. For convenience, these SESAMs are referred to as SESAM 1 (unimplanted) and SESAM 2 ($5 \cdot 10^{10}$ cm^{-2} As implanted). Clearly, the threshold dependence on $\ln\left(\frac{1}{R_{out}}\right)$ is superlinear whilst that of the small signal gain constant, g_0, is sublinear. The two main mechanisms causing departure from linearity in such situations are upconversion and thermal quenching. From the analyses and data presented in [101] it is obvious that the dominating effect here is upconversion. The latter is in fact clearly visible in Nd:YVO_4 through the emission of yellow fluorescence which is greatly suppressed when lasing is established. Nevertheless, it is possible to obtain the linear losses from *Fig. 5.2 - 1* by taking the slope in the low power limit. This was achieved by performing a quadratic fit of the kind $1 + C_1 \cdot x + C_2 \cdot x^2$ to the data which leads to cavity round trip loss

constants of $l_0^{HR} = 0.042$ for the HR and $l_0^{SESAMs} = 0.052$ for either of the SESAMs. These losses are relatively high and are mainly ascribed to the large number of AR-coated surfaces within the cavity. Given the resolution of the measurements at low power as well as the early departure from linearity, the estimated error of this measurement is ≈ ±0.005. The slope efficiencies obtained for $R_{out} = 92.4\%$ under cw operation using a HR, and for mode-locked operation using SESAMs 1 and 2 were 40% and 34% respectively.

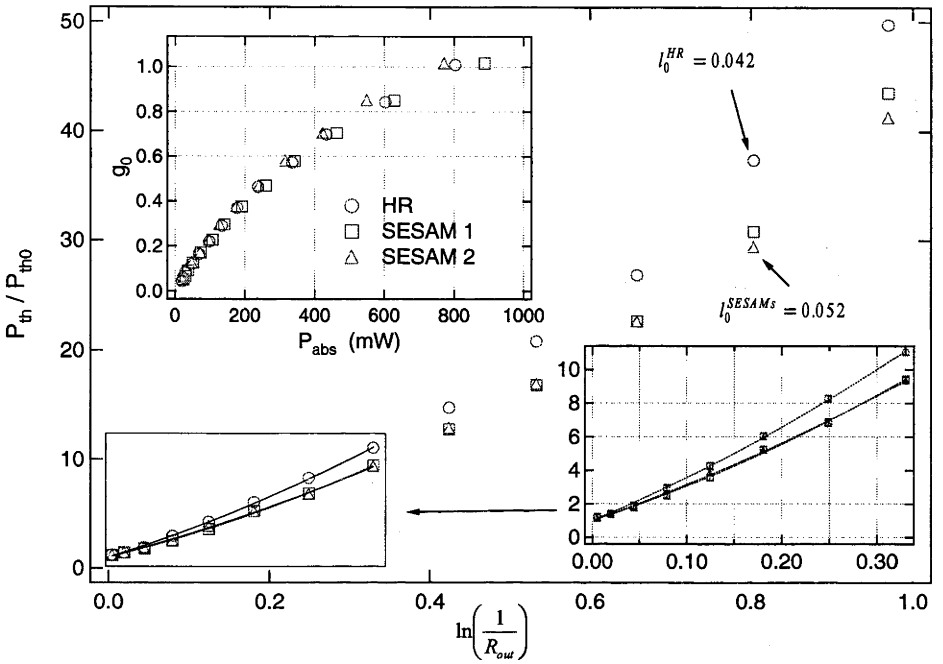

Fig. 5.2 - 1: Findlay-Clay plot of the laser with a HR as well as SESAMs 1 and 2. The threshold behaviour is superlinear due to upconversion in Nd:YVO_4. The linear cavity losses are deduced from the slopes for $R_{out} \rightarrow 1$, found from quadratic fits which are also displayed (fine lines). The insets show the threshold behaviour close to $R_{out} \rightarrow 1$, and the round trip small signal gain constant, g_0, which is sublinear due to the upconversion process.

Mode-locking of the laser was possible with all SESAMs. However, the sample with a 5-layer top mirror caused the laser to operate cw mode-locked only for small values of output coupling but changed to Q-switched mode-locking operation for larger values. On the other hand, the SESAM with a 9-layer top mirror self-started the laser only for small output coupling. Both observations are related to the dependence of the modulation depth on the top mirror reflectivity, outlined before. As was shown in [52] (see also eqn. *(3.2.1 - 1)* and context), for a large modulation depth both the laser gain and the SESAM need to be saturated more strongly in order to avoid Q-switched mode-locking operation. This means that output coupling must be kept low. On the other hand, for too small values of modulation depth, the saturation fluence is too high and the mode-locking driving force of the SESAM, $\frac{dR_{SESAM}}{dI} \cdot I$, is not enough to build-up mode-locking from the mode beating noise, unless the intra-cavity intensity is very high, i. e. for low output coupling. For the laser under consideration, the SESAMs with

a 7-layer top mirror provide a very good compromise and allow stable cw mode-locking for a large enough range of output coupling. Therefore only SESAM 1 and SESAM 2 are considered further on. The appearance of the Q-switched mode-locking instability also depends on the upper state life time of the gain material. Here, Nd:YVO_4 (τ_u = 90μs) fares better than Nd:YAG or Nd:YLF, which both have a τ_u > 200μs, but worse than Ti:Sapphire with an upper state life time of only a few μs.

Fig. 5.2 - 2a depicts the measured output pulsewidths and average output power as a function of the output coupler reflectivity R_{out}. The data were taken over the lasers' self-starting range which usually reached to the point of highest average output power. The SESAM saturation level for P_{abs} = 680mW ranged from 1.5 times ($R_{out} \approx 83\%$) to 10 times ($R_{out} \approx 99.5\%$). Both SESAMs resulted in very similar behaviour, with the shortest pulsewidth ($\tau_{FWHM} \approx$ 6.5ps) achieved for smallest output coupling. With the implanted sample (SESAM 2) in place, the laser was slightly more reluctant to self-start. This is to be expected since implantation decreases the modulation depth as well as the response time, thereby increasing the saturation fluence. *Fig. 5.2 - 2a* indicates that, for high enough small signal gain, it is possible to vary the output pulsewidth by a factor of 2 merely through an adjustment of the output coupling. Using SESAM 1 a factor of 3 was possible, although mode-locking build-up times were in the tens of ms in this case. Disregarding the data points for the smallest output coupling (R_{out} = 0.995), the output power varies only by a factor 2 over the whole range of adjustment. When the output coupler reflectivity was fixed at 92.4% and the pump power, hence small signal gain, was varied, the output pulsewidth also changed (see *Fig. 5.2 - 2b*). However, the variation was smaller in this case.

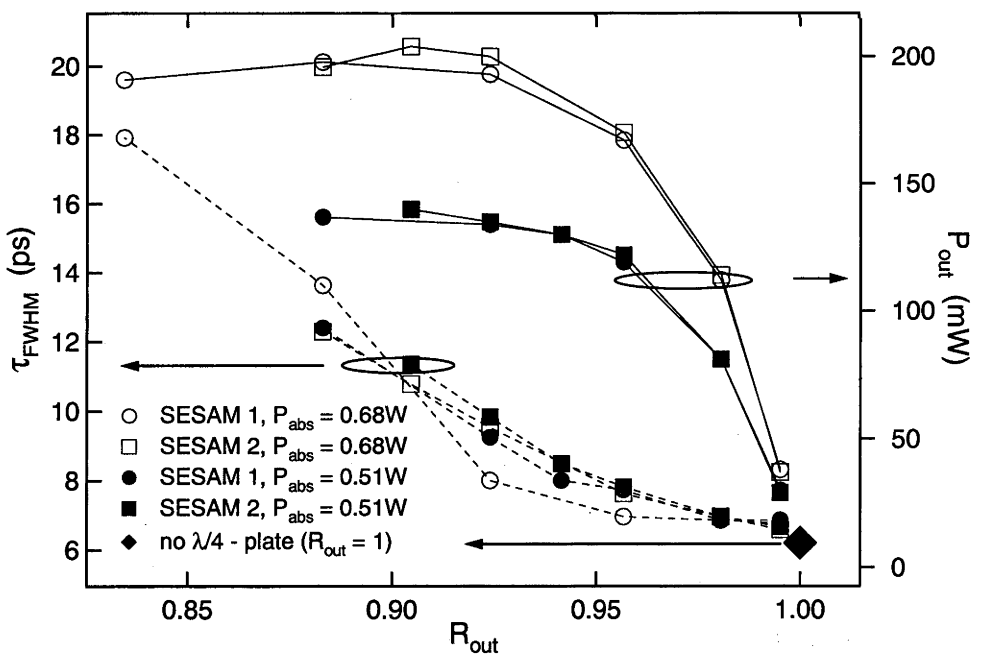

Fig. 5.2 - 2a: Output pulsewidth, τ_{FWHM}, and average output power, P_{out}, for different values of output coupling, R_{out}, and absorbed pump powers, P_{abs}. The data were taken within the self-starting range of the laser.

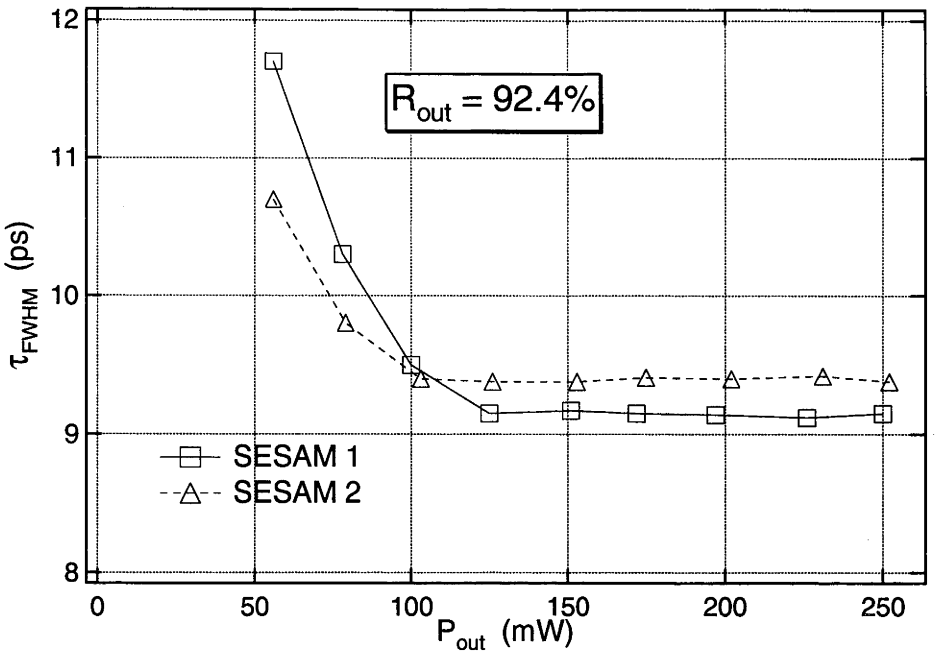

Fig. 5.2 - 2b: Output pulsewidth, τ_{FWHM}, versus average output power, P_{out}. The output coupler reflectivity was fixed at 92.4%.

The τ_{FWHM} values displayed in *Figs. 5.2 - 2a,b* were measured using background free intensity autocorrelation. τ_{FWHM} was calculated from the autocorrelation width, assuming $sech^2$ pulses. However, some of the autocorrelation traces depicted in *Figs. 5.2 - 3a,b* have pedestals and are therefore not $sech^2$ shaped. Furthermore, the traces of the longer pulses could carry small, irregular modulations. These were very sensitive to the tilt angle of the $\lambda/4$ - plate, indicating the presence of etalon effects. Removing the $\lambda/4$ - plate results in a nominal output coupler reflectivity of $R_{out} = 1$. However, both output ports at the TFP display a small leakage (10...20mW for P_{abs} = 680mW), possibly due to a slight impurity in the polarisation state caused by thermally induced stress birefringence. This leakage was enough to perform autocorrelation measurements. For comparison, *Figs. 5.2 - 3a,b* include the autocorrelation for the case when the $\lambda/4$ - plate was removed. In this case the pulses have a τ_{FWHM} = 6.3ps, do not display any pedestals and are very close to the ideal $sech^2$ shape (see *Fig. 5.2 - 3c*). Despite some uncertainty in the pulsewidths introduced by the pedestals, *Figs. 5.2 - 2a,b* indicate a clear trend. Interestingly, the pedestals and modulation were less pronounced in the case of the implanted sample, SESAM 2. This indicates that the faster recovery time of SESAM 2 provides more loss for the low power pedestals than the unimplanted sample. Therefore, despite the generally small difference between the SESAMs' mode-locking performance, a faster recovery time is desirable for the generation of a cleaner pulse shape. Numerical simulations of the fast and slow saturable absorber mode-locking dynamics in the master equation framework [73] led to the same conclusion. However, in the present case it would be preferable to minimise the etalon effects which cause the appearance of the pedestals by optimising the AR-coating of the wave plate. Although no pulse spectra were measured, it is

expected that the pulses have excess bandwidth due to the gain-at-the-end (GE) cavity configuration [97].

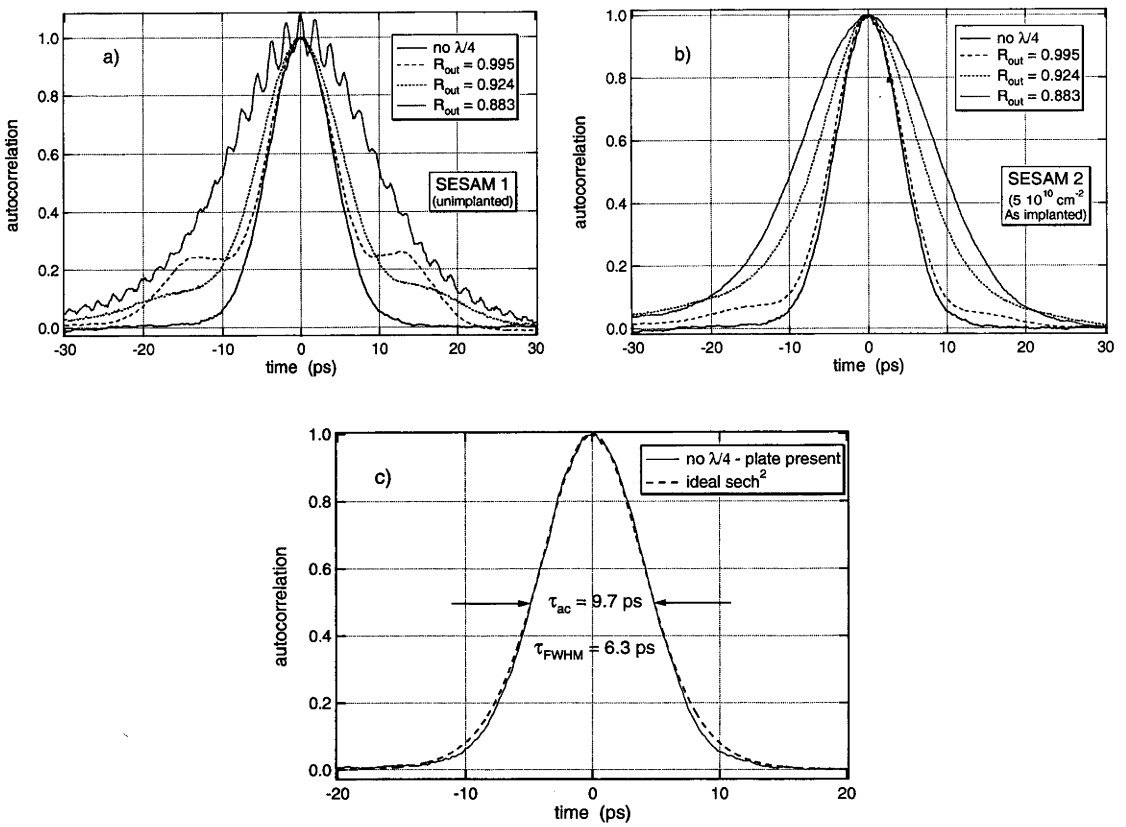

Fig. 5.2 -3a-c: Autocorrelation traces for different output coupler reflectivities R_{out} in the case of (a) mode-locking with SESAM 1 (unimplanted) and (b) mode-locking with SESAM 2 ($5 \cdot 10^{10}$ cm^{-2} As implanted). (c) Autocorrelation for mode-locking without λ/4 plate together with that of an ideal $sech^2$ pulse with τ_{FWHM} = 6.3 ps.

In all applications of cw mode-locking the general stability of the laser is an important issue. Firstly, it is undesirable for a mode-locked laser to operate too closely to the Q-switched mode-locking instability. Secondly, if the mode-locking driving force, $\frac{dR_{SESAM}}{dI} \cdot I$, of a SESAM is not high enough, the laser may take excessive time to build up mode-locking from the mode beating noise or may even need a starting aid (e. g. tapping of an end mirror). In the first case, any slight misalignment usually causes the laser to switch to Q-switched mode-locking operation, whilst in the second case it may simply inhibit mode-locking. A measure for the driving force of a SESAM used in a particular cavity configuration is the mode-locking build-up time τ_{bu}. [52]. *Fig. 5.2 - 4a* shows the build-up times corresponding to the data presented in *Fig. 5.2 - 2a*. τ_{bu} was measured by chopping the cavity, and was defined as the elapsed time between establishing stable pure cw operation and stable cw mode-locking. However, mode-locking build-up is a stochastic process and τ_{bu} a random variable. Therefore, averages of many build-ups were taken. In all cases (except SESAM 1, R_{out} = 83.5% (not displayed in *Fig. 5.2 - 4a*)), the build-up times lay below 1ms and the laser was stable

against mechanical perturbations and slight misalignments. In the case of SESAM 1 and R_{out} = 83.5%, a build-up time could not be determined conclusively, but was larger than 10ms.

As for the Q-switched mode-locking instability, it is common to measure the rf-spectrum of the mode-locked laser [8]. In such a measurement, this instability usually shows up as sidebands of the fundamental cavity frequency which grow from relaxation oscillation noise. Therefore, the degree of sideband suppression is a good indicator for the laser's stability against Q-switched mode-locking. *Fig. 5.2 - 4b* shows a series of rf-spectra for mode-locking with SESAM 2 (P_{abs} = 680mW), for different output coupler reflectivities. For small output coupling (R_{out} = 0.995) no sidebands are observed, whereas for larger values (R_{out} = 0.905) the relaxation oscillation sidebands have risen from the noise and are visible as broad peaks, although still suppressed by -60dBc compared with the peak of the fundamental frequency. Additionally, two narrow sidebands have appeared, suppressed at > -50dBc. For the largest output coupling at which self-starting mode-locking was still possible, the relaxation oscillations have grown to ≈ -50dBc and a very low frequent modulation (≈ 2.8kHz) has appeared. The origin of this slow modulation is not clear. It is interesting to note that, upon varying the output coupling, the laser never actually produced Q-switched mode-locking, regardless of whether SESAM 1 or SESAM 2 was used, and sidebands were always suppressed by greater than 40dBc. This indicates that the 7-layer top mirror SESAM is an ideal choice for mode-locking of Nd:YVO_4.

Finally, cw mode-locking can also be disturbed by the appearance of higher order transverse modes. Usually, one observes a very fast modulation (several tens of MHz) in this case [8]. However, with the laser mode larger than the pump beam inside the Nd:YVO_4 and the cavity in proper alignment, this type of instability was not detected here and the mode was TEM_{00}.

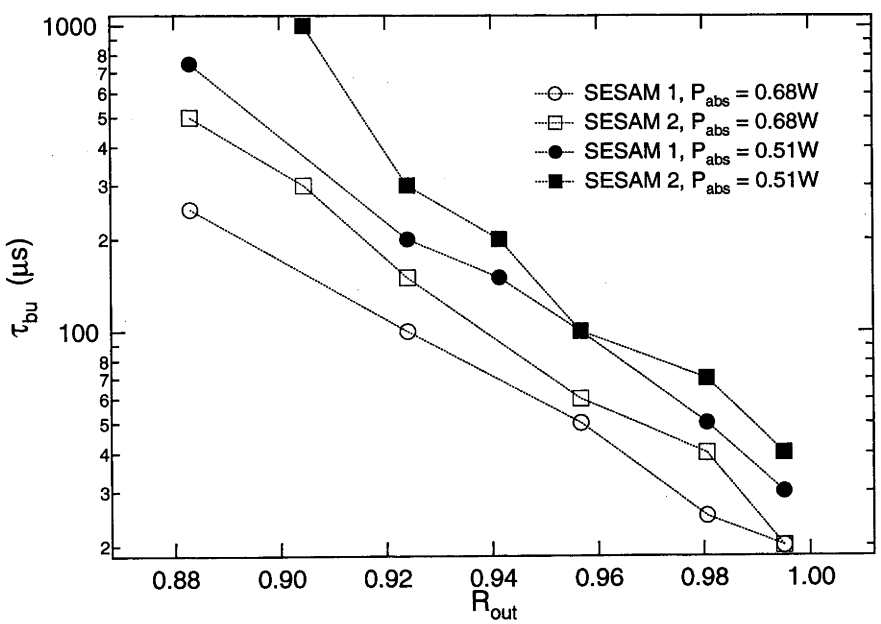

Fig. 5.2 - 4a: Mode-locking build-up times, τ_{bu}, for the data shown in *Fig. 5.2 - 2a.*

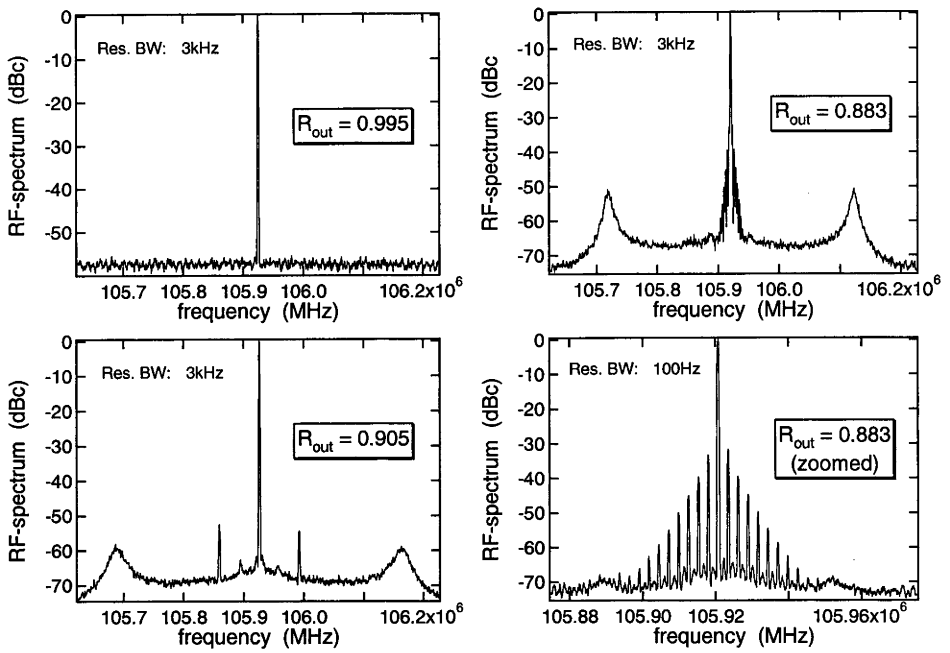

Fig. 5.2 - 4b: rf-spectra of laser mode-locked with SESAM 2 for different output coupler reflectivities. The absorbed pump power was 680mW.

In order to understand the link between output coupling and pulsewidth, it is helpful to realise that in many mode-locked lasers, the dynamic losses of the pulse in the gain filter and the absorber are much smaller than the total linear losses. This is also the case for the present laser where the maximum modulation is ≈ 25 times smaller than the linear losses even for zero output coupling. As a consequence, the saturated gain, hence the average power and the pulse energy, of the laser are more or less determined by the total linear losses, $g \approx l_0$. Therefore, for constant small signal gain, the intra-cavity energy is highest for zero output coupling (R_{out} = 100%) and drops steadily with decreasing values of R_{out}. In terms of the dynamic losses of the laser this means that for smallest output coupling ($R_{out} \approx 100\%$) the absorber saturation is highest and hence the absorber loss is lowest whilst the filter loss can assume its largest value. Therefore, the shortest pulses can be created in this limit. On the other hand, for larger output coupling the intra-cavity energy is lower and the absorber loss is increased whilst the filter loss has to decrease, causing the generation of longer pulses. In order to substantiate these arguments, numerical simulations of the master equation for saturable absorber mode-locking were performed. The relevant equations are *(3.2.2 - 3,4,5)* of chapter *3*, although without dispersion and self-phase modulation. Strictly speaking it is also not necessary to include the gain dynamics, *(3.2.2 - 5)*, in the following simulations since only the steady state pulsewidths and the dynamic losses are of interest. The mode-locking equations were solved for different absorber recovery times, τ_A, each over a range of output coupler reflectivities, R_{out}. The simulation parameters were chosen to match the experimental conditions as closely as possible (see *Table 5.2 - 1*). All simulations started with a 10ps initial condition which was propagated over 50000 round trips after which τ_{out}, P_{out}, and the absorber and filter losses, α and δ, were noted.

Fig. 5.2 - 5a depicts the pulsewidth, τ_{FWHM}, and output power, P_{out}, versus the output coupler reflectivity obtained from the simulations. The dependence of the pulsewidth on the output coupling matches the experimental observations reasonably well. Also, the aforementioned argument concerning the behaviour of the filter and absorber losses is reflected in the simulations (see *Fig. 5.2 - 5b*). For decreasing τ_A the effective absorber saturation decreases whilst the absorber losses increase since the saturation energy of the absorber remained constant in the simulations. This causes the pulsewidth tuning curve to become steeper, possibly indicating a larger tuning range. However, for the practical laser the latter will be limited by the self-starting condition which is likely to be violated for a truly ultrafast absorber.

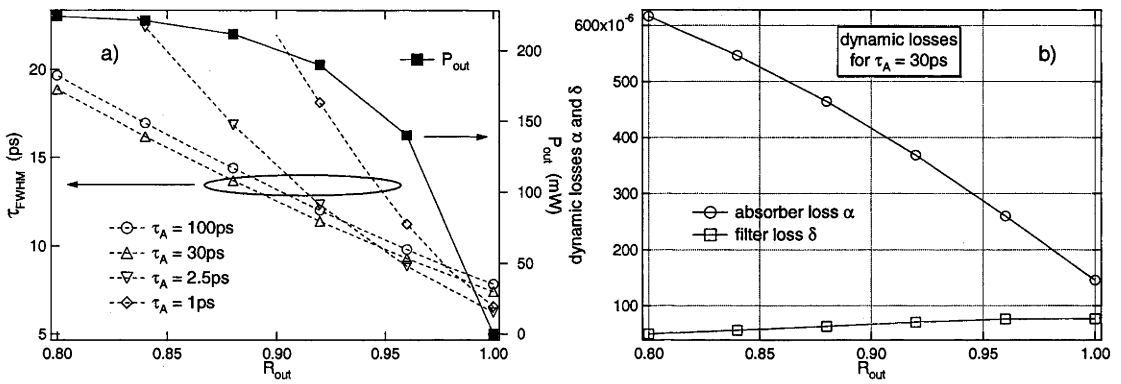

Fig. 5.2 - 5a, b: (a) Dependence of output power and pulsewidth on output coupler reflectivity obtained from mode-locking simulations for different absorber recovery times, τ_A. (b) Absorber loss, α, and filter loss, δ, as a function of output coupling for an absorber recovery time of τ_A = 30ps.

Parameter	Value	Description
l_0	$0.026+\frac{1}{2}\cdot\ln\left(\frac{1}{R_{out}}\right)$	total linear loss per round trip
T_R	9.4ns	round trip time
Ω	$2\pi\cdot 0.5$THz	gain HWHM
q_0	0.001	max. ampl. modulation of SESAM
E_a	7nJ	sat. energy of SESAM
T_a	variable	SESAM recovery time const.
T_g	90µs	upper state life time of Nd:YVO_4
P_g	0.1W	sat. power of Ti:Sapphire
g_0	1.7	small signal round trip gain

Table 5.2 - 1: Relevant parameters for the mode-locking simulations.

Finally, as was mentioned before, the laser performance with diode-pumping was very similar to that with Ti:Sapphire pumping. For an absorbed pump power of P_{abs} = 1W a mode-locked output power of up to 350mW was obtained, and self-starting was possible for output coupler reflectivities as low as 92% using SESAM 2 and 88% using SESAM 1. The build-up times under these conditions were < 5ms. As an example, *Fig. 5.2 - 6* shows the pulsewidth and output power obtained with SESAM 2 for R_{out} values within the self-starting range. It appears that the laser was slightly more reluctant to self-start whilst the range of achievable pulsewidths was slightly larger than for Ti:Sapphire pumping. This was most likely due to the lower small signal gain and higher pump saturation power caused by the increased pump and mode volumes in the gain medium, as well as a slightly larger than calculated SESAM spot size. The diode-pumped laser displayed stability against Q-switched mode-locking and higher order transverse mode, comparable with that for Ti:Sapphire pumping.

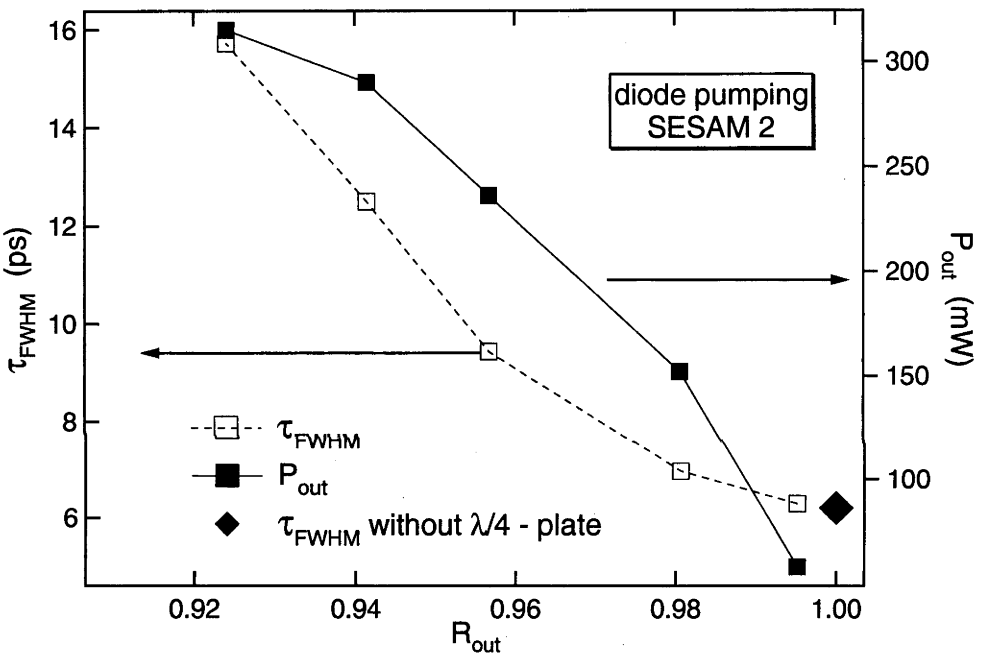

Fig. 5.2 - 6: Output pulsewidth, τ_{FWHM}, and average output power, P_{out}, for different values of output coupling, R_{out}, when the laser was diode-pumped The data were taken within the self-starting range of the laser.

5.3. Summary

A passively mode-locked Nd:YVO_4 laser was presented. Mode-locking was achieved using MOCVD grown high finesse InGaAs SESAMs. Unimplanted as well as Arsenic implanted SESAMs both mode-locked the laser in self-starting fashion. The cavity used focusing lenses instead of mirrors and featured variable output coupling through the use of a thin film polariser (TFP) and a λ/4 plate. Using the Findlay-Clay procedure the linear losses of the laser were found to be relatively high, mainly due to

the large number of AR-coated surfaces. It was shown that SESAMs with a 7-layer top mirror resulted in good self-starting characteristics as well as suppression of the Q-switched mode-locking instability for this cavity design and gain medium. For Ti:Sapphire pumping and output coupler reflectivities > 88% typical mode-locking build-up times were < 1ms and the Q-switching instability sidebands were suppressed by more than 40dBc. The laser produced its shortest pulses ($\tau_{FWHM} \approx 6.5$ps) for an output coupler reflectivity close to 100%. Increasing the output coupling to the self-starting limit increased the pulsewidth by a factor 2. For the unimplanted SESAM a factor 3 could be achieved, however, the build-up times became longer than 10ms in this case. The autocorrelation of the shorter pulses had pedestals whilst the longer pulses could carry small erratic modulation. These effects could be ascribed to nonideal AR-coatings on the $\lambda/4$ plate which would need improvement for better results. Interestingly, the pedestals were smaller when the implanted SESAM was mode-locking the laser, indicating the better pulse cleaning capability of a faster absorber. The dependence of the absorber loss on its saturation level was identified as the main mechanism responsible for the variation of pulsewidth with output coupling. This picture was backed up by numerical simulations of the mode-locking master equation which reflected the experimental observations. For diode-pumping, up to 350mW of mode-locked output power was obtained for an absorbed pump power of 1W. Varying the output coupling within the laser's range of self-starting, the output pulsewidth was variable from 6.5ps - 16ps, i. e. a factor of 2.5. Due to the strong pump absorption and large gain cross-section of Nd:YVO_4 it was possible to pump the laser directly from the fibre output without using re-imaging optics. Using a gain-in-the-middle configuration [97] it could be possible to extend the pulsewidth tunability towards even longer pulses. However, self-starting may also be the limiting factor in this case.

CHAPTER 6

A ND:YVO_4 LASER AMPLIFIER WITH THERMALLY OPTIMISED DESIGN

Section *6.1* provides some introduction and background to the topic of high power, diode-pumped laser amplifiers and explains the need for efficient cooling. A review of the relevant literature is given in section *6.2* where the amplifier design is introduced, and energy gain calculations are performed. Numerical simulations and interferometric measurements are shown in section *6.3* which confirm the thermal management capabilities of the design.

6.1. Background

A general trend in solid state laser technology has been the use of high power laser diodes to replace flash lamps in the pumping of solid state laser materials. Diode-pumping has a number of distinct advantages over the lamp technology. The efficiency of laser diodes is the highest of all lasers currently available (>30%). Their emission wavelength is generally narrow-band (several nm) and can be designed to overlap with the absorption band of common laser materials such as rare earth doped crystals and glasses. This reduces the thermal load on laser crystals considerably. Limited temperature tuning of the emission wavelength further allows one to fine tune for highest absorption efficiency. Due to the directivity of the diode emission, it is possible to collimate, funnel or fibre-couple the pump beams using readily available optics, therefore allowing for better selective energy deposition compared with flash lamps. Last but not least, laser diode arrays for solid state laser pumping are now available which deliver in excess of 100W (cw) or 1kW (pulsed), satisfying the increasing demand for output power in applications where diode lasers cannot be used directly (e. g. machining, gravitational wave detection, ...).

In low power applications, the cooling of diode-pumped solid state laser materials is generally not very difficult. This is due to the relatively high stimulated emission cross-section of many laser crystals in conjunction with their good thermal conductivity. The lasing threshold is reached easily and the slope efficiencies are high with optimised cavity designs. The classical example of such a laser crystal would be Nd:YAG (Yttrium Aluminium Garnet). However, due to the high powers which have become available from pump-diode lasers, proper cooling of the solid state laser material is still an important issue in practice. There are a number of detrimental effects on laser performance caused by large temperature gradients due to poor thermal management. These include refractive index gradients due to the crystal's thermal index change dn/dT. The latter results in a thick-lens characteristic and leads to the effect of 'thermal lensing' which can distort the laser beam severely [102]. Temperature gradients also lead to thermal stress and the mechanical distortion of the

laser material [103], which influence the beam propagation (depolarisation) via the stress optic tensor $B_{i,j,k,l}$, strain $\varepsilon_{i,j}$, and thermal expansion α, of the material. In the worst case, thermal stress can result in fracture. Unfortunately, not all solid state laser materials which have good lasing properties also have good thermal properties. As an example, the laser crystals Nd:YAG and Nd:YVO_4 are compared in *Table 6.1.1*. Clearly, the laser properties of Nd:YAG are inferior to those of Nd:YVO_4. The latter features much higher broad band absorption and a larger $\sigma \cdot \tau$ factor. Furthermore, its thermal index change dn/dT for c-polarised light (preferred for lasing) is three times less than that of Nd:YAG. However, in high power applications, the advantages of Nd:YVO_4 are compromised by its poor thermal conductivity. Therefore, a design incorporating good thermal management is extremely important for this laser crystal.

Property	*Nd:YVO_4*	*Nd:YAG*
λ_{pump} [nm]	808.5	807.5
α_{peak} [cm^{-1}]	31.2 (c), 9.2(a)	7.1
$\Delta\lambda_{abs}$ [nm]	≈16 (c)	≈2.5
σ_l [$10^{-19} \cdot cm^2$]	25 (c)	6
τ_u [μsec]	90 (1.1 atm. %)	230 (0.85 atm. %)
$\sigma_l \cdot \tau_u$ [$10^{-16} \cdot cm^2 \cdot \mu sec$]	2.25	1.38
n(λ=1.06μm) n(λ=0.63μm)	2.16 (c), 1.96 (a) 2.21 (c), 1.99 (a)	1.82 -
dn/dT [$10^{-6} \cdot K^{-1}$]	3 (c), 8.5 (a)	9
α_{th} [$10^{-6} \cdot K^{-1}$]	11.4 (c), 4.4 (a)	7
κ_{th} [$W \cdot K^{-1} \cdot m^{-1}$]	5.1	13
Mohs hardness	≈4.5	≈8.5

Table 6.1.1: Values of some important laser and thermal properties of Nd:YVO_4 (positive uniaxial) and Nd:YAG (cubic) [104, 105].

In view of Electro Optic Systems' applications, it was the aim here to develop a diode-pumped laser amplifier head for use in satellite laser ranging systems. The head should be as compact as possible and capable of amplifying pulses in the order of 10ps to the mJ level at repetition rates of up to several kHz. To avoid the high costs of regenerative amplification, the gain should be as high as possible, allowing the use of a linear configuration. The laser wavelength was to be ≈1.06μm, matched by a suitable oscillator (see chapter 5). Given these requirements it was decided to take advantage of

the good lasing properties of Nd:YVO_4 (strong and broad-band pump absorption, high gain) and develop a suitable cooling arrangement which could minimise the deficiencies from poor thermal conductivity. Using computer simulations and interferometry, it will be shown in the following sections that an amplifier design was found which incorporates very efficient thermal management for Nd:YVO_4, and which is scalable to higher powers. Although actual lasing experiments could not be performed within the time frame of this PhD programme, the design prototype has the potential of producing mJ pulse energies in a double pass configuration, at the required repetition rates.

6.2. Design

It has been shown that slab laser designs, in particular zig-zag slabs, have advantages over laser rod systems. In the slab geometry, symmetry can eliminate stress induced depolarisation and the zig-zag optical path cancels thermal lensing to first order in the plane perpendicular to the zig-zag [102, 103]. Furthermore, the energy extraction efficiency achievable is higher when compared with rod systems [112]. Due to their rectangular cross section, slab lasers are most conveniently side pumped using laser diode bars or arrays. A somewhat degenerate variant of the zig-zag slab is the grazing incident slab design [106]. Here, the laser beam only bounces once, at a very shallow angle, off the pumped surface of the slab. This geometry is particularly interesting for very strongly absorbing, high gain laser materials like Nd:YVO_4, allowing very good energy extraction. For increased energy extraction efficiency in zig-zag slabs operating in TEM_{00}-mode, the multiple-pass configuration was proposed [107]. In this scheme, a second or even third pass is introduced into the slab at a different angle to extract the stored energy from regions not covered by the first pass.

For the cooling of high power lasers and laser amplifiers, two methods are available. These are either purely conductive or involve liquid cooling of the laser material. The simplest technique to conductively cool a slab laser is to bond suitable heat sinks to the unpumped sides of the slab [115]. This results in reasonably good performance, especially for laser crystals with high thermal conductivity. However, in poorly conducting materials this scheme can cause a large temperature rise inside the slab if the laser mode is to stay at a distance from the cooled surface, and pump and mode are optimised for overlap. Cooling of the pumped surfaces has been used extensively in both lamp and diode-pumped rod and slab systems. The advantage of this method is that heat removal occurs preferentially at the location of its deposition, namely the pump input surface. Clearly, for a low conductivity laser crystal with high pump absorption, such as Nd:YVO_4, this would be an ideal cooling method. Cooling through the pumped surface involves water cooling in most cases, since highest possible transmission of the cooling medium is imperative. The performance of such systems is impressive, and 40W cw, TEM_{00} output from a Nd:YAG slab laser have been shown [111]. However, the sealing of the coolant circulation and the prevention of evanescent leakage of the laser mode due to turbulent flow at the surfaces of total internal reflection (TIR), pose considerable problems. Furthermore, some laser

materials posses a very poor water durability and can therefore not be water cooled directly. As a consequence, a number of alternative pump face cooling methods were developed. Most notably these involve the use of highly transparent and thermally conductive plates such as sapphire. Heat is conducted away from the laser material towards the sapphire and heat sink via an 'elastic layer' [108], a layer of silicon gel [109] or a thin film of air [113]. In another case a layer of unspecified thickness of UV curable optical glue was used to bond sapphire to a Cr:LiSAF slab [110].

The design, presented here, incorporates a Nd:YVO_4 slab which allows the use of multiple zig-zag passes in order to maximise the extraction efficiency. It is pumped from two sides using arrays of laser diode bars. Cooling is achieved conductively through the pumped surfaces using sapphire as the transparent heat conductor. This is the most suitable method for the strong absorption and poor thermal conductivity of Nd:YVO_4 whilst the difficulties of direct water cooling are avoided. *Figs. 6.2 - 1a-c* show the various aspects of the design.

A key part of this design lies clearly in the use of an appropriate method for bonding between the Nd:YVO_4 and the sapphire. It was intended to attempt a diffusion bond [114] between the two materials, whilst the use of optical cement was a fall-back option. In a diffusion bond, optical contact is established at first to provide the Van der Waals bonding forces necessary to hold the materials together during the final high temperature diffusion bonding cycle. Using this method, composites of similar materials such as doped and undoped YAG or glass [113] have shown superior strength and very low scattering losses at the interface. Diffusion bonding is a proprietary process of Onyx Optics, Dublin, Ca. who advised that bonding of crystals such as Nd:YVO_4 and sapphire had not yet been tried, and that there was a 50% chance of failure due to the dissimilarity of thermal expansion coefficients of the two crystals. The following bonding attempt indeed failed, leaving the Nd:YVO_4 shattered into little pieces. Therefore, an optical glue had to be used for the bonding.

The Nd:YVO_4 crystal has the dimensions 12×8×1.8 mm^3 and is coated for anti-reflection and high reflection respectively on the two 8×1.8 mm^2 sides. The sapphire slabs were cut to the size of 12×8×0.63 mm^3. The two fast axis collimated bars on each laser diode array have a separation of 3mm, and their output beams are brought to an overlap inside the Nd:YVO_4 using an AR-coated beam steering optic. The latter is bonded to a $\lambda/2$ plate to turn the LD-polarisation parallel to the crystallographic c-axis (vertical in *Fig. 6.2 - 1a*) of Nd:YVO_4 for highest pump absorption. The laser diode arrays and beam steering optics are mounted separately from the laser head. Alternatively, or in a case where more than two bars per LD are used, an optical duct can be used to deliver the pump light. The Nd:YVO_4-sapphire composite is held with two spring loaded bolts from the top and bottom each, between the copper braces which have a horizontal opening tolerance of ±100µm. This allows basically stress free mounting and good control on the elevation angle of the composite.

The zig-zag modes of the amplifier are confined to the Nd:YVO_4 through total internal reflection (TIR) at the Nd:YVO_4-glue interface. The TIR condition leads to a maximum internal angle of incidence with respect to the z-axis (see *Fig. 6.2 - 1b*) of

$$\phi_{\max}^{\text{int}} = \arccos\left(\frac{n_{glue}}{n_{YVO}}\right) \qquad (6.2 - 1),$$

which in turn defines the maximum external angle of incidence

$$\phi_{\max}^{ext} = \arcsin\left(n_{YVO} \cdot \sin\left(\phi_{\max}^{\text{int}}\right)\right) \qquad (6.2 - 2)$$

From *(6.2 - 2)*, the external angles for the zig-zag modes of the composite are then calculated using

$$\phi^{\text{int}} = \arctan\left(\frac{N \cdot t_{YVO}}{l_{YVO}}\right) \qquad (6.2 - 3)$$

for the internal angles. Here, N is the number of bounces per Nd:YVO_4-glue interface, t_{YVO} and l_{YVO} are the Nd:YVO_4 dimensions along the x- and z-axes respectively. For the given dimensions and refractive indices (t_{YVO} = 1.8mm, l_{YVO} = 12mm, n_{YVO} = 2.16, n_{glue} = 1.5), eqns. *(6.2 - 1-3)* result in a maximum of N = 6 bounces off each interface. Only N = 1 and 2 are feasible solutions, however, since there, the external angles of ϕ_1 = 18.7º and ϕ_2 = 38.4° can be covered reasonably well by an anti-reflection coating on the input face.

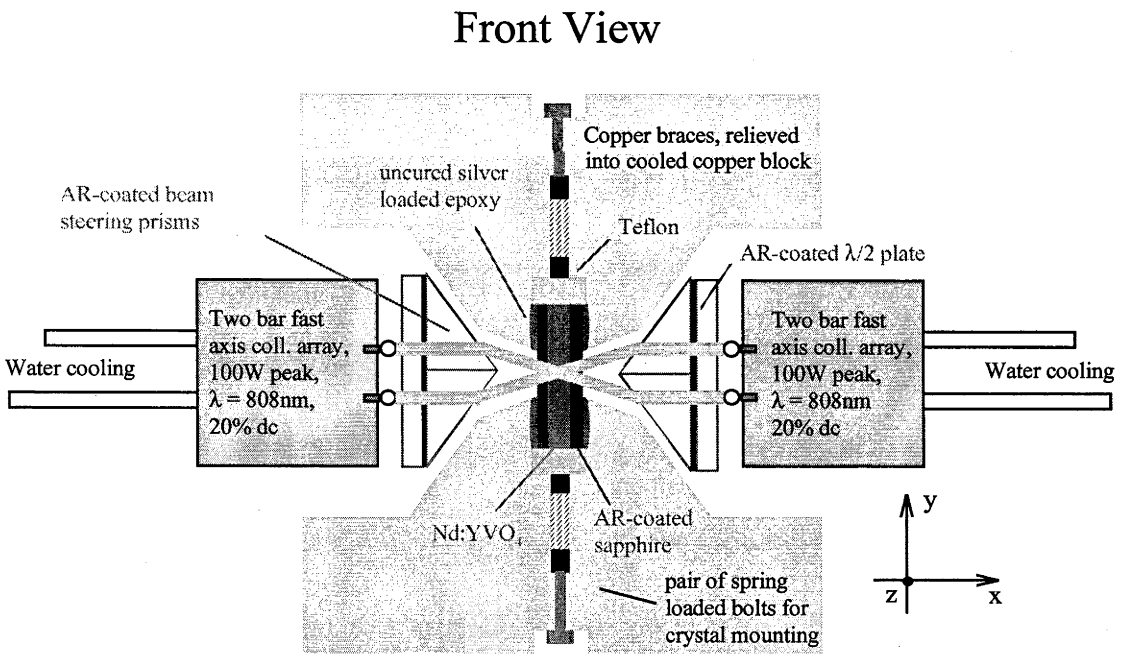

Fig. 6.2 - 1a: Front view of Nd:YVO_4 amplifier head. The crystallographic c-axis lies in the vertical plane. The black lines between the Nd:YVO_4 and sapphire, as well as the λ/2 plates and the prisms, indicate the optical glue (SK-9, Summers Lab). The copper block is not shown.

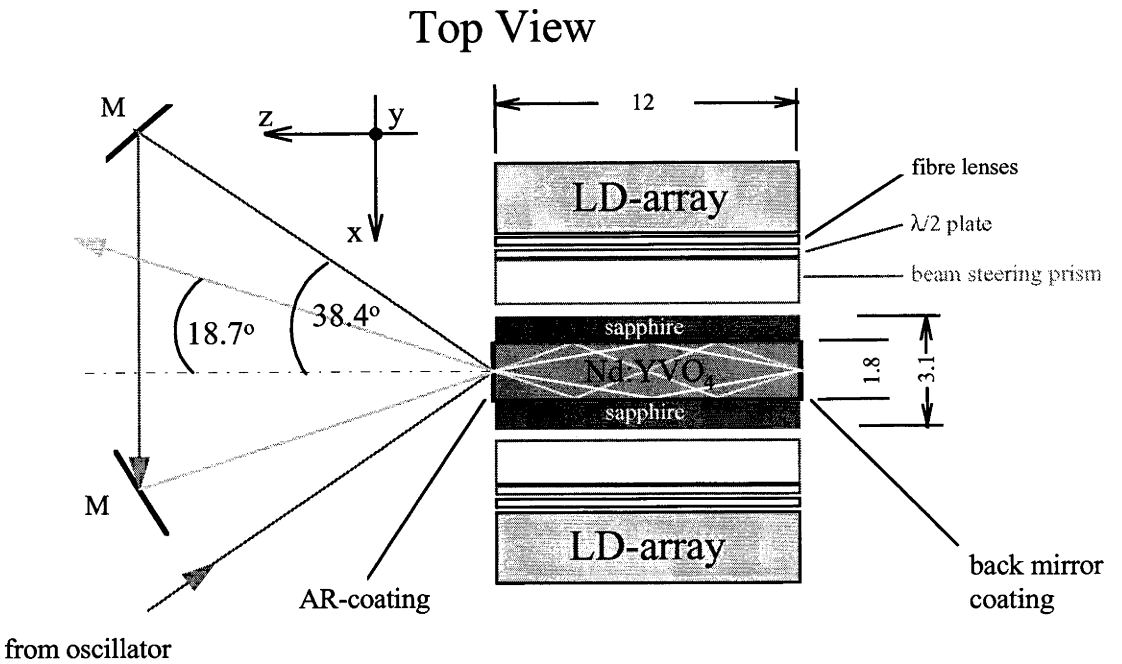

Fig. 6.2 - 1b: Top view of Nd:YVO_4 amplifier head without the copper. Indicated are the two practicable zig-zag modes for this design.

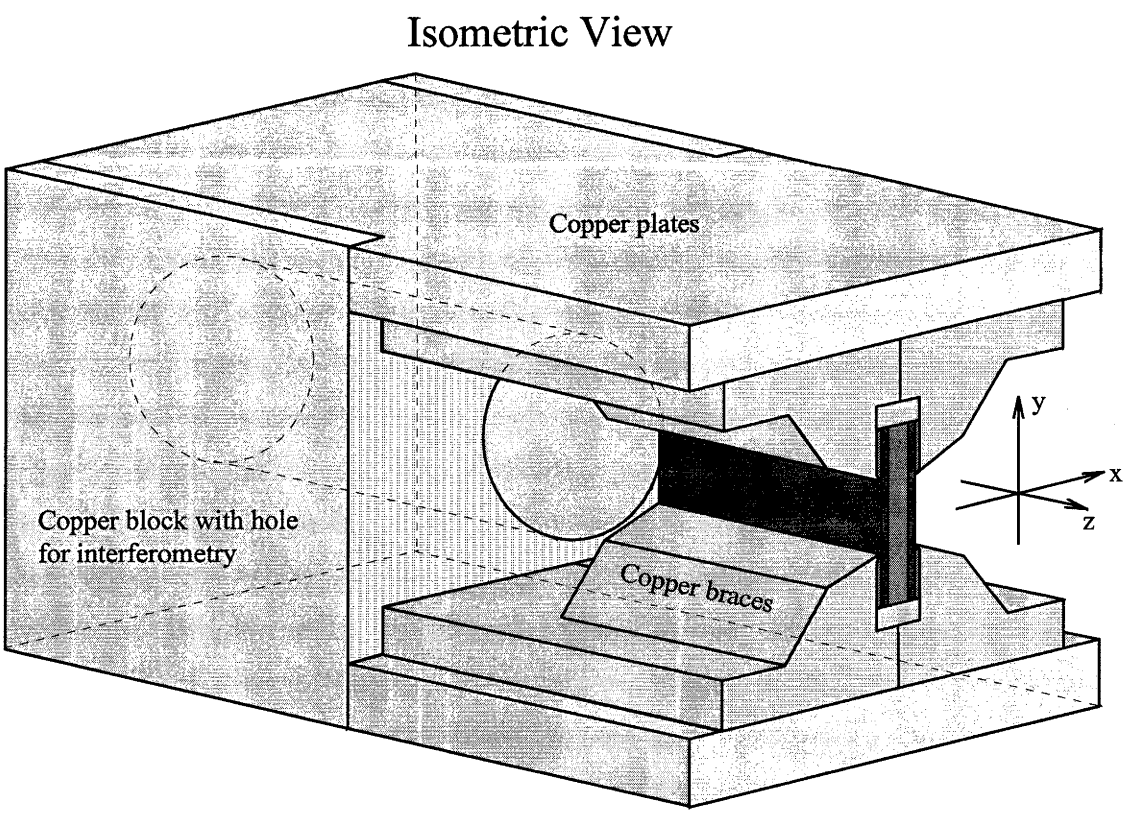

Fig. 6.2 - 1c: Isometric view of Nd:YVO_4 amplifier head. The Nd:YVO_4, sapphire, silver loaded epoxy and Teflon spacers are shown in the same colours as in *Fig. 6.2 - 1a.* The copper block has a hole in order to allow interferometry.

Thermal contact between the composite and the copper braces is established using the glue component of a two-component silver loaded (>70%) epoxy (Radio Spares) which can easily be removed with an appropriate solvent, if needed. No visible flow of the epoxy could be detected over extended periods. However, its viscosity is low enough to allow application into the slightly grooved gap between the copper braces and the composite using a pressurised, thin syringe. Before insertion, the AR-coated sapphire was roughened for good contact with the epoxy, carefully sparing the pump input region. If necessary, the head can be disassembled, cleaned and reassembled in 1-2 hours.

In order to achieve a minimal temperature gradient across the glue layer, it is necessary to make it as thin as possible. However, since the glue is used as the low index dielectric for total internal reflection it should not be much thinner than 1 μm to prevent evanescent coupling into the sapphire. Also, the durability of the cement under high intensity irradiation (≈2kW·cm^{-2} cw) must be guaranteed, and absorptive and scattering losses need to be low. Experiments were therefore conducted with 8×12 mm^2 samples prepared from glass slides and glued together using a number of different optical glues. It was found that the following procedure leads to a very satisfactory bond:

> Under clean room conditions, using a syringe, a droplet of Summers Lab single component, UV-curable optical cement SK-9 (viscosity: 80-100cps, n = 1.5, κ = 0.17 W·m^{-1}·K^{-1}) is applied to one of the solvent-cleaned (Acetone -> Methanol -> Isopropanol) surfaces. The quantity should be appropriate to form a little island of approximately 2.5mm diameter on the glass (or Nd:YVO_4). Then the second component of the composite is placed on the island without applying pressure. Usually, it takes a few minutes for the capillary force to fill the complete gap between the two components with glue, and for the odd gas bubble to disperse. The latter can be observed under the microscope, if necessary. In case of a persistent bubble the components can be cleaned and the procedure repeated. If the interface is satisfactory the composite can be cured for 1 hour under a 365nm UV lamp.

Fig. 6.2 - 2 shows a scanning tunnelling micrograph (STM) of a typical glue layer between two glass slides, achieved with this method. Depending on the exact amount of glue, the layer thickness can vary between 1 and 10 μm. This thickness is well beyond the evanescent coupling length for the zig-zag modes but is nevertheless thin enough to prevent large temperature gradients across it, as will be shown in the next section.

The optical quality of the layers is very good. There are typically only a few small scattering centres visible across the whole 8×12 mm^2 interface, when illuminated with light from a HeNe laser. When inserted into a mode-locked pulse train (λ = 808nm) with an average power density of 25 kW·cm^{-2} (10 times higher than anticipated in the current design) and pulse peak powers of 10 GW·cm^{-2} (τ_{FWHM} = 100fs), there was

no visible scattering from the interface and no heating could be detected. After 1 hour of illumination, the layer was completely unaffected.

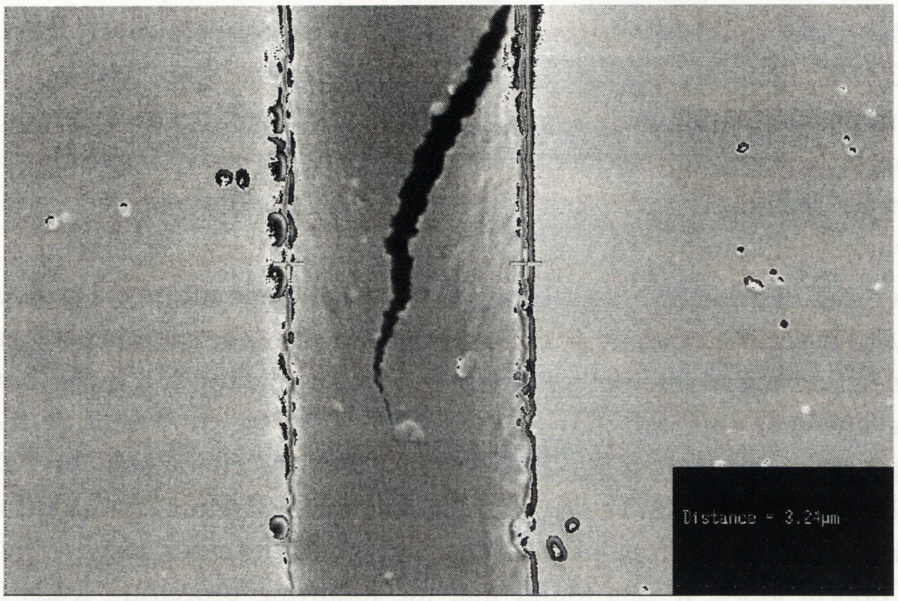

Fig. 6.2 - 2: Scanning tunnelling micrograph (STM) of a 3.24µm thick glue layer (Summers Lab, SK9) between two glass slides. This layer was created using the above procedure.

Finally, the gain and output energy of the amplifier are calculated for double sided pumping. The small signal gain constant g_0 in the Nd:YVO_4 crystal depends on the coordinates (see *Figs. 6.2 -1a-c*) x and y, but not on z since the emission from the laser diode arrays is assumed constant along the z-axis. Therefore, g_0 can be written as

$$g_0(x,y) = N_u(x,y) \cdot \sigma_l \qquad (6.2 - 4)$$

where σ_l is the stimulated emission cross-section and N_u is the population inversion. In a four-level laser medium like Nd:YVO_4, used for short (< 1ns) pulse amplification, the inversion following a rectangular pump pulse of length τ_p is given by

$$N_u(x,y) = \frac{\eta_B \cdot \lambda_p \cdot \tau_u}{c \cdot h} \cdot \left[1 - \exp\left(-\frac{\tau_p}{\tau_u}\right)\right] \cdot \Phi_p(x,y) \qquad (6.2 - 5)$$

with the upper state life time τ_u, the Boltzmann partitioning factor η_B due to the splitting of the two meta-stable levels, and the pump photon density $\Phi_p(x,y)$. In Nd:YVO_4 the meta stable levels are separated by 14 cm^{-1}. This results in a partitioning factor of η_B = 0.52 for the lower, lasing, level which is not replenished through thermalisation during the pulse and for short delays between multiple passes. Assuming a Gaussian distribution of the pump intensity along the y-axis, the suitably normalised pump photon distribution becomes

$$\Phi_p(x,y) = \frac{P_{abs} \cdot \exp\left(-8 \cdot \frac{y^2}{t_{y,pump}^2}\right) \cdot \left[\exp(-\alpha \cdot t_{YVO}) \cdot \exp(\alpha \cdot x) + \exp(-\alpha \cdot x)\right]}{d_x \cdot d_y \cdot d_z} \qquad (6.2\text{-}6).$$

Here, α is the pump absorption, $t_{y,\,pump}$ is the $1/e^2$ pump stripe width and t_{YVO} is the thickness of the laser crystal in x-direction. d_x, d_y and d_z are effective widths obtained from the normalisation relations and are given by

$$d_x = \frac{2}{\alpha} \cdot \left[1 - \exp(-\alpha \cdot t_{YVO})\right], \qquad d_y = \sqrt{\frac{t_y^2 \cdot \pi}{8}} \qquad \text{and} \qquad d_z = 1.2cm \qquad (6.2\text{-}7).$$

Further, P_{abs} is the total absorbed power, calculated from

$$P_{abs} = 2 \cdot P_{pump} \cdot \left[1 - \exp(-\alpha \cdot t_{YVO})\right] \cdot T_{pump} \qquad (6.2\text{-}8)$$

with the peak pump power P_{pump} of one array and the transmission factor T_{pump} due to the sapphire-glue and glue-Nd:YVO_4 interfaces.

For the energy output calculations, the small signal gain $g_0(x,y)$ is then averaged over the signal beam shape in both x- and y-directions. Note, that this average still depends on x_0, the centre of the beam, since the beam assumes different x-positions whilst travelling through the amplifier. After a final averaging in x_0 the small signal gain constant becomes

$$\langle g_0 \rangle = \frac{8 \cdot \int_0^{t_{YVO}} \int_{-\infty}^{\infty} \int_{-\infty}^{\infty} g_0(x,y) \cdot \exp\left(-\frac{8 \cdot y^2}{t_{y,sig}^2} - \frac{8 \cdot (x - x_0)^2}{t_{x,sig}^2}\right) dx dy dx_0}{\pi \cdot t_{YVO} \cdot t_{x,sig} \cdot t_{y,sig}} \qquad (6.2\text{-}9)$$

with the signal beam diameters $t_{x,\,sig}$ and $t_{y,\,sig}$. Following [116] the single pass output energy of a pulse propagating through the amplifier is given by

$$E_{out} = E_{sat} \cdot \ln\left[1 + \left(\exp\left(\frac{E_{in}}{E_{sat}}\right) - 1\right) \cdot \exp\left(\langle g_0 \rangle \cdot 2 \cdot d_z\right)\right] \qquad (6.2\text{-}10)$$

where

$$E_{sat} = \frac{c \cdot h \cdot A_{eff}}{2 \cdot \sigma_l \cdot \lambda_s} \qquad (6.2\text{-}11)$$

is the saturation energy, calculated using the beam area A_{eff}. The factor of 2 appears in the definition of E_{sat} since the terminal level of the laser remains effectively unemptied during the pulse and after the short delay between first and second pass. Using *(6.2-9-11)* to calculate output energies is not strictly valid for zig-zag slabs since the beam interacts twice with the inversion near the points of total internal reflection. However, in a second pass, entering the amplifier at a different angle, the beam interacts with

some previously unbleached inversion. These effects may cancel each other to first order and one can expect a good estimate for the output energy from the calculation. *Fig. 6.2 - 3a* shows the calculated small signal gain distribution $g_0(x,0)$ (peak along y-axis), the small signal gain averaged over the signal beam shape in both x- and y-directions $g_0(x_0)$, and the average small signal gain $\langle g_0 \rangle$ for the parameters listed in the caption. Obviously, the gain near the pump entrance faces can be very high, possibly limiting the energy extraction through amplified spontaneous emission (ASE), in which case the pump beam would need to be widened. Although small signal gain constants as high as 25 cm^{-1} have been reported [106] before ASE became detrimental in a Nd:YVO_4 amplifier, this depends also on the geometry and needs to be considered separately for each case. Assuming a typical mode-locked pulse of energy E_{in} = 1nJ the amplifier produces E_{out} = 1.73mJ for a double pass, as shown in *Fig. 6.2 - 3b*. The extraction efficiency is then 64% of the usefully stored energy of 2.72mJ. Using E_{in} = 100nJ (from a q-switched μ-laser, for instance) still requires a second pass for efficiency and produces 2.65mJ of output at an extraction efficiency of 97%.

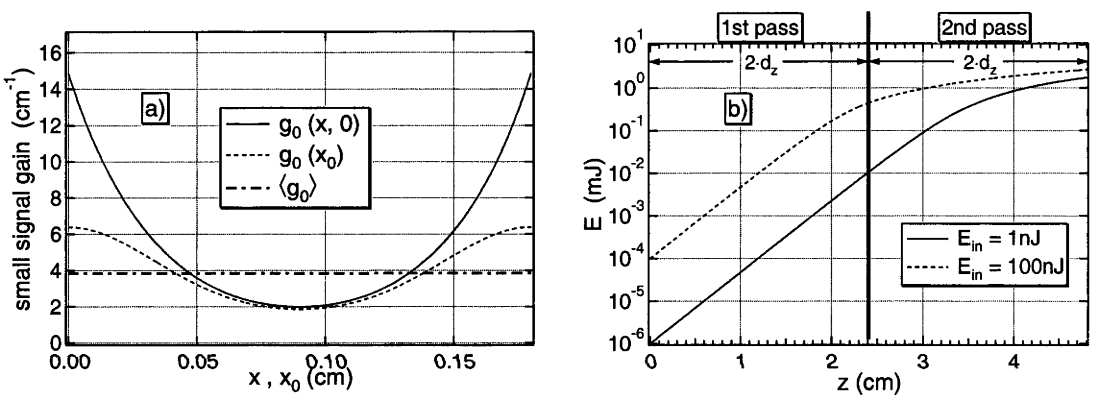

Fig. 6.2 - 3a, b: (a) Small signal gain distribution $g_0(x,0)$ (peak value along y-axis), small signal gain averaged over the signal beam shape in both x- and y-directions $g_0(x_0)$, and the average small signal gain $\langle g_0 \rangle$. (b) Single and double pass energies for 1nJ and 100nJ input energy. The calculation assumed the following parameters: α = 30 cm^{-1}, τ_u = 90μs, P_{pump} = 100W, T_{pump} = 0.96, τ_p = 150μs, $t_{y,pump} = t_{x,sig} = t_{y,sig}$ = 0.1cm.

6.3. Simulations and Experiment

In order to verify the thermal management capability of the amplifier design, numerical simulations of the temperature distribution T(x,y) were performed. The relevant equation is the steady state heat equation

$$\nabla \bullet \left(\kappa(x,y) \cdot \vec{\nabla} T(x,y)\right) + Q(x,y) = 0 \qquad (6.3 - 1)$$

with the density of absorbed heat Q(x,y) and the thermal conductivity κ(x,y). Due to the pump geometry, the temperature distribution is independent of the z-coordinate. For the boundary conditions it was assumed that the copper block was fixed at 20°C, and the ambient air temperature was also 20°C. *Eqn. (6.3 - 1)* was solved using the

finite difference method of energy balance [117]. In this method the energy balance equations for the nodes in the numerical grid of size m×n are combined for the given geometry and boundary conditions to form a system of m×n equations. The system is then solved for the temperature at each node using the Sparse Matrix facility of MATLAB®. *Figs. 6.3 - 1a-g* show the temperature distribution obtained from such calculations (parameters see caption) for different glue thicknesses *(a, b, c)*, sapphire thicknesses *(d, e)*, no sapphire present *(f)*, for a side cooled 1.8×1.8 mm² slab of Nd:YVO_4 *(g)*, and with sapphire but smaller absorption constant *(h)*. The numerical grid covers the Nd:YVO_4, glue, sapphire, air in front of pump entrance window and a small part of the heat sink copper.

a)

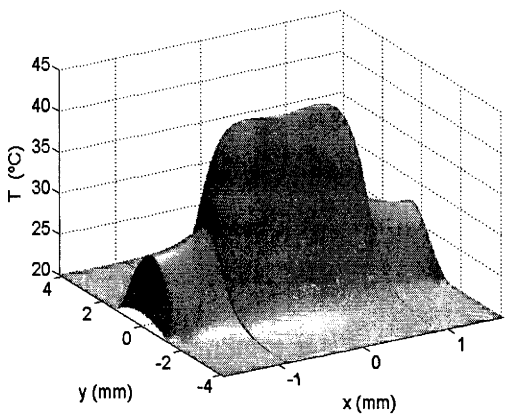

b)

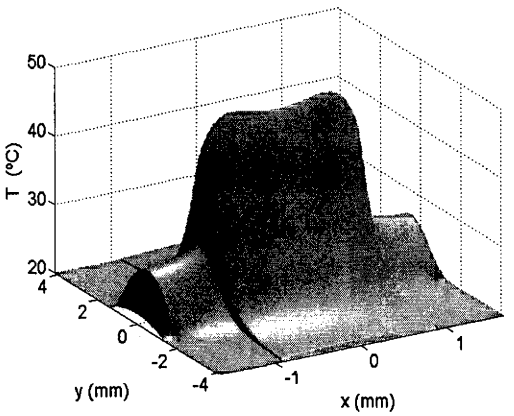

c)

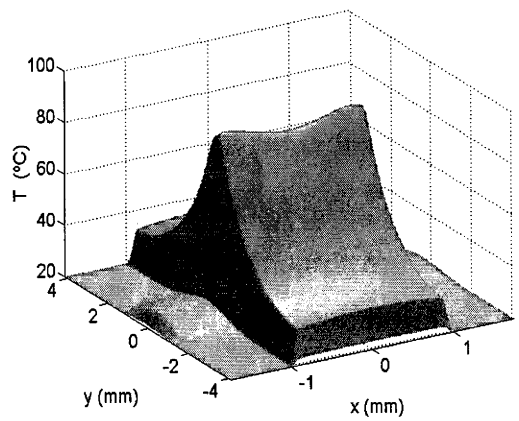

d)

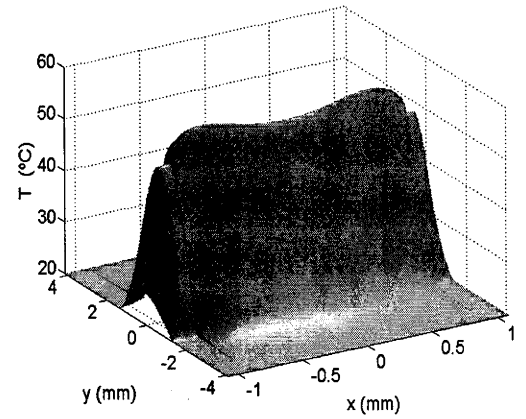

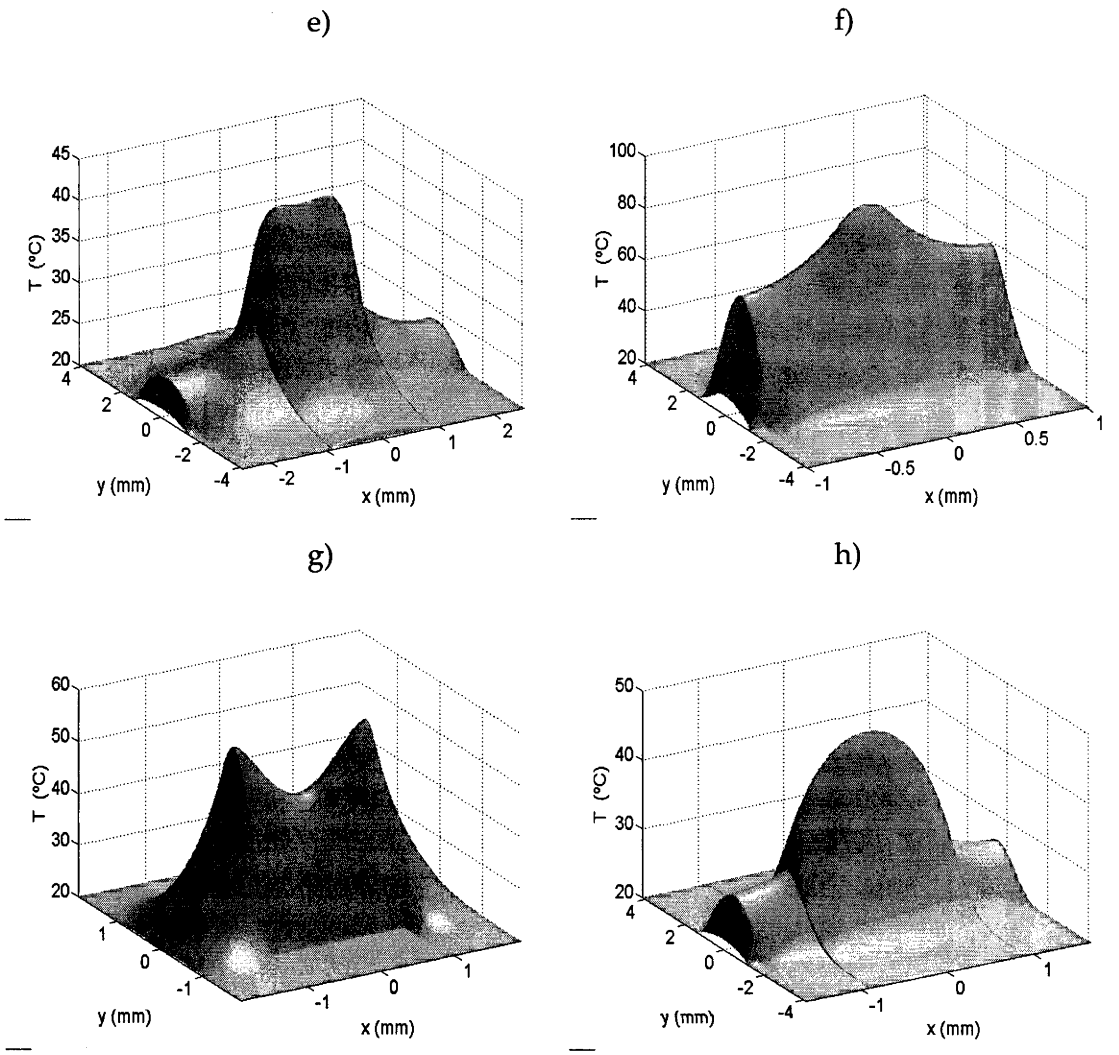

Figs. 6.3 - 1a-h: Temperature distributions for different geometries. The Nd:YVO_4 dimensions are 1.8×8×12 mm^3 unless otherwise mentioned.

(a) t_{sapph} = 0.63mm, t_{glue} = 2.5μm, (b) t_{sapph} = 0.63mm, t_{glue} = 10μm,
(c) t_{sapph} = 0.63mm, t_{glue} = 100μm, (d) t_{sapph} = 0.1mm, t_{glue} = 2.5μm,
(e) t_{sapph} = 1.5mm, t_{glue} = 2.5μm, (f) t_{sapph} = 0, t_{glue} = 0,
(g) t_{sapph} = 0, t_{glue} = 0, YVO_4: 1.8×1.8×12, (h) t_{sapph} = 0, t_{glue} = 0, α = 10cm^{-1}.
P_{pump} = 100W (per array), 20% duty cycle, α = 30 cm^{-1} (except for g), heat load factor = 0.45, κ_{YVO} = 5.1 $W{\cdot}K^{-1}{\cdot}m^{-1}$, κ_{sapph} = 33 $W{\cdot}K^{-1}{\cdot}m^{-1}$, κ_{glue} = 0.17 $W{\cdot}K^{-1}{\cdot}m^{-1}$, κ_{cu} = 384 $W{\cdot}K^{-1}{\cdot}m^{-1}$, κ_{air} = 0.024 $W{\cdot}K^{-1}{\cdot}m^{-1}$, T_{copper} = 20°C, T_{pump} = 96% , $t_{y,\,pump}$ = 1 mm.

For good thermal management in a zig-zag amplifier, two important issues need to be considered. Firstly, to avoid beam distortion through the thermal index change $\Delta n = \frac{\partial n}{\partial T}$, the thermal gradients across the signal beam should be as low as possible. The most important thermal gradients in the zig-zag slab are those perpendicular to the zig-zag plane (x-z plane in this case). The in-plane gradients become averaged out, to first order, because of symmetry. Therefore, the different geometries in *Figs. 6.3 - 1a-h* are best compared by plotting the temperature profile along the y-axis, averaged over the x-coordinate inside the Nd:YVO_4. This is depicted

in *Fig. 6.3 - 2a*, where the maximum temperature $\langle T \rangle_{max}$ was subtracted from $\langle T \rangle_x(y)$ in order to allow for better comparison. At y = 0.5mm (signal beam radius for highest extraction efficiency) the implemented design clearly has the smallest ΔT if a glue layer thickness of 2.5μm was assumed *(a)*. As expected, increasing the glue layers to 10μm *(b)* and 100μm *(c)* increases ΔT. Ideally, the glue should not exceed a thickness of 10μm, indicating the importance of the capillary assisted bonding which can achieve layers of 1-10μm. Using a thicker sapphire slab *(e)* does not improve matters further, whilst a much thinner slab *(d)* clearly increases ΔT. Using no sapphire, cooling the Nd:YVO_4 directly *(f)* in the same geometry (copper braces) is worse again. Changing the cooling geometry to side cooling *(g)*, i. e. perpendicular to the pump, achieves worst results, although the y-dimension of the Nd:YVO_4 was reduced to 1.8mm. Finally, if an absorption constant of $\alpha = 10\ cm^{-1}$ was used *(h)*, ΔT is comparable with that for $30\ cm^{-1}$ *(a)*, whilst the total heat load in this case was only 14.5W, compared to 17.2W for $\alpha = 30\ cm^{-1}$. Therefore, the efficiency of the design is better for higher pump absorption.

The second important issue concerns the stress fracture of laser materials. In order to avoid stress fracture of the laser crystal, the maximum temperature inside the crystal should be as low as possible, compared with its surface temperature [103]. Therefore, to compare the different geometries *(a-h)*, *Fig. 6.3 - 2b*, shows the temperature distribution $\langle T \rangle_x(y)$ over the complete crystal width of 8mm. Again, the implemented design with a glue layer thickness of 2.5μm *(a)* has the smallest temperature rise $\langle T \rangle_{max}$, and will therefore be subject to the smallest temperature induced stress. However, a large temperature rise is observed for a glue layer thickness of 100μm (e) which performs worst together with (f) where no sapphire was present.

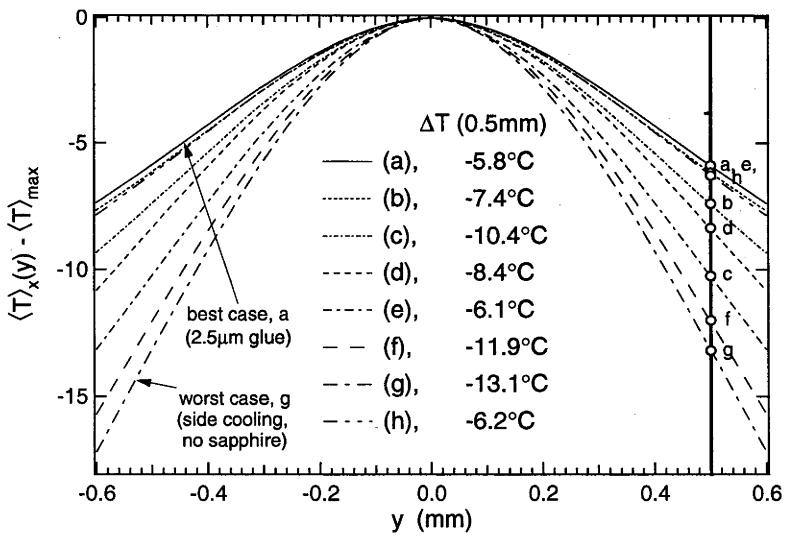

Fig. 6.3 - 2a: Temperature profile along the y-axis around y = 0, averaged over the x-coordinate inside the Nd:YVO_4. The maximum temperature $\langle T \rangle_{max}$ was subtracted from $\langle T \rangle_x(y)$ in order to allow for better comparison at y = 0.5mm (signal beam radius for highest extraction efficiency). The letters *a - h* refer to the designs discussed in the text and *Figs. 6.3. -1a - h*. The smaller the thermal gradient across a signal beam, the smaller the thermal lensing effects. *(a)* is the implemented design using a 2.5μm thick glue layer.

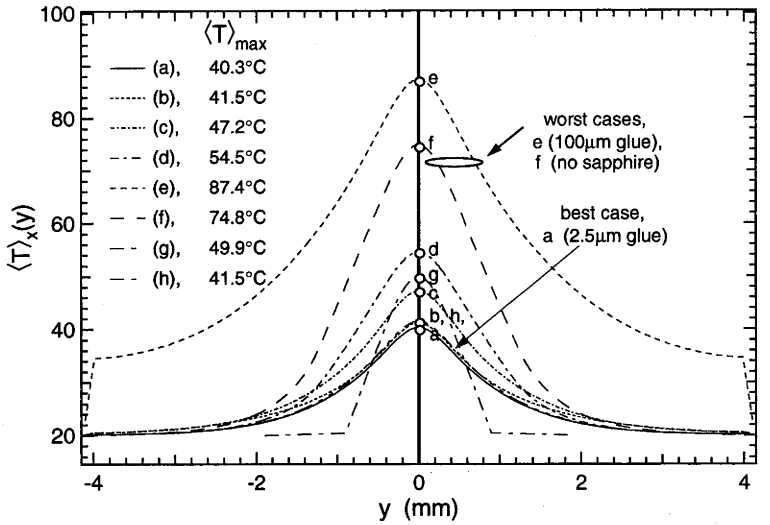

Fig. 6.3 - 2b: Temperature profile along the complete y-axis, averaged over the x-coordinate inside the Nd:YVO_4. The letters *a - h* refer to the designs discussed in the text and *Figs. 6.3. -1a - h*. The maximum temperatures are $\langle T \rangle_{max}$ are given for each design. The smaller $\langle T \rangle_{max}$ for a given pump power, the greater the margin for stress fracture. *(a)* is the implemented design, using a glue layer thickness of 2.5μm.

In summary, the simulations clearly show that the implemented design is optimised for thermal management of laser materials with poor thermal conductivity, high absorption and high gain, such as Nd:YVO_4. The design achieves up to 2.3 times smaller temperature difference ΔT over a typical beam radius, as well as the lowest temperature rise, $\langle T \rangle_{max}$, when compared with other designs.

In order to verify the design experimentally, the temperature distribution in the Nd:YVO_4 slab was measured for double side pumping. This was achieved using a standard Mach-Zehnder interferometer with polarised HeNe illumination. Each pump laser diode array (designated left and right) operated with a pulsewidth of τ_p = 100μs and a duty cycle of 20%, resulting in an average power of $P_l = P_r$ = 17W at each of the pump input faces of the amplifier (after the beam steering optics). Both arrays, as well as the amplifier copper block, were cooled to 20°C using the same chiller. Under these conditions, the left array had a wavelength mismatch of -2.5nm, whilst the right array had + 1.5nm with respect to the wavelength of maximum pump absorption ($\lambda \approx$ 808.5nm). To compensate for the mismatch would require separate cooling which was not feasible at the time. As a result, the absorbed average powers were only about 10W and 16W, with the associated absorption constants of α_l = 5 cm^{-1} and α_r = 20 cm^{-1} respectively.

In the unpumped case the interferogram was a flat fringe, indicating that there was no stress birefringence due to the mounting of the crystal. For the pumped crystal one has to differentiate between two cases, depending on the polarisation of the HeNe laser. Generally, the Mach-Zehnder measures the difference in the optical path L_{opt}, or phase ϕ, between the unpumped and pumped cases. The phase changes are due to

both the thermal expansion along the z-axis (crystallographic a-axis) as well as the thermal index change and are given by

$$\Delta\phi_i = N_i \cdot 2\pi = \frac{2\pi}{\lambda} \cdot L \cdot \left[n_i \cdot \alpha_a + \Delta n_i \right] \cdot \Delta T \qquad (6.3 - 2)$$

where N is the fringe number, n is the refractive index, $\alpha_a = \frac{1}{L} \cdot \frac{\partial L}{\partial T}$ is the expansion coefficient along the a-axis, $\Delta n = \frac{\partial n}{\partial T}$ is the thermal index change, ΔT is the temperature difference and the subscript i = c or a, for c- or a-polarisation respectively. Using *(6.3 - 2)* and the data from *Table 6.1.1* it is possible to calculate temperature differences ΔT from the measured interferograms, or to calculate interferograms from the simulated temperature distribution. *Fig. 6.3 - 3* shows both the measured as well as the calculated interferograms. The measured interference patterns display asymmetry in both x and y directions. In the case of x, this could only be reproduced in the simulation if, apart from the different absorption constants α_l and α_r, the glue layers also had different thicknesses (2μm on the left and 7.5μm on the right). The asymmetry in y is due to the crystal being mounted slightly asymmetrically (1mm lower). Therefore, the top edge of the interferogram corresponds to the actual crystal edge, whereas the bottom edge is due to an obstruction.

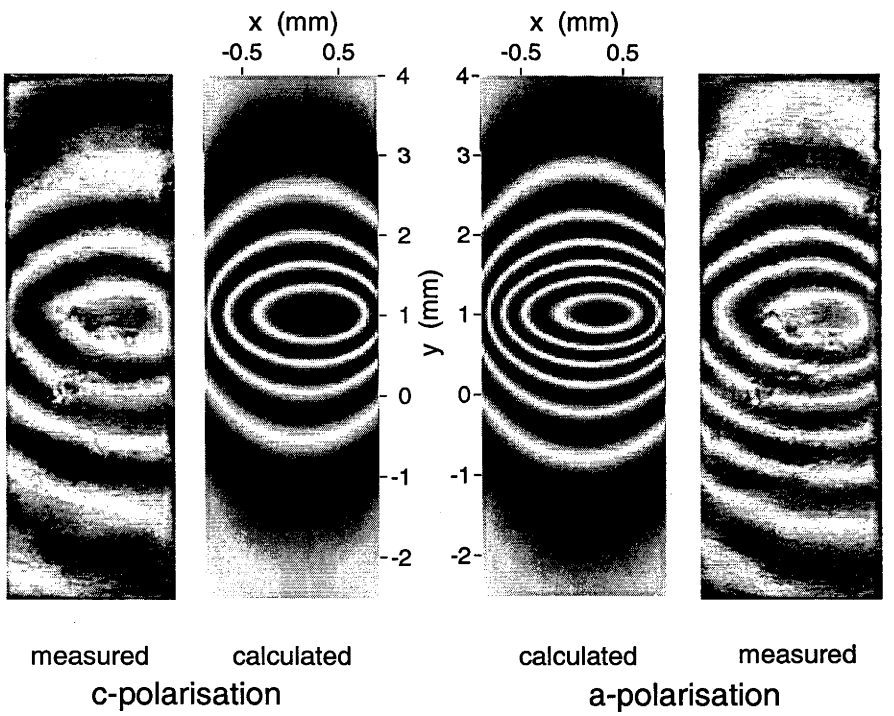

Fig. 6.3 - 3: Measured and calculated interferograms for c- and a-polarisation. The parameters were : $P_l = P_r = 17W$, $\alpha_l = 5\ cm^{-1}$, $\alpha_r = 20\ cm^{-1}$, $d_{glue\_l} = 2\mu m$, $d_{glue\_r} = 7.5\mu m$, heat load factor = 0.45, total absorbed optical power $P_{abs} = 26W$. The asymmetry with respect to the y-axis could only be reproduced in simulation if different glue layer thicknesses were assumed.

The agreement between the measured and calculated patterns is reasonable for both the c- and a-polarisations. As expected, the number of fringes for a-polarisation is greater than for c, since $\Delta n_c = 3 \cdot 10^{-6}$ whilst $\Delta n_a = 8.5 \cdot 10^{-6}$. From *(6.3 - 2)* one calculates a fringe ratio N_a/N_c of 1.35 which is in good agreement with the ratio found from the measured interferograms.

Fig. 6.3 - 4 shows the temperature distribution along the y-axis at x = 0, as calculated from the interference patterns as well as a simulation. The gradients of the measured distribution are actually lower than those of the simulation. However, one must realise that the experimentally obtained interference patterns are due to the integrated phase change along the z-axis, and include the effects of the stress optic tensor for which no values were found. Furthermore, the pump distribution was hardly ideal. The fibre lens blocks were mounted badly in both arrays, resulting in a variable stripe width along the z-axis whilst the output power distribution was also not constant.

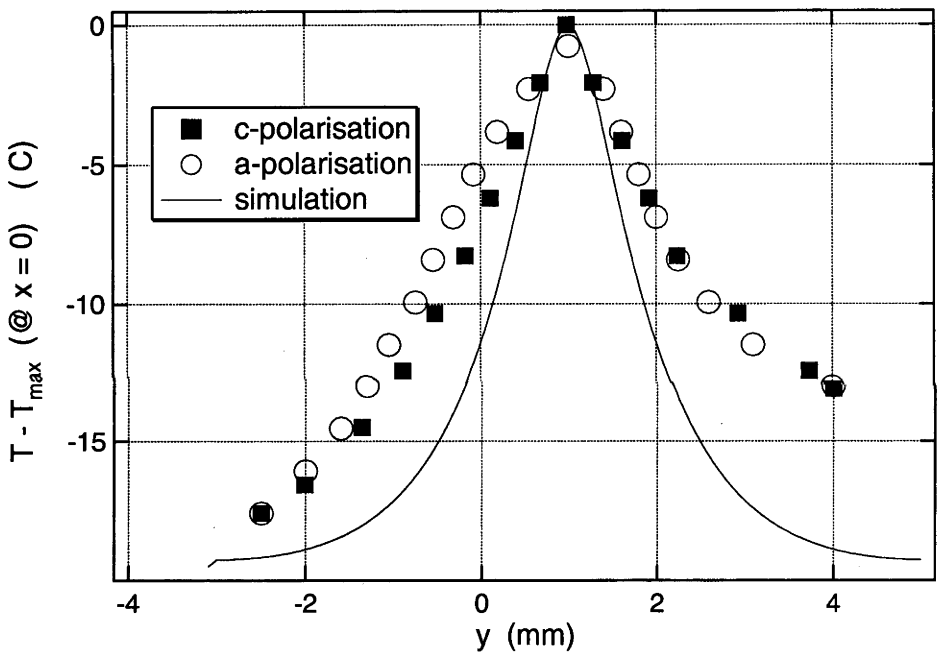

Fig. 6.3 - 4: Temperature distribution T - T_{max} at x = 0, calculated from the interferograms for c- and a-polarisation as well as a simulation using the parameters: $P_l = P_r = 17W$, $\alpha_l = 5\ cm^{-1}$, $\alpha_r = 20\ cm^{-1}$, $d_{glue\_l} = 2\mu m$, $d_{glue\_r} = 7.5\mu m$, heat load factor = 0.45, total absorbed optical power $P_{abs} = 26W$.

Most importantly, however, *Fig. 6.3 - 4* shows that the total temperature difference between the hottest and coolest regions is around 20°C for both experiment and simulation. Therefore, although the experimental conditions could not be chosen for best design performance, i. e. highest possible pump absorption, the agreement between the measured and calculated temperature differences is nevertheless a clear indication for the efficiency of this design.

6.4. Summary

A double side diode-pumped, Nd:YVO_4 zig-zag slab, laser amplifier design was presented. The design makes use of the favourable laser properties (broad-band and strong pump absorption; high stimulated emission cross-section) of this laser crystal. It was shown through modelling that the amplifier is capable of producing mJ output energies in a double pass configuration, assuming ps input pulses of nJ energy, i. e. $G \approx 10^6$. The major disadvantage of Nd:YVO_4, namely its poor thermal conductivity and the associated thermal gradients, were minimised by conductively cooling the slab through the pumped surface. This was accomplished through the use of sapphire slabs, bonded to the Nd:YVO_4 with an optical cement of thickness < 10μm. The latter thicknesses were achieved using a bonding procedure which involved capillary forces and an optical cement of suitable viscosity. In the present design, the glue layer (Summers Lab. SK9) also acts as the low index layer for total internal reflection and was shown to possess very good optical quality and durability under high intensity irradiation. Using numerical simulations of the temperature distribution in the amplifier head, it was shown that the implemented design is optimised for thermal management of laser materials with poor thermal conductivity and high pump absorption, e. g. Nd:YVO_4. It was further shown that glue layer thicknesses < 10μm are desirable in order to keep thermal gradients perpendicular to the zig-zag direction as small as possible. Using interferometry of the double side pumped amplifier head, temperature distributions were obtained experimentally. These were in reasonable agreement with the simulations, further confirming the thermal management capability of the design. Unfortunately, actual amplifier experiments could not be performed within the time frame of the PhD programme. This was due to a coating damage on the high reflector caused by the build-up of amplified spontaneous emission during the thermal loading experiments. In order to prevent recurrence of such damage it will be necessary to achieve a more uniform pump distribution, and possibly replace the end mirror with an anti-reflection coating, using external dielectric mirrors.

CHAPTER 7

CONCLUSION

This PhD project has explored the use of ion-implanted semiconductors as an alternative to low-temperature MBE grown materials in devices for passive mode-locking (SESAMs) and ultrafast saturable absorption modulators in general. Furthermore, the research provides immediately applicable technology for areas such as laser ranging where simple and easy to maintain ps laser sources are required.

Firstly, a low finesse Arsenic ion-implanted GaAs SESAM for mode-locking of a Ti:Sapphire laser was presented and the ion-implantation process was outlined. It was found that As-implantation with high doses reduced the reflectivity of the devices severely, making them useless for mode-locking applications, but that the reflectivity could be restored completely through thermal annealing. Wavelength degenerate pump-probe measurements were made to investigate the dynamic response of the SESAMs. A multi-exponential response was observed. In both the annealed and unannealed samples, the trapping and recombination signals started with a very fast decay, but became slower for longer times. In the annealed case, photo induced absorption appeared - earlier and more pronounced for the higher implantation doses - and was attributed to the excitation of captured carriers, trapped for long times due to a small recombination rate. The small signal response of samples was dominated by the implantation dose, rather than the exact shape of the implantation induced damage profile. The response of all samples became similar under strong excitation, where even the unimplanted sample recovered swiftly to background. This behaviour has been tentatively associated with carrier thermalisation and cooling to a hot lattice. Approximate saturation fluences for the resonant and anti-resonant SESAMs were deduced. These did not depend strongly on the implantation dose or annealing conditions. It was also shown that nonbleachable losses were introduced by the ion-implantation process, similarly to the LT-grown GaAs.

The soliton mode-locking performance of the ion-implanted SESAMs was investigated in a modified commercial Ti:Sapphire laser. All SESAMs, excluding those with the highest implantation doses, mode-locked the laser in a self-starting fashion, producing single pulses as short as 105 fs. Not surprisingly, given the fast recovery of the unimplanted SESAM found for strong excitation, it also mode-locked the laser stably. However, since a swift recovery at any fluence is desirable whilst preserving nearly the modulation of the unimplanted SESAM, a low dose implanted and annealed SESAM is nevertheless preferable. A difference in the samples' ability to suppress the Q-switched mode-locking instability was attributed to the different modulation depths caused by the ion-implantation. An increase of the laser's stability against Q-switched mode-locking for smaller intra-cavity dispersion was shown to be a result of the soliton mode-locking operation. Computer simulations of the

Generalised Complex Ginzburg-Landau Master Equation (GCGLE) showed good agreement with the experimental observations.

Varying the dispersion (or small signal gain) beyond a critical value, the laser could be forced into multi-soliton operation. The transitions were explained within the framework of a soliton perturbations approach as well as the GCGLE. It was found that for a single soliton to break up into two solitions, the condition for shedding and growth of dispersive continuum must be fulfilled. On the other hand, two well-separated solitons in the laser became unstable and coalesced when changes in the filter loss (e. g. induced by a small energy imbalance) were outweighed by the simultaneous changes in absorber loss. This, and the difference in total energy before and after the switching between states, was interpreted as the origin of the observed switching hysteresis. Computer simulations of quasi-stable closely spaced pulse solutions of the GCGLE were in good agreement with the experimental observations of such entities, indicating the existence of rotating and quasi-constant phase doublets. Finally, the regions of existence of single and multiple solitons was mapped in the gain-dispersion plane and the transitions from multiple pulses via chaos-like nonequilibrium to chirped ps pulses was explained.

The nonlinear optical absorption properties of ion-implanted GaAs were then investigated experimentally, with the aim of determining the response times as well as the modulation for different implantation conditions. A large set of As- and O-ion implanted GaAs samples were measured in reflection with a single beam, as well as a pump-probe configuration. Both response time and modulation were found to decrease through ion-implantation, with the decrease in modulation being due to increasing non-bleachable losses. Unannealed samples, although very fast, were found to have very poor modulation which generally increased during high fluence illumination due to an in-situ annealing mechanism. Therefore, unannealed samples are less useful in applications. The data from all annealed samples lay on a well-defined curve in the (τ_A , M_{max}) plane, suggesting that the residual defects after annealing were of a similar nature (point defects) and that the curve defines the achievable (τ_A , M_{max}) performance of ion implanted GaAs. Oxygen can be implanted at higher doses than As without amorphisation, creating more point defects and leading to shorter τ_A whilst preserving highest possible modulation. Recovery times of < 400 fs were measured at a modulation of 80% of that of unimplanted GaAs. Under high fluence excitation, the temporal response of the samples acquired a secondary peak following the pump-probe correlation, attributed to the cooling of hot carriers. The latter could lead to a very high optical gain at the pump probe wavelength. In general, these investigations showed that ion-implantation is a useful and extremely versatile process for making ultrafast absorption modulation devices.

Mode-locking experiments were performed in a Ti:Sapphire (diode) pumped Nd:YVO_4 laser with continuously variable output pulsewidth, using MOCVD grown unimplanted as well as As-implanted high finesse InGaAs SESAMs. SESAMs with a 7-layer top mirror resulted in good self-starting characteristics, as well as suppression of the Q-switched mode-locking instability. The laser produced its shortest pulses (6.5ps)

for an output coupler reflectivity close to 100% whilst the pulsewidth could be increased by a factor of 2-3, by increasing the output coupling to the self-starting limit. Non-ideal AR-coatings were found to cause pedestals on the shorter pulses. The pedestals were smaller when the implanted SESAM was mode-locking the laser, indicating the better pulse cleaning capability of a faster absorber. The main mechanism responsible for the variation of pulsewidth with output coupling was found to be the dependence of the absorber loss on the absorber saturation level. When diode-pumping was used, it was possible to pump the laser directly from the fibre output without using re-imaging optics due to the strong pump absorption and large gain cross-section of Nd:YVO_4.

Finally a Nd:YVO_4 amplifier, optimised for efficient cooling, was designed. It makes use of the broad-band and strong pump absorption and the high stimulated emission cross-section of this laser crystal. It minimises the effects due to poor thermal conductivity by conductively cooling the zig-zag slab through the pumped surfaces, relying on the use of Sapphire and capillary assisted optical cementing. Interferometric measurements and numerical simulations of the temperature distribution in the amplifier head showed that the implemented design is optimised for thermal management of laser materials with poor thermal conductivity and high pump absorption, such as Nd:YVO_4..

It is believed that the objectives of this PhD project were achieved to a large degree, although several obvious extensions for future work can be named. Firstly, the investigation of hot-implantation as a means of avoiding amorphisation, thereby increasing the possible number of point defects in ion-implanted materials and further shorten the response times. Secondly, actual lasing and amplifier experiments need to be carried out with the Nd:YVO_4 amplifier. The cooling concept of the amplifier can also be applied in other laser and amplifier designs (e. g. end-pumped configuration) involving materials with high pump absorption. Work on a passively Q-switched μ-laser, started during the PhD, should be continued since such lasers are interesting from EOS' point of view. Further semiconductor work is needed in order to extend the use of ion-implanted saturable absorbers towards longer wavelengths. Laser development for the longer wavelengths should be carried out in parallel. Finally, work on ultrafast all-optical switching devices, incorporating ion-implanted semiconductors, will be a challenge.

APPENDIX I

Q-SWITCHED MODE-LOCKING INSTABILITY IN SOLITON MODE-LOCKED LASERS

In order to derive the stability condition for Q-switched mode-locking of a soliton mode-locked laser, consider the equations for the soliton energy Q and the laser gain g, similar to the analysis given in section 3.3.2.

$$T_R \frac{dQ}{dT} = 2 \cdot [g - l_0 - \delta - \alpha] \cdot Q \qquad (A.I. - 1)$$

$$\frac{dg}{dT} = -\frac{g - g_0}{T_g} - \frac{Q \cdot g}{P_g \cdot T_g \cdot T_R} \qquad (A.I. - 2)$$

where l_0 is the linear loss, g_0 is the small signal gain, T_R is the round trip time and P_g and T_g are the gain saturation power and upper state life time respectively. The filter and absorber losses for solitons are given by

$$\delta = \frac{\beta}{3 \cdot t_0^2} \qquad (A.I. - 3)$$

$$\alpha = \frac{1}{2 \cdot t_0} \cdot \int_{-\infty}^{\infty} \operatorname{sech}^2\left(\frac{t}{t_0}\right) \cdot q(t) dt \qquad (A.I. - 4)$$

respectively, with

$$t_0 = \frac{2 \cdot |\beta_2|}{\kappa \cdot Q} = \frac{\tau_{FWHM}}{1.763} \qquad (A.I. - 5)$$

and q(t) is the solution of the rate-equation model for the saturable absorber

$$q_t = -\frac{q - q_0}{T_a} - \frac{|\psi|^2 \cdot q}{E_a} \qquad (A.I. - 6)$$

The underlying assumption of this treatment is that, despite the perturbations due to filter and absorber, the pulses remain solitons in the adiabatic sense. As is usual in stability analysis, eqns. *(A.I. - 1,2)* are treated around a working point $(\tilde{Q}, \tilde{\delta}, \tilde{\alpha}, \tilde{g})$ through linearisation. Inserting

$$\begin{pmatrix} Q & \rightarrow & \tilde{Q}+\Delta Q \\ \delta & \rightarrow & \tilde{\delta}+\Delta\delta \\ \alpha & \rightarrow & \tilde{\alpha}+\Delta\alpha \\ g & \rightarrow & \tilde{g}+\Delta g \end{pmatrix} \qquad (A.I-7)$$

in *(A.I- 1,2)* leads to equations for the changes in energy and gain

$$T_R \cdot \frac{d\Delta Q}{dT} = 2 \cdot [Q+\Delta Q] \cdot [\Delta g - \Delta\alpha - \Delta\delta] \qquad (A.I-8)$$

$$\frac{d\Delta g}{dT} = -\Delta g \cdot \left(\frac{1}{T_g} + \frac{\tilde{Q}}{P_g \cdot T_g \cdot T_R} \right) - \frac{\Delta Q \cdot (\tilde{g}+\Delta g)}{P_g \cdot T_g \cdot T_R} \qquad (A.I-9)$$

Neglecting terms in $\Delta Q \cdot \Delta g$ (2nd order) and $Q \cdot (-\Delta\alpha - \Delta\delta)$ (only leads to a driving term irrelevant for stability) and using the substitutions

$$\tilde{Q} = a, \qquad \frac{1}{T_g} + \frac{\tilde{Q}}{P_g \cdot T_g \cdot T_R} = b, \qquad \frac{\tilde{g}}{P_g \cdot T_g \cdot T_R} = c, \qquad -\Delta\alpha - \Delta\delta = f$$

(A.I - 8) and *(A.I - 9)* are combined to the second order differential equation for the changes in the gain Δg

$$\frac{d^2\Delta g}{dT^2} + (b+2f)\frac{d\Delta g}{dT} + 2(a \cdot c + b \cdot f)\Delta g = 0 \qquad (A.I-10)$$

Allowing oscillatory solutions, i. e. Q-switched mode-locking, the most general solution of *(A.I - 10)* is given by

$$\Delta g = C_1 \cdot \exp\left(-\frac{b+2f}{2} \cdot T\right) \cdot \cos\left(\sqrt{2(a \cdot c + b \cdot f) - \frac{(b+2f)^2}{4}} \cdot T\right) + C_2 \cdot \exp\left(-\frac{b+2f}{2} \cdot T\right) \cdot \sin\left(\sqrt{2(a \cdot c + b \cdot f) - \frac{(b+2f)^2}{4}} \cdot T\right) \qquad (A.I-11)$$

Most importantly, the oscillations in Δg remain suppressed if $b+2f>0$ leading to the final condition for stable soliton mode-locking without the Q-switched mode-locking instability

$$\frac{1}{T_g} + \frac{\tilde{Q}}{P_g \cdot T_g \cdot T_R} > 2(-\Delta\alpha - \Delta\delta) \qquad (A.I-12)$$

Without the filter, eqn. *(A.I - 12)* becomes eqn. *(3.2.1 - 1)*. Although no analytical solution exists for $\Delta\alpha$ in the case of the general absorber *(A.I - 6)* it is clear that $\Delta\alpha$ is

negative for positive changes in energy ΔQ. On the other hand, an expression for $\Delta\delta$ due to energy changes ΔQ is easily derived

$$\Delta\delta = \frac{\beta \cdot \kappa^2 \cdot Q}{6 \cdot |\beta_2|^2} \cdot \Delta Q \qquad (A.I - 13)$$

which is always positive for positive ΔQ. Therefore, the effect of the filter is to make the right hand side of *(A.I - 12)* smaller, suppressing Q-switched mode-locking for a greater range of gain saturation.

APPENDIX II

SUMMARY OF THE NUMERICS USED IN CHAPTERS 3 AND 5

In this section, the numerical solution of equations *(3.2.2 - 3,4,5)* is outlined. The GCGLE (eqn. *3.2.2 - 3*) belongs to a class of nonlinear parabolic partial differential equations for which three different numerical schemes are commonly applied. These are (a) finite difference schemes (e. g. Crank-Nicholson), (b) finite element schemes (e. g. Galerkin method) and (c) pseudo spectral schemes (e. g. split-step FFT, path integral method). Of the three, the pseudo spectral schemes, in particular the split-step FFT, are usually preferred due to the speed associated with the Fast-Fourier-Transform (FFT) algorithms available nowadays. The split-step FFT was also used for the simulations contained in chapter 3.

In terms of linear and nonlinear operators, equation *(3.2.2 - 3)* can be written as

$$T_R \cdot i\frac{\partial\psi(T,t)}{\partial T} = \left[\hat{L}(t) + \hat{N}(T,t)\right]\cdot\psi(T,t) \qquad \text{(A.II - 1)}$$

where $\hat{L}(t)$ contains all dispersion effects, including that of the filter. It only depends on the soliton time. On the other hand, $\hat{N}(T,t)$ contains the effects of self-phase-modulation, loss modulation, linear loss, and gain. Note that, through the gain g(T), $\hat{N}(T,t)$ also depends on T. According to the Baker-Hausdorff theorem [75] the integral of equation *(A.II - 1)* between T and T+ΔT can be written, accurate to second order, as

$$\psi(t,T+\Delta T) = \exp\left[-i\hat{L}\cdot\Delta T\right]\cdot\exp\left[-i\hat{N}\cdot\Delta T\right]\cdot\psi(T,t) \qquad \text{(A.II - 2)}$$

This means effectively that the evolution of the field through one round trip ΔT is now accomplished through two separate steps, one containing the linear dispersive effects, the other one the nonlinear effects. Despite the loss in accuracy, one has nevertheless gained the possibility of conveniently evaluating the linear dispersive terms in the frequency domain using FFTs, whereas the nonlinear terms can be solved in the time domain directly. Finally, the exponential operators for the linear and the nonlinear steps are multiplied by the field $\psi(T,t)$ to obtain the field $\psi(T+\Delta T,t)$, one round trip later.

The calculation of the loss modulation q(t) and gain g(T) involves the solution of eqns. *(3.2.2 - 4,5)* for each $\hat{N}(T,t)$. It can be shown that *(3.2.2 - 4)* has the integral solution

$$q(t)=\frac{q_0}{T_a}\cdot\left[\int_{-\infty}^{t}dt'\exp\left(\int_{-\infty}^{t'}dt''\left(\frac{1}{T_a}+\frac{|\psi(t'')|^2}{E_a}\right)\right)+T_a\right]\cdot\exp\left(-\int_{-\infty}^{t}dt'\left(\frac{1}{T_a}+\frac{|\psi(t')|^2}{E_a}\right)\right)$$

(A.II - 3)

which can be evaluated numerically much faster than, for instance, using a Runge-Kutta scheme to solve *(3.2.2 - 4)* at every round trip. Finally, due to the dependence of the gain g(T) on the slow time, an iterative 2nd order Runge-Kutta forward integration of the complete nonlinear operator $\hat{N}(T,t)$ was employed, monitoring the convergence of the gain to assure the numerical accuracy of the procedure.

It should be noted that the above outlined procedure is valid as long as the mean field approach of the GCGLE model is valid itself. Once appreciable variations within one round trip become possible, i. e. the r-parameter (see section *3.2.2*) becomes of the order of 1, then commutators depending on the intra-cavity position would have to be introduced [69, 59]. Alternatively, one can sub-divide the cavity, associating a field transfer operator with every element. Then the field can be propagated through the respective elements using single or multiple steps. For this treatment the location and magnitude of all effects (gain, SPM, dispersion of mirrors...) must be known.

APPENDIX III

FITTING MODELS FOR THE R(F_P) DATA

A.III.1. Travelling Wave Saturable Absorber (TWA) Model

It was shown in [76, 85] that the gain (extinction) R = E_{out} /E_{in} seen by an optical pulse travelling through a gain (absorber) medium with recovery time much longer than the pulsewidth is given by

$$R(E)=\frac{E_{out}}{E_{in}}=\frac{\ln\left(\frac{R_{lin}-1}{R_f-1}\right)}{\ln\left(\frac{R_{lin}-1}{R_f-1}\right)-\ln\left(\frac{R_{lin}}{R_f}\right)} \qquad (A.III.1-1)$$

where the reflectivity notation, relevant here, was used with the low energy reflectivity R_{lin} and the reflectivity after the pulse has passed through the sample $R_f=\frac{R_f}{R_f-(R_f-1)\cdot\exp\left(\frac{E_{in}}{E_{sat}}\right)}$. Eqn. *(A.III.1 - 1)* does not take into account the nonbleachable reflectivity losses which are present in semiconductor saturable absorbers. Usually these losses are distributed, as are the bleachable losses. However, the TWA model cannot be solved analytically for this general case and only localised nonbleachable losses (i.e. imperfect mirror reflectivity, surface scattering etc.) were introduced [22]. Using the new variable $r_{lin}=\frac{R_{lin}}{R_{lin}+\Delta R}=\frac{R_{lin}}{1-\Delta R_{ns}}$ the energy dependent reflectivity then becomes

$$R(E)=\frac{R_{lin}}{r_{lin}}\cdot\frac{\ln\left(\frac{r_{lin}-1}{r_f-1}\right)}{\ln\left(\frac{r_{lin}-1}{r_f-1}\right)-\ln\left(\frac{r_{lin}}{r_f}\right)} \qquad (A.III.1-2)$$

which can be simplified to

$$R(E)=(R_{lin}+\Delta R)\cdot\frac{\ln\left(1+\frac{R_{lin}}{R_{lin}+\Delta R}\cdot\left[\exp\left(\frac{E}{E_{sat}}\right)-1\right]\right)}{\frac{E}{E_{sat}}} \qquad (A.III.1-3)$$

Note, that *(A.III.1 - 3)* is slightly different to the fitting formula (eqn. 18) given in [22] which contains a notational error. Generally, the measurement setup described in section *4.2* measures the nonlinear reflectivity as

$$R(E)=\frac{E_{out}}{E_{in}}=\frac{\iint\limits_{t,A} I_{out}(r,t)dtdA}{\iint\limits_{t,A} I_{in}(r,t)dtdA} \qquad (A.III.1 - 4)$$

which indicates that the fit could still be improved if the output were integrated over the Gaussian beam [84]. This leads to the final TWA fitting formula

$$R(F)=2\cdot\frac{(R_{lin}+\Delta R)\cdot F_{sat}}{F\cdot\omega^2}\cdot\int_0^{\infty} r\cdot\ln\left(1+\frac{R_{lin}}{R_{lin}+\Delta R}\cdot\left[\exp\left(\frac{2\cdot F\cdot\exp\left(-\frac{2\cdot r^2}{\omega^2}\right)}{F_{sat}}\right)-1\right]\right)dr$$

(A.III.1 - 5)

where $F=\frac{E}{\pi\cdot\omega^2}$ is the pulse energy fluence, ω is the Gaussian beam radius and F_{sat} is the saturation fluence. The integral over t is obsolete since it was shown in [85] that R(F) does not depend on the pulse shape.

It is worth identifying the assumptions made in the derivation of the TWA fit. These are: (a) the saturable absorber has a slow response ($T_A \rightarrow \infty$), (b) a single pass travelling wave configuration, (c) the nonbleachable losses are localised, and (d) the absorber is a pure two-level absorber, neglecting mechanisms such as free carrier absorption (FCA) and two-photon absorption (TPA). Clearly, for the samples considered here, all of these assumptions are under certain conditions and to some degree violated. For instance: not all samples can be considered slow compared to the pulsewidth used, there exists a standing wave inside the absorber layer which is effectively passed twice; and for high fluences FCA and TPA may not be negligible.

A.III.2. Instantaneous Two-level Saturable Absorber (ITA) Model

These shortfalls prompt one to ask whether a different fitting model could not be used just as well. In this context, the most straight forward model is that of an instantaneous two-level saturable absorber (ITA). Here, the reflectivity is given by

$$R(F) = \frac{2}{F \cdot \omega^2} \cdot \iint_{A,t} r \cdot I_{in}(t.r) \cdot \exp\left[-2 \cdot d \cdot \left(\frac{\alpha_0}{1 + \frac{I_{in}(t.r)}{F_{sat} \cdot \frac{1.763}{2 \cdot \tau_{FWHM}}}} + \alpha_{ns} \right) \right] dtdr \qquad (A.III.2\text{- }1)$$

where α_0 is the small signal absorption constant, α_{ns} is the nonbleachable absorption constant and the input intensity is defined as

$$I_{in}(t,r) = \frac{F \cdot 1.763}{\tau_{FWHM}} \cdot \operatorname{sech}^2\left(\frac{t \cdot 1.763}{\tau_{FWHM}} \right) \cdot \exp\left(-\frac{2 \cdot r^2}{\omega^2} \right) \qquad (A.III.2 - 2)$$

Both the TWA and the ITA fit were applied to the $R(F_p)$ data of samples 10, 33, and 55 for comparison and are displayed in *Fig. A.III.2 - 1*. The fits were performed for fluences between 10 and 400 $\mu J \cdot cm^{-2}$. R_{lin}, ΔR, ΔR_{ns}, and F_{sat} were then deduced from the fits and given in *Table A.III.2 - 1*. Most importantly, both fits are in good agreement with the data up to fluences of around 400 $\mu J \cdot cm^{-2}$. However, the TWA fit is seen to be slightly better, also extrapolating better to lower and higher fluences. Clearly, both fits fail at high fluences. Finally, because of the different models used in the fits, one arrives at different saturation fluences F_{sat}, as can be seen from *Table A.III.2 - 1*. However, either fit could be applied in a comparative study of different samples when used consistently.

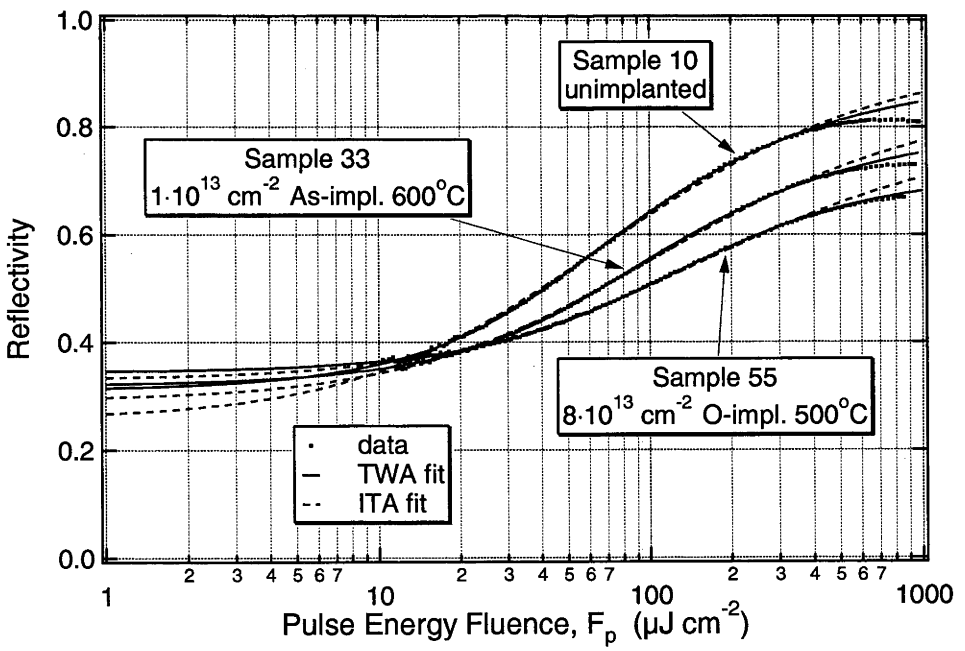

Fig. A.III.2 - 1: Comparing the TWA and ITA fits for samples 10 (unimplanted), 33 ($1 \cdot 10^{13}$ cm^{-2}, As, 600°C) and 55 ($8 \cdot 10^{13}$ cm^{-2}, O, 500°C). The fits were performed for fluences between 10 and 400 $\mu J \cdot cm^{-2}$.

Fit parameters for TWA fit in Fig A.III.2 - 1

Sample	R_{lin}	ΔR	ΔR_{ns}	F_{sat} [μJ·cm^{-2}]
10	0.3095	0.5846	0.1059	21.66
33	0.3194	0.4856	0.1950	31.71
55	0.3438	0.3916	0.2646	44.43

Fit parameters for ITA fit in Fig A.III.2 - 1

Sample	R_{lin}	ΔR	ΔR_{ns}	F_{sat} [μJ·cm^{-2}]
10	0.2570	0.6769	0.0660	32.32
33	0.2923	0.5640	0.1437	56.74
55	0.3313	0.4641	0.2046	92.11

Table A.III.2 - 1: Comparison of parameters of TWA and ITA fitting models for samples 10 (unimplanted), 33 ($1\cdot10^{13}$ cm^{-2}, As, 600°C) and 55 ($8\cdot10^{13}$ cm^{-2}, O, 500°C). The fits were performed for fluences between 10 and 400 μJ·cm^{-2}.

A.III.3. TWA-Fit Including Two-Photon Absorption

When two-photon absorption (TPA) is present, the general equations for the intensity I and saturable absorption (SA) α are given by

$$\frac{\partial I(z,r,t)}{\partial z} = -\left[\alpha(z,r,t)+\alpha_{ns}\right]\cdot I(z,r,t) - \beta\cdot I^2(z,r,t) \qquad (A.III.3 - 1)$$

$$\frac{\partial \alpha(z,r,t)}{\partial t} = -\frac{\left(\alpha(z,r,t)-\alpha_0\right)}{T_A} - \frac{\alpha(z,r,t)\cdot I(z,r,t)}{F_{sat}} \qquad (A.III.3 - 2)$$

Unfortunately, no analytical solution exists for these equations and a fitting algorithm using numerical solutions is usually very time consuming. Therefore, it will be assumed here that the SA and TPA act independently on the intensity. This is valid when the SA is bleached at the intensities where the TPA starts to play a considerable role whilst the nonbleachable absorption α_{ns} is small. Then, the TWA model can be used in conjunction with a factor due to TPA:

$$R(F) = R_{TWA}(F)\cdot R_{TPA}(F) \qquad (A.III.3 - 3)$$

Here, R_{TWA} is the integral *A.III.1 - 5* and R_{TPA} will be derived in the following manner. When the saturable and nonbleachable absorption is neglected in *(A.III.3 - 1)* it is easy to show that it has the solution

$$R(I_{in}(r,t)) = \frac{I_{out}(r,t)}{I_{in}(r,t)} = \frac{1}{1 + 2 \cdot d_{abs} \cdot \beta \cdot I_{in}(r,t)} \qquad (A.III.3 - 4)$$

where the intensity I_{in} is given by

$$I_{in}(r,t) = \frac{F \cdot 1.763}{\tau_{FWHM}} \cdot \operatorname{sech}^2\left(t \cdot \frac{1.763}{\tau_{FWHM}}\right) \cdot \exp\left(-\frac{2 \cdot r^2}{\omega^2}\right) \qquad (A.III.3 - 5)$$

Using *(A.III.3 - 5)* it is possible to eliminate the time dependence in *(A.III.3 - 4)* analytically to arrive at the fluence dependent reflectivity due to TPA

$$R_{TPA}(F) = C \cdot \int_0^{\infty} \frac{r}{A(r)} \cdot \lim_{t \to \infty} \left(\ln \left(\frac{2 \cdot A(r) \cdot \cosh^2\left(\frac{t}{t_0}\right) - A(r) + B \cdot \cosh\left(\frac{t}{t_0}\right) \cdot \sinh\left(\frac{t}{t_0}\right)}{2 \cdot A(r) \cdot \cosh^2\left(\frac{t}{t_0}\right) - A(r) - B \cdot \cosh\left(\frac{t}{t_0}\right) \cdot \sinh\left(\frac{t}{t_0}\right)} \right) \right) dr$$

(A.III.3 - 6)

where

$$A(r) = \sqrt{\frac{2 \cdot d_{abs} \cdot \beta \cdot F}{t_0} + \exp\left(\frac{2 \cdot r^2}{\omega^2}\right)} \qquad (A.III.3 - 7)$$

$$B = \sqrt{\frac{8 \cdot d_{abs} \cdot \beta \cdot F}{t_0}} \qquad (A.III.3 - 8)$$

$$C = \sqrt{\frac{2 \cdot t_0}{F \cdot \omega^4 \cdot d_{abs} \cdot \beta}} \qquad (A.III.3 - 9)$$

$$t_0 = \frac{\tau_{FWHM}}{1.763} \qquad (A.III.3 - 10)$$

BIBLIOGRAPHY

[1] I. P. Christov, V. D. Stoev, M. M. Murnane, and H. C. Kapteyn, "Sub-10-fs operation of Kerr-lens mode-locked lasers," *Opt. Lett.*, **21**, pp. 1493-1495, 1996

[2] A. Kasper and K. J. Witte, "10-fs pulse generation from a unidirectional Kerr-lens mode-locked Ti-sapphire ring laser," *Opt. Lett.*, **21**, pp. 360-362, 1996

[3] G. Cerullo, S. De Silvestri, and V. Magni, "Self-starting Kerr-lens mode locking of a Ti-sapphire laser," *Opt. Lett.*, **19**, pp. 1040-1042, 1994

[4] K. J. Blow and D. Wood, "Mode-locked lasers with nonlinear external cavities," *J. Opt. Soc. Amer. B*, **5**, pp. 629-632, 1988

[5] U. Keller, W. H. Knox, and H. Roskos, "Coupled-cavity resonant passive mode-locked Ti-sapphire laser," *Opt. Lett.*, **15**, pp.1377-1379, 1990

[6] U. Keller, G. W. 'tHooft, W. H. Knox, and J. E. Cunningham, "Femtosecond pulses from a continuously self-starting passively mode-locked Ti:sappire laser," *Opt. Lett.*, **16**, pp. 1022-1024, 1991

[7] U. Keller, T. K. Woodward, D. L. Sivco, and A. Y. Cho, "Coupled-cavity resonant passive mode-locked Nd:yttrium lithium fluoride laser," *Opt. Lett.*, **16**, pp. 390-392, 1991

[8] U. Keller and T. H. Chiu, "Resonant Passive Mode-Locked Nd:YLF Laser," *IEEE J. of Quantum Electr.*, **QE-28**, pp. 1710-1721, 1992

[9] G. R. Jacobovitz-Veselka, U. Keller, and M. T. Asom, "Broadband fast semiconductor saturable absorber," *Opt. Lett.*, **17**, pp. 1791-1793, 1992

[10] U. Keller, D. A. B. Miller, G. D. Boyd, T. H. Chiu, J. F. Ferguson. and M. T. Asom, "Solid-state low-loss intracavity saturable absorber for Nd:YLF lasers: an antiresonant semiconductor Fabry-Perot saturable absorber," *Opt. Lett.*, **17**, pp. 505-507, 1992

[11] I. D. Jung, L. R. Brovelli, M. Kamp, U. Keller, and M. Moser, "Scaling of the antiresonant Fabry-Perot saturable absorber design toward a thin saturable absorber," *Opt. Lett.*, **20**, pp. 1559-1561, 1995

[12] K. J. Weingarten, U. Keller, T. H. Chiu, and J. F. Ferguson, "Passively mode-locked diode-pumped solid-state lasers that use an antiresonant Fabry-Perot saturable absorber," *Opt. Lett.*, **18**, pp. 640-642, 1993

[13] D. Kopf, K. J. Weingarten, L. R. Brovelli, M. Kamp, and U. Keller, "Diode-pumped 100-fs passively mode-locked Cr-LiSAF laser with an antiresonant Fabry-Perot saturable absorber," *Opt. Lett.*, **19**, pp. 2143-2145, 1994

[14] I. D. Jung, F. X. Kärtner, L. R. Brovelli, M. Kamp, and U. Keller, "Experimental verification of soliton mode locking using only a slow saturable absorber," *Opt. Lett.*, **20**, pp. 1892-1894, 1995

[15] C. Hönninger, G. Zhang, U. Keller, and A. Giessen, "Femtosecond Yb:YAG laser using semiconductor saturable absorbers," *Opt. Lett.*, **20**, pp. 2402-2404, 1995

[16] R. Fluck, G. Zhang, U. Keller, K. Weingarten, and M. Moser, "Diode-pumped passively mode-locked 1.3-μm Nd:YVO_4 and Nd:YLF lasers by use of semiconductor saturable absorbers," *Opt. Lett.*, **21**, pp. 1378-1380, 1996

[17] D. Kopf, G. Zhang, R. Fluck, M. Moser, and U. Keller, "All-in-one dispersion-compensating saturable absorber mirror for compact femtosecond laser sources," *Opt. Lett.*, **21**, pp. 486-488, 1996

[18] U. Keller, K. Weingarten, F. Kärtner, D. Kopf, B. Braun, I. Jung, R. Fluck, C. Hönninger, N. Matuschek, and J. Aus der Au, "Semiconductor Saturable Absorber Mirrors (SESAM's) for Femtosecond to Nanosecond Pulse Generation in Solid-State Lasers," *IEEE J. of Sel. Topics in Quantum Electr.*, **2**, pp. 435-453, 1996

[19] B. G. Kim, E. Garmire, S. G. Hummel, and P. D. Dapkus, "Nonlinear Bragg reflector based on saturable absorption," *Appl. Phys. Lett.*, **54**, pp. 1095-1097, 1989

[20] L. R. Brovelli, I. D. Jung, D. Kopf, M. Kamp, M. Moser, F. X. Kärtner, and U. Keller, "Self-starting soliton modelocked Ti-sapphire laser using a thin semiconductor saturable absorber," *Electr. Lett.*, **31**, no. 4, pp. 287-288, 1995

[21] S. Tsuda, W. H. Knox, E. A. de Souza, W. Y. Jan, and J. E. Cunningham, "Low loss intra-cavity AlAs/AlGaAs saturable Bragg reflector for femtosecond mode locking in solid-state lasers," *Opt. Lett.*, **20**, pp. 1406-1408, 1995

[22] L. R. Brovelli, U. Keller, and T. H. Chiu, "Design and operation of antiresonant Fabry-Perot saturable absorbers for mode-locked solid-state lasers," *J. Opt. Soc. Am. B*, **12**, pp. 311-322, 1995

[23] Z. Liliental-Weber, H. J. Cheng, S. Gupta, J. Whitaker, K. Nichols, and F. W. Smith, "Structure and Carrier Lifetime in LT-GaAs," *J. of Electron. Mat.*, **22**, pp. 1465-1469, 1993

[24] U. Keller, T. H. Chiu, and J. F. Ferguson, "Self-starting and self-Q-switching dynamics of passively mode-locked Nd:YLF and Nd:YAG lasers," *Opt. Lett.*, **18**, pp. 217-219, 1992

[25] T. Pfeiffer, J. Kuhl, E. O. Göbel, and L. Palmetshofer, "Temperature dependence of the picosecond carrier relaxation in silicon-irradiated silicon-on-sapphire films," *J. Appl. Phys.*, **54**, pp. 1850-1855, 1987

[26] M. B. Johnson, T. C. McGill, N. G. Paulter, "Carrier lifetimes in ion-damaged GaAs," *Appl. Phys. Lett.*, **54**, pp. 2424-2426, 1989

[27] H. Fujioka, J. Krueger, A. Prasad, X. Liu, and E. R. Weber, "Annealing dynamics of arsenic-rich GaAs formed by ion-implantation," *J. Appl. Phys.*, **78**, pp. 1470-1476, 1995

[28] A. Krotkus, S. Marcinkevicius, J. Jasinski, M. Kaminska, H. H. Tan, and C. Jagadish, "Picosecond carrier lifetime in GaAs implanted with high doses of As ions: An alternative material to low-temperature GaAs for optoelectronic applications," *Appl. Phys. Lett.*, **66**, pp. 3304-3306, 1995

[29] A. Claverie, F. Namavar, and Z. Liliental-Weber, "Formation of As precipitates in GaAs by ion implantation and thermal annealing," *Appl. Phys. Lett.*, **62**, pp. 1271-1273, 1993

[30] H. H. Wang, P. Greiner, J. F. Whitaker, H. Fujioka, J. Jasinski, and Z. Liliental-Weber, "Ultrafast response of As-implanted GaAs photoconductors," *IEEE J. of Sel. Topics in Quantum Electr.*, **2**, pp. 630-635, 1996

[31] J. F. Ziegler, J. P. Biersack, and U. Littmark, "The Stopping and Range of Ions in Solids", 1989, *Pergamon*

[32] H. H. Tan, C. Jagadish, J. Williams, J. Zou, D. J. H. Cockayne, and A. Sikorski, "Ion damage buildup and amorphization process in $Al_xGa_{1-x}As$," *J. Appl. Phys*, **77**, pp. 87-94, 1995

[33] C. Jagadish, H. Tan, J. Jasinski, M. Kaminska, A. Krotkus, and S. Marcinkevicius, "High resistivity and picosecond carrier lifetime of GaAs implanted with MeV Ga ions at high fluences," *Appl. Phys. Lett.*, **67**, pp.1724-1726, 1995

[34] C. Jagadish, H. Tan, J. Jasinski, M. Kaminska, A. Krotkus, and S. Marcinkevicius, "Ultrafast carrier trapping in high energy ion implanted gallium arsenide," *Appl. Phys. Lett.*, **68**, pp. 2225-2227, 1996

[35] W. Walukiewicz, Z. Liliental-Weber, J. Jasinski, M. Almonte, A. Prasad, E. E. Haller, E. R. Weber, P. Greiner, and J. F. Whitaker, "High resistivity and ultrafast carrier lifetime in argon implanted GaAs," *Appl. Phys. Lett.*, **69**, pp.2569-2571, 1996

[36] S. Adachi, Ed., "Properties of Aluminium Gallium Arsenide," *INSPEC*

[37] A. K. Ghatak, K. Thyagarajan, and M. R. Shenoy, "Numerical Analysis of Planar Optical Waveguides Using Matrix Approach," *IEEE J. Lightwave Technol.*, **LT-5**, pp. 660-667, 1987

[38] H. Haug and S. Koch, "Quantum Theory of the Optical and Electronic Properties of Semiconductors", 1994, *World Scientific*

[39] M. Born, E. Wolf, "Principles of Optics", 6th Edition, 1993, *Pergamon*

[40] E. Hecht, "Optics", 2nd Edition, 1987, *Addison-Wesley*

[41] D. C. Hutchings, M. Sheik-Bahae, D. J. Hagan, E. W. Van Stryland, "Kramers-Krönig relations in nonlinear optics," *Optical and Quantum Electron.*, **24**, pp. 1-30, 1992

[42] S. Benjamin, H. Lotka, A. Othonos, and P. Smith, "Ultrafast dynamics of nonlinear absorption in low-temperature-grown GaAs," *Appl. Phys. Lett.*, **68**, pp. 2544-2546, 1996

[43] U. Siegner, R. Fluck, G. Zhang, and U. Keller, "Ultrafast high-intensity nonlinear absorption dynamics in low-temperature grown gallium arsenide," *Appl. Phys. Lett.*, **69**, pp. 2566-2568, 1996

[44] J. Shah, "Ultrafast Spectroscopy of Semiconductors and Semiconductor Nanostructures", 1996, *Springer*

[45] W.-Z. Lin, R. W. Schoenlein, J. G. Fujimoto, and E. P. Ippen, "Femtosecond Absorption Saturation Studies of Hot Carriers in GaAs and AlGaAs," *IEEE J. of Quantum Electr.*, **QE-24**, pp. 267-275, 1988

[46] U. Strauss, W. W. Rühle, K. Köhler, "Auger recombination in intrinsic GaAs," *Appl. Phys. Lett.*, **62**, pp. 55-57, 1993

[47] K. Naganuma, G. Lenz, and E. P. Ippen, "Variable Bandwidth Birefringent Filter for Tunable Femtosecond Lasers," *IEEE J. of Quantum Electr.*, **QE-28**, pp. 2142-2150, 1992

[48] H. W. Kogelnik, E. P. Ippen, A. Dienes, and C. Shank, "Astigmatically Compensated Cavities for CW Dye Lasers," *IEEE J. of Quantum Electr.*, **QE-8**, pp. 373-379, 1972

[49] V. Magni, G. Cerullo, S. De Silvestri, and A. Monguzzi, "Astigmatism in Gaussian-beam self-focusing and in resonators for Kerr-lens mode locking," *J. Opt. Soc. Am. B*, **12**, pp. 476-485, 1995

[50] R. L. Fork, O. E. Martinez, and J. P. Gordon, "Negative dispersion using pairs of prisms," *Opt. Lett.*, **9**, pp. 150-152, 1984

[51] R. L. Fork, C. H. Brito Cruz, P. C. Becker, C. V. Shank, "Compression of optical pulses to six femtoseconds by using cubic phase compensation," *Opt. Lett.*, **12**, pp. 483-485, 1987

[52] F. X. Kärtner, L. R. Brovelli, D. Kopf, M. Kamp, I. Calasso, and U. Keller, "Control of solid state laser dynamics by semiconductor devices," *Opt. Eng.*, **34**, pp. 2024-2036, 1995

[53] C. Huang, M. T. Asaki, S. Backus, M. M. Murnane, H. C. Kapteyn, and H. Nathel, "17-fs pulses from a self-mode-locked Ti-sapphire laser," *Opt. Lett.*, **17**, pp. 1289-1291, 1992

[54] W. H. Knox, D. S. Chemla, G. Livescu, J. E. Cunningham, and J. E. Henry, "Femtosecond carrier thermalization in dense Fermi seas," *Phys. Rev. Lett.*, **61**, pp. 1290-1293, 1988

[55] F. X. Kärtner and U. Keller, "Stabilization of solitonlike pulses with a slow saturable absorber," *Opt. Lett.*, **20**, pp. 16-18, 1995

[56] A. Hasegawa, F. Tappert, "Transmission of stationary nonlinear optical pulses in dispersive dielectric fiber. I. Anomalous dispersion," *Appl. Phys. Lett.*, **23**, pp. 142-144, 1973

[57] F. Salin, P. Grangier, G. Roger, and A. Brun, "Experimental Observation of Nonsymmetrical N=2 Solitons in a Femtosecond Laser," *Phys. Rev. Lett.*, **60**, pp. 569-572, 1988

[58] A. B. Grudinin, D. J. Richardson, and D. N. Payne, "Energy Quantisation in Figure Eight Fibre Laser," *Electron. Lett.*, **28**, pp. 67-68, 1992

[59] C. Spielmann, P. F. Curley, T. Brabec, and F. Krausz, "Ultrabroadband Femtosecond Lasers," *IEEE J. of Quantum Electr.*, **QE-30**, pp. 1100-1114, 1994

[60] J. Aus der Au, D. Kopf, F. Morier-Genoud, M. Moser, and U. Keller, "60-fs pulses from a diode-pumped Nd:glass laser," *Opt. Lett.*, **22**, pp. 307-309, 1997

[61] A. B. Grudinin, D. J. Richardson, and D. N. Payne, "Passive harmonic modelocking of a fibre soliton ring laser," *Electron. Lett.*, **29**, pp. 1860-1861, 1993

[62] M. E. Fermann, and J. D. Minelly, "Cladding-pumped passive harmonically mode-locked fiber laser," *Opt. Lett.*, **22**, pp. 970-972, 1996

[63] A. B. Grudinin, and S. Gray, "Passive harmonic mode locking in soliton fiber lasers," *J. Opt. Soc. Am. B*, **14**, pp. 144-154, 1997

[64] B. C. Collings, K. Bergman, S. T. Cundiff, S. Tsuda, J. N. Kutz, J. E. Cunningham, W. Y. Jan, M. Koch, and W. H. Knox, "Short Cavity Erbium/Ytterbium Fiber Lasers Mode-Locked with a Saturable Bragg Reflector," *IEEE J. of Sel. Topics in Quantum Electr.*, **2**, pp. 1065-1074, 1997

[65] B. C. Collings, K. Bergmann, and W. H. Knox, "Stable multigigahertz pulse-train formation in a short-cavity passively harmonic mode-locked erbium / ytterbium fiber laser," *Opt. Lett.*, **23**, pp. 123-125, 1998

[66] B. C. Collings, K. Bergmann, and W. H. Knox, "True fundamental solitons in a passively mode-locked short-cavity Cr^{4+}-YAG laser," *Opt. Lett.*, **22**, pp. 1098-1100, 1997

[67] A. N. Pilipetskii, E. A. Golovchenko, and C. R. Menyuk, "Acoustic effect in passively mode-locked fiber ring lasers," *Opt. Lett.*, **20**, pp. 907-909, 1994

[68] J. N. Kutz, B. C. Collings, K. Bergman, and W. H. Knox, "Stabilized Pulse Spacing in Soliton Lasers Due to Gain Depletion and Recovery," *IEEE J. Quantum Electron.*, **QE-34**, pp. 1749-1757, 1998

[69] F. Krausz, M. Fermann, T. Brabec, P. Curley, M. Hofer, M. Ober, C. Spielmann, E. Wintner, and A. Schmidt, "Femtosecond Solid-State Lasers," *IEEE J. of Quantum Electr.*, **QE-28**, pp. 2097-2122, 1992

[70] H. A. Haus, "Theory of modelocking with a fast saturable absorber," *J. Appl. Phys.*, **46**, p. 3049, 1975

[71] F. X. Kärtner, I. D. Jung, and U. Keller, "Soliton Mode-Locking with Saturable Absorbers," *IEEE J. of Sel. Topics in Quantum Electr.*, **2**, pp. 540-556, 1996

[72] N. Akhmediev and A. Ankiewicz, "Solitons, Nonlinear Pulses and Beams", 1997, Chapman & Hall (London)

[73] F. X. Kärtner, J. Aus der Au, and U. Keller, "Mode-Locking with Slow and Fast Saturable Absorbers - What's the Difference?," *IEEE J. of Sel. Topics in Quantum Electr.*, **4**, pp. 159-168, 1998

[74] M.J. Lederer, B. Luther-Davies, H.H. Tan, C. Jagadish, N. N. Akhmediev, and J. M. Soto-Crespo, "Multi-pulse Operation of a Ti:Sapphire Laser Mode-locked by an Ion-implanted Semiconductor Saturable Absorber Mirror," *J. Opt. Soc. B*, accepted for publication, Feb. 1999

[75] G. P. Agrawal, "Nonlinear Fiber Optics", 1989, *Academic Press*

[76] A. E. Siegman, "Lasers", 1986, *University Science Books*

[77] R. Takahashi, Y. Kawamura, and H. Iwamura, "Ultrafast 1.55 μm all-optical switching using low-temperature-grown multiple quantum wells," *Appl. Phys. Lett.* **68**, 123-125, 1996

[78] E. S. Harmon, M. R. Melloch, J. M. Woodall, "Carrier lifetime versus anneal in low temperature growth GaAs," D. D. Nolte, N. Otsuka, and C. L. Chang, *Appl. Phys. Lett.* **63**, 2248-2250, 1993

[79] M. Lambsdorff, J. Kuhl, J. Rosenzweig, A. Axmann, and Jo. Schneider, "Subpicosecond carrier lifetimes in radiation-damaged GaAs," *Appl. Phys. Lett.* **58**, 1881-1883, 1991

[80] M. R. Melloch, J. M. Woodall, E. S. Harmon, N. Otsuka, F. H. Pollak, D. D. Nolte, R. M. Feenstra, and M. A. Lutz, "Low-Temperature Grown III-V Materials," *Annu. Rev. Mater. Sci.* **25**, 547-600, 1995

[81] X. Liu, A. Prasad, J. Nishio, E. Weber, Z. Liliental-Weber, and W. Walukiewicz, "Native point defects in low-temperature-grown GaAs," *Appl. Phys. Lett.* **67**, 279-281, 1995

[82] M. Haiml, A. Prasad, F. Morier-Genoud, U. Siegner, U. Keller, and E. Weber, "Ultrafast response times and enhanced optical nonlinearity in annealed and Beryllium doped low-temperature grown GaAs," 10th Conference on Semiconducting and Insulating Materials, SIMC-X 1998, June 1-5, Berkeley, California, talk Tu2.2

[83] R. H. Jacobsen, K. Birkelund, T. Holst, P. U. Jepsen, and S. R. Keiding, "Interpretation of photocurrent correlation measurements used for ultrafast photoconductive switch characterization," *J. Appl. Phys.* **79**, pp. 2649-2657, 1996

[84] personal communication with M. Haiml, Ultrafast Laser Physics, Institute of Quantum Electronics, ETH Zuerich.

[85] G. P. Agrawal, and A. Olsson, "Self-Phase Modulation and Spectral Broadening of Optical Pulses in Semiconductor Laser Amplifiers," *IEEE J. of Quantum Electr.*, **QE-25**, pp. 2297-2306, 1989

[86] H. S. Loka, S. D. Benjamin, and P. W. E. Smith, "Optical Characterization of Low-Temperature-Grown GaAs for Ultrafast All-Optical Switching Devices," *IEEE J. of Quantum Electr.*, **QE-34**, pp. 1426-1437, 1998

[87] J. R. Karin, A. V. Uskov, R. Nagarajan, J. E. Bowers, and J. Mork, "Carrier heating dynamics in semiconductor waveguide saturable absorbers," *Appl. Phys. Lett.* **65**, 2708-2710, 1994

[88] J. R. Karin, R. J. Helkey, D. J. Derickson, R. Nagarajan, D. S. Allin, J. E. Bowers, and R. L. Thornton, "Ultrafast dynamics in field-enhanced saturable absorbers," *Appl. Phys. Lett.* **64**, 676-678, 1994

[89] G. T. Maker, and A. I. Ferguson," Mode locking and Q-switching of a diode laser pumped neodymiundoped yttrium lithium fluoride laser," *Appl. Phys. Lett.* **54**, pp. 403, 1989

[90] K. J. Weingarten, D. C. Shannon, R. W. Wallace, and U. Keller, "Two-gigahertz repetition-rate, diode-pumped, mode-locked Nd:YLF laser," *Opt. Lett.* **15**, pp. 962-964, 1990

[91] N. Sarukura, Y. Ishida, and H. Nakano, "Generation of 50 fsec pulses from a pulse-compressed, cw, passively mode-locked Ti:sapphire laser," *Opt. Lett.*, **16**, pp. 153-155, 1991

[92] B. Braun, F. X. Kärtner, M. Moser, G. Zhang, and U. Keller, "56 ps passively Q-switched diode-pumped microchip laser," *Opt. Lett.*, **21**, pp. 405-407, 1996

[93] L. Turi, and T. Juasz, "Diode-pumped Nd:YLF all-in-one laser," *Opt. Lett.*, **20**, pp. 1541-1543, 1995

[94] K. X. Liu, C. J. Flood, D. R. Walker, and H. M. van Driel, "Kerr lens mode locking of a diode-pumped Nd:YAG laser," *Opt. Lett.*, **17**, pp. 1361-1363, 1992

[95] B. Henrich, and R. Beigang, "Self-starting Kerr-lens mode locking of a Nd:YAG-laser," *Opt. Commun.*, **135**, pp. 300-304, 1997

[96] J. D. Kafka, M. L. Watts, and J. W. Pieterse, "Synchronously pumped optical parametric oscillators with LiB_3O_5," *J. Opt. Soc. Am. B*, **12**, pp. 2147-2157, 1995

[97] B. Braun, K. J. Weingarten, F. X. Kärtner, and U. Keller, "Continuous-wave mode-locked solid-state lasers with enhanced spatial hole burning, Part I: Experiments," *Appl. Phys. B*, **61**, pp. 429-437, 1995

[98] F. X. Kärtner, B. Braun, and U. Keller, "Continuous-wave mode-locked solid-state lasers with enhanced spatial hole burning, Part II: Theory," *Appl. Phys. B*, **61**, pp. 569-579, 1995

[99] J. W. Matthews, and A. E. Blackslee, "Defects in epitaxial Multilayers, I: Misfit dislocation," *J. Cryst. Growth*, **27**, pp. 118-125, 1974 and J. W. Matthews, and A. E. Blackslee, *J. Cryst. Growth*, **32**, pp. 265, 1976

[100] D. Findlay, and R. A. Clay, "The measurement of internal losses in 4-level lasers," *Phys. Lett.*, **20**, pp. 277-278, 1966

[101] F. Balembois, F. Falcoz, F. Kerboull, F. Druon, P. Georges, and A. Brun, "Theoretical and Experimental Investigations of Small-Signal Gain for a Diode-Pumped Q-Switched Cr:LISAF Laser," *IEEE J. of Quantum Electr.*, **QE-33**, pp. 269-278, 1997

[102] T. J. Kane, J. M. Eggleston, and R. L. Byer, "The Slab Geometry Laser - Part II: Thermal Effects in a Finite Slab," *IEEE J. of Quantum Electr.*, **QE-21**, pp. 1195-1210, 1985

[103] J. M. Eggleston, T. J. Kane, K. Kuhn, J. Unternahrer, and R. L. Byer, "The Slab Geometry Laser - Part I: Theory," *IEEE J. of Quantum Electr.*, **QE-20**, pp. 289-301, 1984

[104] http://www.casix.com

[105] A. A. Kaminskii, "Laser Crystals", 1990, *Springer*

[106] J. E. Bernard, E. McCullough, and A. J. Alcock, "High gain, diode-pumped Nd:YVO_4 slab amplifier," *Opt. Commun.*, **109**, pp. 109-114, 1994

[107] K. Chan, "Multiple-pass laser-diode-pumped Nd:YAG amplifier: design," *Appl. Opt.*, **26**, pp. 3177-3179, 1987

[108] US patent 5 317 585

[109] US patent 4 969 155

[110] F. Hanson, "Cr:LiSAF Slab Laser Performance," *IEEE J. of Quantum Electr.*, **QE-31**, pp. 653-656, 1995

[111] R. J. Shine, Jr., A. J. Alfrey, and R. L. Byer, "40-W cw, TEM_{00}-mode, diode-laser-pumped, Nd:YAG miniature-lab laser," *Opt. Lett.*, **20**, pp. 459-461, 1995

[112] J. Eicher, N. Hodgson, and H. Weber, "Output power and efficiencies of slab laser systems," *J. Appl. Phys.*, **66**, pp. 4608-4613, 1989

[113] H. Tajima, M. Moriyama, N. Tadokoro, H. Hara, and T. Mochizuki, "Performance of Composite Glass Slab Laser," *IEEE J. of Quantum Electr.*, **QE-28**, pp. 1562-1569, 1992

[114] *Laser Focus World*, August 1991, p. 45

[115] A. McInnes, and J. Richards, "Thermal Effects in a Coplanar-Pumped Folded Zigzag Slab Laser," *IEEE J. of Quantum Electr.*, **QE-32**, pp. 1243-1252, 1996

[116] W. Köchner, "Solid-State Laser Engineering", 1992, *Springer*

[117] M. Necati Özisik, "Heat Transfer, a Basic Approach," 1985, *McGraw-Hill*

[118] CVI catalogue

[119] F. Ganikhanov, G.-R. Lin, W.-C. Chen, C.-S. Chang, and C.-L. Pan, "Subpicosecond carrier lifetimes in arsenic-ion-implanted GaAs," *Appl. Phys. Lett.* **67**, pp. 3465-3467, 1995